Single-molecule spectroscopy & super-resolution microscopy at the biochemistry bench

Dissertation zur Erlangung des naturwissenschaftlichen Doktorgrades
Dr. rer. nat. an der Fakultät für Biologie der
Ludwig-Maximilians-Universität München

vorgelegt von

Gustavo Gabriel Moya Muñoz

aus Quito, Ecuador

München 2025

Single-molecule spectroscopy & super-resolution microscopy at the biochemistry bench

Dissertation zur Erlangung des naturwissenschaftlichen Doktorgrades
Dr. rer. nat. an der Fakultät für Biologie der
Ludwig-Maximilians-Universität München

vorgelegt von

Gustavo Gabriel Moya Muñoz

aus Quito, Ecuador

München 2025

Diese Dissertation wurde angefertigt
unter der Leitung von Prof. Dr. Thorben Cordes
im Bereich Biophysik am Department für Mikrobiologie der Fakultät für Biologie
der Ludwig-Maximilians-Universität München

Erstgutachter:	Prof. Dr. Thorben Cordes
Zweitgutachter:	Prof. Dr. Philip Tinnefeld
Tag der Abgabe:	30. Januar 2025
Tag der mündlichen Prüfung:	05. Juni 2025

Erklärung

Ich versichere hiermit an Eides statt, dass meine Dissertation selbstständig und ohne unerlaubte Hilfsmittel angefertigt worden ist.
Die vorliegende Dissertation wurde weder ganz noch teilweise bei einer anderen Prüfungskommission vorgelegt.
Ich habe noch zu keine früheren Zeitpunkt versucht, eine Dissertation einzureichen oder an einer Doktorprüfung teilzunehmen.

München, den 8. Juli 2025

Gustavo Gabriel Moya Muñoz

"Just look at the thing!"

-Richard Feynman-

Abbreviations

A	acceptor Fluorophore
AA	acceptor photon-stream (= f_{Aex}^{Aem})
ABC	ATP-binding cassette
ALEX	alternating laser excitation
APBS	all photon burst search
APD	avalanche photodiode
AV	accessible volume
ACV	accessible contact volume
AXSI	Anomalous X-ray Scattering Interferometry
bp	base pair(s)
BFP	back focal plane (
BSA	bovine serum albumin
CAD	computer-aided design
CMOS	complementary metal-oxide-semiconductor
COT	cyclooctatetraene
CryoEM	cryogenic electron microscopy
D	donor Fluorophore
DA	FRET photon-stream (= f_{Dex}^{Aem})
DCBS	dual-colour burst search
DD	donor photon-stream (= f_{Dex}^{Dem})
DDM	n-dodecyl β-D-maltopyranoside
DEER	double electron electron resonance
DIC	dichroic mirror
DMSO	dimethyl sulphoxide
DNA	deoxyribonucleic acid
dNTP	deoxyribose nucleotide triphosphate
dsDNA	double stranded DNA
DTT	1,4-dithiothreitol
E	FRET-efficiency
E.coli	*Escherichia coli*

EDTA	ethylenediaminetetraacetic acid
ELISA	enzyme linked immunosorbent assay
EPR	electron paramagnetic resonance
FCS	fluorescence correlated spectroscopy
FWHM	full width at half maximum
FLIM	fluorescence-lifetime imaging microscopy
FRET	Förster resonance energy transfer
GFP	green fluorescent protein
IB	imaging buffer
IPTG	isopropyl-β-D-thiogalactopyranosid
ISC	inter-system crossing
kbp	kilo basepair
Kd	dissociation constant
LB	Lysogeny Broth (medium)
LC-MS	liquid chromatography mass spectrometry
LMU	Ludwig Maximilian University
MBP	maltose binding protein (= MalE)
MD	molecular dynamics
MST	microscale thermophoresis
NMR	nuclear magnetic resonance (spectroscopy)
NP	nano particle
Obj	objective
OP	optical fiber
PAINT	point accumulation for imaging in nanoscale topography
PALM	photoactivated localization microscopy
PBS	phosphate buffered saline
PCR	polymerase chain reaction
PH	pinhole
PSF	point spread function
PELDOR	pulsed electron-electron double resonance
PET	photoinduced electron transfer
PLA	polylactic acid
PMT	photomultiplier tube

ROI	region of interest
ROXS	reducing and oxidizing system
S	stoichiometry
SAXS	Small-angle X-ray scattering
SBD	substrate binding domain
SBP	substrate binding protein
SD	standard deviation
SDS-PAGE	sodium dodecyl sulfate polyacrylamide gel electrophoresis
SEC	size-exclusion chromatography
sm	single-molecule
SMLM	single-molecule localization microscopy
SPAD	single-photon avalanche diode
ssDNA	single stranded DNA
STED	stimulated emission depletion microscopy
STORM	stochastic optical reconstruction microscopy
TCSPC	Time-correlated single photon counting
TDM	transition dipole moment
TIRF	total internal reflection fluorescence
TL	tube lens
TMR	tetramethylrhodamine
TPU	thermoplastic polyurethane
Tx	Trolox (6-hydroxy-2,5,7,8-tetramethylchroman-2-carboxylic acid)
TMR	tetramethylrhodamine
UV	ultra violet light
wt	wild type
w/v	weight per volume

Abstract

Single-molecule spectroscopy and super-resolution microscopy offer valuable insights into molecular dynamics but have been limited by high costs and technical complexity. These tools are mostly accessible to specialized labs with custom-built systems. This work aims to make them more affordable and accessible to a wider range of researchers, including those in smaller or resource-limited labs.

A major challenge in single-molecule experiments is the variability in experimental setups, often due to the use of home-built systems, a limitation common across all single-molecule techniques. In the context of smFRET, which this study focused on, applying established data correction routines enabled reliable and comparable results across different setups. The most critical parameter influencing data accuracy was the gamma factor, which accounts for differences in the quantum yields of the donor and acceptor fluorophores, as well as the wavelength-dependent detection efficiencies of the point detectors. However, its overall impact was minimal given the typical FRET efficiency differences observed in biomolecules, underscoring the importance of thoughtful protein and fluorophore design to minimize variability.

Comparisons with other techniques, like Pulsed Electron-Electron Double Resonance (PELDOR) and anomalous X-ray scattering interferometry (AXSI), confirmed that smFRET provides consistent distance measurements. Discrepancies arose due to fluorophore-protein interactions but could be mitigated through careful experimental design.

A key development of this work is Brick-MIC, an affordable, open-source platform for single-molecule experiments. Built with 3D printing and open-source software, Brick-MIC allows researchers to customize setups at a fraction of traditional costs. It supports techniques like smFRET, fluorescence correlation spectroscopy (FCS), and super-resolution imaging, making these tools more accessible to the scientific community.

In a simplified iteration, a blue-green FRET system was created using a 488 nm laser, making it cost-effective while still providing valuable insights into biomolecular conformational changes. This system, while lacking stoichiometric information, enables the observation of biomolecule movements, catering to application-driven studies.

Additionally, Brick-MIC was applied to nanoparticle detection, specifically identifying SARS-

CoV-2 virus particles. By combining microfluidics, fluorescence correlation spectroscopy, and dual-layer detection strategies, this work enabled rapid and specific virus detection, demonstrating the practical applications of this affordable platform in diagnostics and public health.

Acknowledgements

I began this journey in 2020, in the midst of a global pandemic. It was during this time that my boss, Thorben Cordes, approached me with what seemed like a completely outrageous idea: ”Hey, let’s build a virus detector.” I laughed at first, thinking it was a joke, but his unwavering expression quickly made me realize he was serious. Trying to compose myself, I asked, ”Well, where do we start?” And the rest, as they say, is history. For this reason, I want to express my deepest gratitude to Thorben, who believed in me, gave me his complete trust, and provided me with the freedom and creative space to dream big and make it possible. I will forever be grateful for his encouragement and for showing me that daring to think big is an option. I am also incredibly happy to continue working together—not just as my boss, but also as a friend.

I also want to extend my heartfelt thanks to my collaborator and good friend Eitan Lerner, who is, without a doubt, a visionary and a bit of a madman (in the best way possible). Your tenacity has been incredibly inspiring, and without your support and relentless drive, I would have accomplished only a fraction of what we did together. I am also deeply grateful to Rainer Erdmann, Jürgen Breitlow, and Felix Koberling for their belief in me and for providing the resources and instrumentation necessary for my work. It is exciting to know that this is just the starting point of what we can achieve together, and I look forward to continuing this journey with all of you.

To my lab mates and former members of the group—you have made every day in the lab a joyful experience. Special thanks to Marija Ram, who cared for me like a mother. I will always be grateful to you. Pazit Con, thank you for grounding me every time I needed it; only wisdom ever came from you. To my students, Philipp Klocke, Konstantin Schütze, Robert Hollmann, and Jorge Luna—besides being immensely talented, you were a joy to work with. Philipp, you were indispensable, and I am still looking for someone like you! Thank you for your support and friendship. To Niels Zijlstra, everything I can do today is thanks to you. I am proud to be a part of your school and am honored to carry on what I’ve learned from you.

To my collaborators, it was a pleasure to share lab spaces, ideas, and laughs with you: Paz Drori, Yair Razvag, Nicolas Wendler, Paul Harris, Oliver Brix, Joana Fort, and Adrià Nicolás-Aragó. Working with you was both inspiring and enjoyable.

To my mentors, who guided me through this journey: Paulina Romo, Adrian Passow, Kai and Maria Lamottke, Michael Boshart, Philipp Landerer, and the entire IEC team—thank you for your guidance and encouragement.

To my family, who has believed in me and supported me unconditionally for as long as I can remember—I hope one day I can give back to you as much as you've given me. A special thanks to my grandfather, Olmedo Muñoz, who was my biggest fan and made it possible for me to pursue my dreams. From the bottom of my heart, thank you, Papa. I would give anything for you to see where I am today. I miss you every day.

Finally, to the person who witnessed every part of this madness, Zane—you bring calmness, joy, and a smile to my face every single day. We truly are the best team, and I love you.

This journey has been one I poured my heart into, and I enjoyed every single step of it because of all of you. I would gladly do it all over again.

Thank you all from the bottom of my heart.

-Gustavo Gabriel Moya Muñoz-

Contents

List of Figures

1

Introduction

Horses have been depicted in prehistoric cave paintings in France, the temples of ancient Egypt, and as statues in ancient Greece during classical antiquity[1,2]. However, due to their fast motion, which the naked eye cannot break down, the precise understanding of their galloping motion—and the broader question of whether all feet are ever simultaneously off the ground—remained an unresolved mystery, leading to artistic guesswork that often resulted in depictions of physically impossible horse postures, which in turn became a contentious point of debate among artists.

The invention of the photo camera in the early 19th century was a step forward in terms of capturing real images of the real world, however the long exposure times needed for capturing an image, made this new tool incapable of depicting the fast locomotion of a horse, resulting in blurry images[3].

This changed with Edward Muybridge, an experimental photographer of the late 19th century, who improved the acquisition time of the camera by experimenting with various equipment and especially with different photo chemicals, reducing the exposure time to a fraction of a second. This advancement made it possible to capture a snapshot of a moving horse. However, this was only one data point, and while it provided groundbreaking evidence of a horse's motion, it was insufficient to fully resolve broader questions about galloping dynamics[4]. In 1876, Muybridge created his most groundbreaking experimental setup, where he lined up 12 state-of-the-art cameras in a row, each triggered automatically by a series of wires ruptured as the horse passed. Using this method, Muybridge successfully captured a series of photographs[4,5] that depicted the complete locomotion of a galloping horse, including two key shots that showed all four feet off the ground.

This milestone was achieved through numerous advancements in photographic camera technology, including the use of lenses instead of pinholes to improve spatial resolution, the development of faster sensors with more photosensitive chemicals[3,4,5], and the alignment of multiple self-triggering cameras in a row to enhance temporal resolution, with the key breakthrough being the ability to capture and analyze time itself, which is crucial for answering questions about motion and dynamic processes, not only in horses but across various scientific fields.

The challenges we face in the 21st century are similar to those mentioned above. A major challenge is to unravel the fundamental laws of life, down to the intricate motion and synchronized choreography of molecules[6,7,8]. While many techniques in biophysics can provide valuable information about biological systems, such as protein structure through X-ray crystallography[9] and CD spectroscopy[10], protein-protein affinities through ITC[11] and MST[12], or biomolecule sizes through SDS-PAGE[13] or SEC[14], remaining limitations blur metastable and temporally heterogeneous biomolecular states, such as in a conformational ensemble, or when spatial interactions occur over the nanometer length scale[15]. One of the main obstacles when studying biomolecules is their mere size, which on average is around 5 to 10 nm[16], which is much smaller than e.g., the diffraction-limited resolution of an optical microscope. Selecting electromagnetic radiation with shorter wavelength to probe biomolecules is not an option given the high ionizing energy for example of X-rays or electron beams, which can damage or destroy the biomolecules. However, it is still possible to visualize biomolecules by crystallizing or immobilizing them, as in the case of X-ray crystallography[9] and cryo-EM[17], though these methods typically provide only a single snapshot of the biomolecule's structure. Therefore, biomolecule interactions, sizes, and processes are typically measured indirectly, e.g., through heat flow when biomolecules bind or undergo conformational changes, such as in ITC[11]; estimation of sizes based on movement and interactions through another medium, such as SDS-PAGE[13] and SEC[14]; or monitoring reaction products or adducts in the visible spectrum using absorbance or fluorescence measurements[18]. However, these techniques require large amounts of highly purified samples, and bulk studies inevitably blur and average out heterogeneous processes at the individual molecule level due to the bulk nature of the measurements[19]. This limitation highlights the challenge of studying dynamic processes at a single-molecule resolution, a challenge not unlike the one faced by early photographers capturing the precise motion of a galloping horse. Just as photographers had to overcome technological limitations to capture movement, biophysicists also had to overcome similar challenges to capture the dynamic behavior of individual biomolecules.

In the past 30 years, advancements in optical instrumentation and the use of fluorescent tags have enabled us to visualize biomolecules and their motion at the single-molecule level, becoming a powerful tool for understanding life from its smallest building blocks[20,21,22,23]. As in the case of Edward Muybridge, this molecular understanding is now possible not only due to advancements in the spatial and temporal resolution of optical systems but also thanks to a deep understanding of fluorophores and the phenomenon of fluorescence, which make biomolecules visible in the first place and go hand in hand with the development of optical microscopes[24,23,25,20,21,22].

The combination of purpose-built optical microscopes and specially designed fluorophores has led to the development of several advanced single-molecule microscopy techniques. This progress was recognized with the 2014 Nobel Prize in Chemistry, awarded to Eric Betzig, Stefan Hell, and William E. Moerner ”for the development of super-resolved fluorescence microscopy.” Their work led to groundbreaking techniques such as stimulated emission depletion microscopy (STED)[26], photo-activated localization microscopy (PALM)[27], and stochastic optical reconstruction microscopy (STORM)[28], which surpass the diffraction limits proposed in by Ernst Abbe's theory. These methods achieve super-resolution by selectively activating or deactivating fluorophores (e.g., STED and PALM) or by inducing fluorophore blinking or transient exchange (e.g., dSTORM and PAINT[29,30]).

In addition to these imaging techniques, other methods like fluorescence correlation spectroscopy (FCS)[31,32,33] and single-molecule Förster resonance energy transfer (smFRET)[34,32,35,36,37] have further expanded our ability to study properties of biomolecules in with high time resolution. FCS allows for the analysis of molecular dynamics by measuring fluctuations in fluorescence intensity, providing insights into diffusion rates and molecular interactions. Meanwhile, smFRET enables the observation of conformational changes and interactions at the single-molecule level by detecting energy transfer between two fluorophores, offering valuable information on the structural dynamics of biomolecules[38,39,40,41].

The success of these techniques relies heavily on the understanding of fluorescence itself, which has undergone significant advancements in recent years. Fluorescence, a phenomenon where a molecule absorbs light at one wavelength and re-emits it at a longer wavelength, is the foundation for many of these methods[32,42,43,44]. The ability to manipulate and control fluorescence emissions through various fluorophores, and to detect and measure these emissions with high precision, has been crucial in developing tools that allow us to probe molecular processes with unprecedented spatial and temporal resolution. Understanding the fundamentals of fluorescence not only enables the improvement of existing techniques but also provides the basis for the creation of new approaches to study biomolecular dynamics at the single-molecule level.

1.1 Fundamentals of Fluorescence[§]

Fluorescent substances and materials are among the smallest light-emitting units down to the molecular level, ranging from 20 to 100 atoms and 1 to 2 nm in dimensions (for organic fluorophores)[46]. These light-emitting materials range from organic fluorophores[32], fluorescent proteins[47], and quantum dots[48], which can be tailored for specific assay requirements[49,50,51]. For example, organic fluorophores are frequently tailored for DNA hybridization assays, where dyes selectively bind to nucleic acids to report on hybridization events[52]. Similarly, tailored fluorescent proteins are used in calcium imaging assays to monitor intracellular calcium levels[53], and in quantum dot-based tracking assays, which allow long-term observation of cellular processes due to their exceptional photostability[46].

Fluorescence was named by the scientist George Gabriel Stokes in his work 'On the Change of Refrangibility of Light' in 1852, where he described the shift of absorption and emission color of light by liquid solutions[54]. Advancements in the understanding of light as an electromagnetic wave, described by Maxwell's electromagnetism theories[55], along with the introduction of quantum mechanics in the 20th century, clarified the underlying mechanisms of electronic transitions within molecules[32].

[§] The concepts discussed in this Sections are based on the textbooks by Sauer, Hofkens, and Enderlein[42] (Chapter 1), Lakowicz[32] (Chapters 1, 3 and 6), Sakurai (Chapter 5) and Walla[45] (Chaper 1

At its core, fluorescence occurs when a substance absorbs a photon of a specific wavelength, elevating an electron to higher energy levels. This absorption process generates an excited singlet state, which is characterized by the temporary presence of an electron in higher energy orbitals (Figure 1.1). The absorption and subsequent deactivation process can be understood considering the frontier orbitals HOMO and LUMO (Highest Occupied Molecular Orbital – Lowest Unoccupied Molecular Orbital) concept: in the ground state, electrons occupy the HOMO, which is the highest energy orbital that contains electrons. When a photon with the right energy is absorbed, an electron from the HOMO is excited to the LUMO, the lowest energy orbital that is unoccupied in the molecule 1.2.

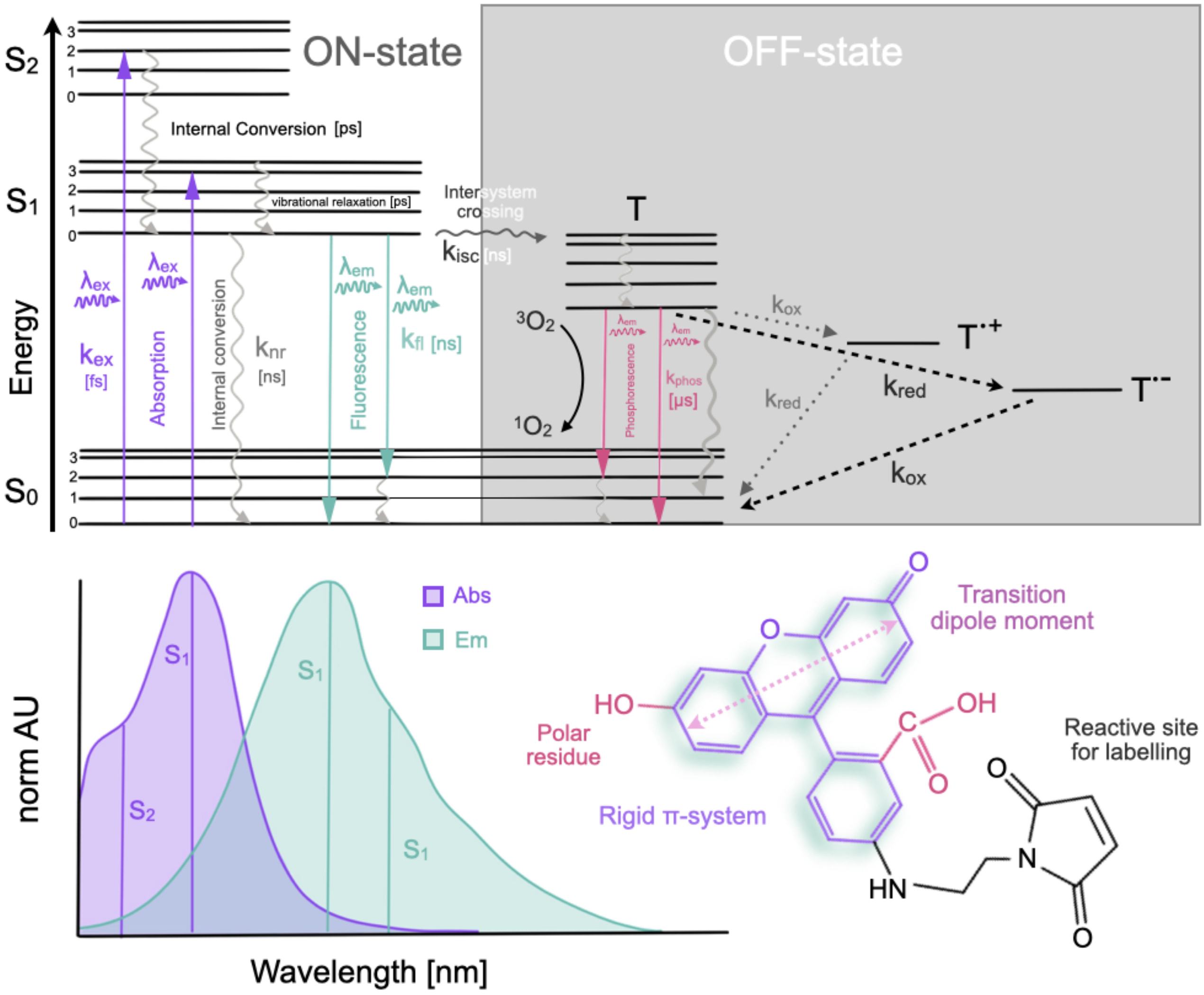

Figure 1.1: Basics of fluorescence: The upper panel depicts a Jablonski diagram of a hypothetical fluorophore, illustrating excitation levels in the ground state (S0), excited states (S1, S2), and the triplet state (T). Colored arrows indicate energy transitions involving the absorption or emission of photons, while curly arrows represent non-radiative transitions such as internal conversions and vibrational relaxation. Dotted arrows signify redox-relaxation pathways in the off-state of a fluorophore. The transition rates are denoted as k_{ex}: excitation rate, k_{fl}: intrinsic fluorescence emission rate, k_{nr}: non-radiative decay rate, k_{ISC}: intersystem crossing rate, k_{pho}: phosphorescence emission rate, and $k_{red/ox}$: redox rate. The lower left panel displays representative absorption and emission spectra of a hypothetical fluorophore, corresponding to the Jablonski diagram above. The lower right panel shows a Rhodamine fluorophore with its functional chemical groups.

The gap between the HOMO and LUMO, known as the band gap, determines the energy required to promote the electron to the excited state. This energy difference also dictates the wavelength of light absorbed: a larger HOMO-LUMO gap requires higher energy (shorter wavelength) light, while a smaller gap corresponds to light of longer wavelengths.

However, the excited state is inherently unstable. The electron quickly relaxes back to a lower energy orbital, usually the HOMO. During relaxation, the excess energy gained from the absorbed photon can be released in the form of light, which has a longer wavelength than the absorbed light due to the energy lost in relaxation. This emitted light is what we perceive as fluorescence. This radiative relaxation process typically takes place on the timescale of nanoseconds.

However, there are alternative relaxation pathways in which the excess energy can be dissipated which explains why not every molecule fluoresces. Quantum mechanics describes the behavior of electrons within molecules in a probabilistic manner, where certain molecular properties and geometries favor different relaxation probabilities from others[32,42,56] (figure 1.1):

For instance, when a molecule absorbs a photon, an electron is excited from the ground state (S0) to an excited singlet state S1, S2, or even higher, depending on the photon energy. From here, several relaxation pathways are possible.

The electron starts dissipating energy through internal conversion, which involves a very rapid transfer of energy through vibrational relaxation, leading to a return to the lowest singlet state (S1) which typically occurs within femtoseconds to picoseconds. The same process can further relax the electron to the ground state (S0) leading to a non-radiative decay within a time scale of picoseconds to nanoseconds[57].

The excited electron can also undergo intersystem crossing, transitioning from the singlet excited state (S1) to a longer-lived triplet excited state (T1) due to a change in electron spin. This process typically occurs at rates ranging from nanoseconds to microseconds and is spin-forbidden.

From the triplet excited state (T1), the molecule can emit a photon and transition back to the ground state (S0), resulting in phosphorescence. This process on the other hand occurs with rates ranging from microseconds to milliseconds[58].

External factors such as collisions with other molecules or impurities can lead to quenching of the excited state's energy without photon emission. This process, known as external quenching, results in a non-radiative return to the ground state (S0) with timescales similar to those of non-radiative decay[49] 1.3.

Fluorophores can also undergo intersystem crossing to populate the longer-lived triplet state (T1). In the presence of molecular oxygen (O_2), the triplet-state fluorophore can interact with oxygen molecules[49]. During this process, energy is transferred from the excited fluorophore to molecular oxygen, promoting the formation of highly reactive singlet oxygen ($^1O_2$). Singlet oxygen is a potent oxidizing agent and can induce chemical reactions that damage the fluorophore molecule, leading to photobleaching (figure 1.1).

The property of fluorophores that favors light absorption and radiative decay are those that possesses a rigid conjugated π-electron system[43]. This arrangement creates a continuous orbital network where electrons can move freely. In this system, the π-electrons are delocalized, meaning they are not localized to specific atoms but instead spread out over multiple atoms.

A large delocalized system shows an overall large transition dipole moment giving rise to high absorption cross sections and high radiative rates. Additionally, the rigidity of the π-electron system prevents non-radiative decay pathways, such as internal conversion or vibrational relaxation, thereby promoting the radiative decay pathway toward the ground state[32,56] (Figure 1.1).

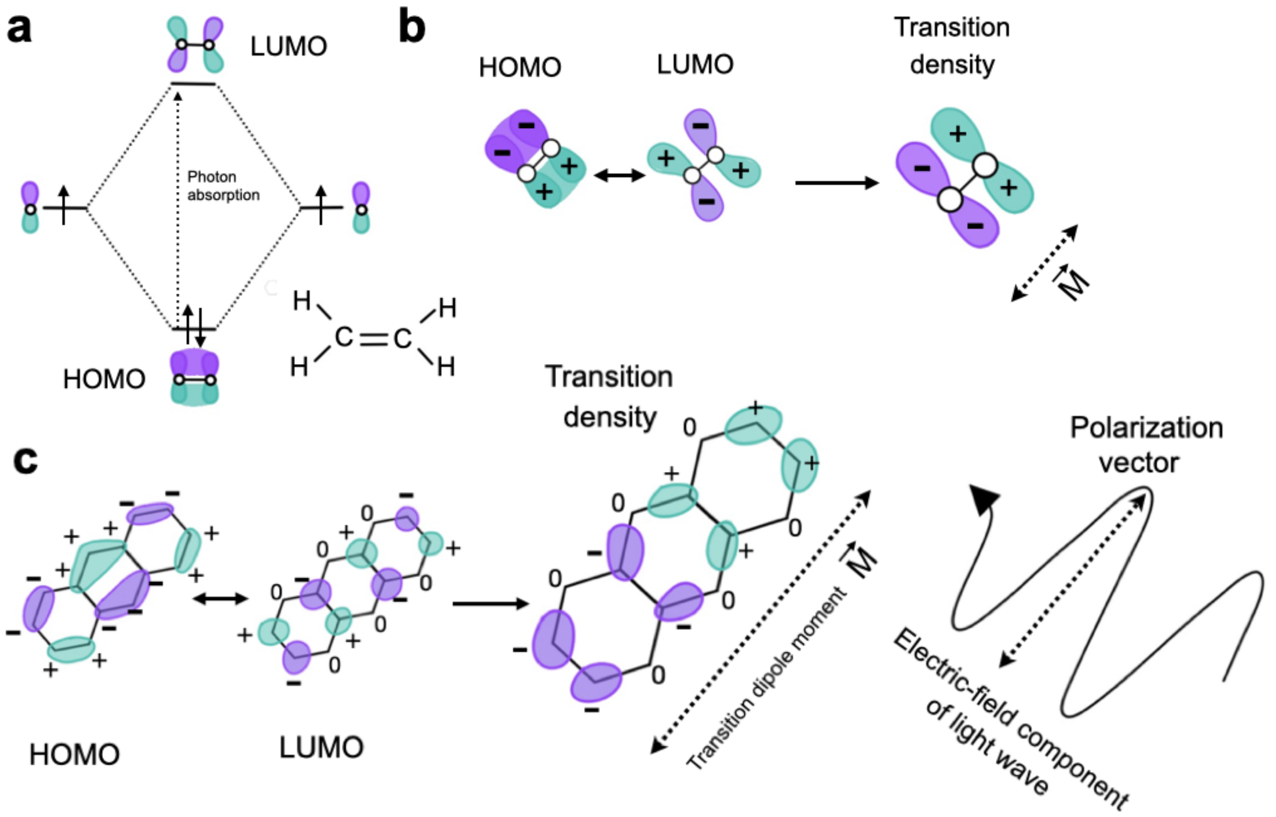

Figure 1.2: Transition dipole moment of ethylene and anthracene: a) Schematic representation of bonding π- and antibonding π^*-orbitals constructed from atomic p-orbitals for ethylene, with lower and higher energy levels corresponding to the ψ_{HOMO} and ψ_{LUMO} orbitals, respectively. Wave function phases are depicted in purple for negative phases and green for positive phases. b) and c) Depict the wave functions of ψ_{HOMO} and ψ_{LUMO} of ethylene and anthracene, respectively, along with the corresponding transition density maps. The resulting transition dipole moments are aligned in the optimal direction of the oscillating electric field component of light (polarization vector) in relation to the direction of the transition dipole moment. The larger π-orbital system and molecular geometry of anthracene produce a larger transition dipole moment compared to ethylene.

A deeper understanding of this behavior involves examining the phase properties of π-orbitals, which are characterized by nodal planes where the wave function changes sign, creating distinct positive and negative regions (figure 1.2). These regions are not related to charge but reflect the oscillatory nature of electrons within molecular orbitals. The phase of the wave function plays an important role in determining the properties of conjugated π-systems, as the overlap of orbitals with matching phases leads to constructive interference and bonding interactions, which lower the energy of the system and stabilize the molecule. In contrast, overlapping regions of opposite phase result in destructive interference and antibonding interactions, which increase the system's energy and can lead to instability or weaker bonding. These binding and antibonding interactions are crucial in understanding the electronic structure and stability of molecules, particularly in conjugated systems where the delocalization of electrons plays a key role in determining their spectroscopic properties.

These interactions also directly influence electronic transitions, such as the $\pi \rightarrow \pi^*$ transition, where an electron is excited from the bonding π orbital (HOMO) to the antibonding π^* orbital (LUMO). The energy difference between these orbitals—shaped by the binding and antibonding interference—determines the absorption of light and the potential for fluorescence. A smaller HOMO-LUMO gap, resulting from extensive conjugation, allows for a transition with lower energy and longer wavelength, contributing to the system's optical properties.

This interplay of orbital phases and electronic transitions is further described by the transition dipole moment (TDM), a vector quantity that provides insight into the interaction of a molecule with light[59,60]. The TDM represents the direction of redistribution of electron density during an electronic transition, such as the excitation of an electron from the HOMO to the LUMO. Its magnitude and direction are determined by the spatial overlap of the molecular orbitals involved in the transition and the phase alignment of their wave functions.

Mathematically, the TDM is calculated as the integral of the product of the HOMO and LUMO wave functions, weighted by the dipole operator, which accounts for the positional distribution of electron density within the molecule. This can be expressed as:

$$\boldsymbol{\mu}_{\mathrm{TDM}} = \int \psi_{\mathrm{HOMO}}(\mathbf{r})^* \, \hat{\mu} \, \psi_{\mathrm{LUMO}}(\mathbf{r}) \, d^3\mathbf{r} \tag{1.1}$$

where ψ_{HOMO} and ψ_{LUMO} are the wave functions of the HOMO and LUMO, respectively, $\hat{\mu}$ is the dipole operator ($\hat{\mu} = -e\mathbf{r}$, with $\mathbf{r}$ being the electron position vector), and $d^3\mathbf{r}$ represents integration over all spatial coordinates. The resulting integral, often referred to as the transition density, quantifies the likelihood of the electronic transition and reflects the spatial and phase relationships between the orbitals.

The alignment of the TDM relative to the polarization direction of the incident light is a crucial factor in determining the likehood of light absorption. When the TDM is oriented parallel to the electric field vector of the polarized light, the fluorophore achieves maximum absorption probability. Contrarily, if the TDM is perpendicular to this field, the absorption probability is minimal.

This geometric dependence has profound implications in fluorescence applications. For instance, the orientation of fluorophores immobilized on surfaces or embedded in biological structures can affect their excitation efficiency and emission intensity. It also forms the basis for techniques like fluorescence anisotropy and polarization microscopy, which exploit variations in TDM orientation to study molecular interactions, conformations, and dynamics.

In conjugated π-systems, the delocalized electron cloud enhances the overlap of wave functions during $\pi \rightarrow \pi^*$ transitions, leading to strong TDMs that favor light absorption and efficient fluorescence. The phase properties of these orbitals also influence the polarization properties of emitted light, making them valuable tools for investigating molecular environments and designing fluorophores with desired photophysical characteristics[61].

1.2 Fluorescence lifetimes and Quantum Yields[§]

Fluorescent lifetimes and quantum yields are important properties of fluorescence that provide quantitative information about the fluorophore and its environment[62,63]. The emission of photons from an excited state follows a single exponential decay. If a number of fluorophores are excited at the same time with a light pulse, the decay towards the ground state is described by:

$$[M^*](t) = [M^*]_0 * e^{(-kt)} \tag{1.2}$$

where $[M^*]_0$ is the population of excited fluorophores at time $t = 0$ and k denotes the sum of all depopulating rates, where $k = \frac{1}{\tau}$. The fluorescence lifetime τ describes the average time a fluorophore spends in the excited state before returning to the ground state. For organic dye molecules, this time is typically in the nanosecond range.

The corresponding emission from the excited fluorophore can be directly related to its fluorescence lifetime:

$$\begin{gathered}[M^*] \propto I \\ I(t) = I_0 * e^{-\frac{t}{\tau}}\end{gathered} \tag{1.3}$$

Where I is the measured light intensity. The fluorescence lifetime is defined here as the time it takes for the intensity to drop to $1/e$ of its initial value I_0 following first-order decay.

The quantum yield Q_{fl} describes the ratio of photons emitted to photons absorbed by a fluorophore. A fluorophore will rarely have an efficiency of 100 percent since the emissive rate k_{fl} competes with

---

[§] The concepts discussed in this Sections are based on the textbooks by Sauer, Hofkens, and Enderlein (Chapter 1), Lakowicz (Chapters 1 and 4) the rate of non-radiative decay k_{nr} that depopulates the singlet state S_1 back to the ground state S_0 1.1. The quantum yield therefore is described by the ratio between emitted and absorbed photons and shows the competition between k_{fl} and k_{nr}, which is given by:

$$Q_{fl} = \frac{k_{fl}}{k_{fl} + k_{nr}} = \frac{Photons_{emitted}}{Photons_{absorbed}} \tag{1.4}$$

The fluorescence lifetime is inversely proportional to the sum of the fluorescence rate k_{fl} and the rate of non-radiative decay k_{nr} that depopulate the excited state:

$$\tau = \frac{1}{k_{fl} + k_{nr}} \tag{1.5}$$

The quantum yield and lifetime of fluorophores are not constant; but depend on the specific environment of the dye molecule which can alter the specific values for both radiative and non-radiative rate constants. Non-radiative decay processes include: internal conversion, intersystem crossing and also intermolecular processes such as energy transfer, collisional quenching, and chemical reactions—like photoinduced electron transfer, protonation/deprotonation, or reactions with oxygen (e.g., singlet oxygen) have to be considered. (figure 1.1). The local environment around the fluorophore, such as solvent polarity, pH, temperature, and the presence of quenchers or other molecules, can influence all rates mentioned above and thus alter the fluorescence lifetime.

1.3 Fluorescence quenching & blinking[§]

Fluorescence quenching refers to the process by which the fluorescence intensity of a fluorophore is reduced through specific interactions or pathways, e.g., with another molecule, environmental factors, or energy transfer. This interaction typically leads to an increased non-radiative relaxation of the excited fluorophore, reducing fluorescence intensity (figure 1.3).

In dynamic quenching, the quencher molecule interacts with the excited state of the fluorophore through collisional encounters. During these collisions, energy is transferred from the excited fluorophore to the quencher molecule, with the energy typically being dissipated non-radiatively instead of via photon emission. Dynamic quenching is described by the Stern-Volmer equation[64,65]:

$$\frac{F_0}{F} = 1 + k_q \tau_0 [Q] = 1 + K_D [Q] \tag{1.6}$$

where F_0 and F are the fluorescence intensities in the absence and presence of a quencher Q, respectively. k_q is the quenching constant, τ_0 is the lifetime of the fluorophore in the absence of a quencher, and $[Q]$ is the concentration of the quencher. The Stern-Volmer constant constant for dynamic quenching is given by $K_D = k_q \tau_0$.

In static quenching, the quencher forms a stable complex with the fluorophore in its ground state, typically through non-covalent interactions. This complex formation effectively reduces the population of free fluorophores and thus the number of excited states available for fluorescence emission. In static quenching, the dependence of fluorescence intensity on quencher concentration is derived by the association constant for complex formation:

$$K_s = \frac{[F-Q]}{[F][Q]} \tag{1.7}$$

where K_s is the association constant, $[F-Q]$ is the concentration of the complex, $[F]$ is the concentration of the uncomplexed fluorophore, and $[Q]$ is the concentration of the quencher. Assuming that the complexed species are non-fluorescent, the ratio of non-emitting to emitting species can be described in a linear dependence on the association constant and the concentration of the quencher:

$$\frac{F_0}{F} = 1 + K_s [Q] \tag{1.8}$$

Static and dynamic quenching can be distinguished by their differing dependence on temperature, viscosity, and fluorescence lifetimes. Higher temperatures and/or lower viscosity result in faster diffusion

---

[§] The concepts discussed in this Sections are based on the textbooks by Sauer, Hofkens, and Enderlein (Chapter 1), Lakowicz (Chapters 1, 6, 7,8 and 9) and hence an increased number of collision events. On the other hand, higher temperatures typically destabilize weakly bound complexes and thus reduce the amount of static quenching.

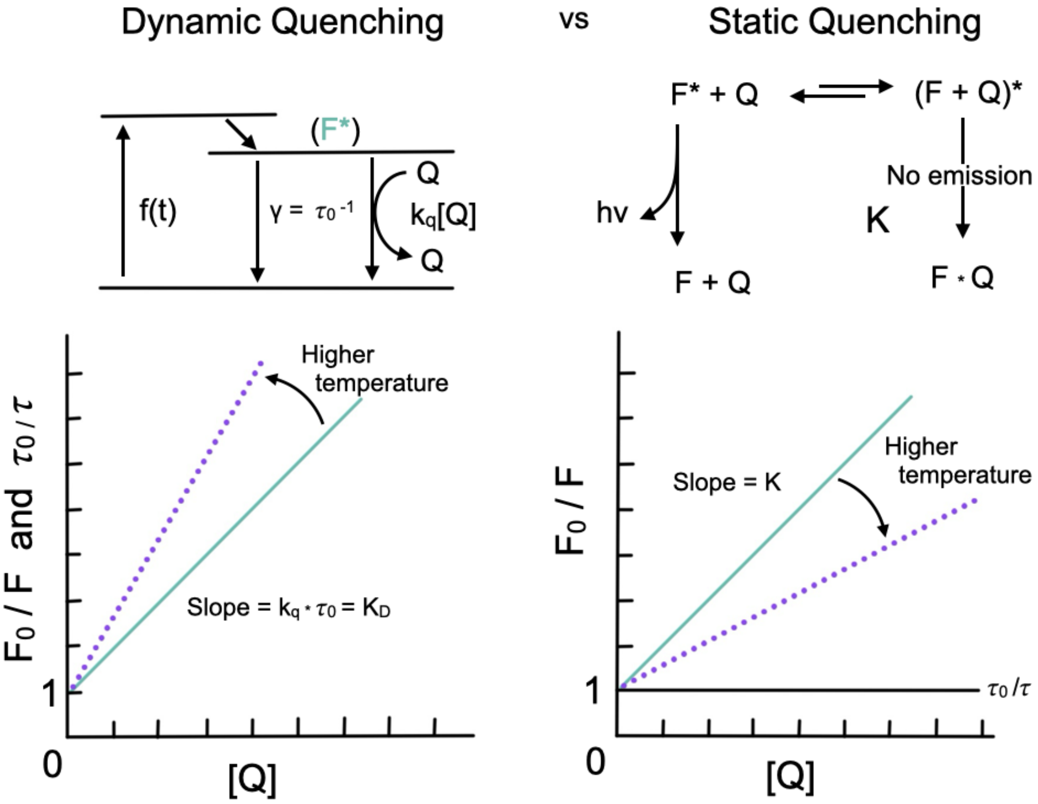

Figure 1.3: Dynamic and Static Quenching: The upper panels show the quenching mechanisms of dynamic (left, Jablonski diagram) and static quenching (right, kinetics diagram), where F^* denotes the excited state of the fluorophore. The lower panels show the linear F_0/F dependence on quencher concentration $[Q]$ for dynamic and static quenching, respectively, and their inverse dependence on temperature changes.

The fluorescence intensity can be also quenched by energy transfer when the excited state energy of a fluorophore is transferred non-radiatively for example to a nearby acceptor. Also this leads to a reduction in fluorescence emission (see section 1.4 and figure 1.5).

It is important to note that the long-lived triplet state can also be depopulated through similar mechanisms:

As mentioned before, fluorophores in the triplet state can be considered to be a fluorescent dark-state (off-state), as the likelihood of returning to the ground state via phosphorescence occurs on slow timescales with low count rates. The triplet state can also be quenched by directly molecular oxygen. The resulting singlet-oxygen can produce free radicals, ultimately leading to the photobleaching of the fluorophore (figure 1.1). By reducing the concentration of oxygen from $\approx 0.5mM$ to low μM levels using enzymatic oxygen scavenging systems, such as a combination of glucose, glucose oxidase, and catalase, extends the triplet lifetime into the millisecond range. This effectively induces blinking of single fluorophores as this cycle is continuously repeated[49,51] (figure 1.4).

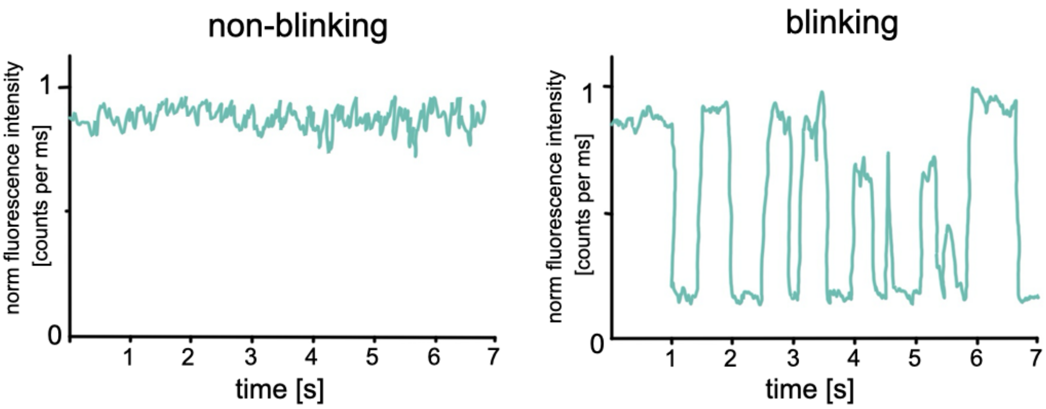

Figure 1.4: timetraces of a surface-immobilized non-blinking (left panel) and blinking fluorophore (right panel).

These long-lived ”off-states” can be shortened by quenching the triplet state with alternative molecules, such as β-mercaptoethanol, Trolox, and analogs of vitamin E, rather than molecular oxygen[66,67].

The effect is called photo-induced electron transfer (PET), a mechanism through which fluorophores can transition to the off-state. In this process, an excited fluorophore interacts with electron donors or acceptors, leading to electron transfer and the formation of non-fluorescent radical ions[68] (figure 1.1). However, it’s important to note that this phenomenon is primarily observed from the triplet state of the fluorophore, given its longer lifetime compared to the first excited singlet state. This process induces redox blinking and can effectively recycle fluorophores from their triplet states by depopulating them more efficiently through PET and a complementary redox reaction[66,67]. At concentrations above 1 nM, the singlet state can also be quenched directly, reducing fluorescence by preventing the fluorophore from emitting light. For example, when a triplet state interacts with a reductant such as Trolox, it forms a radical anion, whose lifetime depends on the availability of a second electron transfer reaction to return to the ground state. Adding an oxidizing agent accelerates this process, stabilizing the fluorophore and minimizing off-states—a strategy often referred to as a Reducing and Oxidizing System (ROXS)[67] in fluorescence spectroscopy.

To mitigate photobleaching and blinking, a typical ROXS cocktail might include Trolox as a reductant and oxygen scavengers (such as sodium ascorbate) to remove oxygen, alongside an oxidizing agent like methyl viologen or molecular oxygen. This combination has been shown to improve the photostability of fluorophores such as ATTO647N. However, the success of this approach can be dye-dependent, as some fluorophores may show enhanced photostability, while others might experience increased blinking under similar conditions.

1.4 Förster resonance energy transfer[§]

Another fluorescence quenching mechanism based on excited state energy transfer, was described by Theodor Förster in 1948[34] (figure 1.5). Förster Resonance Energy Transfer (FRET) describes the transfer of excited-state energy from the donor (D), to the acceptor (A), reducing down fluorescence. FRET occurs non-radiatively and is the result of long-range dipole–dipole interactions, which lead to a typical distance dependency of $k_{FRET} \propto \frac{1}{r^6}$ for the energy transfer rate, where r denotes the distance between donor and acceptor. This dependency makes FRET a powerful tool for measuring small interprobe distances and distance changes between 2 nm and 10 nm[69]. What differentiates FRET from a typical dipole-dipole coupled system is that not only do the distance and the orientation of the transition dipole moments play a role in the energy transfer, but also an overlap between the spectra of the donor emission and the acceptor absorbance is required for FRET to occur (figure 1.5).

[§] The concepts discussed in this Sections are based on the textbooks by Sauer, Hofkens, and Enderlein (Chapter 6), Lakowicz (Chapters 1, 4,8 and 13)

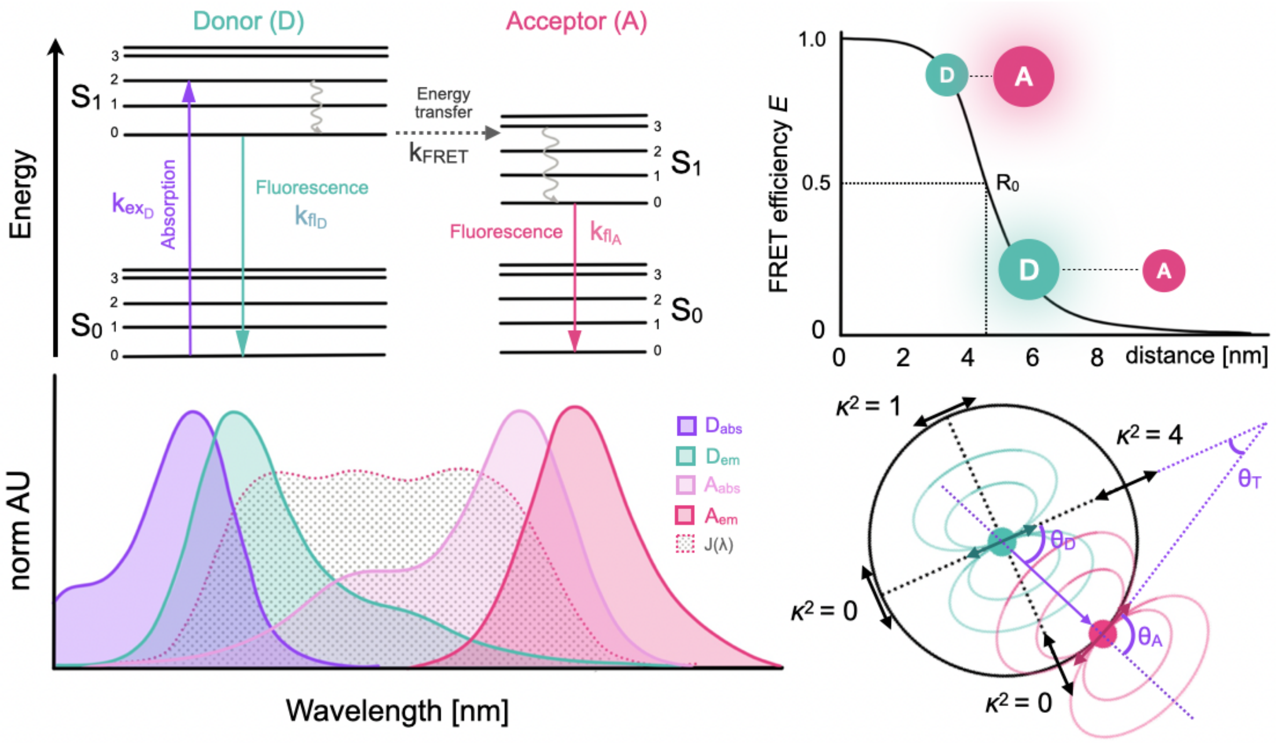

Figure 1.5: Förster Energy Transfer (FRET) Principle: The upper left panel depicts a Jablonski diagram of a hypothetical fluorophore pair as the donor (D) and acceptor (A), illustrating excitation levels in the ground state (S0) and excited states (S1) of the donor and acceptor respectively. Colored arrows indicate energy transitions involving the absorption or emission of photons, while curly arrows represent vibrational relaxation. The dotted arrow represents energy transfer from the donor to the acceptor fluorophore. The transition rates are denoted as k_{ex}: excitation rate, k_{fl_D}, k_{fl_A}: fluorescence emission rate for the donor and acceptor, respectively, and k_{FRET}: energy transfer rate. The lower left panel displays representative absorption and emission spectra of a hypothetical fluorophore pair, corresponding to the Jablonski diagram above, where $J(\lambda)$ denotes the overlap between the emission spectrum of the donor and the absorption spectrum of the acceptor. The upper right panel shows FRET efficiency as a function of the distance between a donor and an acceptor, where R_0 stands for the Förster radius. The lower right panel shows all possible dipole orientations between the donor (green arrow) and acceptor (red arrow) within one plane ($\cos\phi = 1$), where θ_D and θ_A denote the angles formed between these dipoles and the vector connecting the donor and the acceptor (purple arrow), and θ_T signifies the angle between the emission transition dipole of the donor and the transition absorption dipole of the acceptor.

The efficiency of this energy transfer, as an equivalent of fluorescence quantum yield of the donor (Q_D) is also known as FRET efficiency (E) and can be estimated by comparing the energy transfer rate k_{FRET} with all possible relaxation pathway rates of the donor excited state:

$$E = \frac{k_{FRET}}{k_{fl_D} + k_{nr_D} + k_{FRET}} \tag{1.9}$$

Here the energy transfer rate k_{FRET} is described as a function dependent on the distance between the donor and the acceptor dye (r)

$$k_{FRET}(r) = \frac{1}{\tau_D}(\frac{R_0}{r})^6 \tag{1.10}$$

Where τ_D represents the lifetime of the donor in the absence of the acceptor, and R_0 denotes the Förster radius. This radius describes the distance between donor and acceptor when the energy transfer efficiency E equals 50 percent. Determining the Förster radius requires a more elaborate process, as various factors contribute to it. These factors include the unique characteristics of the donor and acceptor, such as the overlap of their emission and absorption spectra, respectively, as well as their relative orientation to each other[70] (figure 1.5).

$$R_0 = \sqrt[6]{\frac{9000\ ln(10)}{128\ \pi\ N_A}\frac{\kappa^2}{n^4}\ Q_D\ J(\lambda)} \tag{1.11}$$

Here, Q_D is the quantum yield of the donor in the absence of the acceptor, κ^2 describes the orientation of the two dipoles in respect to each other, N_A is Avogrados's number and n is the refractive index of the medium, which is typically assumed to be 1.4 for biomolecules in aqueous solution. J is an integral that describes the overlap between the emission light spectrum of the donor and the absorption spectrum of the acceptor, as shown below (figure 1.5)

$$J(\lambda) = \frac{\int_0^\infty F_D(\lambda)\ \epsilon_A(\lambda)\ \lambda^4 d\lambda}{\int_0^\infty F_D\ (\lambda) d\lambda} = \int_0^\infty F_D(\lambda)\ \epsilon_A(\lambda)\ \lambda^4 d\lambda \tag{1.12}$$

where F_D is the wavelenght-dependent emission spectrum of the donor, normalized such that $\int_0^\infty F_D(\lambda) d\lambda = 1$ and the acceptor absorption spectrum is expressed in its exctinction coefficient ϵ_A.

The orientation factor κ^2 describes all possible orientations by averaging the dipole-dipole interaction over all potential orientations of the donor transition dipole moment and acceptor transition dipole moment[71] (figure 1.5).

$$\begin{aligned}\kappa^2 &= (\cos\theta_T - 3\cos\theta_D \ \cos\theta_A)^2 \\ \kappa^2 &= (\sin\theta_D \ \sin\theta_A \ \cos\phi - 2\cos\theta_D \ \cos\theta_A)^2\end{aligned} \tag{1.13}$$

Within these equations, θ_T signifies the angle between the emission transition dipole moment of the donor and the absorption transition dipole moment of the acceptor. Meanwhile, θ_D and θ_A describe the angles formed between these dipoles and the vector connecting the donor and the acceptor. Additionally, ϕ characterizes the angle between the planes involved in the process. Figure 1.5 depicts all possible orientations of κ^2 within one plane, eg. when $\cos\phi = 1$. When the transition dipole of the donor and the acceptor align parallelly, κ^2 assumes a value of 1, while perpendicular dipoles yield a value of zero, indicating no energy transfer at this alignment 1.13. The peak value of κ^2 arises when the dipoles are parallel and oriented head-to-tail, yielding a value of 4. However, assuming rapid isotropic motion of the dipoles, the average value of κ^2 becomes $\frac{2}{3}$. Isotropic motion and a constant κ^2 is a prerequisite to use FRET as a distance ruler that is independent of dipole orientation.

From equations 1.9 and 1.10, we can directly estimate the FRET efficiency (E) by measuring the lifetime of the donor in the absence of an acceptor, $\tau_D = \frac{1}{k_{fl_D}+k_{nr_D}}$, and comparing it with the lifetime of the donor under FRET conditions, e.g. in the presence of an acceptor, $\tau_{DA} = \frac{1}{k_{fl_{DA}}+k_{nr_{DA}}+k_{FRET}}$.

$$\begin{aligned}E = & \ 1 - \frac{\tau_{DA}}{\tau_D} \\ = & \ \frac{1}{1+(\frac{r}{R_0})^6}\end{aligned} \tag{1.14}$$

As shown above, by measuring the donor's lifetime alone, it is possible to determine/calculate the distance between the donor and the acceptor, provided that R_0 is known.

If acceptor molecule itself is a fluorophore, the sensitized acceptor fluorescence is another useful indicator of energy transfer from the donor. To determine FRET efficiency based on this value is advantageous because, as demonstrated in equation 1.3, the lifetime of fluorophores is proportional to their fluorescence intensity. Consequently, it becomes feasible to directly determine FRET efficiencies by simply comparing the fluorescence intensities of the donor and the acceptor.

$$E^* = \frac{I_{A_{FRET}}}{I_{D_{FRET}} + I_{A_{FRET}}} \tag{1.15}$$

Where, $I_{A_{FRET}}$ is the light intensity of the accpetor via direct FRET excitation and $I_{D_{FRET}}$ is the light intensity of the donor in the presence of the acceptor dye. It is important to note that E* is a setup-dependent proximity ratio which requires correction for background, spectral cross-talk and differences in quantum yield and detection efficiences for donor and acceptor before direct correlation of E and interprobe distance are possible.

1.5 Confocal and Widefield Microscopy: Instrumentation for Single Molecule Detection[§]

Optical microscopes were invented to magnify and enlarge objects that are too small for the human eye to see. The human eye has a resolution limit of approximately 0.1 millimeters, meaning it cannot distinguish objects that are in closer proximity than this distance. In its most basic configuration, an optical microscope consists of an arrangement of two lenses: a lens with a small focal length called the objective, which collects light from the sample at the focal plane of the objective, and a tube lens with a longer focal length than the objective, which collects the collimated light beam from the objective and projects it as a magnified image onto the detector or eyepiece (figure 1.11). This arrangement allows for the detailed observation of microscopic structures with varying degrees of magnification and clarity.

Basic optical microscopes can achieve a resolution of approximately 200 nanometers, a limit imposed by the wavelength wave nature of light and the resulting diffraction and intereference phenomena at apertures e.g., of the objective lense. The numerical aperture (NA) is a critical parameter in microscopy that quantifies the light-gathering ability of a lens and determines its resolving power. Mathematically, NA is defined as:

$$NA = n \cdot \sin(\theta) \tag{1.16}$$

where n is the refractive index of the medium between the lens and the sample (e.g., air, water, or immersion oil), and θ is the half-angle of the maximum cone of light that can enter the objective lens. A higher NA value indicates the ability to collect more light and resolve finer details. This parameter directly impacts both the resolution and brightness of the image.

The resolution of a microscope is fundamentally limited by diffraction, and this limit is mathematically related to the NA of the lens. The diffraction-limited resolution, d, is given by:

$$d = \frac{\lambda}{2 \cdot NA} \tag{1.17}$$

[§] The concepts discussed in this Section are based on the textbooks by Sauer, Hofkens, and Enderlein (Chapter 8), Lakowicz (Chapters 2 and 23) where d is the resolution, or the smallest distance between two points that can still be distinguished as separate; λ is the wavelength of light used for imaging and NA is the Numerical Aperture of the objective lens.

This equation shows that the resolution d improves (i.e., decreases) as the NA increases. A higher NA allows the lens to gather more light, which results in a finer resolution. Conversely, a lower NA results in a lower resolution.

For example, using an objective with a higher NA or using immersion oil with a higher refractive index allows for greater light collection and better spatial resolution. However, these improvements are constrained by the wavelength of light used, as shorter wavelengths can resolve finer details. The highest Numerical Aperture (NA) achievable with traditional optical microscopy was ¡0.9 (for air objectives) and can be improved by using immersion oil reaching NA values up 1.5-1.7. This corresponds to a resolution limit of approximately 200 nm, which is typical for diffraction-limited resolution using visible light, depending on the numerical aperture (NA) and wavelength (λ) of the system (equation 1.17) and figure 1.11 and 1.12 upper left panel).

In addition to resolution, contrast is crucial for effective imaging, as high spatial resolution alone is not useful if the sample cannot be distinguished from its background. Many biological samples, for instance, are transparent, making them difficult to see without proper contrast. This is typically addressed through staining techniques, which add color to specific components of the sample, enhancing visibility. Alternatively, contrast can be achieved without staining by using techniques like phase contrast[72], dark field[73], or differential interference contrast (DIC)[74], all of which enhance the contrast of transparent specimens, allowing for clearer observation of structures that would otherwise be difficult to detect.

Fluorescence microscopy provides a unique form of molecular contrast by utilizing the sample's own emitted light. Unlike traditional staining methods that require external dyes to enhance contrast, fluorescence allows the sample to generate its own signal. By labeling specific molecules with fluorescent probes, the sample becomes self-illuminating, providing high contrast without the need for additional contrast agents[75]. This makes fluorescence microscopy particularly useful for imaging live cells or dynamic processes.

Fluorescence microscopes rely on the Stokes shift, where the emitted light has a longer wavelength than the excitation light. This shift is fundamental, as it enables the microscope to distinguish between the two types of light—excitation and emission—by exploiting their different wavelengths.

In fluorescence microscopy, the sample is epi-illuminated, with excitation light directed onto it from the objective, rather than using transmitted light as in traditional microscopy. To effectively separate the excitation light from the emitted fluorescence, several optical filters are employed. A dichroic mirror reflects the excitation light towards the sample while allowing the emitted fluorescence to pass through toward the detector.

Additionally, a combination of bandpass, long-pass, and short-pass filters is used to isolate and select the relevant emission wavelengths[75]. Bandpass filters are used to transmit a narrow range of wavelengths corresponding to the fluorophore's emission spectrum, ensuring that only the relevant emission signals are captured (figure 1.10). Long-pass filters allow longer wavelengths to pass while blocking shorter ones, and short-pass filters allow only shorter wavelengths to pass while blocking longer ones. When multiple fluorophores are used in a sample, these filters can be combined to effectively separate emission signals from different emitters.

In the case of confocal microscopy, these filters help isolate specific emission spectra from different fluorophores. Additionally, multiple point detectors—such as photomultiplier tubes (PMTs) or avalanche photodiodes (APDs)—can be used to separately capture the emission from different fluorophores in distinct detection channels (figure 1.9). This allows for sensitive imaging of multiple emitters, either in a single image through careful filter combinations or across different detectors, reducing crosstalk and enhancing clarity. By selecting and combining these filters and detectors, fluorescence microscopes can capture precise, molecular-level information with high contrast and minimal interference. Microscopes are now capable of detecting single photons emitted from individual fluorophores, allowing for high-precision, molecular-level imaging[76,77,78].

Fluorescence microscopy has since expanded, tailored around fluorophores and taking advantage of many fluorescence phenomena as described above, creating a large array of methods and microscope configurations, such as PALM[27], STORM[28], STED[26], and FLIM[79], to name a few. Importantly, all existing microscopy methods are built upon two foundational configurations: wide-field (figure 1.11) and confocal microscopy (figure 1.7 and 1.9), distinguished primarily by their illumination and detection approaches:

In the wide-field approach, the entire sample plane is illuminated with a broad beam of light. To create this even illumination, the excitation light beam must be focused onto the back focal plane of the objective lens. This ensures that the objective produces a uniform illumination over the entire field of view. The light is transmitted through the sample, exciting all fluorophores within the illuminated field. The emitted fluorescence from these fluorophores is then collected by the objective and guided through a tube lens, which creates a real image at the camera sensor plane, where the image is formed. However, this approach suffers from out-of-focus noise, as the emitted light from fluorophores not in the focal plane (but above and below it) is also captured. This leads to blurred images and reduced contrast. While traditional wide-field microscopy inherently captures this unwanted out-of-focus light, newer imaging techniques like lightsheet microscopy[80] and total internal reflection fluorescence (TIRF) microscopy[81] have been developed to mitigate this problem. Lightsheet microscopy uses a thin sheet of light to illuminate only a specific plane of the sample, reducing the amount of out-of-focus light detected. TIRF, on the other hand, uses an evanescent wave to illuminate only the region near the sample surface, significantly reducing background noise from out-of-focus areas and allowing for high-contrast imaging of surface interactions.

In contrast, confocal microscopy uses a different approach for illumination. The excitation light is directed into the objective lens in a collimated beam, meaning the light rays are parallel as they enter the objective[82]. The objective then focuses this collimated light into a very small, diffraction-limited spot within the sample[83] (Figure 1.7). This tightly focused laser excites fluorophores only within a specific, small region of the sample. The emitted fluorescent light is then collected through a small aperture, or pinhole, which acts as a spatial filter[84,85]. The pinhole only allows light coming from the focal plane to pass through, blocking out-of-focus light from above and below the plane of interest. The result is a cleaner, sharper image with reduced background noise[86]. To generate the final image, the sample is scanned in a raster pattern, with the laser beam moving across the sample in small steps, capturing fluorescence data "pixel by pixel." The detector used in confocal systems is typically a photomultiplier tube (PMT) or an avalanche photodiode (APD), which are sensitive enough to detect low-intensity fluorescence signals down to single photons. This scanning process, together with the pinhole aperture, allows confocal microscopy to achieve greater optical sectioning compared to wide-field microscopy, effectively eliminating out-of-focus blur and improving resolution. However, this comes at the cost of longer acquisition times, as the entire sample must be scanned point by point to build the image. Despite these differences, confocal microscopy's ability to perform optical sectioning and reduce background noise makes it particularly useful for 3D imaging and detailed studies of thick or complex samples, whereas wide-field microscopy is generally faster and better suited for imaging large areas or dynamic processes.

1.5.1 Confocal and Widefield Microscopy: Instrumentation for Single Molecule Detection[§]

As mentioned briefly above, confocal microscopes create a very small observation volume, also known as the confocal volume, if diffracted limited for visible light and high NA objectives in the femto liter range[87]. Additionally, the most powerful point detectors (APDs) possess not only a single photon detection efficiency but also high temporal resolution down to the nano and pico second timescale. This means that confocal setups can be used to obtain information from freely diffusing fluorophores when they enter the confocal volume randomly and gain enough photons in the short period of a diffusional transit[33].

The effective volume of a confocal microscopy can be calculated based on the light intensity profile. When focusing a collimated laser beam operating in the fundamental transverse mode (TEM_{00}), which has a Gaussian intensity profile, a diffraction-limited spot in the shape of an ellipse is generated[88] (figure 1.7):

$$I(x,y,z) = I_0 \, e^{-2(x^2+y^2+\frac{z^2}{\kappa^2})/w_0^2} \tag{1.18}$$

Here, I_0 represents the maximal intensity at the center of the confocal volume, also known as the beam waist (w_0) in the xy axis, and decreases inversely proportional to the beam radius in the z-axis

---

[§] The concepts discussed in this Section are based on the textbooks by Sauer, Hofkens, and Enderlein (Chapter 8), Lakowicz (Chapters 2 and 23)

$(w(z))$. κ is the structural factor, describing the ellipticity of the confocal volume by dividing the focal length (z_0) by the xy resolution (w_0). The beam waist and focal length can be approximated by Gaussian optics by $w_0 = \frac{0.61\lambda}{NA}$ and $z_0 = \frac{2n\lambda}{NA^2}$, respectively, where λ is the wavelength of the laser, n is the refractive index of the sample, and NA is the numerical aperture of the objective.

Operating with a laser source at a 550 nm wavelength, using an objective with a high numerical aperture ($NA > 1$), and imaging a sample with a refractive index $n = 1.3$, the effective confocal volume can be calculated by:

$$V_{eff} = \pi^{\frac{3}{2}}\ w_0^2 z_0 \tag{1.19}$$

This yields a volume of approximately 1 femtoliter. This small observation window leads to a Poisson-distributed probability of detecting diffusing fluorophores at a given concentration:

$$P(n, N) = \frac{N^n}{n!} e^{-N} \tag{1.20}$$

Here, $P(n, N)$ describes the probability of finding n fluorophores in the confocal volume, given an average number of fluorophores in the confocal volume of N. For example, with a fluorophore solution of 1 nM, the average number of fluorophores in the confocal volume would be $N \approx 0.6$. This means that at this concentration, there is a 55% probability of having no fluorophore in the confocal volume, 33% probability of detecting one fluorophore, 10% probability of detecting two, and 2% probability of detecting three (figure 1.6, middle panel).

In contrast, for a 5 nM fluorophore solution where $N \approx 3$, the probability of finding no fluorophore would decrease to 5%. The probabilities for detecting one, two, or three fluorophores would be 15%, 22%, and 22%, respectively (figure 1.6, left panel).

At a lower concentration of 0.1 nM, the average number of fluorophores in the confocal volume reduces to $N \approx 0.2$. This means the probability of finding no fluorophore in the confocal volume increases to 82%, while the probabilities of finding one and two fluorophores drop to 16% and 2%, respectively (figure 1.6, right panel).

This example demonstrates that lowering the concentration of the fluorophore solution increases the likelihood of detecting a single fluorophore compared to multiple fluorophores. This principle forms the basis of diffusion-based single-molecule detection, where it becomes possible to extract information about individual events, such as the amplitude and duration of recorded bursts.

The detection and analysis of bursts—short-lived photon emission events from individual fluorophores—are critical for example in single-molecule Förster resonance energy transfer (smFRET) and related techniques. To distinguish these bursts from background noise, various burst detection algorithms have been developed. A common approach is to segment the intensity time traces into fixed time bins, roughly matching the diffusion time of the fluorophores, and apply a threshold to identify bursts within these bins.

Advanced methods, such as sliding window algorithms, dynamically identify the start and end points of bursts by integrating photons within defined time intervals. The all-photon burst search (APBS) algorithm aggregates photon streams from multiple detection channels into a single dataset for simpler burst identification[89,90,91]. In contrast, the dual-channel burst search (DCBS) algorithm analyzes separate detection channels independently, helping to account for artifacts like photobleaching, blinking, or coincident detection of multiple molecules in the focal volume[92].

These methods rely on specific parameters for optimal burst identification, such as a time window size (500 μs), a minimum photon count per window (5–15 photons), and a total photon count threshold for a valid burst (30–200 photons).

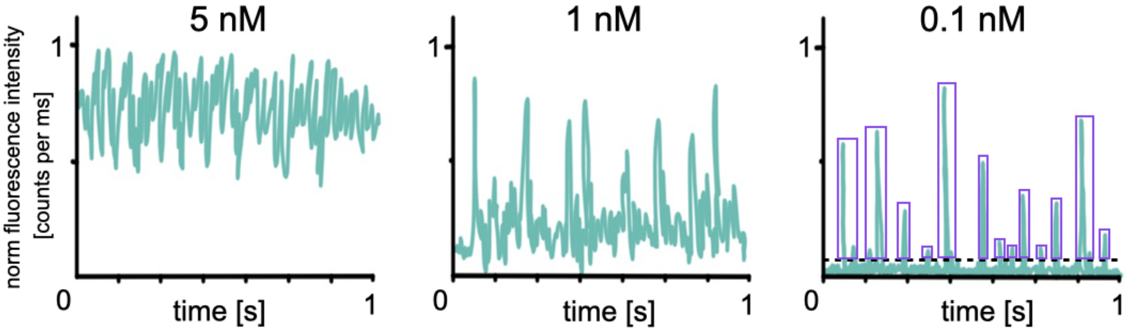

Figure 1.6: Time traces comparing the concentrations of different freely diffusing fluorophores: The left and middle panels show fluorescence intensity fluctuations of freely diffusing fluorophores at 5 nM and 1 nM, respectively. The right panel displays single burst events from individual diffusing fluorophores at a low concentration (0.1 nM). Here, it is possible to determine the burst amplitude and duration (highlighted by purple rectangles) by distinguishing the bursts from the background noise (dashed line).

.

1.5.2 Fluorescence correlation spectroscopy FCS[§]

Fluorescence correlation spectroscopy (FCS) takes advantage of the probabilities of finding small numbers of fluorophores in a confocal volume, so that the fluorescence signal changes with their dynamic properties[91,31]. This makes FCS a potent tool for determining diffusion times, concentrations, molecular rotations, and estimating triplet state lifetimes of a sample. In practice, FCS measures fluorescence intensity fluctuations over time that arise from changing fluorophore occupation or activity numbers in the confocal volume over time (figure 1.7). The fundamental concept behind FCS involves

---

[§] The concepts discussed in this Section are based on the textbooks by Sauer, Hofkens, and Enderlein (Chapter 7), Lakowicz (Chapters 2, 23 and 24) measuring fluorescence intensity at a specific time point $I(t)$ and comparing it with the intensity a little later in time $I(t+\tau)$. If the diffusion of a molecule is very slow, it can be assumed that the fluorescence intensity would not change over time, i.e., $I(t) = I(t+\tau)$. In contrast, for fast-diffusing molecules, a change in intensity is expected, i.e., $I(t) \neq I(t+\tau)$. This distinction heavily depends on the chosen time shift τ. However, by opting for even shorter time shifts, it is possible to distinguish fluorescence fluctuations not arising from pure diffusion but resulting from photophysical effects, such as transitioning into an off-state of a fluorophore or the rapid rotation in solution. In FCS, the timescales of dynamic fluorescence changes are, calculated by the correlation of $I(t)$ and $I(t+\tau)$ for a range of different time shifts (τ) which results in an autocorrelation function $G(\tau)$ defined by

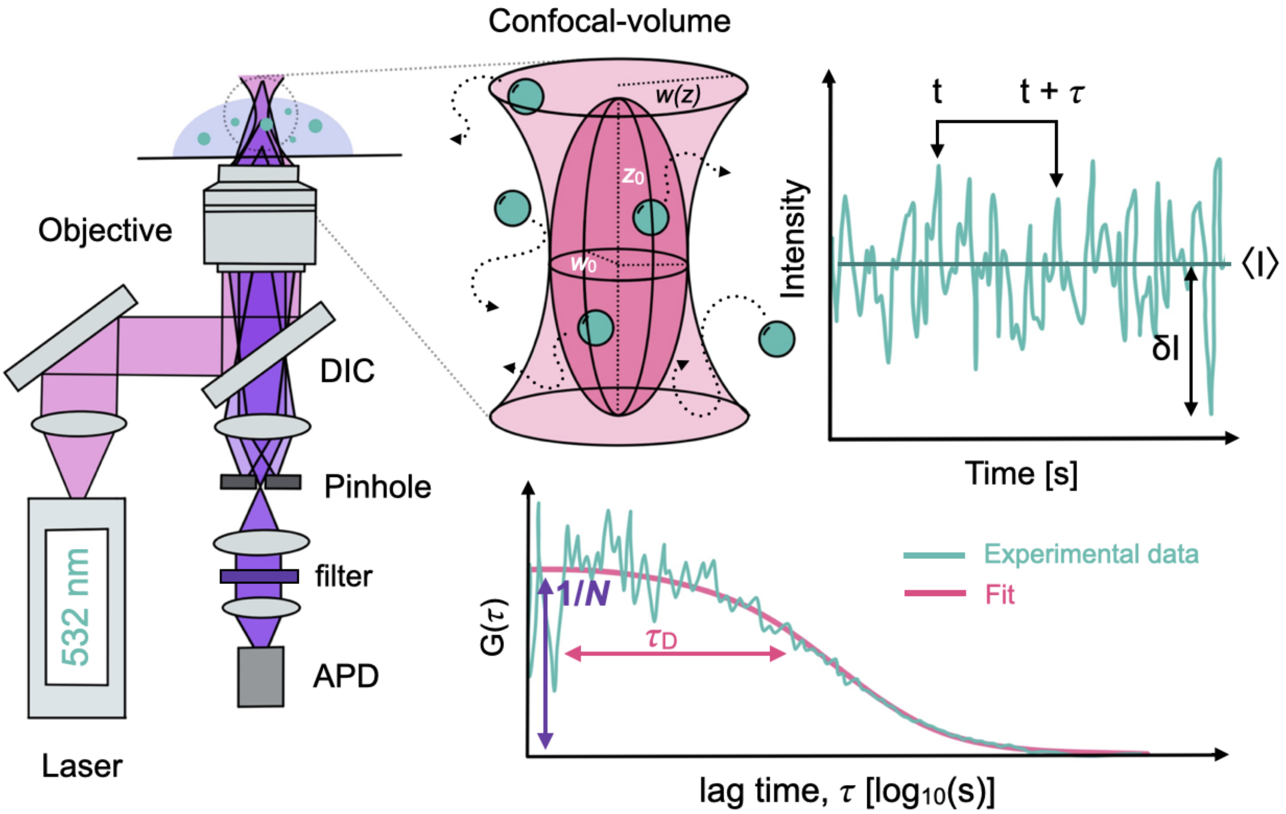

Figure 1.7: Fluorescence correlation spectroscopy (FCS): The left panel depicts the basic construction and light path of a confocal microscope, where a collimated laser beam (pink light path) is reflected through a dichroic mirror (DIC) and focused with an objective with a high numerical aperture into the sample, creating a diffraction-limited excitation spot (confocal volume). Fluorescence (purple light path), originating from the fluorophores (green balls) diffusing through the femtoliter excitation volume, is collected by the same objective and spatially filtered with a pinhole before reaching the point detector. The upper middle panel depicts the elliptical confocal volume with its dimensions, where w_0 is the x, y dimension, also known as the beam waist, and z_0 is the lateral resolution in z. $w(z)$ represents the beam radius dependent on z. The green marbles represent diffusing fluorescent particles. The upper right panel shows a representative FCS time trace where δI is the fluctuation intensity difference of the mean intensity $\langle I \rangle$ at time point t, and τ stands for the time lag. The lower right panel shows a representative FCS autocorrelation curve where $G(\tau)$ is the autocorrelation function, N is the average number of molecules in the confocal volume, and τ_D is the diffusion time of the molecules.

$$G(\tau) = \frac{\langle \delta I(t) \delta I(t+\tau)\rangle}{\langle I(t)\rangle^2} \tag{1.21}$$

Here $\langle I(t)\rangle$ is the average fluorecence intesity and $\delta I(t) = I(t) - \langle I(t)\rangle$ is the deviation from the mean intensity at time t (figure 1.7). The autocorrelation funtion is normalized by $\langle I(t)\rangle^2$ because then the correlation at $\tau = 0$ is related to the average number of fluorophores in the confocal volume (see below). It is now possible to model $G(\tau)$ for diffusing molecules with the geometry of the confocal volume V_{eff} and a mobility term Γ:

$$\begin{aligned} G(\tau) &= \frac{1}{\langle C\rangle V_{eff}} \cdot \Gamma \\ G(\tau) &= \frac{1}{\langle C\rangle \pi^{\frac{3}{2}}\ w_0^2 z_0}\ (1+\frac{4D\tau}{w_0^2})^{-\frac{1}{2}}\ (1+\frac{4D\tau}{w_0^2})^{-\frac{1}{2}}\ (1+\frac{4D\tau}{z_0^2})^{-\frac{1}{2}} + 1 \end{aligned} \tag{1.22}$$

where $\langle C\rangle$ is the averange concentration of the fluorphore and D is its diffusion coefficient. In the left part of the equation the denominator describes the effective confocal volume mentioned previously in the equation 1.19. The next terms essentially describe the diffusion mean square displacements within the xy axis (w_0) and z axis (z_0) of the confocal volume, from which we can extract average diffusion times as $\tau_D = \frac{w_0^2}{4D}$. From here $G(\tau)$ can be rewritten with useful variables that extract information of the diffusing sample:

$$G(\tau) = \frac{1}{N}\ \cdot\ (1+\frac{\tau}{\tau_D})^{-1}\ \cdot\ (1+\frac{\tau}{\kappa^2 \tau_D})^{-\frac{1}{2}} + 1 \tag{1.23}$$

Where N is the average number of molecules in the confocal volume and κ is the structural factor already mentioned before. Although the previous derivation assumes only diffusion and constant photon emission rates for the fluorophores based on their location in the confocal volume, the reality is more complex. As mentioned earlier, common fluorophores show variations in their emission rates due inter-system crossing (ISC). Taking these effects into account, the auto-correlation function becomes a product of these contributing factors.

$$G(\tau) = \frac{1}{N}\ \cdot\ G_{diff}(\tau)\ G_{ISC}(\tau) + 1 \tag{1.24}$$

Here the autocorrelation function $G_{ISC}(\tau)$ includes singlet-triplet kinetics:

$$G_{ISC}(\tau) = \frac{1 - T + T\ e^{-\frac{\tau}{\tau_T}}}{1-T} \tag{1.25}$$

where, T is the average population of fluorophores which are in the triplet state and τ_T is the relaxation time for the triplet relaxation. Both T and τ_T depend on all kinetic rates involved in this process:

$$\begin{aligned} T &= \frac{k_{ex}\, k_{ISC}}{k_{ex}(k_{ISC}\, k_T) + k_{fl}\, k_T} \\ k_T &= (k_T + \frac{k_{ex}\, k_{ISC}}{k_{ex} + k_{fl}})^{-1} \end{aligned} \tag{1.26}$$

As shown in the equation 1.24 a complete auto-correlation function is a a product of many contributing factors, each describing fluctuations in a different time scale (figure 1.8):

$$G(\tau) = \frac{1}{N} \cdot G_{diff}(\tau) \cdot G_{ISC}(\tau) \cdot G_{dynamics}(\tau) \cdot G_{antibunching}(\tau) + 1 \tag{1.27}$$

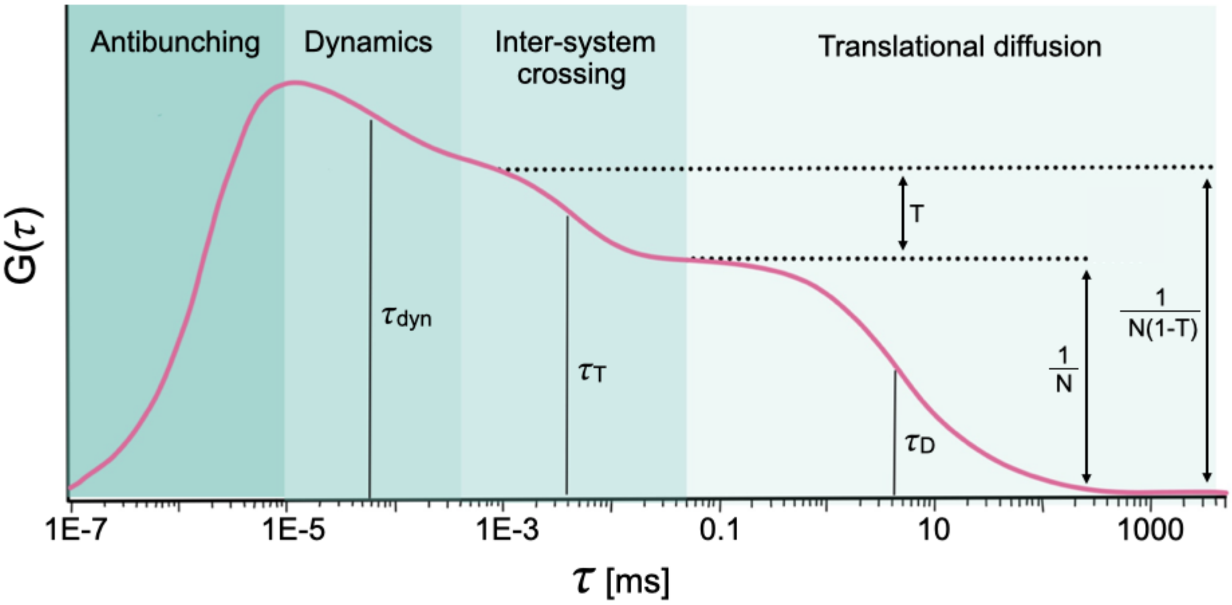

Figure 1.8: Complete FCS autocorrelation function illustrating four distinct regions characterized by antibunching, dynamics, intersystem crossing, and translational diffusion.

.

1.5.3 Alternating laser excitation (ALEX) for smFRET

Equation 1.15 demonstrates how FRET efficiencies can be determined by measuring fluorescence intensities from both the donor and acceptor in energy transfer conditions. A confocal microscope equipped with a second point detector (figure 1.5) is ideal for observing diffusing FRET species at a single-molecule level.

$$E = \frac{f_{Dex}^{Aem}}{(f_{Dex}^{Dem} + f_{Dex}^{Aem})} \tag{1.28}$$

Here, f_{Dex}^{Dem} is the photon-stream within the donor emission spectrum window, excited by a donor-specific light source, while f_{Dex}^{Aem} photon-stream within the acceptor emission spectrum window under the same excitation.

However, FRET efficiencies determined through this approach contain artifacts due to fluorophores, setup configuration, and sample properties, yielding only apparent FRET efficiencies (E_{app}).

The practicality of accurately measuring FRET efficiencies becomes challenging due to cross-talk between the donor and acceptor signals, influenced by the emission and absorption spectra of both fluorophores.

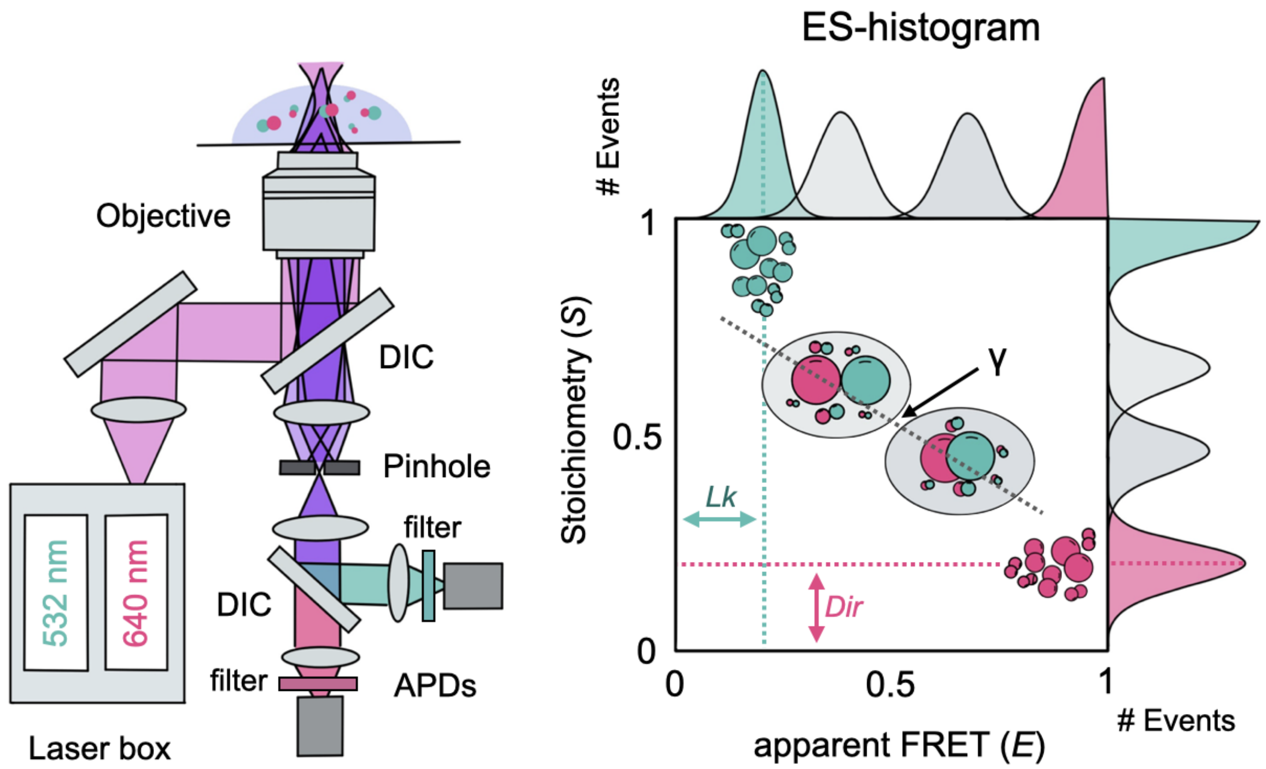

Figure 1.9: Alternating laser excitation (ALEX) smFRET setup: The left panel depicts the basic construction and light path of an ALEX microscope. The light source emits a collimated alternating red and green laser beam (pink light path), which is reflected through a dichroic mirror (DIC) and focused with an objective with a high numerical aperture into the sample, creating a diffraction-limited excitation spot (confocal volume). Fluorescence (purple light path), originating from the biomolecules diffusing through the femtoliter excitation volume, is collected by the same objective and filtered for background with a pinhole before it is split into green and red detection channels. On the right side, a representative ES histogram is shown, where the green and red marbles represent donor-only and acceptor-only populations, respectively, and green-red marbles represent FRET populations. Crosstalk aberrations are depicted as Lk for leakage and Dir for direct excitation. The gamma factor γ is depicted as the slope of the line between two FRET populations with different FRET efficiencies E.

Cross-talk is categorized into two effects: leakage (Lk) and direct excitation (Dir). Leakage occurs when the long emission tail of the donor spectrum reaches the spectral window for acceptor emission recording, leading to erroneous readings in the f_{Dex}^{Aem} photon-stream. Direct excitation happens when the long absorption tail of the acceptor interferes with the wavelength region of the donor excitation light source, resulting in non-FRET-related acceptor emission.

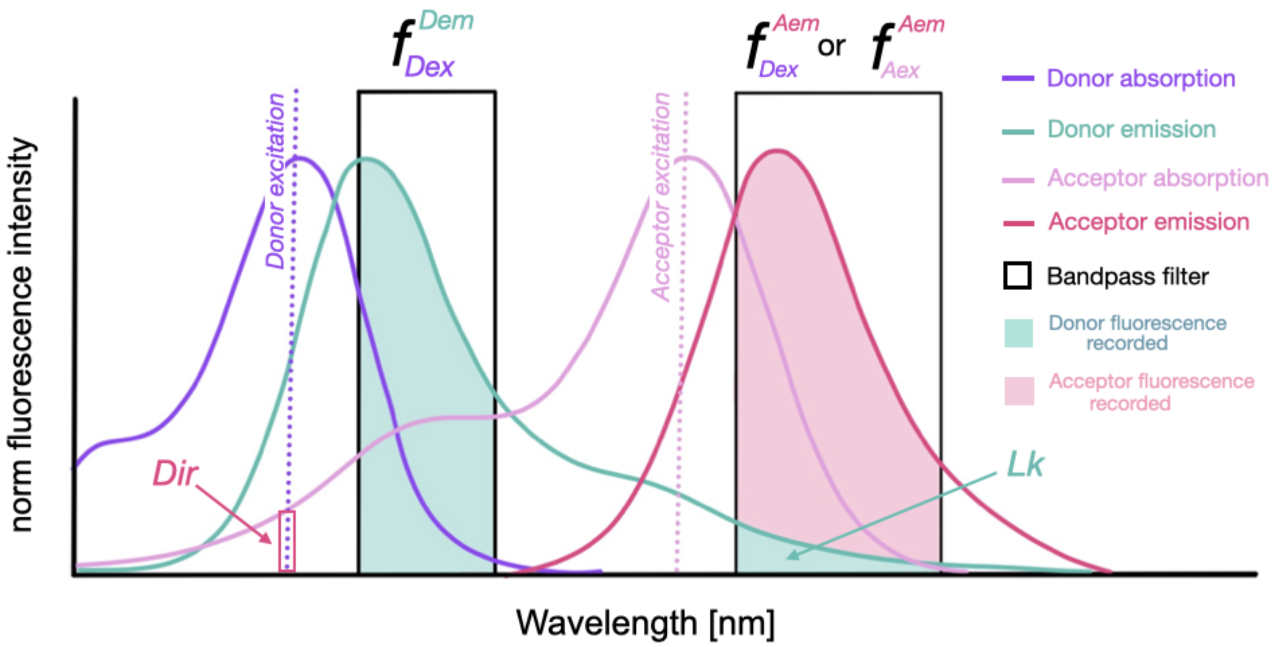

Figure 1.10: Fluorescence crosstalk between two different fluorophore pairings: Absorption and emission spectra of the donor and acceptor fluorophores. Dashed lines indicate the excitation light source wavelengths—purple for the donor and pink for the acceptor. The black boxes represent the bandpass filters used to record the fluorescence of the donor and acceptor, respectively. The shaded areas within the emission spectra depict the fluorescence captured by the respective bandpass filters. The donor window is used for the f_{Dex}^{Dem} photon-stream, while the acceptor window is used for the f_{Dex}^{Aem} and f_{Aex}^{Aem} photon-streams.
The donor excitation light source also excites the acceptor due to the overlap between the donor excitation wavelength and the acceptor absorption spectrum (Dir, direct excitation). Similarly, part of the donor fluorescence leaks into the f_{Dex}^{Aem} photon-stream because the donor emission spectrum overlaps with the bandpass filter window of the acceptor (Lk, leakage).

Moreover, differences in the quantum yields of the donor and acceptor, as well as disparities in the detection efficiencies of the point detectors at a given wavelength, significantly impact the determination of intensity-based FRET efficiencies.

Moreover, the ideal sample consists solely of FRET species, yet this is often not the case. In protein-based samples, a common strategy involves labeling with a donor and acceptor fluorophore through direct mutagenesis. This process replaces endogenous amino acids with more chemically reactive ones, such as cysteine, capable of reacting with maleimide chemistry. This labeling occurs in a one-pot reaction, resulting in eight plus one unlabeled distinct stoichiometric populations:

$$\begin{aligned} unlabeled &= P \\ FRET &= P_D^A \; P_A^D \\ D_{only} &= P^D \; P_D \; P_D^D \\ A_{only} &= P^A \; P_A \; P_A^A \end{aligned} \tag{1.29}$$

Here, P_x^y denotes the sample number of molecules, and the subscripts represent the labeling sites with either a donor or an acceptor. The challenge lies in filtering undesired species from FRET species while simultaneously correcting for the aforementioned artifacts. In contrast to fluorescence correlation spectroscopy (FCS), single-molecule FRET (smFRET) relies on direct observation of individual molecules to distinguish between different species in the sample. This is achieved by reducing the sample concentration to the picomolar range: using a 50 pM solution after equation 1.20 would result in an average occupation probability of 1.5%, thereby reducing the likelihood of encountering two molecules simultaneously to 0.011% (figure 1.6).

Furthermore, the introduction of Alternating Laser Excitation (ALEX) enhances smFRET measurements by addressing cross-talk and the differences in quantum yields and detection efficiences. In ALEX, an acceptor excitation laser is added which alternates with the donor excitation laser, providing for different photon-streams[37,93,94]:

$$
\begin{aligned}
f_{Dex}^{Dem} &= {}^{D}f_{Dex}^{Dem} + {}^{A}f_{Dex}^{Dem} + {}^{D\to A}f_{Dex}^{Dem} \\
&= {}^{D}f_{Dex}^{Dem} + 0 + 0 \\
&= (P_D^D + P_D^A(1-E)) \cdot {}^{D}f_{Dex}^{Dem} \\
\\
f_{Dex}^{Aem} &= {}^{D}f_{Dex}^{Aem} + {}^{A}f_{Dex}^{Aem} + {}^{D\to A}f_{Dex}^{Aem} \\
&= Lk + Dir + f^{FRET} \\
&= ((P_D^D + P_D^A(1-E)) \cdot {}^{D}f_{Dex}^{Aem}) \\
&\quad + ((P_A^A + P_D^A) \cdot {}^{A}f_{Dex}^{Aem}) \\
&\quad + (P_D^A \cdot E \cdot {}^{D\to A}f_{Dex}^{Aem}) \\
\\
f_{Aex}^{Aem} &= {}^{D}f_{Aex}^{Aem} + {}^{A}f_{Aex}^{Aem} + {}^{D\to A}f_{Aex}^{Aem} \\
&= 0 + {}^{D}f_{Aex}^{Aem} + 0 \\
&= (P_A^A + P_D^A) \cdot {}^{A}f_{Aex}^{Aem} \\
\\
f_{Aex}^{Dem} &= {}^{D}f_{Aex}^{Dem} + {}^{A}f_{Aex}^{Dem} + {}^{D\to A}f_{Aex}^{Dem} \\
&= 0
\end{aligned}
\tag{1.30}
$$

Here, all the possible emission sources that a given photon-stream could record are dissected into three different light sources using the following nomenclature ${}^{Z}f_{X}^{Y}$, where f represents the fluorescence quantity emitted by the fluorophore ^{Z} upon being excited with light source X and recorded with detector ^{Y}. P_D^D, P_A^A, and P_D^A denote the number of sub-populations species of donor-only, acceptor-only, and FRET populations, respectively[35].

The photon-stream f_{Dex}^{Dem} records signals coming from D_{only} and $FRET$ species. Here, the emission coming from the $FRET$ species is subjected to FRET, and after equation (1.15), the loss of donor emission, in energy transfer conditions, is proportional to the FRET efficiency E. This loss of donor emission is manifested in the equation by multiplying the FRET species with $(1-E)$.

The photon-stream f_{Dex}^{Aem} records signals coming only from $FRET$ species, along with distorted signals, a product of leakage and direct excitation.

f_{Aex}^{Aem} records signals emitted from A_{only} and $FRET$ species. After equation (1.28), the excitation of acceptor fluorophores will not have an effect on FRET. Subsequently, the recorded fluorescence f_{Aex}^{Aem} comes from the A_{only} and FRET populations.

The photon-stream f_{Aex}^{Dem} theoretically cannot record any signal: The emission of a donor fluorophore upon acceptor excitation would break the energy conservation law and considers only background signals of the donor channel. Therefore, this photon-stream will be ignored for the rest of this work.

The equations in (1.30) describing the photon-streams can also be expressed as a function of the excitation and emission properties and FRET efficiencies:

$$\begin{aligned}
f_{Dex}^{Dem} &= I_{Dex} \cdot \sigma_{Dex}^{D} \cdot \phi_D \cdot \eta_{Dem}^{D} \left((1-E) \cdot P_D^A + P_D^D\right) \\
f_{Dex}^{Aem} &= I_{Dex} \cdot \sigma_{Dex}^{D} \cdot \phi_D \cdot \eta_{Aem}^{D} \left((1-E) \cdot P_D^A + P_D^D\right) \\
&\quad + I_{Dex} \cdot \sigma_{Aex}^{D} \cdot \phi_A \cdot \eta_{Aem}^{A} \left(P_D^A + P_A^A\right) \\
&\quad + I_{Dex} \cdot \sigma_{Dex}^{D} \cdot \phi_A \cdot \eta_{Aem}^{A} \left(E \cdot P_D^A\right) \\
f_{Aex}^{Aem} &= I_{Aex} \cdot \sigma_{Aex}^{A} \cdot \phi_A \cdot \eta_{Aem}^{A} \left(P_D^A + P_A^A\right),
\end{aligned} \tag{1.31}$$

where I denotes the excitation powers of the two light sources; σ stands for the excitation cross-section at the wavelength given by the light source, which is denoted in the upper index and of the given fluorophore denoted in the lower index; ϕ denotes the quantum efficiencies of donor and acceptor. Finally, η represents the detection efficiency of the given point detector in the lower index at the emission wavelength of the given fluorophore in the upper index.

The introduction of f_{Aex}^{Aem} enables the introduction of another dimension called stoichiometry (S).

$$S = \frac{(f_{Dex}^{Dem} + f_{Dex}^{Aem})}{(f_{Dex}^{Dem} + f_{Dex}^{Aem} + f_{Aex}^{Aem})} \tag{1.32}$$

Stoichiometry enables the separation of donor-only, acceptor-only, and FRET species, with donor-only populations with a S value of 1, acceptor-only a value of 0, and FRET species of intermediate values. Plotting E against S generates an ES-histogram (figure 1.5), a powerful tool with multidimensional layers of information. The ES-histogram visualizes cross-talk effects and differences in donor-acceptor quantum yields, allowing for the estimation of correction factors.

As shown in equation 1.30, leakage is contributed by P_D^D and P_D^A species in the f_{Dex}^{Aem} photon-stream. With the ES-histogram now available, it is possible to isolate P_D^D species and visualize and quantify the leakage directly: P_D^D species should have an E value of zero (equation 1.28); the slightly shifted population towards higher E values indicates a direct leakage contribution. The division of the f_{Dex}^{Aem} and f_{Dex}^{Dem} photon-streams of the isolated P_D^D species results in the quantification of leakage in percent.

$$\frac{f_{Dex}^{Aem}}{f_{Dex}^{Dem}} = \frac{I_{Dex} \cdot \sigma_{Dex}^{D} \cdot \phi_D \cdot \eta_{Dem}^{D} \; P_D^D}{I_{Dex} \cdot \sigma_{Dex}^{D} \cdot \phi_D \cdot \eta_{Aem}^{D} \; P_D^D} = \frac{\eta_{Dem}^{D}}{\eta_{Aem}^{D}} = lk \tag{1.33}$$

Similar to leakage, it is possible to visualize direct excitation by isolating P_A^A. In this case, S is shifted towards higher values. The division of the f_{Dex}^{Aem} and f_{Aex}^{Aem} photon-streams of the isolated P_A^A species also results in the quantification of direct excitation in percent.

$$\frac{f_{Dex}^{Aem}}{f_{Aex}^{Aem}} = \frac{I_{Dex} \cdot \sigma_{Aex}^{D} \cdot \phi_A \cdot \eta_{Aem}^{A} \; P_A^A}{I_{Aex} \cdot \sigma_{Aex}^{A} \cdot \phi_A \cdot \eta_{Aem}^{A} \; P_A^A} = \frac{I_{Dex} \cdot \sigma_{Aex}^{D}}{I_{Aex} \cdot \sigma_{Aex}^{A}} = dir \tag{1.34}$$

Now, with dir and lk, it is possible to correct the f_{Dex}^{Aem} photon-stream, leaving a cross-talk-free signal f^{FRET} with which it is possible to calculate proximity FRET efficiencies E_{pr}.

$$\begin{aligned} f^{FRET} &= f_{Dex}^{Aem} - lk \cdot f_{Dex}^{Dem} - dir \cdot f_{Aex}^{Aem} \\ \Rightarrow \; E_{pr} &= \frac{f^{FRET}}{(f_{Dex}^{Dem} + f^{FRET})} \end{aligned} \tag{1.35}$$

The final step is to correct for the different quantum yields of the donor and acceptor, as well as for the different detection efficiencies of the point detectors. This can be estimated by a single factor called the gamma factor (γ).

$$\gamma = \frac{\phi_A \cdot \eta_{Aem}^{A}}{\phi_D \cdot \eta_{Dem}^{D}} \tag{1.36}$$

The gamma factor is also visible in the ES histogram, represented by a distinct S value between two FRET populations, resulting in a linear relationship between $1/S$ and E_{pr}.

$$\frac{1}{S} = 1 + \gamma\beta + \beta(1-\gamma)E_{pr} \tag{1.37}$$

Where $\beta = I_{Aex} \; \sigma_{Aex}^{A} / I_{Dex} \; \sigma_{Dex}^{D}$. This implies that with different FRET populations, a $y = ax + b$ line can be fitted between them, where the intercept $b = 1 + \gamma\beta$ and the slope is $a = \beta(1-\gamma)$. By doing so, γ and β can be estimated.

$$\begin{aligned} \gamma &= \frac{(b-1)}{(b+a-1)} \\ \beta &= b+a-1 \end{aligned} \tag{1.38}$$

With the gamma factor, it is now possible to calculate accurate FRET efficiencies (E_{acc}) as shown below[35].

$$E_{acc} = \frac{f^{FRET}}{(\gamma\ f_{Dex}^{Dem} + f^{FRET})} \tag{1.39}$$

.

1.5.4 Super-resulotin imaging through single-molecule localization microscopy (SMLM)[§]

Ernst discovered that diffracted light from a periodic specimen such as a grating produces a diffraction pattern at the rear focal plane of the objective – this diffraction pattern is reponsible for image formation and the minimal distance between two objects to observe the pattern is the resolution:

$$d_{min} = \frac{\lambda}{2 \cdot n \cdot \sin\theta} = \frac{\lambda}{2 \cdot NA} \tag{1.40}$$

where d_{min} is the minimal distance between two points, λ is the wavelength of the light, n is the refractive index and $\sin\theta$ is the maximal half-angle of the light cone entering the lens. $n \cdot \sin\theta$ is also called the numerical aperture.

Diffraction is the cause of this limitation, wherein the image formed by a lens-based microscope of even a single emitter is not a point but an Airy disc. Mathematically, a single point source is convolved with the microscope's point spread function (PSF), resulting in an Airy pattern. This pattern features a central peak approximately 200–300 nm in width (Figure 1.11). Consequently, structures smaller than the diffraction limit cannot be resolved.

However, in the case of a single emitter, its location and center of mass can be determined with high precision by computing the x-y location (centroid) of the airy disc. There are many localization algorithms available, among which a Gaussian approximation of the PSF is the most commonly used. The primary parameter that defines the accuracy of the position of a single fluorophore is essentially the standard error of the mean of the fitted Gaussian over the PSF[95,96].

$$\sigma_{loc} \propto \frac{\sigma_{PSF}}{\sqrt{N}} \tag{1.41}$$

where σ_{PSF} is the standard deviation of the PSF an N is the number of photons recorded from the single emitter.

[§] The concepts discussed in this Section are based on the textbooks by Sauer, Hofkens, and Enderlein (Chapter 8), Lakowicz (Chapters 2, 8 and 23)

The principle behind single molecule localization microscopy is the spatiotemporal separation of fluorophore signals that are in close proximity. When individual signals are separated, their point spread functions can be fitted individually, essentially enabling the determination of their positions below Abbe's diffraction limit[95] (figure 1.12).

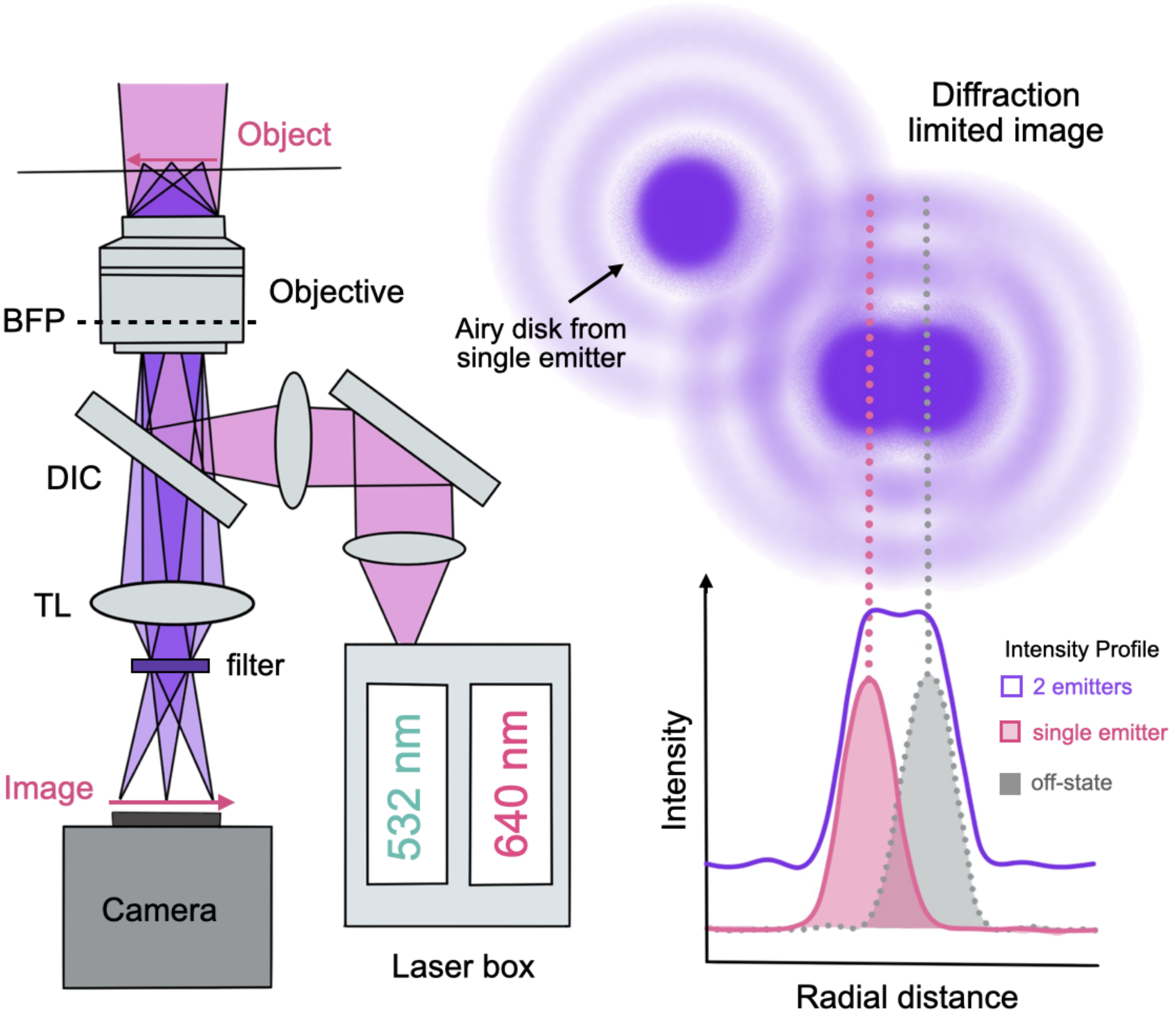

Figure 1.11: Single molecule localization microscopy (SMLM): The left panel depicts the basic construction and light path of a widefield epi-fluorescence microscope. The excitation laser beam (pink light path) is focused and reflected through a dichroic mirror (DIC) into the back focal plane (BFP) of an objective, producing a wide collimated light beam that illuminates the complete field of view. The fluorescence (purple light path) emitted from the sample (pink arrow) is collected by the objective and focused with a tube lens (TL) onto a camera, creating a real image (pink arrow) of the sample. The upper right panel shows a diffraction-limited image of a single emitter (left side) and two emitters in close proximity (right side). The lower right panel shows an intensity profile of the two emitters in close proximity mentioned previously (purple line), as well as the intensity profile of the emitter on the left side (pink line) while the right one is in an off state.

$$d_{SMLM} = \frac{\lambda}{2 \cdot NA \cdot \sqrt{N}} \tag{1.42}$$

The spatiotemporal separation of fluorophore signals is enabled by switching them on and off. One way of achieving this is with PALM or photoactivated localization microscopy, which employs mutants of fluorescent proteins displaying controllable photochromism, such as photo-activatable GFP[27]. The principle behind it is to activate a handful of fluorescent proteins with a short UV light pulse. After determining their positions, the emitters are photo-bleached, after which the cycle can be repeated. In contrast, stochastic optical reconstruction microscopy (STORM) takes advantage of intersystem crossing (ISC) to the dark triplet state of organic fluorophores[28]. Here, the on-off states can be tuned with different laser powers combined with the usage of a mixture of oxygen scavenging buffers with reducing agents, such as -mercaptoethanol[49,97,51]. The main limitation of PALM and STORM is the inevitable photobleaching of the emitters, which consequently limits the number of photons that can be collected and, as a result, limits their localization precision. A possible solution for this problem is the use of transiently binding probes as done in PAINT and DNA-PAINT. The latter technique uses short oligonucleotides (imager) that bind to complementary (docking) strands, thereby creating the necessary spatiotemporal separation of single localization events[29,30]. In contrast to STORM and PALM, PAINT does not suffer from photobleaching events since the imager is constantly replaced by another imager, resulting in even higher localization precision.

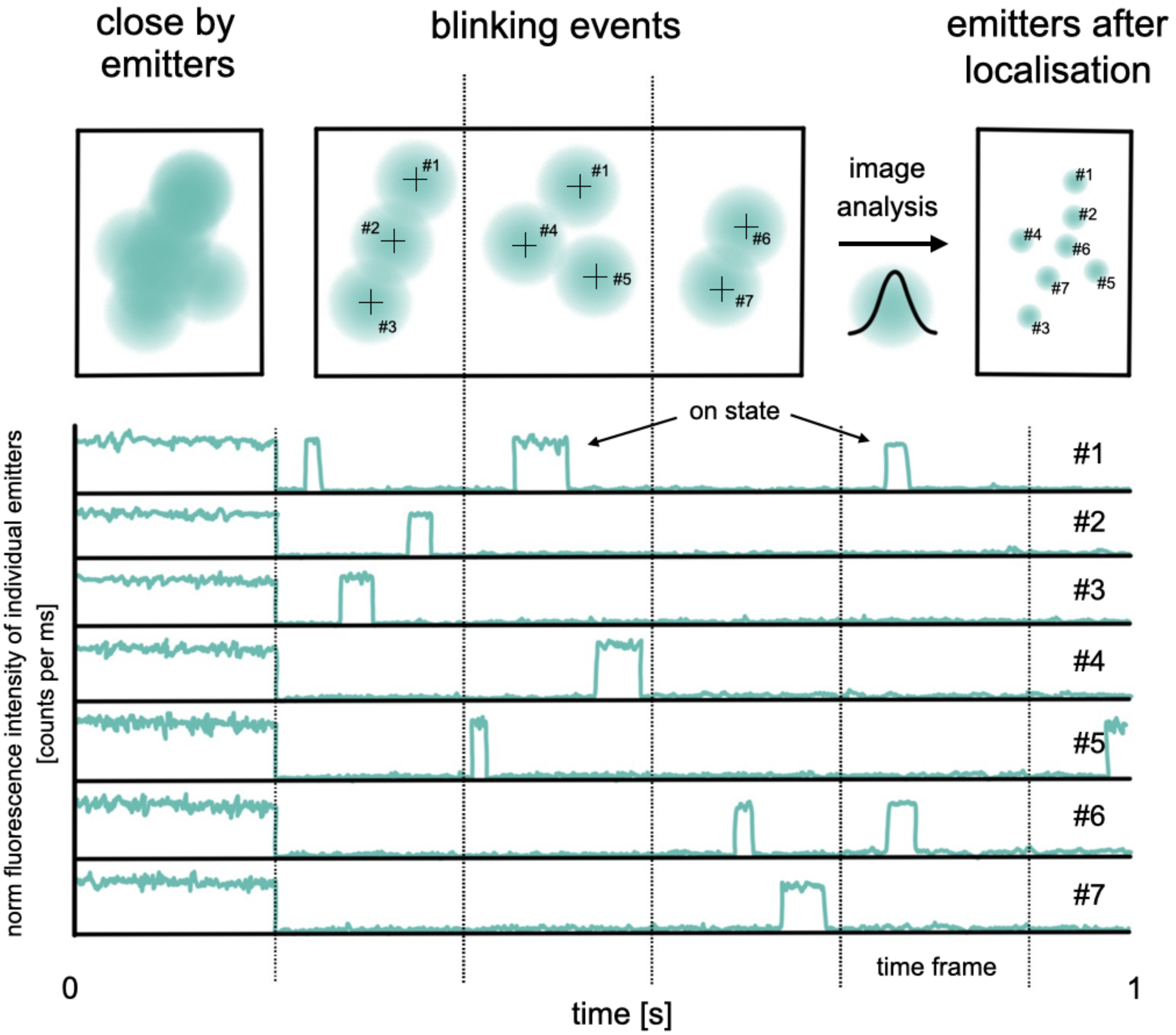

Figure 1.12: Principle of Single-Molecule Localization Microscopy (SMLM): The upper-left panel illustrates seven fluorophores in close proximity, emitting simultaneously and resulting in a diffraction-limited image. The lower panel presents fluorescence intensity time traces of individual fluorophores (1–7).
SMLM techniques such as PALM, STORM, and PAINT induce stochastic blinking events, enabling spatiotemporal separation of single emitters. The camera's frame rate must be fast enough to capture these events. The dashed lines indicate the camera's time frames: the first frame shows all fluorophores emitting simultaneously; the second frame captures the "on" states of fluorophores 1–3; the third frame captures fluorophores 1, 4, and 5; and the fourth frame captures fluorophores 6 and 7.
The corresponding images are displayed in the upper-middle panel, where crosses represent the localization precision (σ_{loc}) of each emitter. These localizations are subsequently used to reconstruct a super-resolution image that exceeds the diffraction limit."

1.6 Aims and milestones for this thesis

Edward Muybridge's milestone was achieved through advancements in the spatial and temporal resolution of optical instrumentation, enabling the depiction of a single horse in galloping motion with all feet in the air. However, access to his invention, now recognized as a video camera, was limited to individuals with skill, understanding of imaging, and financial resources. This limitation seems almost unimaginable today, given the widespread availability of cameras in our modern world.

Today, single-molecule spectroscopy and super-resolution microscopy have advanced significantly and by now represent important tools for life science research. Yet, there remains a gap between state-of-the-art technology and its accessibility to non-optics specialists, such as biologists, biochemists, medical researchers, and laboratories with financial constraints.

This thesis aims to bridge the accessibility gap by making cutting-edge single-molecule spectroscopy and super-resolution microscopy more accessible in terms of both usage and costs. My vision is that this work represents a significant step forward in bringing single-molecule spectroscopy and super-resolution microscopy beyond the confines of academia, transforming them into tools not only for life sciences but also for more application-oriented fields such as drug discovery, early clinical diagnostics, or even environmental pollutant detection.

There are a series of early milestones that will facilitate the initial steps of this transition, forming the backbone of this thesis:

Emerging technologies require consensus and validation from multiple experts in the field. This thesis particularly focuses on the implementation and advancement of single-molecule Förster resonance energy transfer (smFRET) and super-resolution microscopy. SmFRET is widely used in structural biology, where pairs of fluorophores are strategically placed at specific sites on biomolecules to monitor their dynamics and conformational changes.

One of the significant obstacles in smFRET and super-resolution microscopy is that many of the devices used for these techniques are home-built, tailored specifically to the needs of individual labs. This introduces a high degree of experimental variability, as each setup is unique in terms of hardware, software, and calibration protocols. As a result, comparing data across labs becomes challenging, and discrepancies in results can arise from these setup-dependent differences. While the community has made progress in advancing the understanding of smFRET in DNA-based systems, the same level of precision and accuracy has not been achieved for protein systems, which are more complex and dynamic.

The use of proteins, in particular, adds another layer of complexity to sample preparation. Unlike DNA, proteins are highly complex biomolecules with diverse structures and functions. Their intricate interactions within biological systems and dynamic surfaces, which show a rich array of physicochemical properties—such as varied charge distributions, hydrophobic regions, and binding sites—make them significantly harder to work with in experimental settings.

In collaboration with Agam et al., as published in *Nature Methods* (*"Reliability and reproducibility in single-molecule fluorescence experiments across laboratories"*)[98], we focused on addressing these challenges, particularly those introduced by the variability in home-built setups. Interestingly, despite the differences in setups worldwide, the data produced across these diverse systems were surprisingly similar. This finding suggests that the key factors influencing the data were not necessarily the differences in the setups themselves, but rather the methods used to correct for setup-specific artifacts. Our study relied on established data correction procedures that accounted for several setup-specific factors, including background noise, fluorescence crosstalk, and the gamma factor[35,94]. These calibration corrections were essential for ensuring that data collected from different setups could be compared reliably.

Despite the complexities involved, the variation in the outcomes was surprisingly low. However, when a single person analyzed the data, the variation decreased even further, demonstrating a clear human factor in the analysis. This reduction in variability highlights the importance of consistency in data processing, as even small differences in how data is handled can influence results.

The most delicate correction factor in the procedure was the gamma factor, as even small changes in its value can dramatically alter the results. However, an interesting observation from the study was that when there was a significant difference in the FRET efficiencies between two states—greater than 0.1, which is the average range in which proteins typically move—the relative uncertainty of the gamma factor decreased to below 0.1%. This explains why the results from different labs worldwide were similar, despite the variability in their home-built setups.

While the gamma factor is crucial and its precise determination is challenging, careful protein design and optimal fluorophore pairing can significantly reduce the relative error. This is key to ensuring that the gamma factor correction does not introduce significant deviations in the data, even when working with highly dynamic protein systems. Despite its sensitivity, when handled properly, the gamma factor allows for more accurate and reproducible smFRET measurements across diverse experimental setups.

Furthermore, smFRET was compared with Pulsed Electron-Electron Double Resonance or Double Electron-Electron Resonance (PELDOR/DEER) spectroscopy and anomalous X-ray scattering interferometry (AXSI) to establish the reliability and consistency of the methods when applied to the same macromolecular systems, using model proteins known for their conformational changes upon ligand binding.

In both the study by Martin F. Peter et al., *"Cross-validation of distance measurements in proteins by PELDOR/DEER and single-molecule FRET,"* published in *Nature Communications*[99], and the work by Samuel Stubhan et al., *"Determination of absolute intramolecular distances in proteins using anomalous X-ray scattering interferometry,"* published in *Nanoscale*[100], the key focus was on comparing the performance of smFRET with other techniques, namely PELDOR/DEER and AXSI, in measuring distances within proteins. Both PELDOR/DEER and AXSI were found to show good agreement with smFRET under most conditions, confirming the reliability of smFRET in protein distance measurements. However, both studies also revealed isolated instances where discrepancies arose, which were attributed to specific interactions between the protein and the fluorophores used in smFRET. These interactions, such as fluorophore sticking or changes in the microenvironment of the fluorophores, led to artifacts in the smFRET data. Both studies highlighted that these issues could be corrected by carefully selecting fluorophore pairings with distinct properties, thus minimizing such artifacts and improving the accuracy of the measurements. Although PELDOR/DEER and AXSI offered complementary insights, the findings showed that smFRET remains a powerful and versatile method, with the key challenges related to fluorophore-specific interactions being effectively mitigated through thoughtful experimental design.

The next step toward the democratization of single-molecule spectroscopy and super-resolution microscopy was the availability of the instruments themselves. While core facilities for imaging and biophysical techniques existed, they were often limited in number, provided restricted or infrequent access, and sometimes required travel. These limitations were particularly challenging since many biological and medicinal studies required long iterative refinements, local sample analysis, or point-of-care applications that were not feasible under these constraints. Beyond the financial barriers posed by the high cost of equipment, the expertise required for calibration and operation further restricted accessibility. Addressing these challenges required user-friendly interfaces, standardized protocols, and training programs to enable a broader range of researchers to effectively use these advanced tools.

In the paper titled *"Single-molecule detection and super-resolution imaging with a portable and adaptable 3D-printed microscopy platform (Brick-MIC),"* published in *Science Advances,*[101] We introduced an innovative solution to these accessibility challenges. Brick-MIC, a versatile, open-source, and affordable 3D-printed platform, was designed for micro-spectroscopy and imaging. Supporting a range of fluorescence techniques—including smFRET, fluorescence correlation spectroscopy (FCS), and super-resolution methods like STORM and PAINT—this platform enabled sophisticated single-molecule experiments in a cost-effective and user-friendly manner. By eliminating the need for specialized laboratories and making these techniques accessible to researchers in smaller labs or resource-limited settings, Brick-MIC represented a key step toward making single-molecule spectroscopy and super-resolution imaging more widely accessible.

This platform was specifically designed to be modular, flexible, and easy to assemble using 3D-printed parts, which significantly reduces the cost of building such setups. Moreover, its open-source nature ensures that the system can be easily adapted and customized to fit the needs of different research groups. The Brick-MIC platform not only provides an affordable alternative to traditional single-molecule spectroscopy and super-resolution microscopy setups, but it also empowers researchers to conduct experiments in their own labs without the need for specialized training or expensive equipment.

Building on the flexibility of *Brick-MIC*, an innovative assay for nanoparticle detection was developed and applied to identify SARS-CoV-2 virus particles. This work, published by Paz Drori et al. as *"Rapid and specific detection of nanoparticles and viruses one at a time using microfluidic laminar flow and confocal fluorescence microscopy,"* in *iScience*[102], highlighted the potential of *Brick-MIC* for practical diagnostics. The assay leverages microfluidic laminar flow and confocal fluorescence microscopy to detect individual nanoparticles and viruses with high specificity, demonstrating how *Brick-MIC* can be adapted for real-world applications, such as disease detection, and bringing the platform closer to point-of-care diagnostics.

The detection process combined direct labeling of virus particles with an additional indirect signal inspired by intensity-based Fluorescence Correlation Spectroscopy (iFCS). In this method, the detection volume was saturated with a high concentration of freely diffusing fluorophores, creating a constant background signal. When a virus particle moved through this volume, it displaced some of the fluorophores, producing a void in the fluorescent signal. The size of this void was directly proportional to the size of the particle. By correlating this void signal with the specific fluorescence from labeled virus particles, we were able to achieve a reliable and specific detection.

The incorporation of laminar flow in the microfluidic design further enhanced the detection process, increasing the number of recorded events and improving throughput. This approach bypassed the need for sample replication, allowing for direct and efficient detection. The dual-layer information—specific labeling and particle size—provided by this assay makes it a robust and versatile method for virus detection.

By integrating these techniques, Brick-MIC demonstrated its adaptability to real-world challenges, offering a straightforward, cost-effective, and innovative tool for nanoparticle and virus detection with significant implications for diagnostics and public health.

As a final contribution of this thesis, we developed a new modality of Brick-MIC that we believe represents the most affordable approach to performing smFRET to date. This iteration focused on simplifying both the instrumentation and methodology, making it more accessible for application-oriented users. Instead of the conventional red-green FRET pair, we opted for a blue-green FRET system. This choice was motivated by the poor detection efficiency of the photomultiplier tube (PMT) used in this setup, which performs better in the blue-green spectral range.

To further simplify the system, we employed a 488 nm continuous-wave laser diode instead of using alternating laser excitation (ALEX), a common approach in smFRET experiments requiring two lasers. While this decision meant we lacked stoichiometric information about the sample, we implemented a dual-channel burst search algorithm to identify real FRET species. This allowed us to measure inter-fluorophore distances using DNA samples as test systems.

Although the data collected in this setup is insufficient for correcting FRET efficiencies to accurate values, the focus of this work was not on achieving the highest precision but rather on enabling users to observe relative movements of biomolecules. This trade-off aligns with the needs of application-oriented users, where the goal is often to monitor conformational changes or interactions rather than determine absolute molecular distances.

This modality of Brick-MIC demonstrates that even with minimal and cost-effective instrumentation, smFRET can be made accessible to a broader audience. By prioritizing ease of use and affordability, this work takes another step toward democratizing single-molecule fluorescence techniques for researchers with limited resources or expertise in optical setups.

In this thesis, the goal is to make single-molecule spectroscopy and super-resolution microscopy as accessible and widespread as the video camera, which has become a ubiquitous tool in everyday life. To illustrate this, one can look back at the work of Edward Muybridge, whose experiments with photography at the end of the 19th century captured the first high-speed images of a galloping horse. At the time, Muybridge's setup involved a series of cameras, each capturing one frame as the horse moved past, thus revealing the motion of all four hooves leaving the ground. While his invention was groundbreaking, it was still limited by the technology of the time—requiring a complex and expensive setup, and only accessible to a small number of researchers.

Today, thanks to the invention of the video camera, which stemmed from Muybridge's work, capturing motion has become as simple as pressing a button on a smartphone. Everyone now has the ability to record high-speed motion, a task that was once restricted to specialized labs and expensive equipment. Muybridge's groundbreaking work with motion photography has, in a sense, paved the way for the democratization of motion capture. Similarly, the goal of this thesis is to move single-molecule techniques, such as smFRET and super-resolution microscopy, along a similar trajectory—making these powerful tools widely accessible for researchers and even applied users in a variety of fields.

In this context, the Brick-MIC platform developed during this thesis acts as a step toward this vision. Just as Muybridge's series of cameras enabled the capture of complex movements, the Brick-MIC platform allows for the visualization of complex molecular interactions and dynamics at the single-molecule level, but with a focus on cost-effective and user-friendly design. By simplifying the setup and making it accessible to a wider range of researchers, this thesis aims to bring single-molecule techniques closer to the level of ubiquity that video recording reached with Muybridge's initial innovations.

Just as smartphones today can replicate what once required expensive and specialized equipment, the hope is that in the future, single-molecule techniques will follow a similar path. As this thesis demonstrates, the development of affordable, versatile, and easy-to-use tools for molecular spectroscopy is a crucial step forward in making these methods commonplace, enabling more researchers to explore biomolecular dynamics in real-time.

2

Methodology

2.1 Sample preparation

2.1.1 DNA-labelling & annealing

Fluorescently labeled DNA probes are well-suited for single-molecule diffusion-based experiments due to their structural rigidity, which results from their long persistence length, and their high hydrodynamic radius, which prolongs diffusion times. The double-stranded DNA (dsDNA) structure provides an efficient platform for testing various fluorophore combinations and inter-dye distances.

The DNA template used in this study consisted of a top strand (T) with the sequence 5'-TAAAT CTAAA GTAAC ATAAG GTAAC ATAAC GTAAG CTCAT TCGCG-3', labeled with a donor fluorophore, typically at the 5' end (T1) or at specific thymine residues. The complementary bottom strand (B) had the sequence 3'-ATTTA GATTT CATTG TATTC CATTG TATTG CATTG GAGTA AGCGC-5', carrying the acceptor dye at designated thymine positions. Fluorophore-labeled oligonucleotides were synthesized as described in ref.[103] and obtained from IBA (Göttingen, Germany).

For annealing, the single-stranded oligonucleotides were mixed in equimolar concentrations (1 µM) in a 100 µL solution of annealing buffer containing 500 mM sodium chloride, 20 mM TRIS-HCl, and 1 mM EDTA at pH 8. The solution was heated to 95°C for 4 minutes and then cooled gradually to 4°C at a rate of 1°C/min to ensure proper hybridization of the complementary strands.

2.1.2 Protein stochastic cysteine labeling & purification

Proteins, composed of 21 amino acids, fold into complex functional structures, with certain residues like lysines (amine groups) or cysteines (thiol groups) offering reactive sites for covalent binding with functionalized fluorophores via NHS or Maleimide chemistry[104]. For cysteine-labeling, the protein must include desired labeling sites introduced via mutagenesis, favoring solvent-exposed and non-conserved regions to optimize labeling efficiency, maintain functionality, and suit the intended assay[105].

For FRET assays, labeling sites should ideally be at distances close to the Förster radius, enabling dynamic range measurements for different conformational states. Additionally, endogenous solvent-exposed lysines or cysteines must be removed to prevent non-specific labeling.

Histag labeling is another widely used approach. This method utilizes a histidine tag, typically 6-10 residues long, appended to the N- or C-terminus of the protein[106,107]. The histag's affinity for bivalent metal ions, commonly used for purification via Ni-NTA resin, is extended by labeling with fluorophores functionalized with Ni-NTA groups. However, since this labeling is based on affinity, neither the number nor the position of attached dyes can be precisely controlled. Moreover, this method is unsuitable for single-molecule assays, as the high dilution needed for such assays can result in dye dissociation due to weak affinity.

Incorporating unnatural amino acids (UAAs) offers an alternative labeling strategy for cases where the above methods fall short[108]. However, this thesis focuses exclusively on cysteine labeling.

Protein Labeling Protocol

For each labeling reaction, 600 µg of protein from frozen stocks was used. Proteins were incubated for 30-60 minutes in PL1 buffer (50 mM Tris-HCl pH 7.4, 50 mM KCl) supplemented with 1 mM DTT to maintain the reduced state of cysteine residues. Labeling was performed using a Bio-Rad Poly-Prep Chromatography column containing 160 µL of Ni Sepharose 6 Fast Flow resin. After washing the resin with milli-Q water and equilibrating it with PL1 buffer, proteins were added to the column and immobilized on the resin. Remaining DTT was removed by washing with PL1 buffer.

For labeling, a dye mixture containing 25 nmol dye for FCS/anisotropy measurements or 25 nmol each of donor and acceptor dye (for FRET experiments) was prepared in 5 µL DMSO. The dye mixture was added to the immobilized protein, gently mixed, and incubated overnight at 4°C. Excess dyes were removed by washing with PL1 buffer, followed by PL2 buffer (PL1 with 50

The labeled protein was further purified using size-exclusion chromatography to separate aggregates, free fluorophores, and contaminants. A Superdex 75 Increase column (GE Healthcare), selective for proteins in the 3-70 kDa range, was used, and protein elution was monitored via absorbance at 280 nm (protein) and the fluorophore's maximum wavelength.

2.1.3 Sample surface immobilization for dSTORM

For each experiment, an ibidi µ-Slide 8 Well Glass Bottom chamber was used (μ-Slide VI 0.5 Glass Bottom, Ibidi). Prior to use, the chamber was washed three times with 500 µL of PBS. Then, 200 µL of a BSA-biotin solution (1 mg/mL in PBS; 140 mM NaCl, 10 mM phosphate buffer, 3 mM KCl, pH 7.4) containing 100 nm fluorescent tracking beads (TetraSpeck, Thermo Fisher) was added and incubated for 10 minutes. After incubation, the solution was removed, and the chamber was carefully washed three times with 500 µL PBS.

Subsequently, 200 µL of streptavidin solution (1 mg/mL in PBS) was added to the chamber and incubated for another 10 minutes. The streptavidin solution was removed, and the chamber was washed three times with imaging buffer (IB; PBS with 10 mM magnesium chloride). A 1–10 µL solution of DNA origami nanorods (Gatta-STORM 94R, Gattaquant) was diluted in 200 µL IB and added to the chamber. DNA origamis were incubated until a density of $1/\mu\text{m}^2$ was achieved. The DNA origami solution was then removed, and the chamber was washed three times with 500 µL IB.

For photoswitching during imaging, 500 µL of an oxygen scavenging system buffer was used. This buffer contained pyranose oxidase (3 U/mL), catalase (90 U/mL), and 40 mM glucose in PBS, mixed with 0.1% (v/v) -mercaptoethanol[51].

2.1.4 DNA-PAINT

DNA-PAINT samples were obtained pre-prepared from Gattaquant (Gatta-PAINT 80RG, Gattaquant, Germany).

2.1.5 Preparation of Polystyrene Beads for Size Determination Assays

For proof-of-concept experiments and size comparisons, polystyrene beads with mean diameters of 1,100 ± 100 nm (LB11, Sigma), 600 ± 30 nm (LB6, Sigma), and 300 ± 30 nm (LB3, Sigma), as well as red polystyrene carboxylate-modified beads (FluoSpheres Size Kit 1, F8887, Thermo-Fisher) (excitation/emission $\lambda_{\max} = 580/610$ nm) with mean diameters of 100 nm (110 ± 8 nm), 200 nm (170 ± 8.8 nm), and 500 nm (490 ± 11 nm), were used. The beads were added to a buffer containing 75 mM KCl (Sigma, 60128), 0.025% Triton (Sigma, 93443), 20 mM TRIS (pH 8.6), and 1% PEG 10,000. The particle concentration was adjusted to range from 10^5 to 10^8 particles/mL.

The mixture was sonicated for 20 to 35 minutes to ensure proper dispersion. Free dye (Fluorescein, excitation/emission $\lambda_{\max} = 488/510$ nm) was then added to a final concentration of 500 μM. The prepared sample was loaded into a 1 mL syringe for use in microfluidic experiments. The samples were pumped at a constant flow rate into a microfluidic channel (μ-Slide VI 0.5 Glass Bottom, Ibidi) for analysis.

2.2 Microscopy Setups, Measurements & Data Analysis

2.2.1 Lab´s confocal microscope

The experimental setup utilized alternating laser excitation (ALEX) with two diode lasers: OBIS 532-100-LS (Coherent, USA), operated at 60 W for donor molecules at 532 nm, and OBIS 640-100-LX (Coherent, USA), operated at 25 W for acceptor molecules at 640 nm. For FCS measurements, the 532 nm diode laser was set to continuous-wave (CW) mode and operated at 25 W, while the 640 nm laser was turned off. The lasers were combined and coupled into a polarization-maintaining single-mode fiber (P3-488PM-FC-2, Thorlabs, USA) and directed into an epi-illuminated confocal microscope (Olympus IX71, Hamburg, Germany).

The laser light was guided to the sample using a dual-edge beamsplitter (ZT532/640rpc, Chroma/AHF) and focused through a water-immersion objective (UPlanSApo 60×/1.2w, Olympus, Hamburg, Germany). Emitted fluorescence was collected through the same objective, spatially filtered using a 50 m diameter pinhole, and spectrally separated into donor and acceptor channels by a single-edge dichroic mirror (H643 LPXR, AHF).

Fluorescence emission was filtered by band-pass filters placed in front of each detector: for the donor channel, FF01-582/75-25 (Semrock/AHF, Germany), and for the acceptor channel, ET700/75m (Chroma/AHF, Germany). The detector outputs for μALEX were recorded by an NI-Card PCI-6602 (National Instruments, USA) using LabView data acquisition software from the Weiss laboratory[109].

ALEX data analysis

All samples for smFRET analysis were measured in a 100 μL PBS droplet with concentrations ranging from 50 to 100 pM, placed on a coverslip passivated with BSA (1 mg/mL in PBS). Data analysis was performed using a home-written software package[39]. Single bursts were first identified using All-Photon-Burst-Search (APBS) with a threshold for burst start/stop of 15 photons[91], a time window of 500 μs, and a minimum total photon number of 150 within the burst. Based on these data, donor leakage (Lk) and direct acceptor excitation (Dir) were determined as mean values from a 1D fit of background-corrected donor-only (E*) and acceptor-only (S*) distributions. Next, a Dual-Channel-Burst-Search (DCBS) was performed with similar parameters to determine excitation flux (β), detection efficiency, and quantum yields (γ)[35,98]. E-histograms of double-labeled FRET species were generally extracted by selecting $0.3 < S < 0.7$. The E-histograms were fitted with a Gaussian function of the form:

$$\frac{1}{\sigma\sqrt{2\pi}} \exp\left(-\frac{(E-\mu)^2}{2\sigma^2}\right) \tag{2.1}$$

where E represents the measured FRET efficiency for each detected molecule, μ is the mean, and σ is the standard deviation.

For the conversion of FRET efficiency to inter-dye distance, the Förster equation was used:

$$R_{DA} = R_0 \sqrt{\frac{6(1-E)}{E}} \tag{2.2}$$

The Förster radius R_0 is given by the following equation[110]:

$$R_0^6 = \frac{9\ln(10)}{128\pi^5 N_A}\kappa^2 \frac{1}{n^4} Q_D \left(\int_0^\infty F_D(\lambda)\epsilon_A(\lambda)\lambda^4 d\lambda\right) \Big/ \left(\int_0^\infty F_D(\lambda) d\lambda\right) \tag{2.3}$$

where N_A is Avogadro's constant, κ^2 is the dipole orientation factor, n is the average refractive index of the medium, Q_D is the donor quantum yield, F_D is the donor emission spectrum, and ϵ_A is the acceptor absorbance spectrum.

FCS data analysis

All samples were studied by positioning the confocal excitation volume into a 100-l PBS droplet with concentrations ranging from 5 to 10 nM on a coverslip passivated with BSA (1 mg/ml in PBS). Data analysis was performed using a home-written Python script (https://github.com/PSBlmu/FCS-analysis), where the intensity fluctuation of freely diffusing molecules, $F(t)$, is analyzed via autocorrelation.

$$G(\tau) = \frac{\langle F(t)F(t+\tau)\rangle}{\langle F(t)^2\rangle} - 1 \tag{2.4}$$

The correlation amplitude, $G(\tau)$, describes the self-similarity of the signal in time. Average fluorescence intensities at time points t and later lag times τ were used for analysis. $G(\tau)$ was analyzed with a 3D diffusion model,

$$G(\tau) = \frac{1}{N}\left(1+\frac{\tau}{\tau_D}\right)^{-1}\left(1+\frac{\tau}{\tau_D}\cdot\frac{r_0^2}{z_0^2}\right)^{-\frac{1}{2}} \tag{2.5}$$

where N represents the average number of molecules in the confocal volume, τ_D is the average diffusion time, and r_0 and z_0 define the lateral and axial radial distances of the detection volume, which together determine the geometry parameter $\kappa = \frac{z_0}{r_0}$.

2.2.2 3D Printing of the Brick-MIC Platform

All models were designed and created using Onshape versions 1.114 to 1.172. 3D printing was conducted with PLATech filament (OLYMPfila) on an Ultimaker +2 Extended, equipped with a 0.4 mm nozzle. All models were printed with an infill density of 17%, three outer wall layers, and a layer height of 0.1 mm. The printing speed was set to 50 mm/s, and the nozzle temperature was maintained at 210°C. To prevent warping, all parts were printed with a brim and without any support structures.

2.2.3 3D-printed FCS microscope (μFCS)

The experimental setup used a 532-nm wavelength CW laser diode (5-mW output; CPS532, Thorlabs) contained in the excitation layer of the Brick-MIC as the excitation light source. The beam passed through a clean-up filter (FL05532-10 12.5 mm, Thorlabs), underwent attenuation via a continuous neutral density filter wheel (NDC-50C-2M, Thorlabs), and was expanded using a telescope consisting of a biconcave lens (f = 50 mm, KBC043AR.14, Newport) and a plano-convex lens (f = 150 mm, LA1433-A-ML, Thorlabs). A dichroic beam splitter with high reflectivity at 532 nm (ZT532/640rpc, Chroma, USA) separated the excitation and emission beams to and from a high-NA apochromatic objective (60×, NA 1.2, UPlanSAPO 60XW, Olympus, Japan).

The emitted fluorescence was collected by the same objective and guided into the emission layer of the Brick-MIC. It was then directed via a mirror into a piezo-controlled optical mount (AG-M100N, Newport) and passed through an inversely mounted 12-mm reflective collimator (RC12FC-P01, Thorlabs). This collimator focused and coupled the emission beam into a multimode optical fiber (10-µm core diameter, M64L01, Thorlabs). The fiber guided the emission light into a detection box, where it was collimated with a fixed-focus collimator (F220FC-532, Thorlabs) and spectrally split into two separate photon streams by a dichroic mirror (DM, ZT640rdc longpass, Chroma, USA).

Each photon stream was filtered with band-pass filters: for the green channel, FF01-582/75-25 25 mm (Semrock, Rochester, NY, USA), and for the red channel, ET700/75m (Chroma). These streams were detected by two distinct photomultiplier tubes (PMTs) with different spectral sensitivities: for the green channel, H10682-210 (Hamamatsu, Japan), and for the red channel, H10682-01 (Hamamatsu, Japan).

The detector outputs for FCS analysis were either recorded by a NI-Card PCI-6602 (National Instruments, USA) using LabView data acquisition software from the Weiss laboratory[109], or via a counter/timer device module (USB-CTR04, Measurement Computing, USA) with custom-made acquisition software written in Python, which is available for download as a compiled executable or editable Python code at https://github.com/harripd/mcc-daq-acquisition.

Data analysis was performed as described in section 2.2.1

2.2.4 3D-printed ALEX microscope ($\mu ALEX$)

The experimental setup utilized alternating laser excitation (ALEX) with two diode lasers: OBIS 532-100-LS (Coherent, USA), operated at 60 μW for donor molecules at 532 nm, and OBIS 640-100-LX (Coherent, USA), operated at 25 μW for acceptor molecules at 640 nm. Both lasers alternated with a 100 μs period. The lasers were combined through an aspheric fiber port (PAF2S-11A, Thorlabs, USA) and coupled into a polarization-maintaining single-mode fiber (P3-57 488PM-FC-2, Thorlabs, USA), which guided the light into the excitation layer of the Brick-MIC. The light was then collimated (RC12APC-P01, Thorlabs, USA) before entering an epi-illuminated confocal microscope (Olympus IX71, Hamburg, Germany).

Excitation and emission collection were performed using the same water-immersion objective (60×, NA 1.2, UPlanSAPO 60XW, Olympus, Japan), and spectral separation was achieved using a dual-edge beamsplitter (ZT532/640rpc, Chroma/AHF, Germany). Fluorescence emitted from the sample was collected by the same objective, guided to the emission layer of the Brick-MIC, and focused via an achromatic lens (AC254-200-A, Thorlabs) directly onto single-photon avalanche diodes (PDM 50-Micron, MPD). The small active area of the detectors (ø 50 μm) served as a pinhole.

Before detection, the photon streams were spectrally split into donor and acceptor channels by a single-edge dichroic mirror (H643 LPXR, AHF, Germany). Fluorescence emission was filtered by band-pass filters placed in front of each detector: for the donor channel, FF01-582/75-25 (Semrock/AHF, Germany), and for the acceptor channel, ET700/75m (Chroma/AHF, Germany). The detector outputs for μALEX were recorded by an NI-Card PCI-6602 (National Instruments, USA) using LabView data acquisition software from the Weiss laboratory[109].

Data analysis was performed as described in section 2.2.1

2.2.5 3D-printed Time-correlated-single-photon-counting microscope ($\mu TCSPC$)

The setup for fluorescence lifetime decay measurements combined the excitation layer of the ALEX modality with the emission layer of the FCS modality (see section 2.3.3-4) The configuration employed a 532 nm fiber-coupled pulsed laser operating at a repetition rate of 20 MHz and a power of 55 μW (LDH-P-FA-530B with PDL 828 'Sepia II' controller, Picoquant, Germany). Detection was performed using PMTs connected to a Multiharp 150 8N module (Picoquant, Germany).

All samples were measured in a 50 μL PBS droplet at a concentration of 10 nM on a coverslip for 10 minutes. The instrument response function (IRF) was acquired by measuring a 50 μL PBS droplet for 60 minutes.

Fluorescence lifetime decays were analyzed using the SymPhoTime 64 software and fitted with a single exponential tail-fit model ($n = 1$). A fitting window of 21.79 ns was used for all measurements.

2.2.6 3D-printed blue-green CW smFRET microscope (μBG)

The setup for blue-green smFRET measurements integrated the excitation layer of the ALEX modality with the emission layer of the FCS modality (see Section 2.3.3-4). Key modifications included the use of a USB-powered 488 nm CW laser pointer (488-30-1235-BL, Q-LINE), which was coupled into an optical fiber (P5-488PM-FC-2, Thorlabs) via an inversely mounted reflective collimator (RC08FC-P01, Thorlabs). To accommodate the new excitation and emission wavelengths, the DIC mirrors and emission filters were swapped: DICex: ZT491rdc (Chroma), DICem: ZT543rdc (Chroma), and the donor channel filter FF03-525/50 (Semrock). A notch filter (NF488-15, Thorlabs) was introduced in the acceptor channel to block scattered light and optimize photon collection across the full emission spectrum of the acceptor.

Data collection & analysis

All samples for smFRET analysis were measured in 100 L PBS droplets, with concentrations ranging from 50 to 100 pM.

Detector outputs were recorded using a counter/timer device module (USB-CTR04, Measurement Computing, USA) with custom acquisition software written in Python (described in Section 2.2.3). For smFRET assays, the software exported photon arrival times in a binned format (1 ms bins) to a CSV file.

FRET efficiencies were determined by processing the binned data with an R script. FRET events were identified when the photon counts from both the donor and acceptor channels exceeded predefined thresholds (10 counts/ms for the donor and 25 counts/ms for the acceptor) simultaneously. A FRET event was registered as long as both signals remained above the thresholds. If both signal traces exceeded the thresholds for consecutive time stamps, the corresponding bins were combined and considered part of the same FRET burst. These thresholds were chosen to minimize the inclusion of donor-only and acceptor-only events, while ensuring that FRET events with distinguishable donor and acceptor signals were accurately captured. FRET efficiencies were calculated as described in Equation 1.28. FCS measurements were performed as described in Section 2.2.3.

2.2.7 3D-printed epi-fluorescent microscope

The setup for widefield imaging employs an external fiber-coupled laser unit (READY Beam™ ind 2 1007773, Fisba, Switzerland) with a 640 nm continuous-wave excitation laser, delivering 30 mW output (measured after the objective). The beam is collimated using a parabolic mirror (RC04APC-P01, Thorlabs), passed through a clean-up filter (ZET 635/10 25 mm, Chroma), and expanded with a plano-concave lens (f = -25 mm, LC1054-ML, Thorlabs). A plano-convex lens (f = 60 mm, LA1134-A-ML, Thorlabs) focuses the beam into the back focal plane of the objective. A dichroic beam splitter with high reflectivity at 640 nm (ZT532/640rpc, Chroma, USA) separates the excitation and emission beams into and from the high numerical aperture (NA) apo-chromatic oil immersion objective (60X, NA 1.35, UPlanSApo60XO, Olympus, Japan).

Fluorescence emitted from the sample is collected by the same objective, then further focused using an achromatic lens (AC254-150-A-ML, Thorlabs) to project a real image onto the chip of a CMOS camera (U3-30C0CP-M-GL rev.2.2, IDS)[111]. The photon stream is filtered with a band-pass filter (ET700/75m, Chroma, AHF, Germany) before reaching the camera sensor.

Data collection & analysis

Photoswitching of the fluorophores was facilitated by adding 500 L of an oxygen-scavenging buffer[51], composed of pyranose oxidase (3 U/mL), catalase (90 U/mL), and 40 mM glucose in PBS, mixed with 0.1% (v/v) -mercaptoethanol. The laser power used for imaging was 30 mW, corresponding to approximately 37 kW/cm^2 in an illuminated area of 80 x 80 $µm^2$. Diffraction-limited recordings were acquired using the original software provided with the camera. Imaging was performed at 10 frames per second, with an exposure time of 100 ms, and the analog gain set to maximum.

Super-resolution image reconstruction was performed using the ImageJ plug-in Thunderstorm[96]. Localizations were filtered using a B-Spline wavelet filter. Molecule localization was performed using the local maxima method, followed by sub-pixel localization via fitting an Integrated Gaussian model using a weighted least-squares approach with a 3-pixel fitting radius. The resulting super-resolution image had a pixel size of 12 x 12 nm^2.

For STORM, drift correction was achieved using the fiducial marker algorithm with fluorescent tetraspeck beads (100 nm, Thermo Fisher), and lateral drift was monitored by tracking bead positions over approximately 30 minutes. The maximal search tracking distance was set at 20 nm, and the minimum visibility ratio was kept at 0.9 per frame. For PAINT, drift correction was applied using a cross-correlation algorithm, correlating the positioning of all blinking events of each molecule across the movie's duration.

2.3 Label-free microscale thermophoresis

Binding affinities were determined using Microscale Thermophoresis (Monolith NT.LabelFree, Nanotemper), where the ratio of fluorescence intensity of the target before and after heating, $\Delta F_{\text{norm}} = \frac{F_{\text{cold}}}{F_{\text{hot}}}$, was recorded at varying concentrations of ligand[112]. The fluorescence data were normalized to the minimum and maximum fluorescence intensities.

For the measurement of binding affinities for MalE and its mutant variants, a 400 μM maltose stock solution was prepared by mixing 8 μL of a 10 mM maltose solution with 192 μL of dilution buffer. This stock was then serially diluted in PCR tubes, starting from 400 μM down to 0.5 μM. To each dilution, 10 μL of 500 nM MalE was added, and the samples were incubated for 5 minutes at room temperature in the dark before being loaded into capillaries.

The binding data were analyzed using a standard receptor-ligand binding model:

$$\Delta F_{\text{norm}} = \frac{K_d + c_P + c_{\text{malt}} - p\left(\sqrt{(K_d + c_P + c_{\text{malt}})^2 - 4c_P c_{\text{malt}}}\right)}{2c_P} \tag{2.6}$$

where K_d is the dissociation constant, c_P is the protein concentration (set to 0.25 μM), and c_{malt} is the maltose concentration.

2.4 Quantum yield determination via UV/Vis absorption & fluorescence spectroscopy

2.4.1 Absorption and Fluorescence Spectroscopy

Absorbance measurements were conducted in a buffer solution (50 mM Tris-HCl, pH 7.4, 50 mM KCl) using a continuous-wave UV/VIS spectrometer (LAMBDA 465, Perkin Elmer). The absorbance spectra were recorded at an absorbance of approximately 0.4, with baseline correction applied to eliminate background interference.

Fluorescence emission was measured in the same buffer solution on a fluorescence spectrometer (LS 55, Perkin Elmer) with an excitation/emission slit width of 5 nm and a PMT gain set to 775 V (Hamamatsu R928). The recorded spectra were corrected for variations in detection efficiency as a function of wavelength. For subsequent analysis and Förster radius calculation, the absorbance and emission spectra were averaged over three measurements and normalized.

2.4.2 Quantum Yield

For quantum yield determination, six different concentrations of the fluorophore were prepared in triplicates, and absorbance and fluorescence emission measurements were taken. The absorbance at the excitation wavelength was averaged over the range 510±2.5 nm for green fluorophores. The integrated fluorescence was calculated by the following equation:

$$I = \int_{\infty} I(\lambda)\, d\lambda \tag{2.7}$$

Absorbance values (A) at the excitation wavelength of 510 nm for green fluorophores were fitted to the model function:

$$I(A) = m \cdot A \cdot 10^{-A_{\lambda_{\text{ex}}}/2} \tag{2.8}$$

Here, the factor $10^{-A_{\lambda_{\text{ex}}}/2}$ accounts for the absorption of the excitation light during emission spectrum measurement. The fitting procedure yielded initial slopes (m), where m_{fluo} is the slope for the fluorophore of interest, and m_{ref} is the slope for a reference fluorophore with a known quantum yield. The fluorescence quantum yield (Φ) of the fluorophore was calculated using the equation:

$$\Phi_{\text{fluo}} = \frac{m_{\text{fluo}}}{m_{\text{ref}}} \cdot \Phi_{\text{ref}} \tag{2.9}$$

Rhodamine 6G ($\Phi_{\text{ref}} = 91\%$) was used as the reference fluorophore, with the quantum yield value taken from the literature[113]. All quantum yield measurements were performed in triplicate, and the reported values and standard deviations reflect the results from three independent experiments.

3

Results

3.1 Reliability and accuracy of single-molecule FRET studies in proteins[§]

Single-molecule Förster-resonance energy transfer (smFRET) studies have evolved into an essential tool in structural biology, offering valuable insights into biomolecular interactions and conformational changes. The energy transfer between a donor and acceptor fluorophore within a specific distance range enables the probing of biomolecular structures at the nanometer scale. Additionally, smFRET allows for the recording of short-lived heterogeneous conformational states on time scales ranging from nanoseconds to microseconds, occurrences that are often masked in bulk measurements or crystal structures[114,115,116,117,118,119].

In previuos work, Hellenkamp et al.[120] conducted an extensive multilaboratory smFRET blind study to affirm the reliability of smFRET in structural measurements, employing standardized data analysis routines initially proposed by Lee et al[35]. By utilizing static double-stranded DNA (dsDNA) as model system, they revealed a high level of precision and accuracy among the 20 different participating laboratories, achieving an uncertainty of 6Å for the FRET-derived distances.

However, in contrast to DNA molecules, proteins are highly complex macromolecules characterized by significant variation in physical properties such as flexibility, surface charges, and hydrophobicity, while also maintaining a high degree of conservation for their specific functions. This complexity thus poses a greater challenge for smFRET studies[114]. The Cordes lab addressed this challenge and

---

[§] This study, titled "Reliability and accuracy of single-molecule FRET studies in proteins," was published in Nature Methods in 2023[98]. My contributions included labeling and purifying MalE variants, assessing their functionality through binding assays before and after stoichiometric labeling with Alexa546 and Alexa647 dyes, using label-free microscale thermophoresis (MST). I also conducted single-molecule FRET (smFRET) experiments, where I carefully monitored FRET efficiencies in the open (apo) and closed (holo) states, as well as under equilibrium conditions (K_D). Data analysis of the smFRET experiments involved accurate FRET value extraction through multiple correction steps: background correction, crosstalk correction, and gamma factor correction, as outlined by Lee et al.[35].

published its results in 2023 through a similar multilaboratory blind study involving 19 participants, akin to the one conducted by Hellenkamp et al.[120]

In this study, two distinct model proteins known for exhibiting large conformational changes and dynamics across various time scales were examined. These proteins included the maltose-binding protein MalE from *E. coli*[121,122,123], supplied by the Cordes lab, and the human U2 Auxiliary Factor 2 (U2AF2)[124,125,126] from the Sattler lab at TU-Munich.

The Cordes lab prepared multiple double cysteine mutants of MalE, designed to span the dynamic range of FRET and exhibit varying FRET efficiencies upon binding to its substrate maltose (figure3.1 a-b). MalE1 (K29C-S352C) features labeling sites on each lobe of the protein, which come into close proximity during a closed conformation. MalE2 (D87C-A134C) has labeling sites adjacent to the protein's hinge region, separating during a closed conformation. Finally, MalE3 (A134C-A186C) possesses labeling sites on the same lobe of the protein, resulting in no distance change between the open and closed conformations.

My personal contribution to this study involved assessing the functionality of the MalE variants through binding assays both before and after stoichiometric labeling with Alexa546 and Alexa647 dyes using label-free microscale thermophoresis (MST) (Figure 3.1 c-d). Additionally, I monitored the resulting accurate FRET efficiencies in the open (apo) and closed (holo) states, as well as under equilibrium conditions (K_D) (Figure 3.1 e), utilizing standardized data analysis procedures as outlined by Lee et al.[35]

The measured affinities for all mutants were consistent with the literature K_D values of the wild type (1 µM), suggesting no loss of function, notably even after the labeling procedure. These K_D values were further confirmed via smFRET, where populations of both conformational states were observed with an equal number of events (in equilibrium) using 1 µM substrate. (Figure 3.2 e middle row). Importantly, MST measurements of MalE-3 confirmed its functionality, as the lack of interdye distance change between conformations would not have provided any functional information using smFRET.

To assess potential influences between fluorophores and the high concentration of maltose used for the closed conformation in the assay (1 mM), another MalE-1 variant (D65A) with a reduced maltose-binding affinity of approximately 5 mM was employed (Figure 3.2 a). Here, no changes in FRET efficiencies were observed upon the addition of 1 mM substrate when testing the binding-deficient MalE-1 variant, suggesting the absence of interactions between the fluorophores and the substrate (Figure 3.2 b, right panel). Therefore, the FRET efficiency changes observed in MalE-1 could be ensured to arise from changes in interdye distances, rather than being affected by any unforeseen artifact originating from the substrate (Figure 3.2 b, left panel).

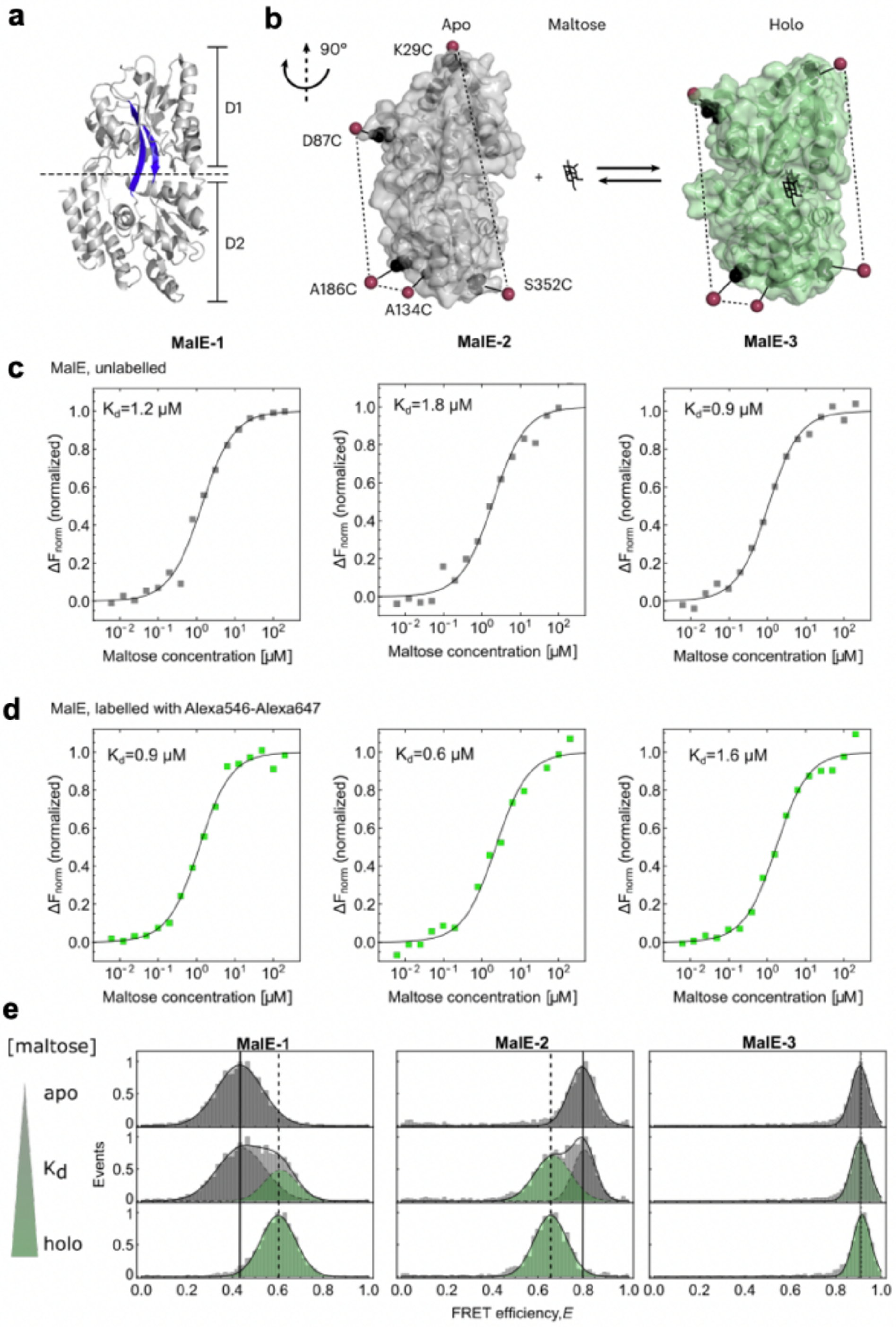

Figure 3.1: Functionality test of MalE variants adapted from Agam et al.[98]: **a**, Crystal structure of MalE in its ligand-free apo state (PDB ID: 1OMP) with domains D1 and D2 linked by flexible beta sheets (highlighted in blue). **b**, Comparison of the crystal structure of MalE in the apo (gray, PDB ID: 1OMP) and holo (green, PDB ID: 1ANF) states with mutations at K29C-S352C (MalE-1), D87C-A186C (MalE-2), and A134C-A186C (MalE-3). **c,d** show binding affinities of maltose to MalE measured with microscale thermophoresis (Monolith NT.LabelFree, Nanotemper) where the ratio of fluorescence before and after heating $\Delta F_{norm} = F_{cold}/F_{hot}$ is recorded at different maltose concentrations. **c** shows binding affinities of the unlabeled MalE variants, while **d** shows the binding affinities of fluorescently-labeled MalE (Alexa547 and Alexa647) mutants. **e**, Shows accurate FRET efficiency E histograms for the MalE mutant MalE-1 (left), the mutant MalE-2 (middle), and the mutant MalE-3 (right) in the presence of 0 (top), 1 µM (middle), and 1 mM maltose (bottom). The peak positions of the apo and holo populations are shown with a solid line and dashed line, respectively.

The reported accurate FRET mean values of the different laboratories aligned with good agreement and reproducibility, demonstrating the anticipated changes for MalE-1 and MalE-2, while no shift was observed for MalE-3[127] (figure 3.3 a). MalE-1 exhibited an average FRET efficiency of 0.49 ± 0.06 in the apo state, which increased to 0.67 ± 0.05 in the holo state. Conversely, MalE-2 demonstrated the expected decrease in FRET efficiency, transitioning from 0.83 ± 0.03 to 0.71 ± 0.05 in the apo and holo states, respectively. Meanwhile, for MalE-3, showed no significant alteration in FRET efficiency ($E_{apo} = 0.91 \pm 0.02$ and $E_{holo} = 0.92 \pm 0.02$). Across all participating laboratories, the standard deviation of the mean FRET efficiency was less than ±0.06, demonstrating a level of precision comparable to that observed by Hellenkamp et al. for dsDNA[120].

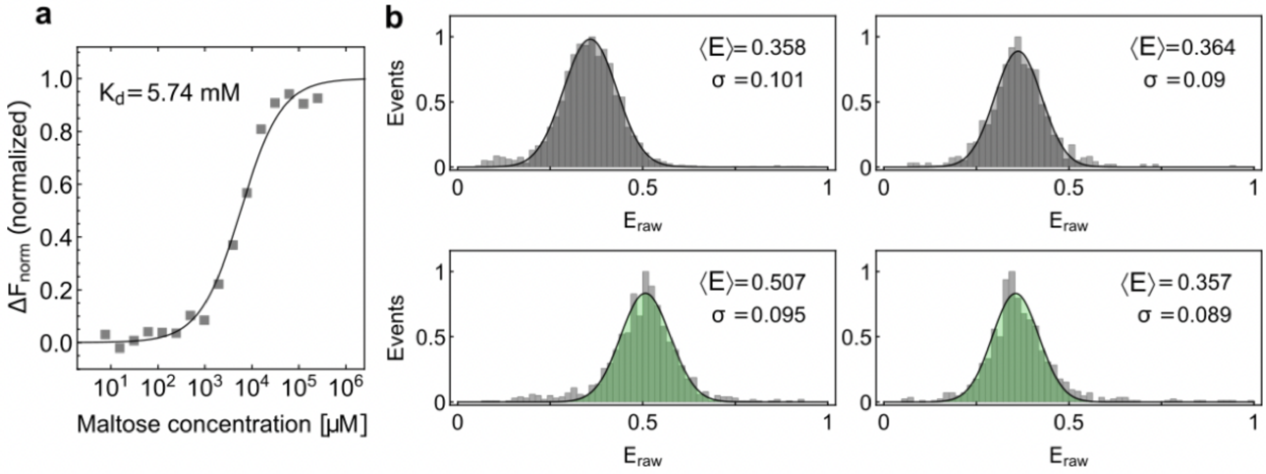

Figure 3.2: MST and smFRET measurements of the low-affinity MalE variant MalE(29/352)-D65A adapted from Agam et al.[98] **a** shows the binding affinity measurement of the maltose binding-deficient MalE variant using microscale thermophoresis[112] (Monolith NT.LabelFree, Nanotemper). **b** shows apparent FRET efficiency histograms for MalE(29/352) (left side) and the low-affinity MalE variant MalE(29/352)-D65A (right side) labeled with Alexa546/Alexa647. The top panel displays FRET efficiencies without ligand, and the lower panel shows the addition of 1 mM maltose. The low-affinity MalE variant MalE(29/352)-D65A does not exhibit any change in FRET efficiency between both conditions.

Notably, the comparison revealed systematic deviations among the participants, a finding confirmed by analyzing the difference between the determined apo and holo FRET efficiencies of each lab (refer to Figure 3.3 b). This process reduced the standard deviation by half, indicating that the errors were systematic. Importantly, this finding suggests significant uncertainties in determining each correction factor necessary for accurate FRET determination, which then propagate throughout the analysis.

Since the study used the same dye pair the correction factors for leakage (lk), excitation flux (β), detection efficiency and quantum yields (γ), and direct excitation (dir) were setup-specific, depending only on dichroic mirrors, emission filters, detectors, excitation wavelengths, and laser powers.

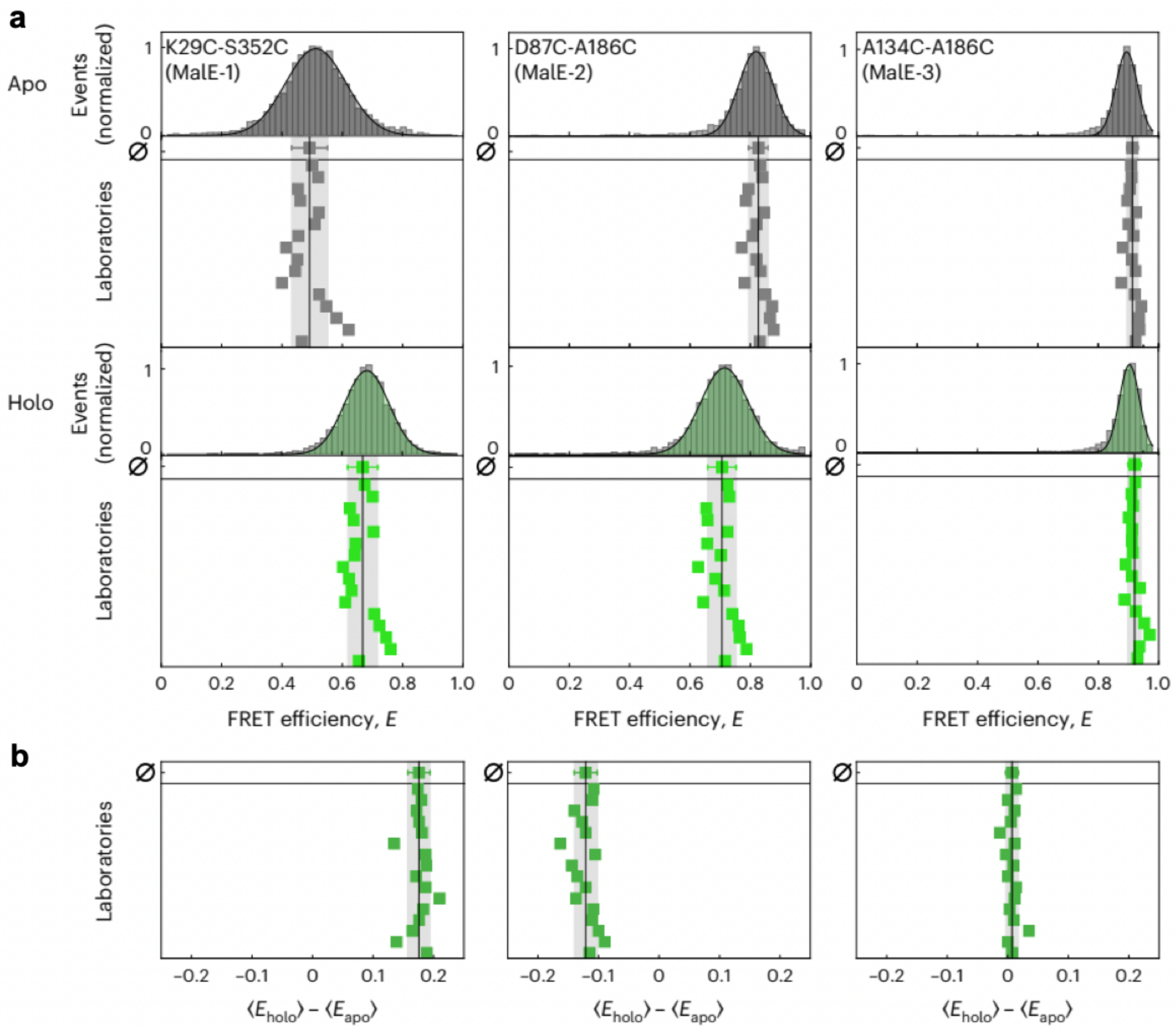

Figure 3.3: Multilaboratory determination of accurate FRET efficiencies for MalE variants labeled with Alexa546/Alexa647 adapted from Agam et al.[98] **a** shows FRET efficiency values of MalE(29/352), MalE(87/186), and MalE(134/186) in absence (top panel) and presence (bottom panel) of 1 mM maltose, accros 16 different labs. The mean FRET efficiency and the standard deviation of all 16 laboratories are shown by the black line and gray area. **b** shows individual FRET efficiency differences for each laboratory, between the apo and holo states ($\langle E_{holo}\rangle - \langle E_{apo}\rangle$. The mean FRET efficiency difference and the standard deviation of all 16 laboratories are shown by the black line and gray area.

Figure 3.4 a shows the distributions of all correction factors reported by each lab. Here, leakage (lk) showed the narrowest spread (0.05 ± 0.01) which is determined by the emission filters and detectors in both detection channels and is, therefore, the only pure setup-specific correction factor. In contrast, both direct excitation (dir) and β additionally depend on the laser powers chosen by each laboratory, resulting in a wider spread in their distribution, with values of 0.12 ± 0.08 and 1.6 ± 0.6, respectively.

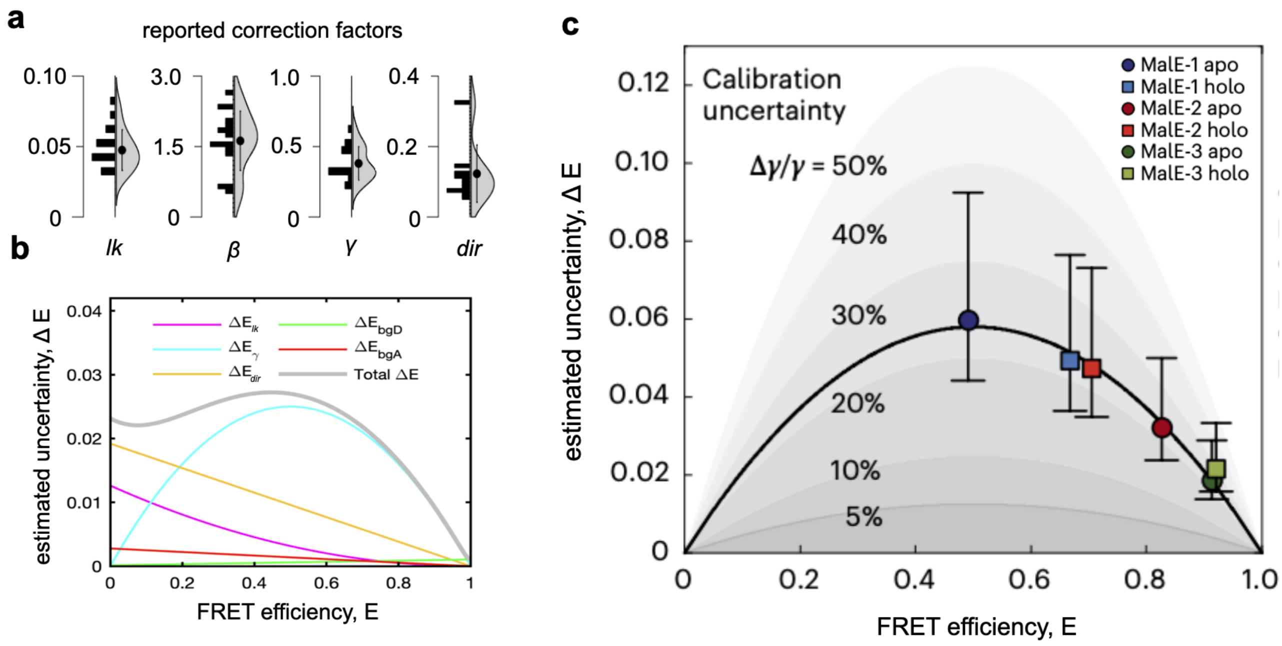

Figure 3.4: Correction factors & error propagation adapted from Agam et al[98]: **a** displays the distributions in the form of histograms and violin plots for each correction factor used in calculating accurate FRET efficiencies, as determined by each lab individually. In the violin plot, the dot represents the mean, and the line represents the standard deviation. **b** illustrates the error propagation of uncertainties on the FRET efficiency, ΔE. The contributions of the uncertainty in different correction factors to the total uncertainty are shown as colored lines (ΔE_{lk}, leakage; ΔE_{dir}, direct excitation; ΔE_{γ} γ-factor; and ΔE_{bgD} and ΔE_{bgA}, background in donor and acceptor channels). The total uncertainty, ΔE, is represented by a gray line, evaluated according to 3.1. The following values and uncertainties were used for the correction factors: $lk = 0.048 \pm 0.005$, $\beta = 1.6$, $\gamma = 0.38 \pm 0.04$, $dir = 0.12 \pm 0.01$, and $\Delta I^{BG}/\langle F \rangle = 0.003$. **c** depicts the standard deviation of the reported FRET efficiencies from all laboratories (as a measure of the experimental uncertainty) plotted against the average FRET efficiency for all MalE variants. The black line represents a fit of the estimated uncertainties under the assumption that the variations arise solely due to uncertainty in the γ factor. The inferred relative uncertainty of the γ factor is around 23%. Shaded areas indicate relative uncertainties of 5–50%. Error bars indicate 95% confidence intervals around the average value.

The γ factor that corrects for the different quantum yields of the fluorophores as well as the different detection efficiencies of the detectors had an average of 0.4 ± 0.1 and is arguably the most difficult factor to obtain and therefore prompt for large uncertainties. While correcting for background, spectral crosstalk, and direct excitation can be carried out with confidence, the correction factor γ poses greater challenges, with the best approach depending mostly on the specific characteristics of the sample. The determination of γ requires at least two or a ladder of multiple static FRET populations on an ES-histogram to be accurately established. In contrast to DNA samples, proteins are dynamic and it is often observed that labeling proteins can alter the quantum yield of the fluorophores and even shift the spectra due to variations in the local environment, potentially leading to an inaccurate determination of γ.

Additionally, the process involves a step-wise workflow comprising background subtraction followed by leakage and direct excitation correction, followed by the determination of γ and β[35,94,120]. Any errors made in prior steps would consequently propagate into the determination of γ.

The last point suggests that the γ-factor effectively combines the uncertainties from all correction factors, establishing it as the primary contributor to error and thereby serving as a reliable indicator for the total calibration uncertainty. This was further validated through the application of standard error propagation, which calculates the uncertainty of the reported FRET efficiency (ΔE) by considering the uncertainties associated with all correction factors. The total uncertainty of the FRET efficiency is then given by:

$$\begin{aligned}
\Delta E &= \sqrt{(\Delta E_{lk})^2 + (\Delta E_{dir})^2 + (\Delta E_{bgD})^2 + (\Delta E_{bgA})^2 + (\Delta E_{\gamma})^2} \\
\Delta E_{lk} &= \frac{(1-E)^2}{\gamma} \Delta lk \\
\Delta E_{dir} &= (1-E)\beta \Delta dir \\
\Delta E_{bgD} &= [\gamma E + lk(1-E)] \, \frac{\Delta I_D^{BG}}{\langle F \rangle} \\
\Delta E_{bgA} &= (1-E) \, \frac{\Delta I_A^{BG}}{\langle F \rangle} \\
\Delta E_{\gamma} &= E(1-E) \, \frac{\Delta \gamma}{\gamma}
\end{aligned} \tag{3.1}$$

Where ΔE represents the total reported uncertainty in FRET efficiency, and ΔE_x denotes the propagated uncertainty of the specified correction factor with the lower subscript. ΔE_{bgD} and ΔE_{bgA} are the propagated uncertainties of the background signal in the donor or acceptor channel, respectively, where ΔI_D^{BG} and ΔI_D^{BG} stand for the uncertainties associated with the estimated background signal in the donor and acceptor detection channels, and $\langle F \rangle$ indicates the average sum of the corrected donor and acceptor fluorescence collected during a single-molecule event.

For the calculation of ΔE, the absolute values for the correction factors (lk, dir, β and γ) were extracted from the average values reported by the participants (Figure 3.4 a), while the relative uncertainties were derived from the estimations provided by Hellenkamp et al.[120], yielding $\frac{\Delta lk}{lk} = \frac{\Delta dir}{dir} = \frac{\Delta \gamma}{\gamma} = 0.1$. This input resulted in the following values for the correction factors and their uncertainties: $lk = 0.048 \pm 0.005$, $dir = 0.12 \pm 0.01$, $\gamma = 0.038 \pm 0.04$, and β, which is not required for the propagation, set at 1.6. The background uncertainties were assumed to be $\Delta I_D^{BG} = \Delta I_A^{BG} = 0.25$, considering a relative uncertainty of $\frac{\Delta I^{BG}}{I^{BG}} \leq 0.1$, and $\langle F \rangle$ was set at 90 photons. Figure 3.4b illustrates the total estimated uncertainty, ΔE, along with all the independent uncertainties per correction factor. Here,

ΔE_γ follows a parabolic shape since it is proportional to $E(1-E)$ (refer to equation 3.1), but more notably, it describes the majority of the total uncertainty in the range of FRET efficiency higher than 0.4. Remarkably, the reported FRET values and their uncertainties (figure 3.3a) cover this range of FRET efficiency higher than 0.4, and their trend can be precisely described by ΔE_γ of equation 3.1 (figure 3.4 c). With this recognition, the relative uncertainty $\frac{\Delta\gamma}{\gamma}$ for proteins could be determined, resulting in 23%, corresponding to $\Delta\gamma = 0.07$.

The study also explored how variations in absolute γ values and the separation between the two FRET populations would impact its uncertainty (see figure 3.5). For the simulation, the positions of the two populations were symmetrically placed with respect to $E = 0.5$, expressed as $E_{PR,i} = 0.5 \pm \frac{(E_{PR,2}-E_{PR,1})}{2}$. Figures 3.5 a-c demonstrate that $\Delta\gamma$ increases with higher γ values and smaller changes in FRET efficiency between the two populations. Interestingly, $\Delta\gamma$ is also influenced by β, showing a broader spread in its trajectories with higher β values. Notably, when computing the relative error $\frac{\Delta\gamma}{\gamma}$, the different trajectories converge into a narrow range (Figures 3.5 d-f), suggesting that the relative uncertainty is largely unaffected by the absolute values of the correction factors γ and β. This was further confirmed by analyzing the relative uncertainty with fixed $(E_{PR,2} - E_{PR,1})$ values and varying absolute γ and β values (Figures 3.5 g-i). As anticipated, the uncertainty is highest when the difference between the FRET populations is minimal. However, the relative uncertainty remains low across a wide interval of γ and β values, approximately ranging from 0.1 to 3, which encloses the range where most experimental values lie (figure 3.4 a). This finding indicates that the primary determinant of uncertainty in the γ factor is predominantly the low contrast between FRET populations, while varying γ and β values have minimal impact on uncertainty over a broad range.

To gain structural information of biomolecules, FRET efficiencies have to be converted into distances. Due to the flexible and highly dynamic fluorophore linker, typically in the range of 10 carbon atoms long, the measured FRET efficiencies and consequently, the calculated distances are an average of the relative position between the two fluorophores $R_{\langle E\rangle}$.

The accuracy of the FRET-derived distances was compared with crystal structure modeling using FPS (FRET positioning and screening), where all possible positions of the fluorophores are modeled into accessible volumes (AVs)[116,117,128,129,130,131]. From there it is possible to calculate average distances between the fluorophores $R_{\langle E\rangle}^{Model}$ (Figure 3.6 a, c).

With the Förster radius of Alexa546–Alexa647 on MalE determined to be $R_0 = 65 \pm 3\mathring{A}$ it was possible to extract apo and holo distances with an uncertainty of 3–5 Å over all variants and compare it to the distances obtained with AV models. For this, additional MalE variants were included (MalE-4, K34C-N205C and MalE-5, T36C-N205C) with a larger FRET efficiency contrast between the apo and holo states, complementing the results of the other variants.

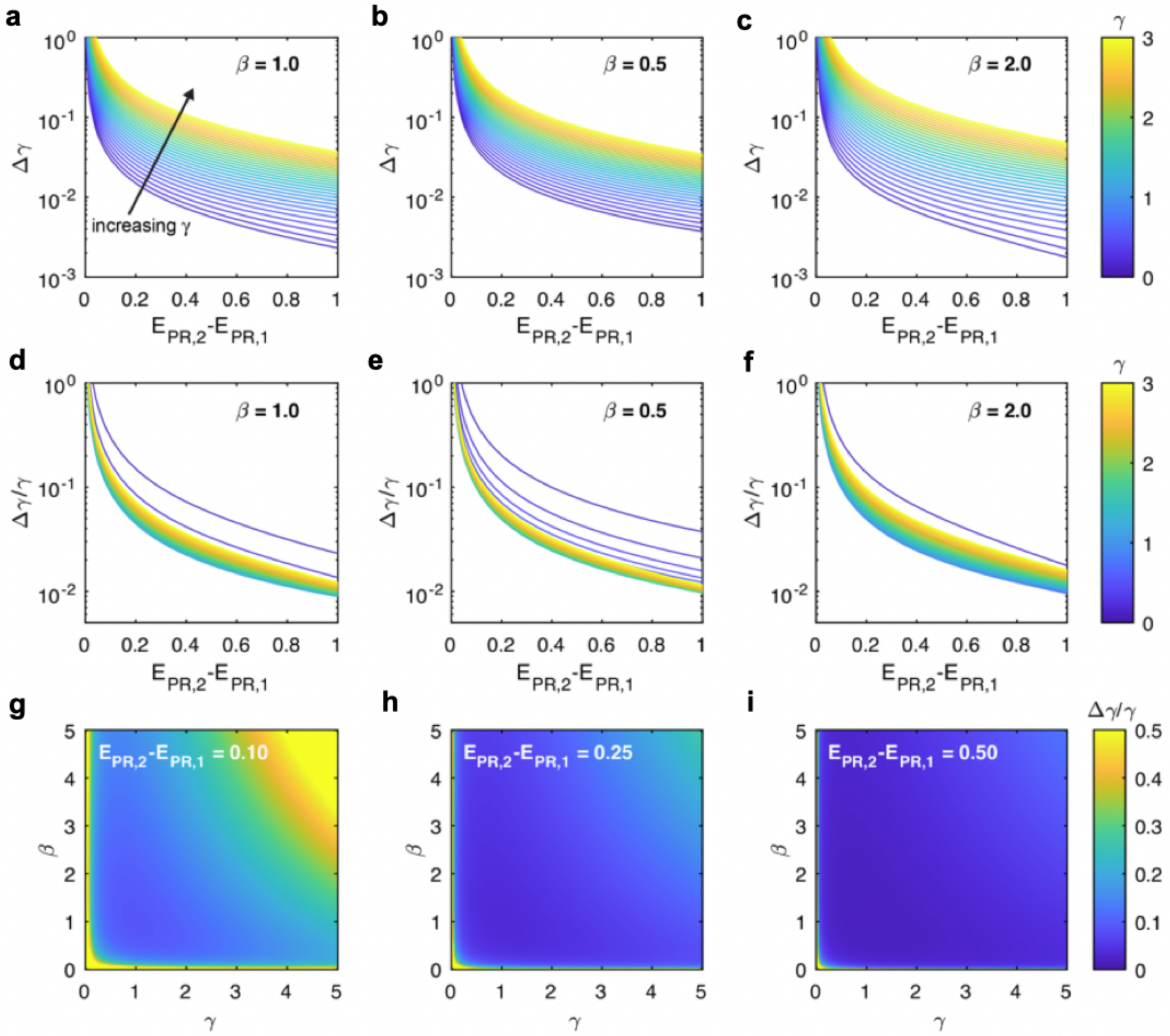

Figure 3.5: Simulations of the γ-factor error propagation, adapted from Agam et al.[98] $E_{PR,i}$ denotes the FRET efficiency of a theoretical population at a given position. For the simulation, the positions of the two populations ($E_{PR,1}$ and $E_{PR,2}$) are chosen to be symmetric with respect to the Förster radius (R_0), i.e., $E_{PR,i} = 0.5 \pm (E_{PR,2} - E_{PR,1})/2$. **a-c** The absolute uncertainty $\Delta\gamma$ is evaluated as a function of the difference of the apparent FRET efficiencies of the two states, $E_{PR,2} - E_{PR,1}$, at the indicated absolute values of the γ-factor (see color bar) and different β values of 1 (**a**), 0.5 (**b**), and 2 (**c**). **d-f** show the same data as in **a-c** normalized with respect to the absolute value of γ to compute the relative uncertainty $\frac{\Delta\gamma}{\gamma}$. **g-i** show the relative uncertainty $\frac{\Delta\gamma}{\gamma}$ evaluated as a function of the absolute values of γ and β, and are plotted for contrast between the apparent FRET efficiencies of 0.1 (**g**), 0.25 (**h**), and 0.5 (**i**).

The comparison showed a high correlation between the experimental and modeled results, except for MalE1 (Figure 3.6 d).

Further investigation on the role of dye–protein interactions using single-cysteine variants of MalE1 by measuring the fluorescence lifetimes, and time-resolved and steady-state anisotropies, revealed sticking of both fluorophores at labeling site S352C and only the acceptor fluorophore at labeling site K29C[61] (Figure 3.6 b). These position-specific interactions can cause the observed deviations in the experimental data, by changing their mean position on the protein. Hence, an improved accessible contact volume (ACV) approach was implemented, which accounts for dye–protein interactions[132] (Figure 3.6 c). This approach led to a more favorable agreement between the experimental and modeled distances.

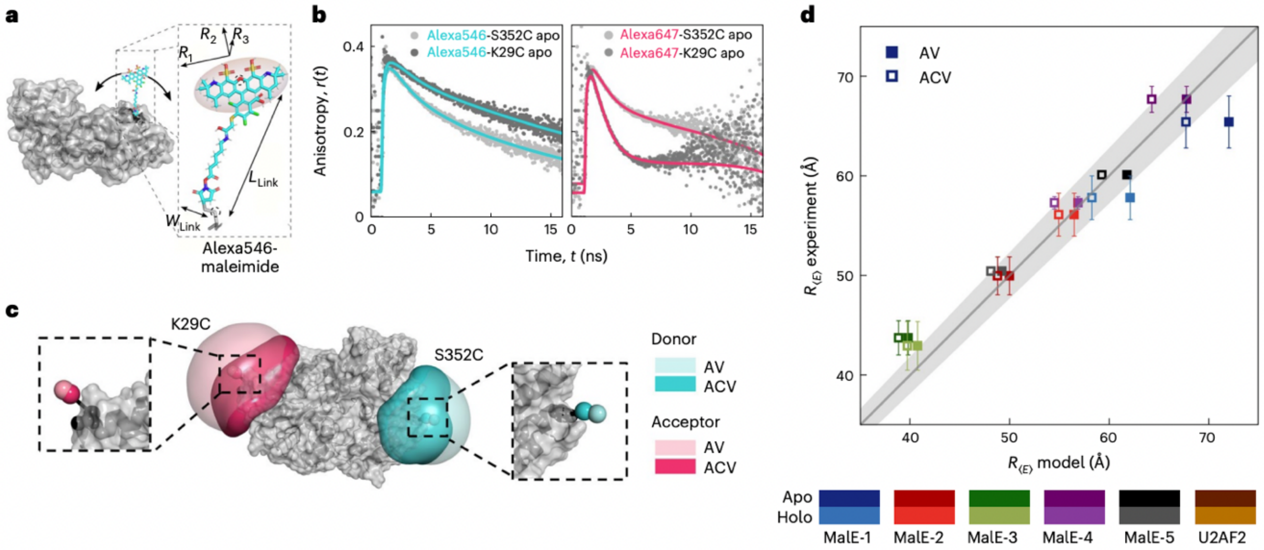

Figure 3.6: Assessing the accuracy of FRET-derived distances with FPS adapted from Agam et al.[98] **a** Schematic of Alexa546 attached to MalE (PDB 1OMP) showing the parameters needed for the AV calculations. **b** Fluorescence anisotropy decays of single-cysteine mutants for the donor (Alexa546, left) and acceptor (Alexa647, right) at the labeling positions K29C and S352C. **c** AV (light color) and ACV (dark color) calculations for Alexa546 (cyan) and Alexa647 (pink) at labeling positions 352 and 29. The zoom-ins show the mean positions of the dyes based on the AV (light shade) and ACV (darker shade) models. **d** Comparison of the experimentally obtained FRET-averaged distance $R_{\langle E \rangle}$ with the theoretical model distances using the AV (filled squares) and ACV (empty squares) calculations. Errors represent the standard deviation in experimental distances. The solid line represents a 1:1 relation, and the gray area indicates an uncertainty of $\pm 3 \mathring{A}$ for a Förster radius of $R_0 = 65 \mathring{A}$.

Despite the complexities inherent in protein samples, the study achieved a precision in FRET efficiencies comparable to that reported for dsDNA (ranging between ±0.02 and ±0.06). This high level of agreement is noteworthy, especially considering the diverse experimental setups employed. Accurate FRET efficiencies resulted in consistent inter-dye distances, with a precision of 3 Å and an accuracy of 5 Å against structural models of MalE, similar to findings in dsDNA samples. This positive outcome is particularly significant given that dsDNA provides a consistent and homogeneous chemical environment for each labeling position, contrasting with the variable dye environment encountered in proteins. Improving distance determination could involve considering the interaction of fluorophores with the protein surface using ACV calculations[132].

3.2 Cross-validation of distance measurements in proteins by PELDOR/DEER and AXSI[§]

Biophysical methods are essential tools in life sciences, yet none of them are immune to the presence of unforeseen artifacts that can lead to misleading interpretations of acquired data. Predicting, identifying, or preventing such artifacts is difficult, if not impossible, and therefore remains a constant challenge for researchers to navigate and mitigate potential pitfalls in their experimental designs and data analysis pipelines. However, the ground truth of the biosystem in question can be narrowed down by comparing many different tools with similar outputs, which differ considerably in the physical phenomena they exploit for measurement.

In line with this, smFRET-derived distance measurements in proteins were compared to and cross-validated with alternative methods that also extract distance information from proteins. These studies were conducted in collaboration with the Hagelueken lab, where smFRET was compared to Pulsed Electron-Electron Double Resonance Spectroscopy (PELDOR/DEER), published in *Nature Communications* in 2022 under the title "Cross-validation of distance measurements in proteins by PELDOR/DEER and single-molecule FRET"[99], and in collaboration with the Lipfert lab, where smFRET was compared with Anomalous X-ray Scattering Interferometry (AXSI), published in *Nanoscale* in 2025 under the title "Determination of absolute intramolecular distances in proteins using anomalous X-ray scattering interferometry"[100]. These two methods were ideal for cross-validation, as the determined distances also originate from labels within the protein (spin-labels for PELDOR/DEER and gold nanoparticles for AXSI), both of which utilize thiol groups in cysteines for their site-specific labeling. Consequently, the same protein construct can be utilized for all three different methods, facilitating a direct comparison of their outcomes[133,134,135,136,137,138,139].

Pulsed Electron-Electron Double Resonance Spectroscopy (PELDOR/DEER) is a powerful technique used to measure distances between paramagnetic centers of spin labels[140]. This method relies on the magnetic dipole-dipole interactions between unpaired electron spins. Similar to smFRET, this interaction depends on the distance between the spins and the orientation of their magnetic moments relative to each other[141,142,99].

PELDOR/DEER applies modulated microwave pulses (pump and observer pulses) to selectively manipulate the spins and measure the resulting electron spin echo decay. By analyzing the time evolution

---

[§] This chapter includes collaborative work with the Hagelueken and Lipfert labs, which resulted in two publications: "Cross-validation of distance measurements in proteins by PELDOR/DEER and single-molecule FRET," published in Nature Communications in 2022[99], and "Determination of absolute intramolecular distances in proteins using anomalous X-ray scattering interferometry," published in Nanoscale in 2025[100]. My personal contribution to the first study involved replicating all measurements, except for YopO. This included preparing all samples, conducting all smFRET measurements, processing the data to obtain accurate FRET values, and converting them into distances. Additionally, I determined the quantum yield of TMR, which was necessary for calculating the Förster radius (R_0) for the Acceptor Cy5. For the second study, my personal contribution involved replicating all measurements, including stochastic labeling of all samples with Alexa555 and Alexa647, conducting all smFRET measurements, and processing the data to acquire accurate FRET values, which were then converted into distances.

of the echo decay, information about the distances between the spin labels can be extracted (Figure 3.7).

The typical workflow of a PELDOR/DEER experiment consists of identifying microwave frequencies for the pump and observer pulses. This is accomplished by recording an Electron Paramagnetic Resonance (EPR) spectrum of a highly concentrated frozen solution of the sample, labeled with spin labes (10-13 µM)((Figure 3.7 b,c). By utilizing these pump and observer frequencies, specific subpopulations of spin centers within the sample can be excited, resulting in the formation of either pump spins or observer spins[143,144,145,146,147]. This characteristic explains why PELDOR/DEER effectively requires only a single label type for the measurement, unlike smFRET, which necessitates both a donor and acceptor label.

The actual PELDOR/DEER experiment involves applying a sequence of three microwave pulses at the probe frequency, generating an electron spin echo signal (refocused echo) from a subset of spin centers in the sample (probe spin). A fourth pump pulse, positioned variably between the last two probe pulses, flips the spins of the remaining spin centers subpopulation (pump spin)(Figure 3.7 d). At this point, probe and pump spins can interact through dipolar coupling if they are in close proximity, e.g., within the same protein, resulting in a change in the spin echo's amplitude. By analyzing the shape and amplitude of the spin echo signal, it is possible to extract distance information between the paramagnetic centers. The modulation of the echo decay curve, caused by the dipolar interactions between spins, provides the basis for distance measurements.

For this comparative study, four different model proteins were used. The Hageleuken Lab provided the four double cysteine variants of the periplasmic substrate binding protein from the sialic acid TRAP transporter of *Haemophilus influenzae* ,HiSiaP[148,149] (HiSiaP-58/134, HiSiaP-175/228, HiSiaP-55/175 and HiSiaP-122/175) and a double cysteine mutant of YopO (YopO-113/497) from *Yersinia enterocolitica*, a type-III-secretion system effector protein[150,151] . The Cordes lab provided four double cysteine variants of MalE[122,152,153](MalE-87/127, MalE-134/186, MalE-36/352 and MalE-29/352) and two double cysteine variants of SBD2 (SBD2-319/392 and SBD2-369/451), the second of two substrate-binding domains that are constituents of the glutamine ABC transporter GlnPQ from *Lactococcus lactis*[39,154,155,156].

The samples for PELDOR/DEER experiments were labeled with MTSSL spin labels (S-(1-oxyl 2,2,5,5-tetramethyl-2,5-dihydro-1H-pyrrol-3-yl)methyl methanesulfonothioate) and measured with cryo-protectants (ethylene glycol) at 50° K. The distance distributions were determined using Tikhonov regularization[157,158] and DeerNet[159] and the distance predictions were calculated with mtsslWizard[160]. The samples for smFRET experiments were stochastically labeled with Alexa555 and Alexa647[127,161] and the distance predictions were calculated with FPS (FRET positioning and screening)[117].

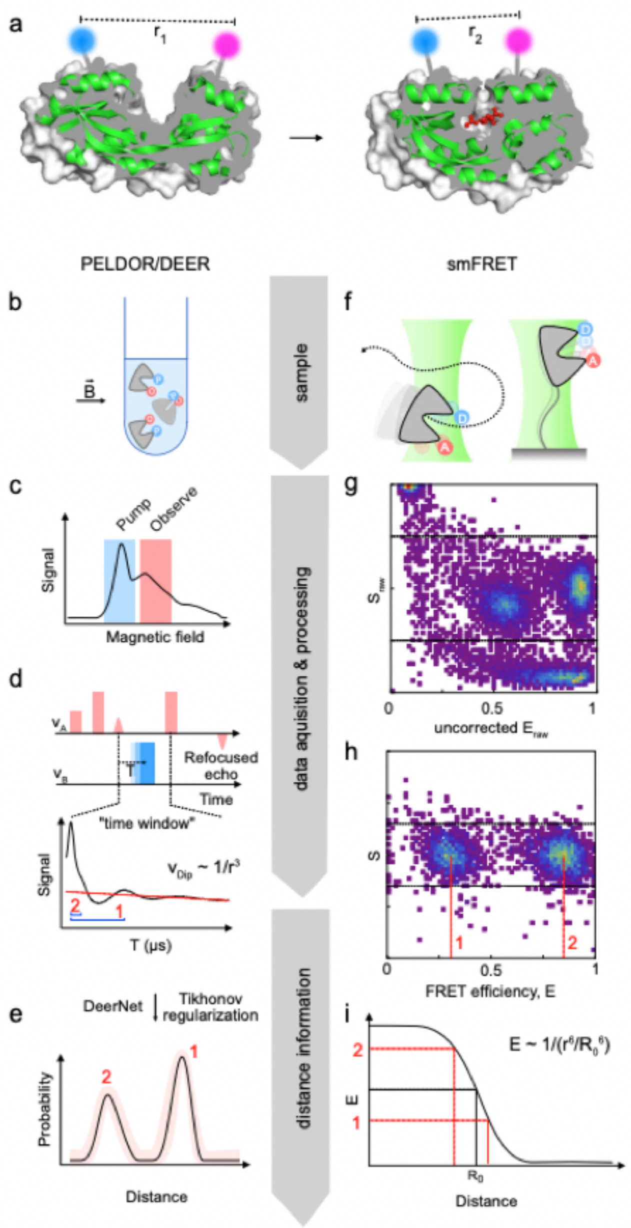

Figure 3.7: Workflow comparison between PELDOR/DEER & smFRET adapted from Peter et al[99]. **a** Two conformations (apo, left and holo, right) of HiSiaP (PDB-IDs: 3B50 and 2CEY). The labeling positions are indicated by the blue and magenta spheres. **b–e** Workflow of a PELDOR/DEER experiment. **b** Schematic representation of a frozen micromolar solution of the sample, labeled with spin labels under an external magnetic field. **c** Field-sweep EPR spectrum of the sample in **b**; microwave frequencies chosen for the observer and pump pulses are depicted in the pink and blue regions, respectively. **f** Pulsed microwave sequence pattern for the observer (pink) and pump (blue). Subpopulations of the spin centers can serve as either pump or observer spins for the pulse sequence. Integration of the refocused echo signal for different times T of the pump pulse leads to the time trace. The distance information is contained in the different oscillation frequencies of the time trace (blue brackets). **e** Time traces are converted to distance distributions through Tikhonov regularization or DerrNET. **f–i** Workflow of smFRET experiments. **f** Schematic representation of a diffusion-based smFRET measurement. **g** Representative raw ES histogram depicting two FRET populations, as well as donor-only (upper left corner) and acceptor-only (lower right corner) populations. **h** Corrected ES histogram depicting accurate FRET efficiencies of the FRET populations shown in **g**. **i** Theoretical function of FRET efficiencies and its conversion into distances.

My personal contribution to this study involved replicating all measurements, except for YopO. This included preparing all samples and conducting all smFRET measurements, along with processing the data to acquire accurate FRET values and converting them into distances. Additionally, I determined the quantum yield of TMR, which was necessary for determining the Förster radius (R_0) with the Acceptor Cy5 (see below).

The initial comparison conducted on the sialic acid binding protein HiSiaP resulted in unexpected discrepancies between the two methods, particularly concerning the predicted distances and the experimental distances obtained through smFRET. All four HiSiaP variants were selected based on pronounced distance changes between the open and closed conformations. In this study, all labeling sites were positioned at the lobes of the protein, with the expectation of a reduction in distance between them when transitioning into a closed conformation (figure 3.8 a,b). Figure 3.8 b shows the open (PDB-ID: 2CEY) and closed structures (PDB-ID: 3B50) of HiSiaP with the predicted accessible volumes of the spin- (magenta) and FRET-(blue) labels at the selected labeling sites. The PELDOR/DEER experiments demonstrated well-defined distance distributions for all variants (Figure 3.8c, black curves, with red shading indicating uncertainties), revealing the anticipated reduction in distance between the spin-labels upon substrate binding. These findings were largely consistent with the in silico modeled and predicted distances (grey areas). In contrast, the experimental distances obtained with smFRET (black line, with red shading denoting uncertainties) yielded contradicting results compared to the expected changes in distances and the in FPS predicted distances (grey line), except for variant 58/134. Especially variants 175/288 and 112/175 exhibited an unexpected increase in distances in the closed conformation, contrary to both expectations and predictions from in silico calculations. Importantly, this finding revealed an unforeseen artifact in the experimental data obtained from smFRET, as it contradicted all predictions and expectations. A closer look into the data revealed that the open conformation in variants 55/175, 175/288, and 112/175 was the problematic condition, where experimental and in silico data were in disagreement by a large margin. Interestingly, the source of the artifact seemed to be linked to the labeling site 175, since all variants showing discrepancies carried the same labeling site.

For this reason, single-mutant variants of HisiaP were selected, one containing the problematic 175 residue, and a control mutant (HiSiaP-58), which were labeled with either donor (Alexa555) or acceptor (Alexa647) fluorophores. Fluorescence anisotropy and lifetime decay measurements of these mutants revealed significant differences between the residues[61] (Figure 3.9a,b). The control variant 58 did not exhibit any differences in its anisotropy and lifetimes for both fluorophores in open and closed conformations; attributes desired and essential for smFRET measurements: Changes in fluorophore lifetimes may be problematic for the determination of the γ factor since it is linked to the quantum yield of the fluorophore[162,163,164,103]. On the other hand, the free rotation of fluorophores, characterized by fast decay of initial anisotropy values, is essential for the determination of the Förster Radius (R_0), which is described by the orientation factor κ^2.

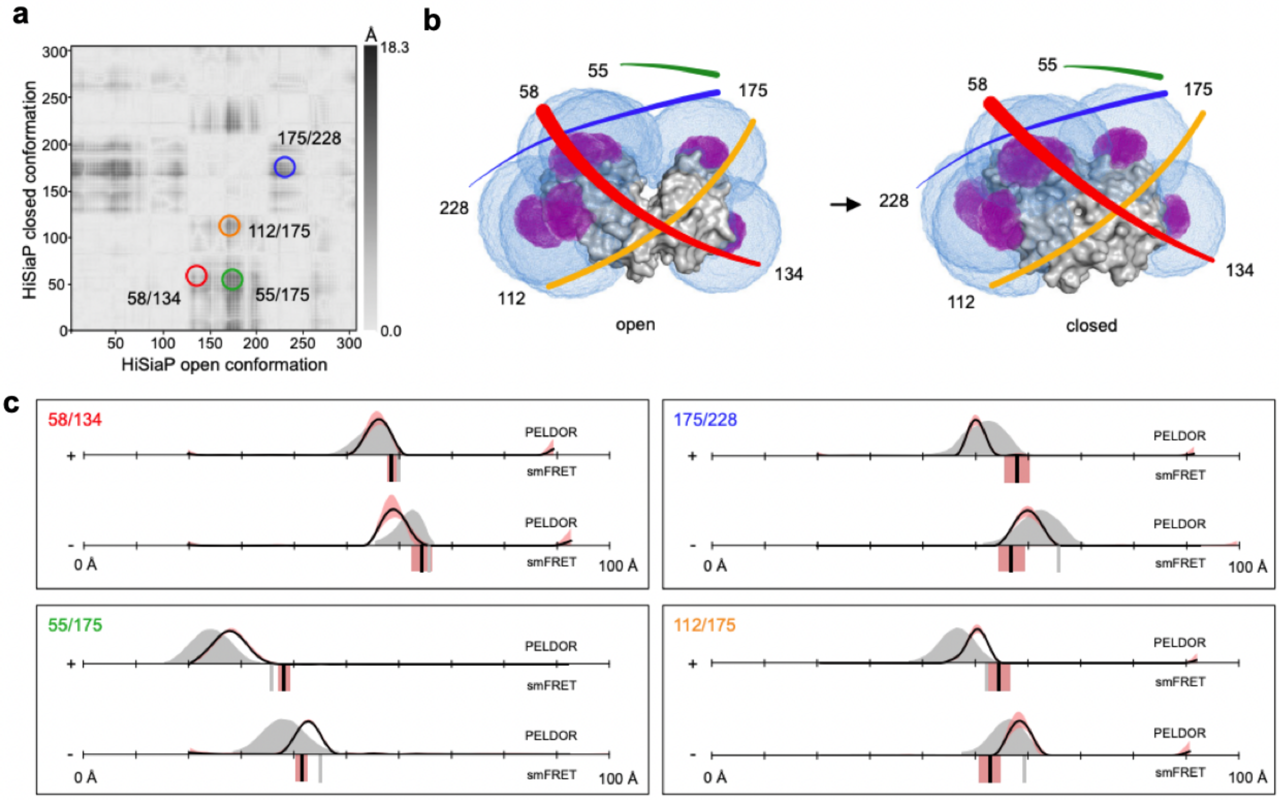

Figure 3.8: Distance measurements on HiSiaP determined with PELDOR/DEER & smFRET, adapted from Peter et. al.[99] **a** shows a difference distance map of HiSiaP in the open (PDB-ID: 2CEY) and closed (PDB-ID: 3B50) conformation. The dark regions show amino acid positions which undergo large conformational changes relative to each other. The double variants for distance measurements are highlighted with colored circles. **b** depicts the surface presentation of HiSiaP (grey) in the open (left) and closed (right) conformation. The accessible volumes of the spin label at six different labelling positions were calculated with mtsslWizard and are represented by magenta meshes. Accessible volumes of FRET label maleimide-Alexa647 were calculated with FPS, and are shown as blue meshes. The double variants that were used for experiments are identified with coloured lines, corresponding to the circles in **a**. **c** Distance measurements with four different double variants of HiSiaP without (−) and with (+) substrate. The PELDOR/DEER results are shown above (grey curves for simulation, black curves for experiment) and the FRET distances below the x-axis (grey bars for simulation, black bars are the mean of n=3 independent experiments). The red shade around the PELDOR/DEER data is the error margin calculated using the validation tool of DeerAnalysis. The red shades around the experimental smFRET distances are error bars based on the standard deviation of n=3 independent experiments.

In contrast, HiSiaP-175 exhibited differences in its anisotropy and lifetimes for both fluorophores in the open conformation. Here, high anisotropy values in the open conformation suggested restricted motion of the fluorophore due to unwanted dye-protein interactions, highlighting the source of the unexpected results in smFRET involving this residue. This dye-protein interaction seemed to be specific to the fluorophores chosen for the experiment, and therefore, another dye pair consisting of TMR and Cy5 was selected. These dyes showed, in contrast to the previous combination, no difference in their anisotropy and lifetimes values between the open and closed conformation (Figure 3.9 c).

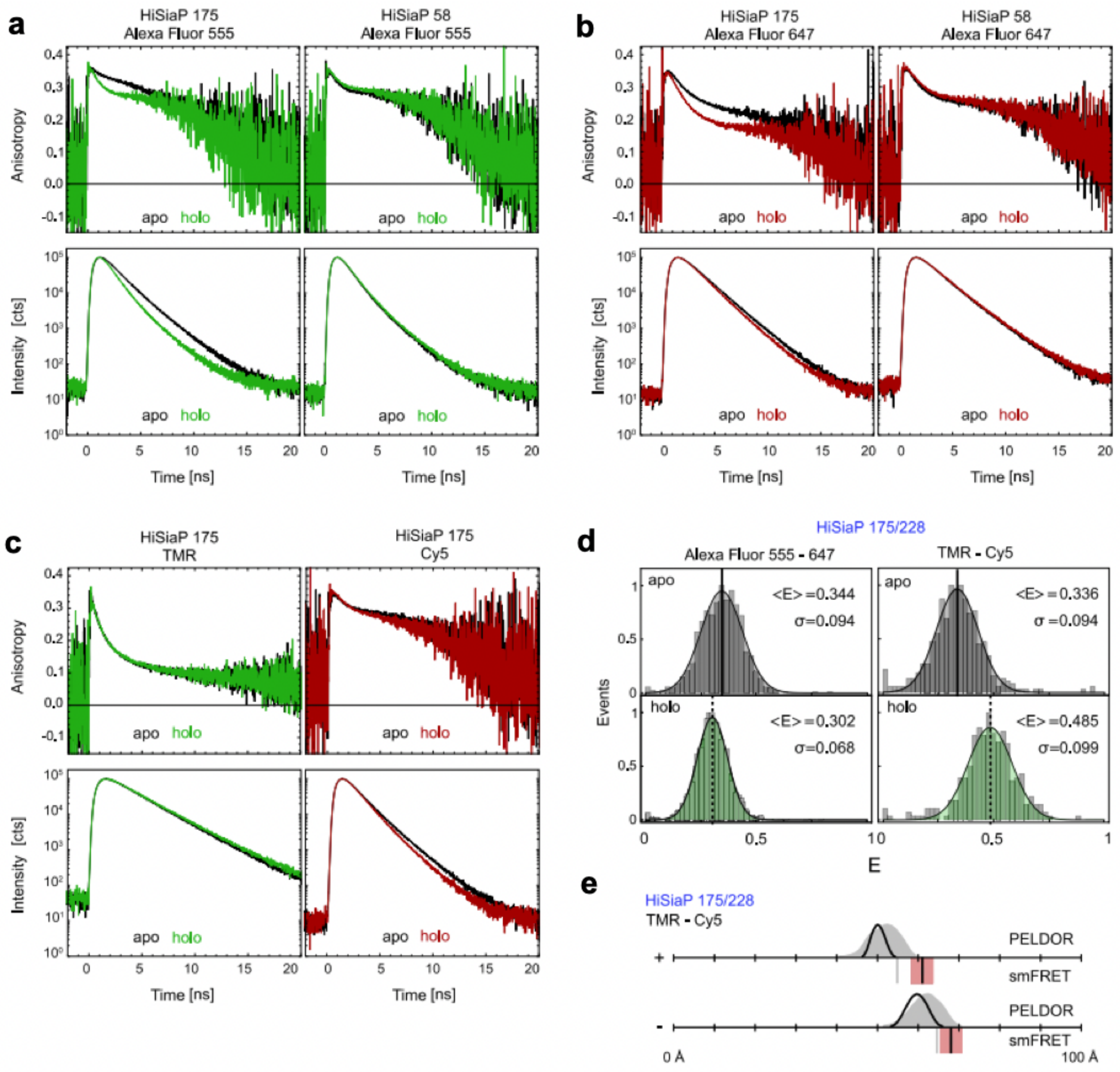

Figure 3.9: Time resolved fluorescence anisotropy and lifetime measurements on HiSiaP, adapted from Peter et. al.[99] **a** Anisotropy decay curves of Alexa555 (top row) at residue 175 (left) and 58 (right) and lifetime decay curves (bottom row) for apo (black) and holo state (green). **b** Same measurements as in **a** with Alexa647 in apo (black) and holo state (red). **c** Anisotropy decay curves of TMR (top left) and Cy5 (top right) at residue 175 and lifetime decay curves of TMR (bottom left) and Cy5 (bottom right) for apo (black) and holo state (coloured). **d** FRET efficiency distributions of HiSiaP variant 175/228 for Alexa555 – Alexa647 (left) and TMR – Cy5 (right) in apo (grey) and holo state (green). **e** Converted distances from the mean FRET efficiencies are shown as black bars (mean of n = 3 independent experiments) in comparison to simulation (grey bar) and PELDOR/DEER results from Fig 3.8 . The red shade around the experimental smFRET distance are error bars based on the standard deviation of n = 3 independent experiments.

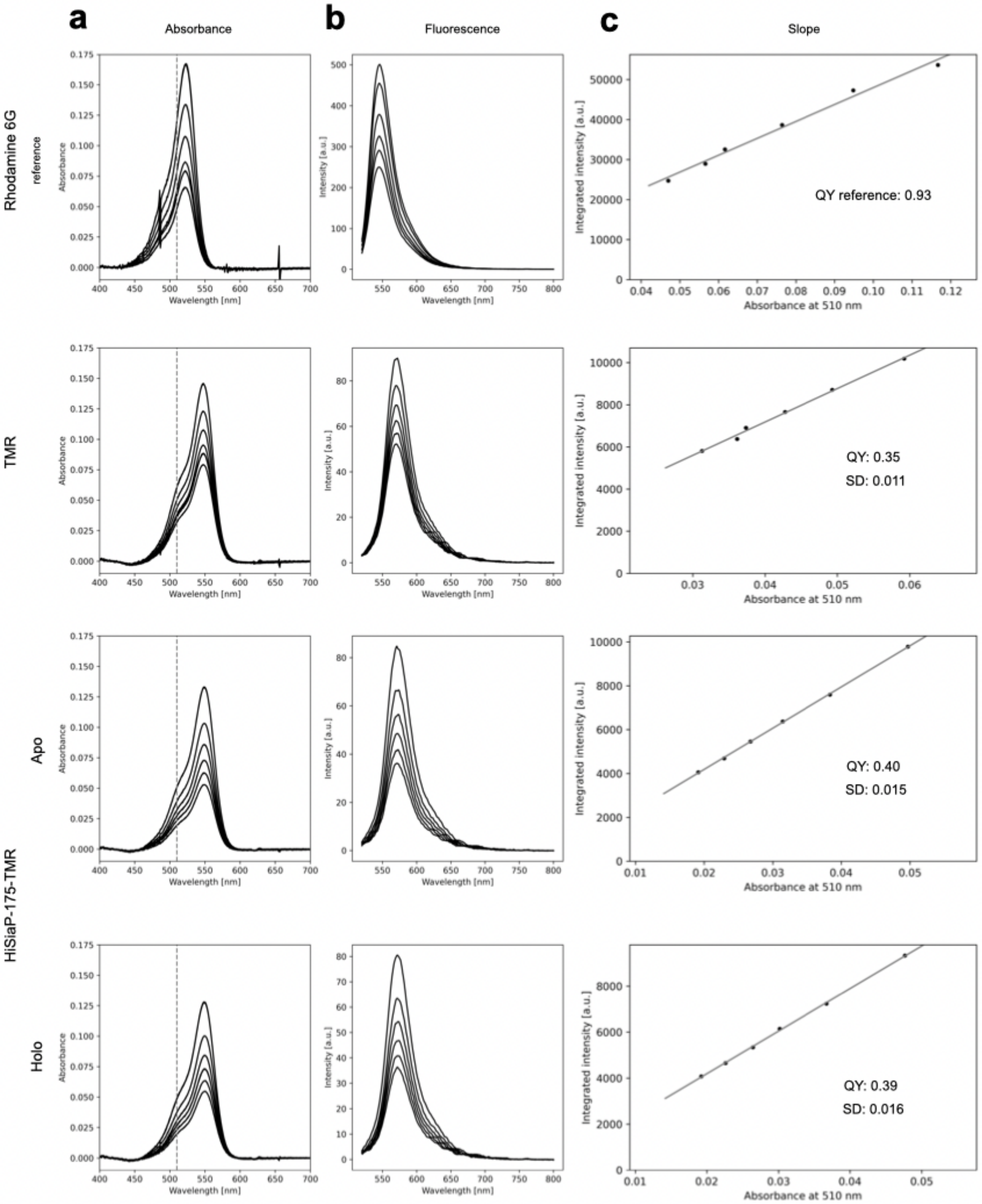

Figure 3.10: Quantum yield measurement of TMR in reference to Rhodamine 6G, adapted from Peter et. al.[99] **a** Shows the absorbance spectra of Rhodamine 6G (top), TMR (middle), HiSiaP-175-TMR in apo and holo states (bottom) at 6 different concentrations. The dashed line indicates the extracted absorbance values from the excitation wavelength at 510 nm. **b** shows the emission spectra of Rhodamine 6G (top), TMR (middle), HiSiaP-175-TMR in apo and holo states (bottom) of the sample in **a** excited at 510 nm. **c** The integrated emission from **b** is plotted against the absorbance extracted from **a** and fitted to the function $I_{int} = m * A$. Triplicates were used to determine the quantum yield (QY) of TMR.

Furthermore, smFRET experiments with the new dye pair for the HiSiaP-175/228 variant showed the expected change in FRET efficiency changes compared to the previous combination of dye pairs (Figure 3.9 d). For the conversion into distances, the Förster radius of TMR and Cy5 had to be determined. For this, the quantum yield of the donor (TMR) was experimentally determined by using the literature quantum yield of rhodamine 6G (93%) as a reference[113] (Figure 3.10). The quantum yield of free TMR dye in the imaging buffer yielded an efficiency of 35%, which increased to 40% once labeled to HiSiaP. More importantly, the determined quantum yield did not change between the open and closed conformation of HiSiaP, which was in agreement with the results of fluorescence lifetime decays (Figure 3.9 c). The resulting Förster radius for TMR and Cy5 was determined to be 62.7 Å, with which the acquired FRET efficiencies could be converted into distances (Figure 3.9 d,e), which were in much better agreement with the crystal structures FPS calculations.

For the MalE comparison, the mutants selected were the same as those used in the multilaboratory comparison: MalE-1 (K29C-S352C), MalE-2 (D87C-A134C), and MalE-3 (A134C-A186C) (figure 3.11 a,b). Additionally, another variant, 29/352, with a similar change in inter-residual distance as the MalE-1 variant, was included (exhibiting closer proximity of the labeling sites when in the closed conformation). As expected through previous studies, smFRET experiments and predicted distances were in good agreement with each other for all variants (firgue 3.11 c).

PELDOR/DEER experiments, although having a lower signal to noise ratio (SNR) compared to HiSiaP measurements it was possible to measure time traces with sufficient length to resolve the expected distances (firgue 3.11c). Here only variants 87/127 and 134/186 showed good agreement between the experimental and the predicted distances. In contrast variants 36/352 and 29/352 showed only agreement in the open configuration of MalE, whereas the condition with ligand showed a mix between the open and closed configuration.

The possibility of altering the binding constants of the protein due to the frozen state in which PELDOR/DEER experiments are conducted was eliminated by applying a substrate concentration ten times higher (10 mM maltose), which yielded consistent results. However, the discrepancy was found to be caused by the cryoprotectant used in the assay (ethylene glycol). Removing this additive resulted in a single population showing distance probabilities close to the predicted in silico values (Figure 3.11, magenta line).

The third comparison involved the Glutamate/Glutamine binding protein SBD2 of the GlnPQ amino acid transporter (Figure 3.12a,b). The selected variants (319/392 and 369/451) had previously been utilized in smFRET studies to elucidate their binding mechanism and their involvement in amino acid transport. In these experiments, the conducted smFRET experiments and the resulting distances obtained were in good agreement with the in-silico predictions (Figure 3.12 c).

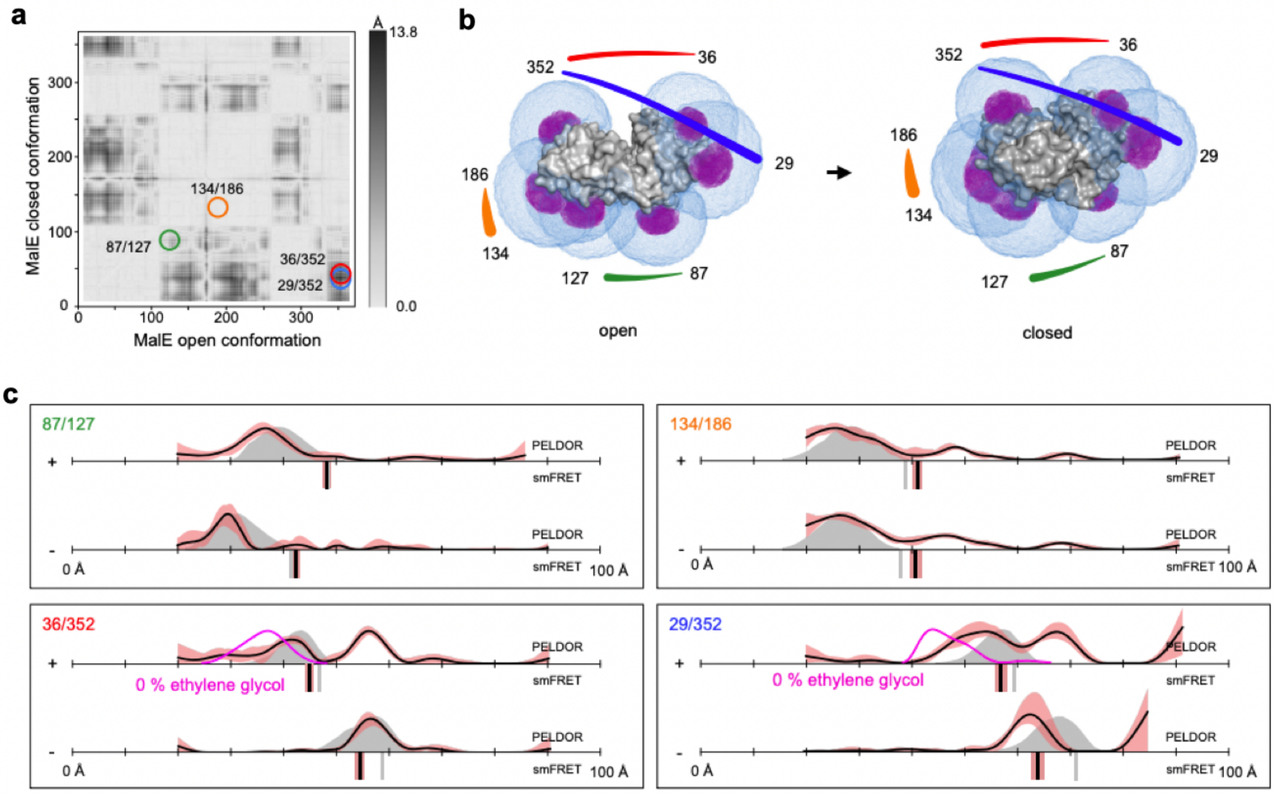

Figure 3.11: Distance measurements on MalE determined with PELDOR/DEER & smFRET, adapted from Peter et. al.[99] **a** shows a difference distance map of MalE in the open (PDB-ID: 1OMP) and closed (PDB-ID: 1ANF) conformation. The dark regions show amino acid positions which undergo large conformational changes relative to each other. The double variants for distance measurements are highlighted with colored circles. **b** depicts the surface presentation of MalE (grey) in the open (left) and closed (right) conformation. The accessible volumes of the spin label at six different labelling positions were calculated with mtsslWizard and are represented by magenta meshes. Accessible volumes of FRET label maleimide-Alexa647 were calculated with FPS, and are shown as blue meshes. The double variants that were used for experiments are identified with coloured lines, corresponding to the circles in **a**. **c** Distance measurements with four different double variants of MalE without (−) and with (+) substrate. The PELDOR/DEER results are shown above (grey curves for simulation, black curves for experiment) and the FRET distances below the x-axis (grey bars for simulation, black bars are the mean of n=3 independent experiments). PELDOR/DEER results without cryoprotectant are shown as magenta curves. The red shade around the PELDOR/DEER data is the error margin calculated using the validation tool of DeerAnalysis. The red shades around the experimental smFRET distances are error bars based on the standard deviation of n=3 independent experiments.

However, PELDOR/DEER experiments in the apo conditions displayed two and even three prominent distance peaks for SBD2-369/451 and SBD2-319/392 variants, respectively. The in-silico predictions indicated that at least two peaks corresponded to the open and closed conformations. The addition of the substrate glutamate variants shifted the distance distribution towards the closed conformation, but at least 10% of the open conformation remained present. The possibility of substrate contamination due to co-purified glutamine was ruled out after no detectable traces of glutamine were found following liquid chromatography mass spectrometry (LC-MS) experiments. In contrast to the MalE PELDOR/DEER experiments, the removal of cryoprotectants did not show any improvements in the results. The reason for this result remains elusive.

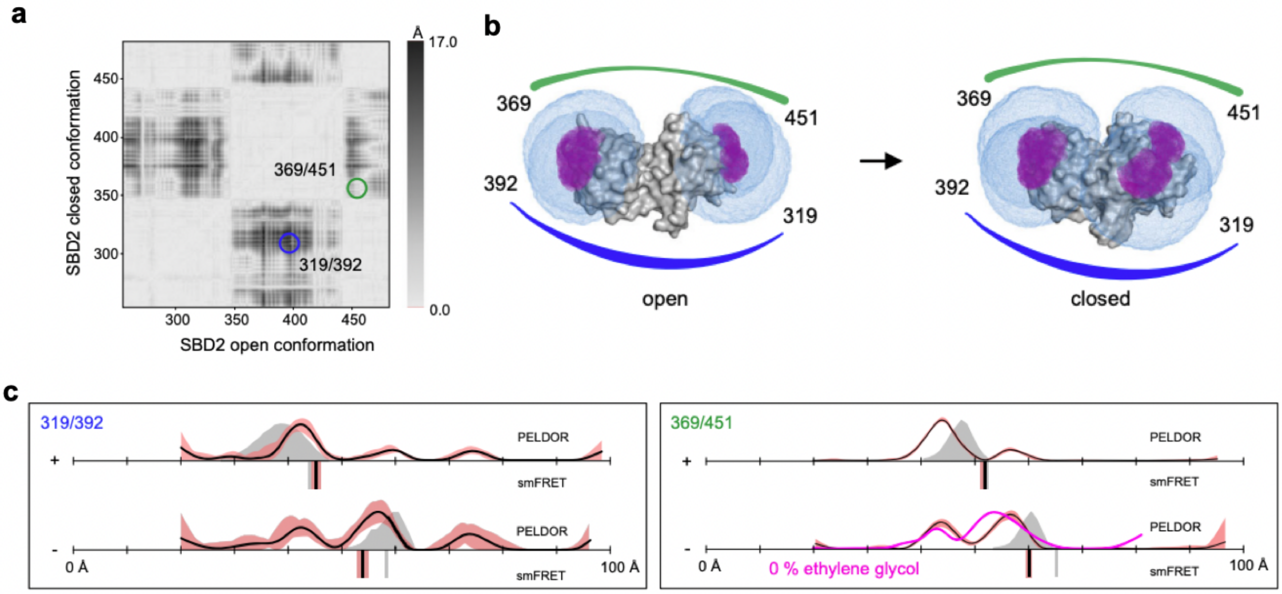

Figure 3.12: Distance measurements on SBD2 determined with PELDOR/DEER & smFRET, adapted from Peter et. al.[99] **a** shows a difference distance map of SBD2 in the open (PDB-ID: 4KR5) and closed (PDB-ID: 4KQP) conformation. The dark regions show amino acid positions which undergo large conformational changes relative to each other. The double variants for distance measurements are highlighted with colored circles. **b** depicts the surface presentation of SBD2 (grey) in the open (left) and closed (right) conformation. The accessible volumes of the spin label at six different labelling positions were calculated with mtsslWizard and are represented by magenta meshes. Accessible volumes of FRET label maleimide-Alexa647 were calculated with FPS, and are shown as blue meshes. The double variants that were used for experiments are identified with coloured lines, corresponding to the circles in **a**. **c** Distance measurements with two different double variants of SBD2 without (−) and with (+) substrate. The PELDOR/DEER results are shown above (grey curves for simulation, black curves for experiment) and the FRET distances below the x-axis (grey bars for simulation, black bars are the mean of n=3 independent experiments). PELDOR/DEER results without cryoprotectant are shown as magenta curves. The red shade around the PELDOR/DEER data is the error margin calculated using the validation tool of DeerAnalysis. The red shades around the experimental smFRET distances are error bars based on the standard deviation of n=3 independent experiments.

Anomalous X-ray Scattering Interferometry (AXSI) is a method that builds upon traditional X-ray scattering methods, such as Small-angle X-ray scattering (SAXS), with the ability to resolve the positions of atoms and measure intramolecular distances within biomolecules with high precision[165,166,167].

AXSI relies on the usage of electron-rich labels, such as heavy atoms like gold[168,169,170], which scatter X-rays strongly[100] (figure 3.13 a). X-rays are directed at the sample, and the scattering pattern that results is collected (figure 3.13 b). The scattered X-rays produce interference patterns when they recombine after scattering. These interference patterns contain information about the relative phases and amplitudes of the scattered waves, which in turn are related to the positions and scattering strengths of the labels within the biomolecule. In AXSI, the scattering is made "anomalous" by tuning the X-ray energy to a level where the scattering from the heavy atom labels is particularly strong and distinctive (figure 3.14a). By isolating and analyzing the anomalous interference term, it is possible to extract information about the distances between the labeled positions within the biomolecule[169,170,171,172,173](figure 3.14b). A Fourier transformation converts the anomalous interference term into a spatial distance distribution of pairwise distances within the molecule (figure 3.14 c). This distribution is often denoted as $P(d)$, where d represents the distance between labeled points. AXSI has several advantages over other techniques for measuring intramolecular distances. It provides distance measurements on an absolute length scale and is not sensitive to label orientation or the specific label environment[98]. Additionally, AXSI can be applied to distances greater than 10 nm, which is challenging for other methods like NMR, EPR[174,175,176], or smFRET[177].

Anomalous X-ray Scattering Interferometry (AXSI) is a relatively new method that has been successfully applied to measure distances in DNA samples[173] but not in proteins. This study represents the initial exploration of distance measurements in proteins using AXSI, validating its results with the well-characterized protein model MalE[178,179] and established distance measurements using smFRET[127,122,98]. For this study, two MalE variants were provided by the Cordes lab: MalE-36/352, which was utilized in the multilaboratory and PELDOR/DEER studies[99], and MalE-31/212, an unpublished mutant.

My personal contribution to this study involved replicating all measurements. This included stochastic labeling of all samples with Alexa555 and Alexa647, conducting all smFRET measurements, and processing the data to acquire accurate FRET values, which were then converted into distances.

Stubhan et al. successfully labeled the MalE variants with gold nanoparticles consisting of approximately 85 atoms and a radius of 0.7 nm by coating them with thiol glucose following a one-phase Brust-Schiffrin method[180] (Figure 3.13a). The thiol group in the sugar was then used to specifically attach the nanoparticles to the MalE cysteines using a conventional procedure, similar to that used for FRET labeling. However, size exclusion chromatograms and gel electrophoresis analysis indicated low labeling efficiency for both variants, resulting in approximately 60% unlabeled species, 30% single-labeled species, and 10% double-labeled species.

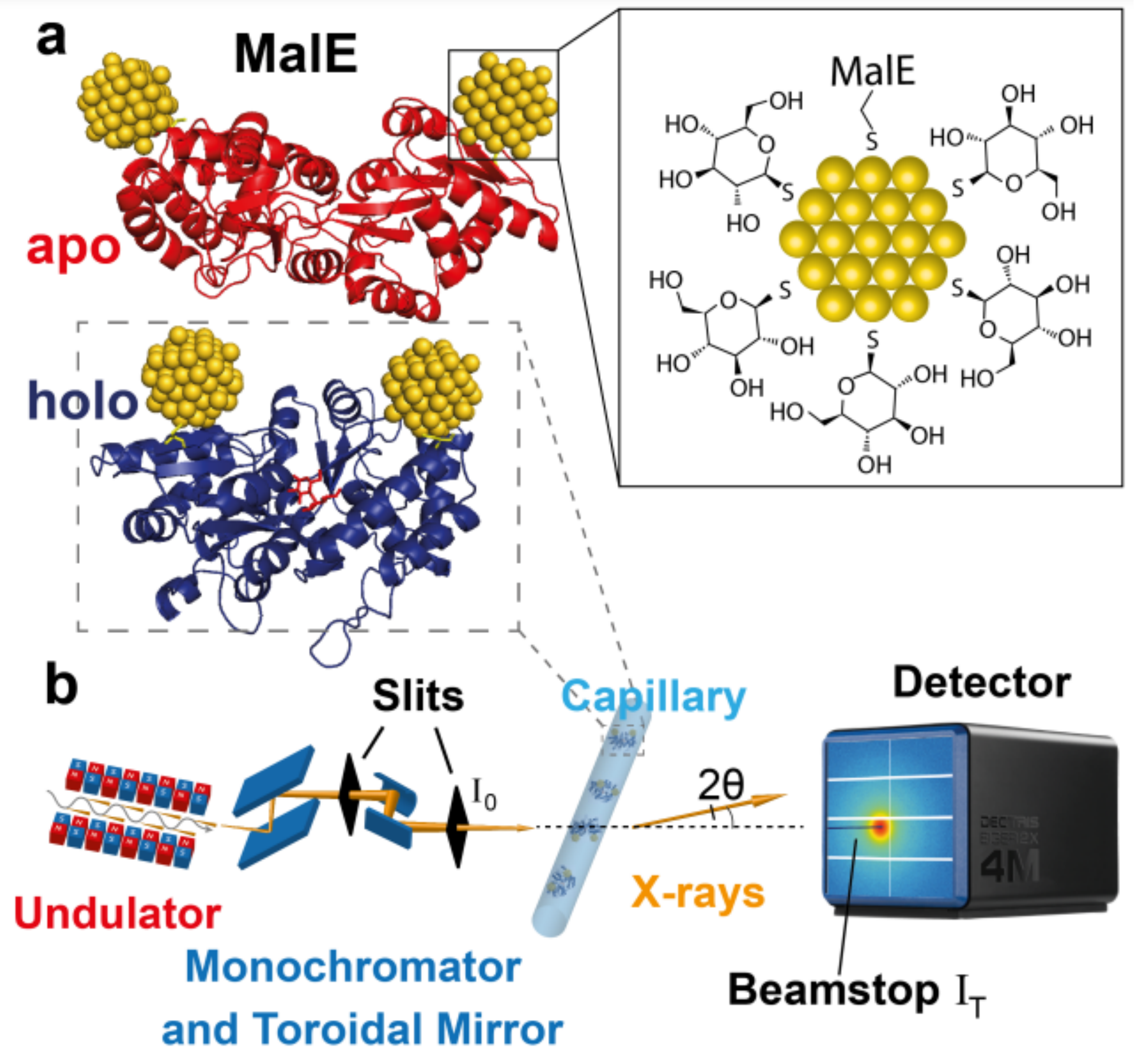

Figure 3.13: Schematic of anomalous X-ray scattering measurements to determine intramolecular distance distributions, adapted from Stubhan et. al.[100] **a** Illustrations of double-labeled MalE in the apo and holo state with gold nano particle labels at amino acid positions 36 and 352 (rendered from PDB ID 1OMP (red – apo) and 1ANF (blue – holo), respectively. The zoom depicts the thioglucose shell on the gold nano particles as well as the S-Au attachment to the protein. **b** Illustration of the SAXS experiment. The undulator and X-ray optics at the synchrotron beam line provide X-rays with tunable energy. The monochromator is used to select energies and collimated X-rays being are scattered by the sample in a quartz capillary. Scattered photons are collected with a camera

Scattering profiles of both MalE constructs were recorded at 9 different energy levels around the gold L-III absorption edge at 11.919 keV (Figure 3.14 a). Oscillations in the scattering profile in the range $q = 0.1 - 0.2\ \AA^{-1}$ were responsive and shifted after the addition of 10 mM maltose, indicative of gold-gold interference contributions (Figure 3.14 a,b).

In principle, only the double-labeled sample population should contribute to the gold-gold term in the scattering pattern. However, the presence of unlabeled and single-labeled species might deteriorate the signal by adding their scattering contributions. This background noise was corrected by additionally measuring unlabeled samples, as well as single mutant variants of the double cysteine mutants. This way, their scattering contributions could be identified and subsequently subtracted from the raw scattering profile, according to the percentage population of the subspecies, e.g., 60% unlabeled and 30% single-labeled species (Figure 3.15 a).

Subsequent analysis of the corrected scattering profiles, and the resulting gold-gold interference contributions, yielded the gold label-gold label distance distributions $P(d)$ for the two MalE variants (Figure 3.14 c) with standard deviations of the main peak positions averaging 0.5 Å.

However, the obtained distance distributions were only possible to acquire by considering the contributions of the non-labeled and single-labeled subspecies, as well as their exact percentage presence in the sample. Subtracting different percentage ratios from the raw scattering profile resulted in many secondary distance distribution peaks; however, the main peak remained the most predominant and shifted by at most 1 Å (Figure 3.15b).

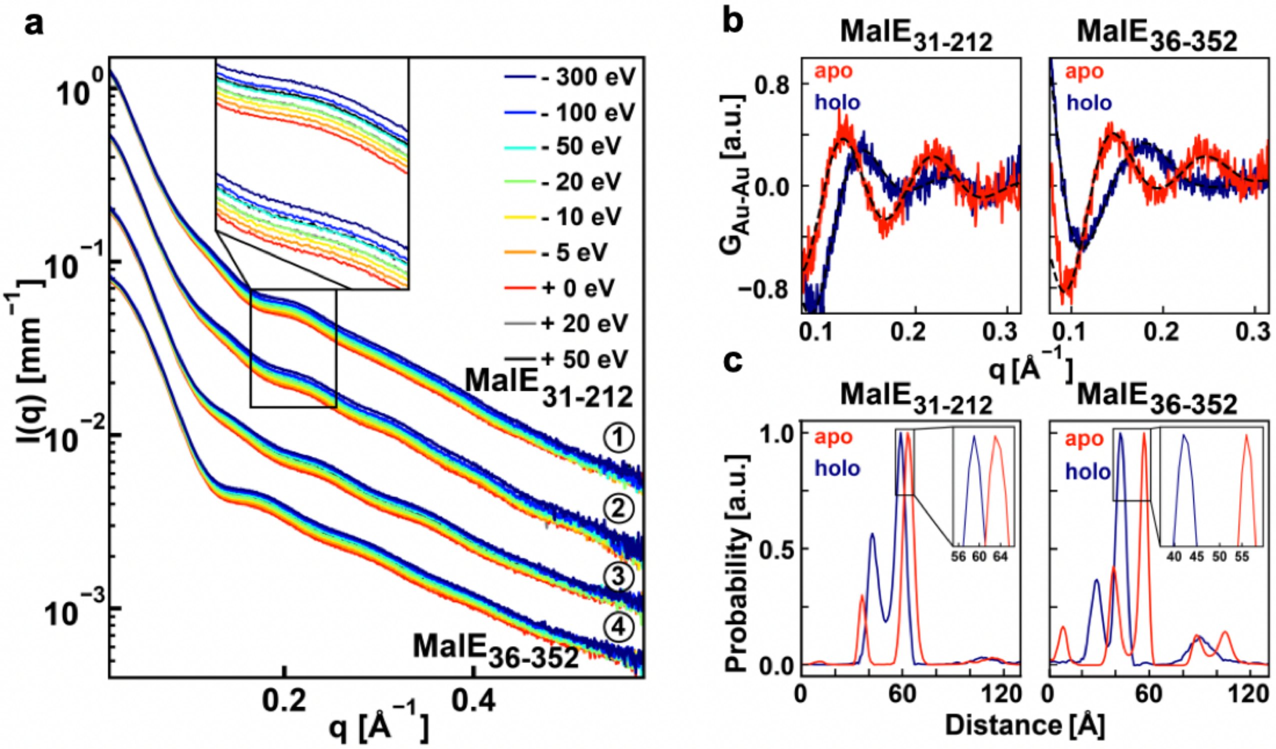

Figure 3.14: AXSI data and distance distribution for MalE variants, adapted from Stubhan et. al.[100] **a** AXSI measurements of both double-labeled MalE mutants with and without maltose measured at 9 energies around the gold L-III absorption edge. ① MalE31-212 ② MalE31-212 with 10 mM maltose ③ MalE36-352 and ④ MalE36-352 with 10 mM maltose. Data are vertically offset for clarity (by scaling factors ①:10, ②:6, ③:2 and ④:1). Indicated energies are relative to the Au L-III edge. **b** Goldgold scattering interference terms for MalE36-352 (left) and MalE31-212 (right) in the absence and presence of 10 mM maltose after correction for 60% single-labeled and 30% unlabeled contributions. **c** Distance distributions $P(d)$ obtained by maximum entropy inversion from the interference terms in panel **b**. The insets show a zoom on the main peaks in the distance distributions

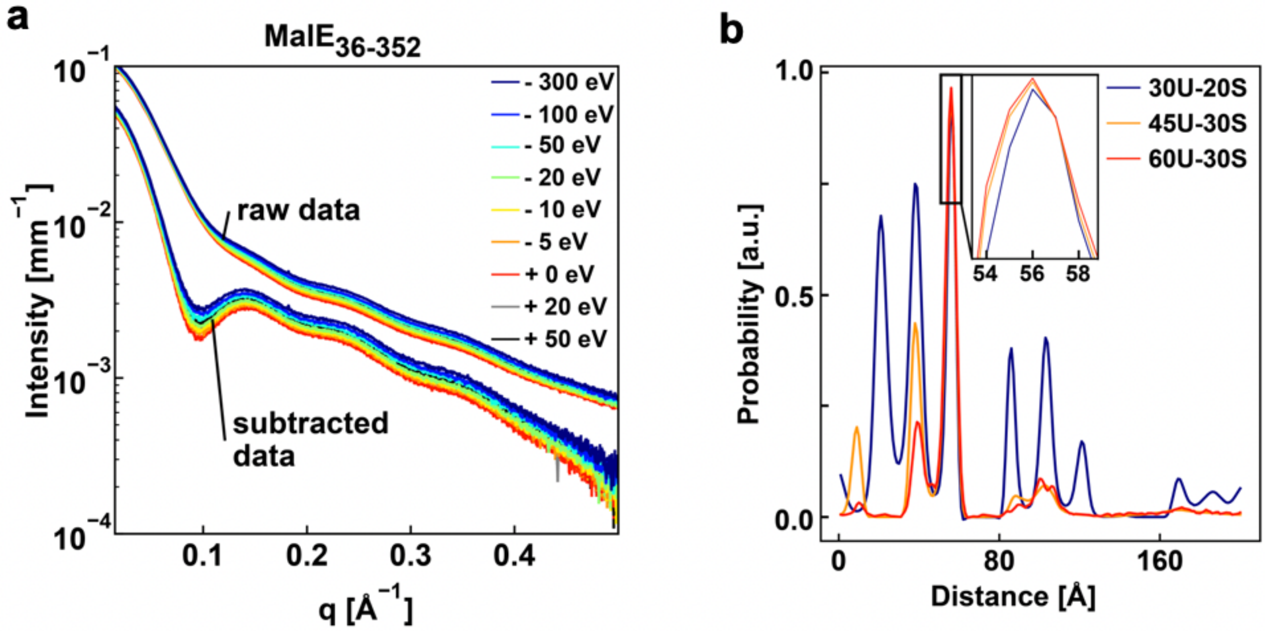

Figure 3.15: Corrections for unlabeled and single labeled proteins, adapted from Stubhan et. al.[100] **a** Scattering Data after the subtraction of unlabeled (60%) and single labeled (30%) proteins. **b** Distance distributions for MalE36-352 for different background subtraction schemes. Example distributions for different subtraction of unlabeled and single-labeled. 30% unlabeled 20% single-labeled (blue), 45% unlabeled 30% single-labeled (orange) and 60% unlabeled 30% single-labeled (red). The zoom in depicts the main peak positions.

The experimental intramolecular distances determined by AXSI and FRET agreed for both MalE31-212 and MalE36-352 in both the apo and holo states (Figure 3.16 d). This agreement, despite the use of different labels with distinct physicochemical properties and geometries, suggested that these differences did not significantly affect the mean positions of the labels. Consequently, the accuracy of the AXSI-derived distances was further investigated by comparing them to simulated label positions in crystal structures of MalE. Stubhan et al. had developed an additional modeling tool similar to FPS (FRET positioning and screening)[117] to generate accessible volumes for the gold nanoparticles based on coarse-grained simulations (Figure 3.16 c).

Upon comparing the experimentally determined distances to the modeled distance distributions for both FRET and AXSI results, strong agreement of the mean distances in the closed or holo states for both MalE31-212 and MalE36-352 was observed (Figure 3.16 e). However, in the open state, the predicted distances tended to surpass the experimentally determined values, particularly noticeable for MalE36-352.

It is noteworthy that in the open conformation, the challenges of modeling were more pronounced compared to the closed conformation. Specifically, predictions based on accessible surface volume using FRETraj (ACV)[117,181] aligned better with experimental data for FRET than accessible volume-based predictions[128,130,131], suggesting that fluorescent labels had a tendency to adhere to the protein's surface. In contrast, AXSI-modeled distance distributions did not deviate as significantly from the experimental data, likely due to the restricted movement of the labels on the protein surface, as predicted by all modeled simulations.

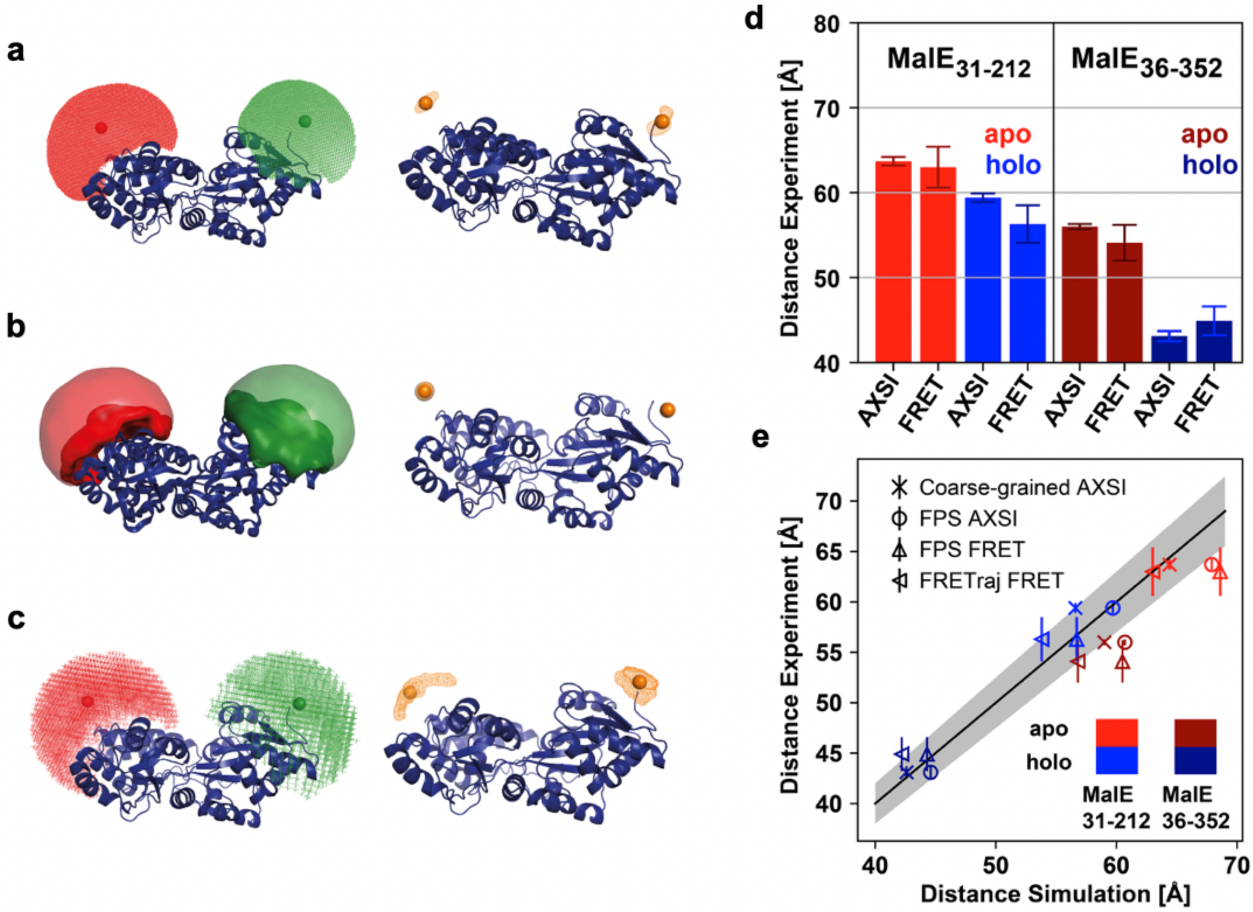

Figure 3.16: Comparison of AXSI and smFRET derived distances, adapted from Stubhan et. al.[100] **a-c** Simulations of label positions for FRET dyes and gold nanoparticles using FPS (**a**), FRETraj[117,181](**b**), and a coarse-grained computation of accessible volumes (**c**). All panels show MalE36-352 in the apo state (PDB ID: 1OMP). The left side depicts positions for the FRET dyes Alexa555 and Alexa647 are shown as colored clouds as computed with FPS (**a**), FRETraj (**b**), and coarse-grained simulations (**c**). The right side depicts Positions of the gold nanoparticles used for AXSI measurements computed with FPS (**a**), FRETraj (**b**), and coarse-grained simulations (**c**).**d** Experimentally determined distances from AXSI and FRET for both MalE variants. Errorbars depict experimental errors. **e** Comparison of experimentally determined distances and the structural models: coarse-grained for AXSI labels (crosses), FPS for AXSI labels (circles), FPS for FRET labels (upward triangles) and FRETraj for FRET labels (left triangles). Experimental uncertainties of the respective techniques are shown. The solid line marks a 1:1 relation and the grey area indicates 5% deviation.

3.3 Single-molecule detection and super-resolution imaging with 3D-printed microscopy platform[§]

Single-molecule detection based biophysical methods have advanced significantly in the past decade and by now represent important emerging tools for life science research.

This is attributed to the rapid advancement of instrumentation, which continuously enhances spatial and temporal resolution as well as sensitivity[182,183,184,185,186]. Consequently, these advancements push the possibilities and progress of single-molecule-based assays, as demonstrated in the preceding sections on smFRET.

This progress, however, typically takes place in engineering and in specialized (bio)physics labs and it is difficult to benefit from it in more application-oriented research such as molecular biology, biomedicine and even clinical diagnostics[187,188].

The reasons for this can be attributed to the high cost associated with the instrumentation and the large dimensions of the setups, which typically necessitate a completely separate room, thereby restricting their operability outside of lab conditions. Moreover, emerging state-of-the-art single molecule-based spectroscopy and microscopy often require instrumentation that is not commercially available e.g. home-built by modification of existing microscope bodies. The expertise needed for the assembly, calibration, maintenance, operation, and data analysis is likely the primary factor contributing to the inaccessibility of state-of-the-art single molecule-based experiments.

Consequently, there is a growing gap between the possibilities of the state-of-the-art in microscopy and spectroscopy and what is accessible to all interested users[188,189].

In recent years, different research groups and companies have started to bridge this gap by miniaturizing microscopy research platforms and reducing costs of commercial systems. Currently, the available compact microscopy setups offer high spatial- and temporal-resolution or high sensitivity. The setups often utilize commercially available optomechanical components, as has been implemented in the smfBOX[190] and miCUBE[191]. On one hand, despite their performance, these setups still cannot be used easily outside of optical laboratories and still requires significant expertise for setting them up, maintaining them, and operating them – making them less suitable for application-oriented users. On the other hand, Oxford Nanoimager's video-based device is small, powerful, and user-friendly, but is inflexible in terms of microscope modalities[192,193,194]. Another drawback of all the microscopes mentioned above are high costs, which are well over 100,000 €. On the contrary, 3D-printing with plastic materials has gained popularity to replace expensive optomechanics and parts of the microscope frame. AttoBright, a user-friendly, minimalist, confocal microscope, showed that a 3D-printed setup

---

[§] This study, titled "Single-molecule detection and super-resolution imaging with a portable and adaptable 3D-printed microscopy platform (Brick-MIC)," was published in Science Advances on September 27, 2024[101]. As a co-first and co-corresponding author, my contributions included conceiving and designing the modular platform architecture, planning the microscope layouts, building the microscopes, conducting experiments, analyzing data, preparing all figures, and writing the manuscript.

can facilitate singlemolecule detection[195]. It comes, however, with significant limitations in terms of data quality and general adaptability compared to the smfBOX or miCUBE. Another option, the "UC2", a camera-based microscope, represents an adaptable platform for various imaging modalities, including bright field, dark field, and fluorescence microscopy[196]. Recently, it has been updated to perform STORM imaging[197].

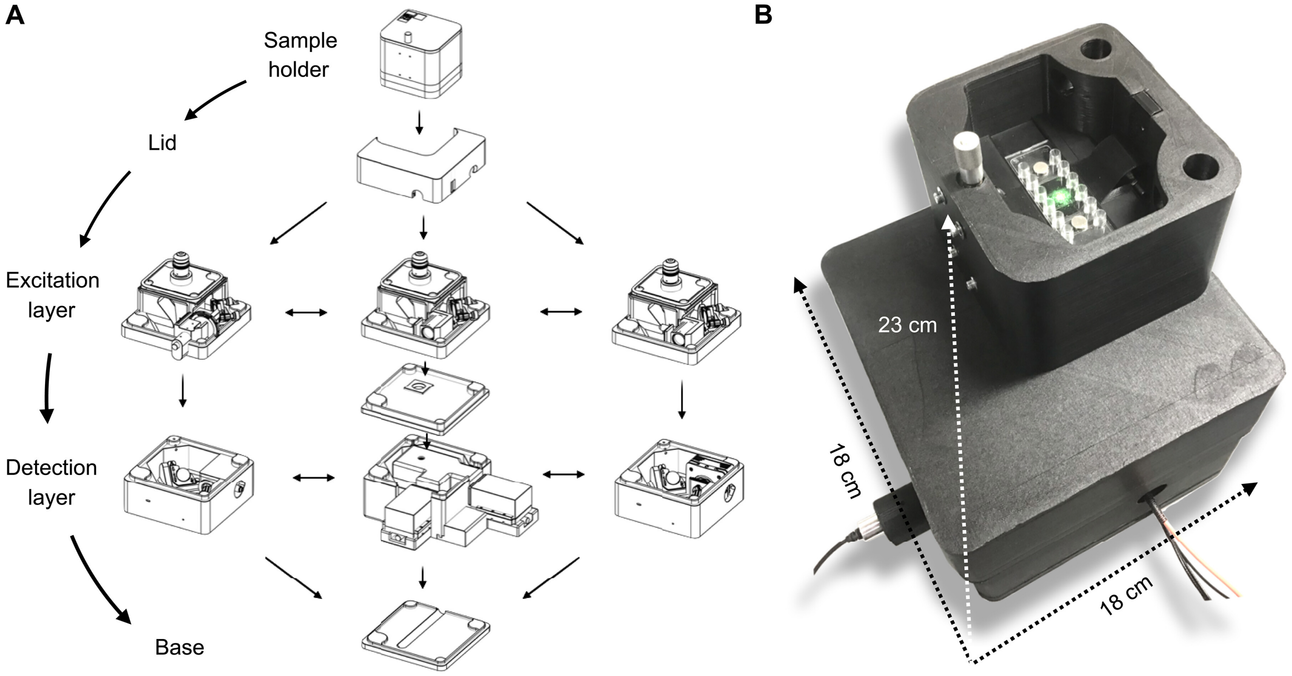

Figure 3.17: Overview of the adaptable Brick-MIC design. **A** The platform uses shape-complementary parts that can be stacked (Lego-like or Japanese “poka yoke”), consisting of different layers: the sample holder, lid, excitation, detection and base layers. The excitation and detection layers are interchangeable, allowing to establish different imaging methods with the same platform and easy exchange of components. **B** Photograph of a confocal Brick-MIC modality as used below for analysis of labelled biomolecules in free diffusion (section “Single particle fluorescence detection and fluorescence correlation spectroscopy”)

To overcome those challenges, we introduced an open-source microscopy platform named Brick-MIC. Brick-MIC was designed with the philosophy to create a user-friendly, portable and stable, cost-effective and adaptable platform that can be used outside of optical labs under ambient light.

It offers the possibility to realize various microscopy modalities, including confocal and video detection, fluorescence spectroscopy assays, state-of-the-art single-molecule detection, and super-resolution optical imaging using the same platform. To reduce costs and facilitate robust operation, an adaptable microscope body was established, fully 3D-printed.

The scaffold of the microscope comprises four layers crafted from 3D-printed plastic material: a sample holder, an excitation layer, a detection layer, and a base plate designed for interchangeable excitation and detection layers (Figure 3.17).

This platform is combined with optical components such as mirrors, filters, etc. from commercial suppliers to establish one microscope modality. Once the microscope frames for all modalities are printed, the Brick-MIC platform enables rapid exchange between distinct microscopy modalities within minutes. The enclosed sample holder is suitable for the incorporation of microfluidics components, such as Ibidi microfluidics slides and tubing, and allows to fix microscope slides with magnets. A single-axis translation stage, which is integrated into a rack and pinion system, controls the Z-axis position of the coverslip and sample, and ensures high positional stability. The design was tested to generally ensure mechanical stability via an accurate fit of the different layers and vibration dampening by use of thermoplastic Polyurethane (TPU), a resilient and rubber-like material, as the base layer of the microscope (Figure 3.17). The detection layers of Brick-MIC are all equipped with essential optical components mounted onto piezo motors for convenient alignment of the setup and use of autocalibration software. We further provide (compiled) Python-based data acquisition and analysis software to perform experiments with different confocal modalities, making the Brick-MIC a true open-source microscopy platform. The only requirement to start your own Brick-MIC is access to a standard, low-cost 3D printer and to purchase of a minimal list of optomechanical and optical components.

To date, we have established various distinct modalities of the platform, from which we use three as representative examples in this paper. The first is a confocal microscope for single-particle detection, fluorescence correlation spectroscopy (FCS)[31], and time-correlated single-photon counting (TCSPC)[32,198], with which we were able to detect individual fluorescent particles, such as freely diffusing nano-sized fluorescent beads, dye molecules, and labeled biomolecules of varying sizes. Second, we established a two-color confocal microscope that we used for single-molecule Förster resonance energy transfer (smFRET)[199,200] experiments with microsecond alternating-laser excitation (sALEX)[93,94]. Last, we realized a camera-based microscope that allows standard wide-field or dark-field imaging and can be upgraded to an epifluorescence microscope for fluorescence and super-resolution imaging via STORM[28,97] and DNA-PAINT[29,30]. We consider our approach a “Swiss-knife” microscope with full flexibility and hope that Brick-MIC will be used inside and outside of research laboratories in the future due to its small size and portability, high stability, and state-of-the-art performance.

Single particle fluorescence detection and fluorescence correlation spectroscopy (FCS). The first modality presented is a minimalist confocal microscope with a single cw-laser excitation source and dual-channel detection using photomultipliers, PMTs (Figure 3.18). The confocal geometry of the setup is achieved using an inversely mounted parabolic collimator that couples the emitted light into an optical fiber (OF). The OF serves as a pinhole (PH) with a diameter related to its core size. The emitted light is captured by a high NA water-immersion microscope objective (60X, NA = 1.2, Olympus – UPLSAPO60XW) and directed by the OF into an external detection box. Here, the emission is spectrally separated via a dichroic mirror (DM) into short (green) and long wavelength emission (red) before reaching two photomultiplier tubes (PMTs; Figure 3.18 B). Signals of both PMTs are read out via an affordable single-photon counter (MCC-DAQ-USB-counter)[195] in combination with in-house written Python software. The data can be used for online inspection of fluorescence time traces in binned format, e.g., for calibration purposes, or can be exported to hdf5 single-photon data

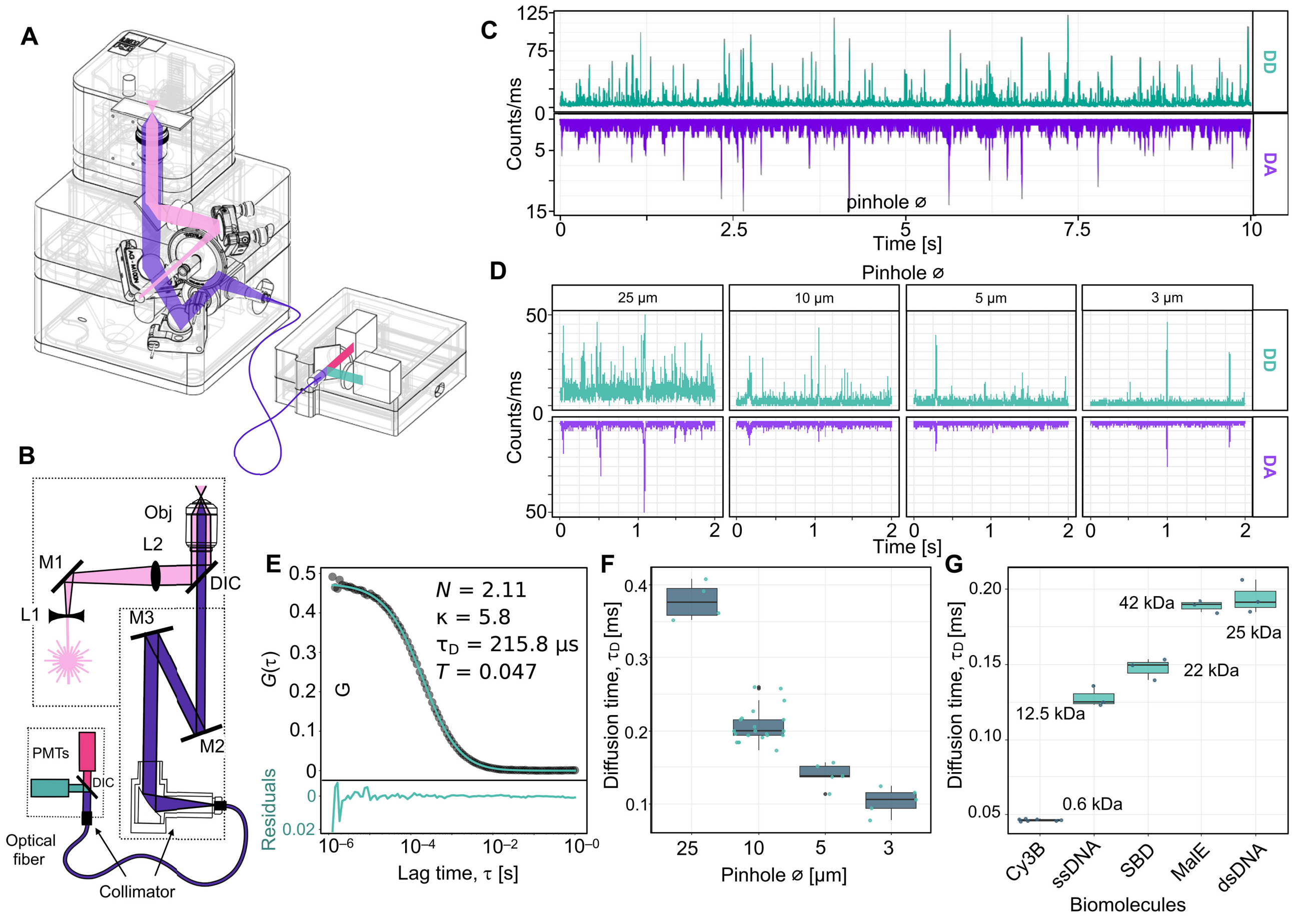

Figure 3.18: Single molecule detection and fluorescence correlation spectroscopy (FCS) with Brick-MIC. **A** CAD model showing Brick-MIC including optical components and the light path (pink: excitation; purple: emission; green and red: spectral split emission after dichroic mirror (DM)). **B** Overview of the optical layout. The modality utilizes a single laser diode (pink), which is expanded using a telescope comprising a bi-concave lens (L1) and a plano-convex (L2) and focused into the sample through an objective lens (Obj), for excitation. The emission is collected through the same objective lens and directed via a pair of mirrors on piezo-directed optical mounts (M2 and M3) through an inversely mounted reflective collimator, which focuses and couples the emission beam into an optical fiber. The optical fiber directs the coupled emission light into an external detection box, where it is collimated with a fixed-focus reflective collimator for spectral separation by a dichroic mirror and detection by PMTs. Further details are provided in the Online Methods. **C** Single molecule time trace of a 100 pM dsDNA sample labeled with Cy3B donor (D) and ATTO647N acceptor (A) dye at a 13 bp inter-dye distance. Individual bursts are recorded in two different photon-streams under continuous green excitation: donor (DD) and acceptor emission (DA). **D** Zoom-in on time traces (max counts: 50 kHz) of 500 nm Tetraspeck-beads (TS) in laminar flow (2.5 µl/s) measured with different core diameters of the OF, which acts as a pinhole. **E** Representative FCS curve of a 5 nM solution of a 40-mer dsDNA sample labeled with Cy3B recorded using a 10 µm pinhole core diameter; fit parameters are number of molecules N, geometry parameter κ, diffusion time τ_D and tripletfraction T. **F** Boxplot showing FCS-based best-fit average diffusion times of a 5 nM solution of a 40-mer dsDNA sample labeled with Cy3B measured using different PH sizes. **G** Boxplot showing FCS-based best-fit average diffusion times of different biomacromolecules labeled with Cy3B with different masses and hydrodynamic radii recorded using a 10 µm PH. Error bars are standard deviations from $n > 3$ repeats.

(https://github.com/harripd/mcc-daq-acquisition) for further processing. Alignment of the setup can be achieved with an automated self-alignment procedure via two piezo mirrors using concentrated solutions of, e.g., 100 nM Cy3B.

A notable benefit of this design is the convenient accessibility and interchangeability of the OF, serving as a PH with tunable diameter. This allows for easy modifications to the detection volume of the microscope by selecting optical fibers with varying core diameters, thereby offering enhanced flexibility in tailoring the parameters to specific experimental requirements.

Using this setup, single fluorescently-labeled nanoparticles of varying diameters (100 nm) and individual fluorophore-labeled double-stranded DNA (dsDNA) molecules were observed. Diffusional transits of donor-acceptor labeled dsDNA molecules (donor Cy3B, acceptor ATTO647N in 13 bp distance) were clearly visible as coinciding bursts in both detection channels (Figure 3.18 C). Variation of the OF core size revealed the effect of shrinking excitation volume in fluorescence time traces (Figure 3.18 D, F). Larger PH sizes, i.e., large detection volumes, showed higher and longer signal periods, higher burst detection frequency, as well as increased background compared to smaller PH diameters (Figure 3.18 D). Further implementation of fluorescence correlation spectroscopy (FCS) was conducted to characterize the setup. Measurements were performed on a 5 - 10 nM solution of 40mer-dsDNA labeled with Cy3B, with varying setup parameters such as laser power and PH diameters (Figure 3.18 E,F, Figure 3.19, and Figure 3.20).

Using a custom analysis script based on Jupyter, molecular brightness (B), diffusion times (τ_D), triplet fraction (T), triplet lifetime (T_D), and their associated amplitude were extracted from a standard diffusion and triplet fit (Figure 3.18 E). Laser power dependency assays were conducted to establish a suitable working window for Cy3B samples (between $25 - 50\mu W$), ensuring that the triplet fraction (T) did not exceed 5% and the geometry parameter (κ) remained below 8 (Figure 3.19). Furthermore, the effects of different pinhole (PH) diameters were examined while maintaining a constant excitation power of $50\mu W$. As expected, the average diffusion times of dsDNA increased to approximately 100 µs, 150 µs, 200 µs, and 250 µs for increasing PH diameters. Similarly, the average number of molecules observed was approximately 0.75, 1.8, 2.2, and 6.5, respectively (Figure 3.20 and Figure 3.18 F).

The use of an OF with a core size diameter of 10 µm resulted in comparable results to those obtained from a custom-built confocal microscope which employs a 50 µm PH. The brightness of Cy3B was lower in the Brick-MIC microscope (10 kHz vs. 80 kHz per molecule, Figure 3.21 and 3.22) according to a reduced PH diameter. The analysis of diffusion times of biomolecules with varying masses and hydrodynamic radii revealed that both setups correctly assessed the expected trends related to molecular mass differences (except for the non-spherical dsDNA sample; Figure 3.21 and Figure 3.18 G).

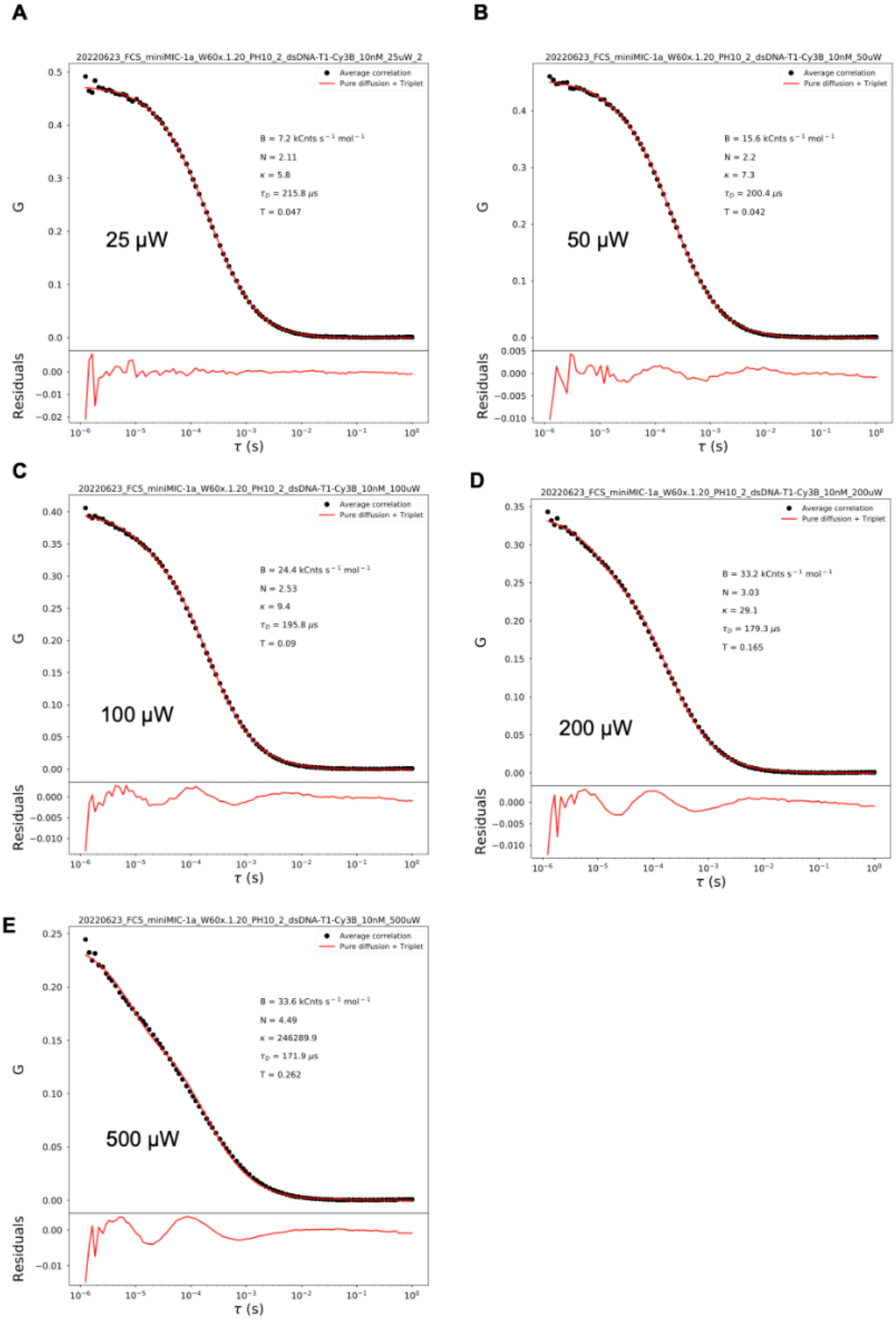

Figure 3.19: FCS laser power dependency with Brick-MIC. Measurements were done on a 10 nM solution of a 40mer dsDNA sample labeled with Cy3b using the 10 µm pinhole configuration. The same sample was measured at 25 μW (**A**), 50 μW (**B**), 100 μW (**C**), 200 μW (**D**), and 500 μW (**E**) laser power exciting at 532 nm wavelength, respectively. Fit parameters are depicted as molecular brightness B, number of molecules N, geometry parameter κ, diffusion time τ_D, and triplet fraction T.

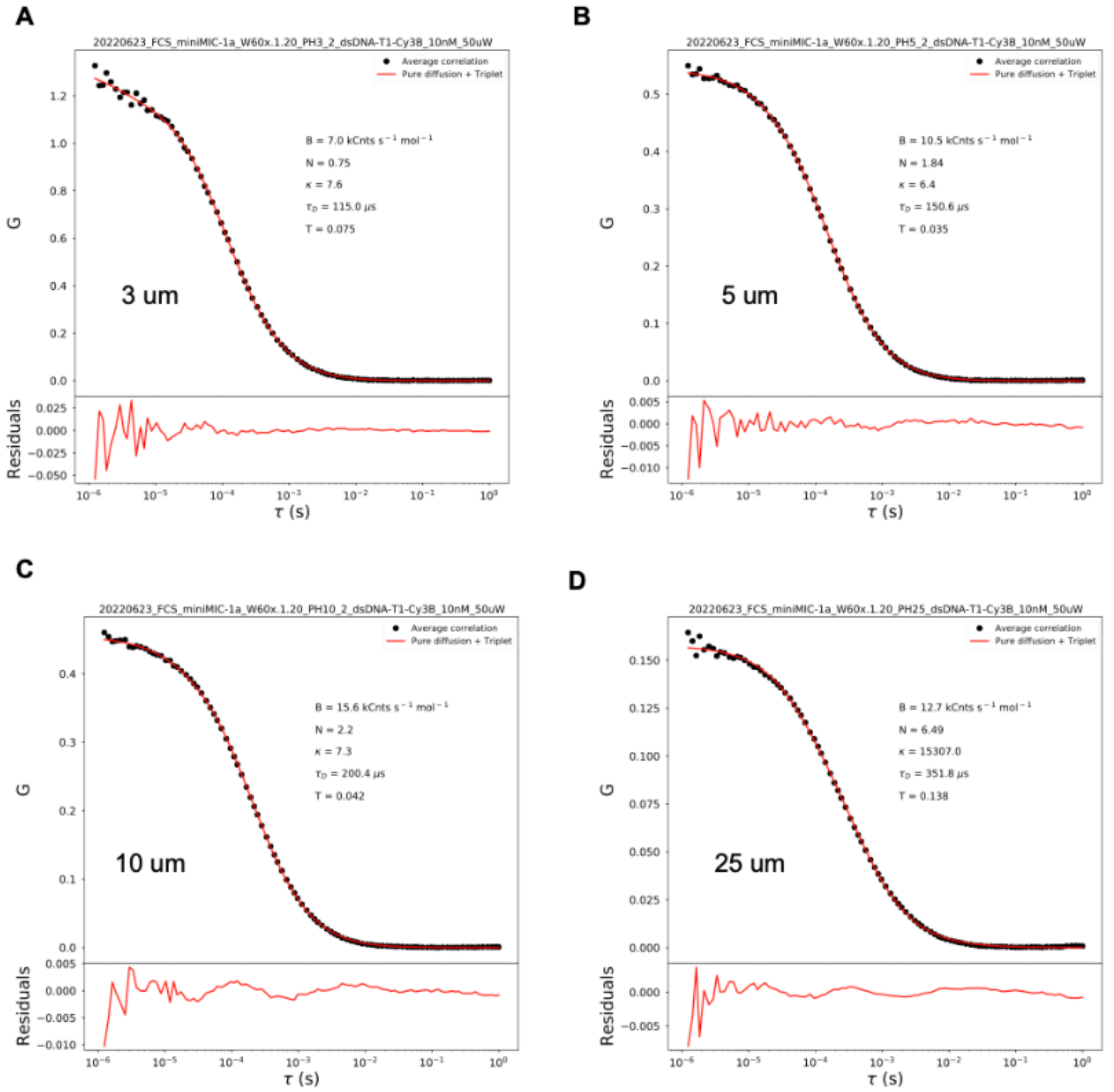

Figure 3.20: FCS Pinhole size dependency of Brick-MIC. Measurements were done on a 10 nM solution of a 40mer dsDNA sample labeled with Cy3b excited at 532 nm wavelength with 50 µW laser power. The same sample was measured using a pinhole diameter of 3 μm (**A**), 5 μm (**B**), 10 μm (**C**), and 25 μm (**D**), respectively. Fit parameters are depicted as molecular brightness B, number of molecules N, geometry parameter κ, diffusion time τ_D, and triplet fraction T.

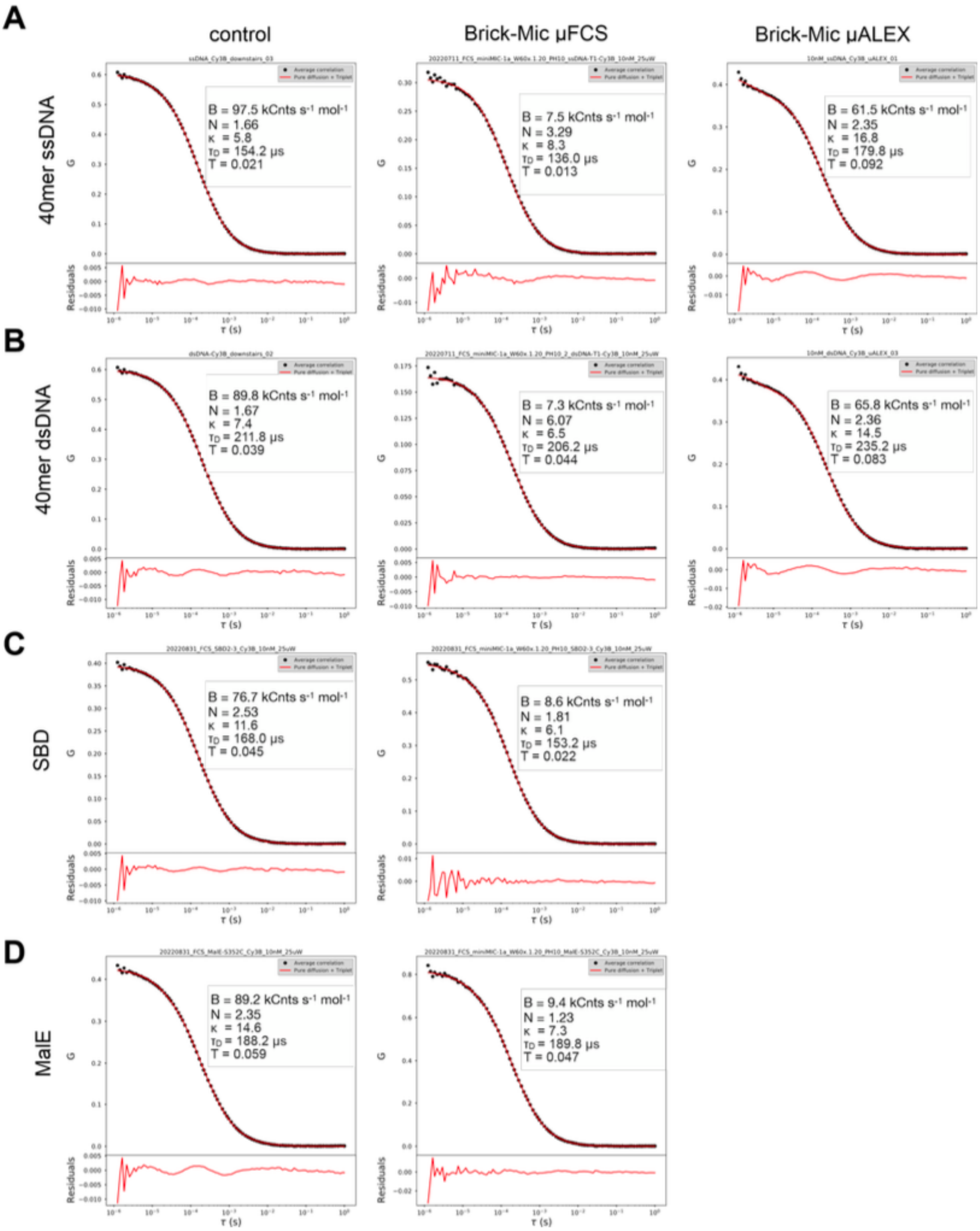

Figure 3.21: Comparative FCS performance of a home-built confocal setup and the Brick-MIC modalities. FCS experiments of the home-built confocal microscope (left), the PMT detection-based Brick-MIC with a 10 m pinhole diameter (middle), and the APD detection-based Brick- MIC variant (right) . Measurements were carried out using various biomolecules with different masses and hydrodynamic radii labeled with Cy3b and excited at 532 nm wavelength at a 25 μW laser power. Samples were (**A**) 40mer single-stranded DNA (12.5 kDa), (**B**) 40mer double-stranded DNA (25 kDa), (**C**) the glutamate substrate binding protein of *L. lactis* SBD2 (22 kDa), and (**D**) the maltose substrate binding protein of *E. coli* MalE (42 kDa). Fit parameters are depicted as molecular brightness B, number of molecules N, geometry parameter κ, diffusion time τ_D, and triplet fraction T.

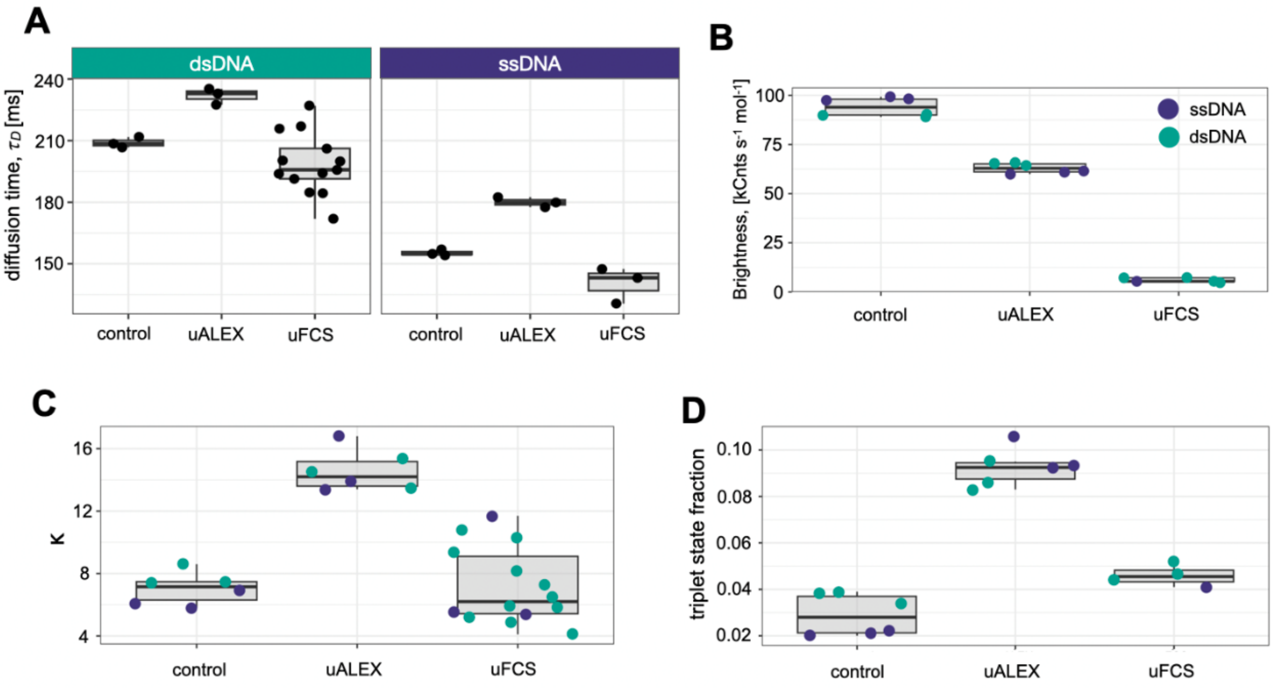

Figure 3.22: Comparative FCS analysis of a home-built confocal setup and the Brick-MIC modalities: Boxplots of FCS fit values comparison shown in Figure 3.21. Comparison between the a home-built confocal setup (control) and two modalities of Brick-MIC: the PMT variant using a 10 m pinhole diameter (FCS), and the APD variant (ALEX). A) diffusion times of dsDNA and ssDNA shown for all setups. B) molecular brightness, C) confocal structure parameter , and D) triplet state fraction.

To highlight the versatility of Brick-MIC, such as the ability to switch from continuous to pulsed laser excitation, we modified the excitation layer by incorporating a reflective collimator connected to a fiber-coupled laser (Fig. 3.24, A and B). With this updated excitation layer combined with the emission layer from the FCS modality (Fig. 3.18), we demonstrated time-correlated single-photon counting (TCSPC) by determining fluorescence lifetimes for Cy3B, Alexa 546, and Atto550 fluorophore–labeled dsDNA samples. The measured lifetimes for Cy3B, Alexa 546, and Atto550 were 2.82 ± 0.01 ns, 3.91 ± 0.01 ns, and 4.15 ± 0.04 ns, respectively (Fig. 3.23), consistent with values obtained using a previously described home-built cuvette-based setup equipped with a single avalanche photodiode (APD)[61]. Each measurement was performed in triplicate using pulsed laser excitation at a 532-nm wavelength, a repetition rate of 20 MHz, and a power of 55 W (LDH-P-FA-530B with PDL 828 ”Sepia II” controller, Picoquant), while detection was carried out by a Multiharp 150 8N (Picoquant) for the PMT variant.

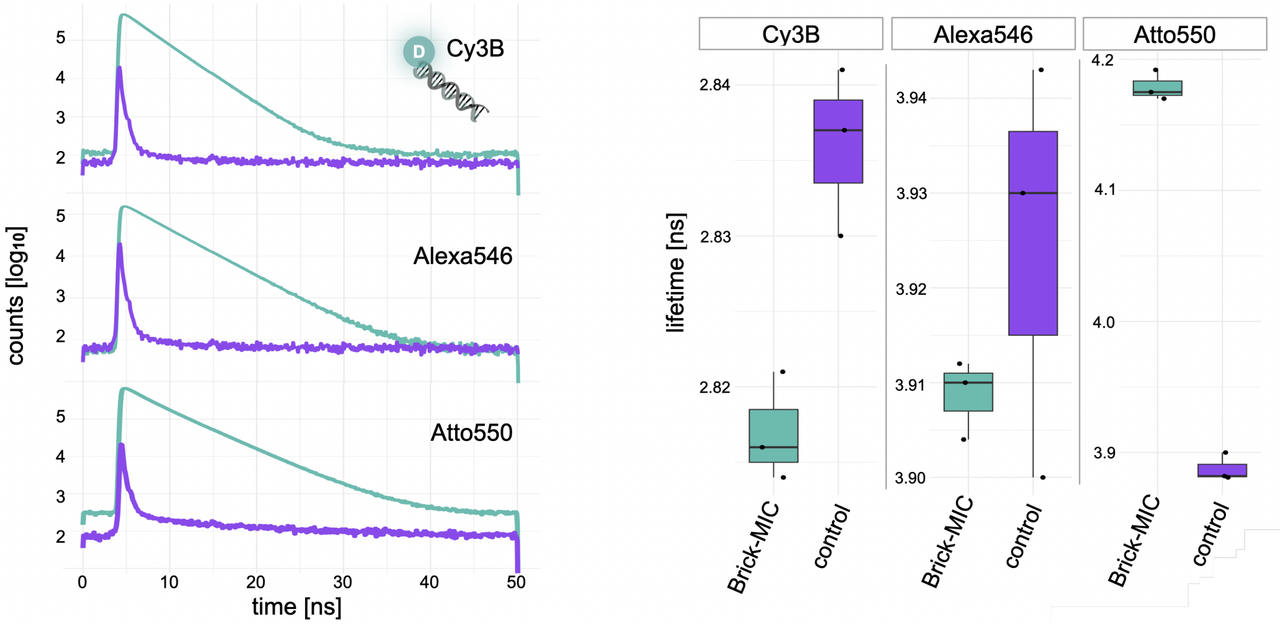

Figure 3.23: Fluorescence lifetime comparison. Time-correlated single-photon counting (TCSPC) measurements of 40-mer dsDNA labeled with three different fluorophores (rows) were obtained using the Brick-MIC platform (left panel). Lifetimes were determined by a single exponential (n=1) tail fit. The determined lifetimes for Cy3B, Alexa546, and Atto550 were 2.82±0.01 ns, 3.91±0.01 ns, and 4.15±0.04 ns, respectively, matching values obtained from a home-built cuvette-based setup with one APD. The IRF (purple line) FWHM were 0.32 ns and 0.65 ns for the Brick-MIC and the control, respectively.

Single-molecule FRET and ALEX modality

FRET and its single-pair variant, spFRET (or smFRET), have become key methods in the expanding toolkit of integrative structural biology[98,120,201,115,114,35,116,117,202,118,132]. With smFRET, it is possible to examine biomacromolecules in aqueous solution at ambient temperature, uncover conformational heterogeneity and subpopulations, accurately measure distances, and characterize conformational changes (kinetic exchange rates)[200,94,61,98,202,201,115,114,35,203,204,99,205,206,103,207].

As anticipated from the sensitivity of the setup, we were able to use the PMT version of our microscope (shown in Fig. 3.18) for ratiometric determination of the apparent FRET efficiency (E*) of single donor-acceptor pairs under continuous green excitation with PMTs (Fig. 3.18 C). However, we observed that the sensitivity of the red detection channel was less than optimal, and the dynamic range of E* was relatively limited compared to our home-built setups. To address this, we further optimized the system for this specific application. We enhanced the detection efficiency by incorporating two single-photon avalanche diodes (SPADs; model PDM 50-Micron, Micro Photon Devices) in the detection layer. These detectors, with a small active detection area of 50 m in diameter, function as both single-photon counters and pinholes[193]. As illustrated in the optical setup scheme (Fig. 3.24, A and B), this design significantly reduces the number of required optical and optomechanical components compared to traditional home-built setups.

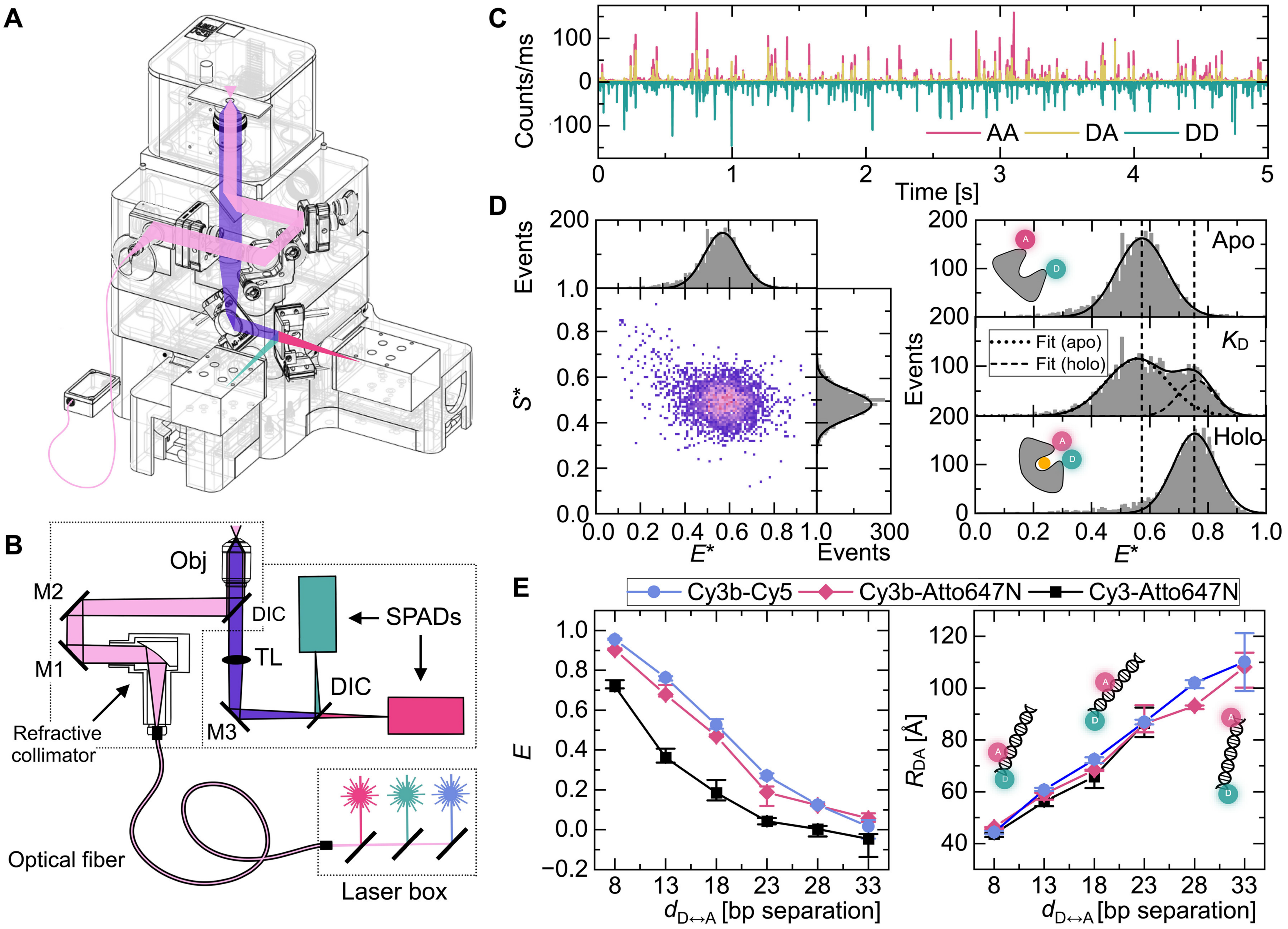

Figure 3.24: Single-molecule FRET and µsALEX modality. **A** CAD model showing all optical components including the light path (pink: excitation; purple: emission; green and red: spectral split emission after the DIC). **B** Overview of the optical layout: The modality uses an external laser coupled to the microscope through an OF. In this arrangement, the excitation beam is collimated with a reflective collimator and then focused into the sample through an objective lens. The emission is collected by the same objective lens and is further focused via an achromatic tube lens (TL) directly onto two different single-photon avalanche diodes (SPADs). Spectral separation is achieved by a DM and appropriate bandpass filters for each detector. The M3 Mirror and the DIC in the emission layer are mounted onto piezo-directed mirror holders, which are used to direct the photon stream into each detector channel. **C** Time trace of a 100 pM dsDNA sample labeled with Cy3B donor (D) and ATTO647N acceptor (A) dye at a 13 bp inter-dye distance. Individual bursts are recorded in three different photon-streams: DD (green) for donor excitation and donor emission; AA (red) for acceptor excitation and acceptor emission; and DA (yellow) for donor excitation and acceptor emission. **D** Representative ES-histogram of the open conformation of the substrate binding protein MalE (left side). (Right side) Observation of different conformational states of MalE (open, closed, and KD conditions) for apo (no substrate), holo (100 µM maltose), and K_D (1µM maltose). **E** Determination of accurate FRET efficiency values and corresponding distances (R_{DA}) using a DNA ladder for different dye combinations.

Employing this modality in combination with microsecond alternating laser excitation (µsALEX) of fiber-coupled green and red lasers at an alternation rate of 20 kHz (50 µs excitation periods), bursts from individual freely-diffusing FRET-labeled biomolecules were observed (Figure3.24). The molecular brightness of Cy3B in this setup was around 60 kHz and thus far superior compared to the PMT variant (10 kHz) and only slightly lower than that of a home-built setup (80 kHz; Figure 3.21 and 3.22). From these setups, we extracted photon streams relevant for ratiometric FRET determination

(Fig. 3.24, D and E; apparent FRET efficiency $E*$) and apparent fraction of donor brightness ($S*$) for each single-molecule transit through the confocal excitation volume. The well-characterized MalE variant (T36C-S352) labeled with Alexa555-Alexa647 dyes[122] was utilized to evaluate Brick-MIC and compare it with the laboratory-built ALEX microscope (Figure 3.25 and Figure 3.24 D). Brick-MIC successfully detected the expected change in FRET efficiencies for both the open and closed conformations, as well as for both states at maltose concentrations near the dissociation equilibrium (Figure 3.25 and Figure 3.24 D). Additionally, the data quality obtained with Brick-MIC was comparable to that of the laboratory-built ALEX microscope, albeit with slightly lower FRET efficiency values and differences in stoichiometry value changes between the open and closed conformations of MalE (Figure 3.25). This could be attributed to the use of different point detectors in each setup, as well as the employment of different filters for the red channel (Brick-MIC utilizing a band-pass filter, while the laboratory home-built ALEX microscope utilizing a long-pass filter). All other components remained identical between the setups.

Thus, the ability of the setup to determine accurate FRET efficiencies was assessed by correcting all setup-dependent parameters using established procedures, as described in previous sections[98,202,35].

The comparison of the E values for an inter-dye base-pair (bp) separation of DNA ladder samples with different distances (in five bp steps) between the donor and acceptor dyes was conducted, ranging from 8 to 33 bp. Additionally, various dye pair combinations were tested to study differing Förster radii (R_0) known from the literature: Cy3-ATTO647N: $R_0 = 5.1$ nm[205,206](Figure 3.26); Cy3B-ATTO647N: $R_0 = 6.7$ nm[206,103,207](Figure 3.27); Cy3B-Cy5: $R_0 = 7.4$ nm (Figure 3.28).

Importantly, all experiments were consistent between Brick-MIC and the corresponding experiments performed on laboratory home-built ALEX microscope, exhibiting the same deviation trends as described above, before applying corrections.

Furthermore, the independently determined accurate FRET values and subsequently the derived R_{DA} values of all three dye-combinations are internally consistent and the inter-dye distances derived from the different dye pairs cannot be distinguished within the error margins, except for large distances ($> 8nm$) that are outside of the sensitive dynamic range of the FRET approach (Figure 3.24 E and Figure 3.29).

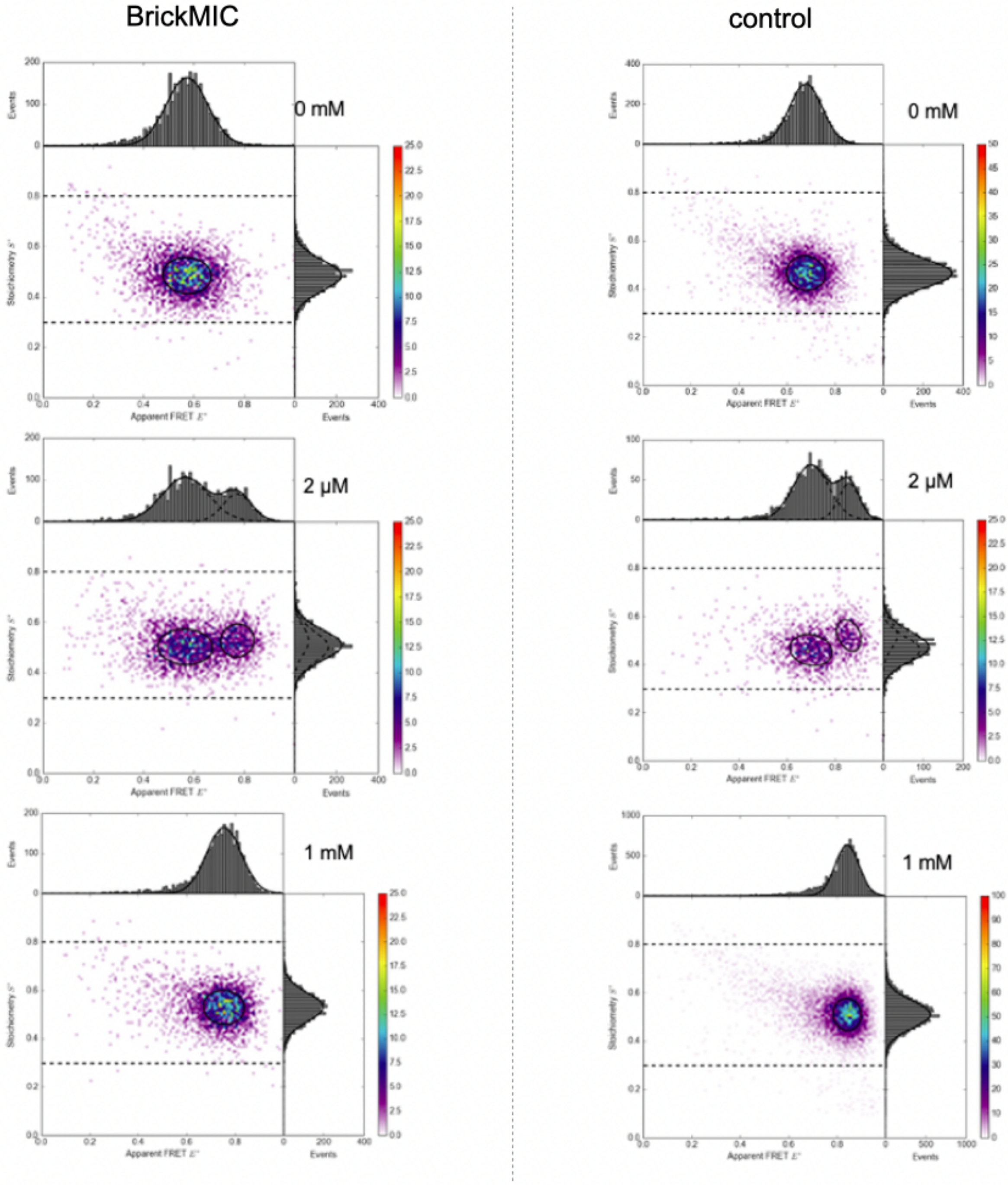

Figure 3.25: Raw smFRET data (apparent ES histograms) from the *E. coli* maltose substrate binding protein variant MalE (T36C-S352) labeled with Alexa555-Alexa647 dye pair, measured with Brick-MIC (left side) and the lab's ALEX microscope (right side). All measurements were carried out using 532 nm wavelength at 60 μW laser power for donor excitation and a 640 nm wavelength at 25 μW laser power for acceptor excitation. The measurements were carried out using different maltose concentrations: 0 mM (upper panels), 2 µM (middle panels), and 1 mM (lower panels), reflecting the apo, K_D, and holo states of the protein, respectively.

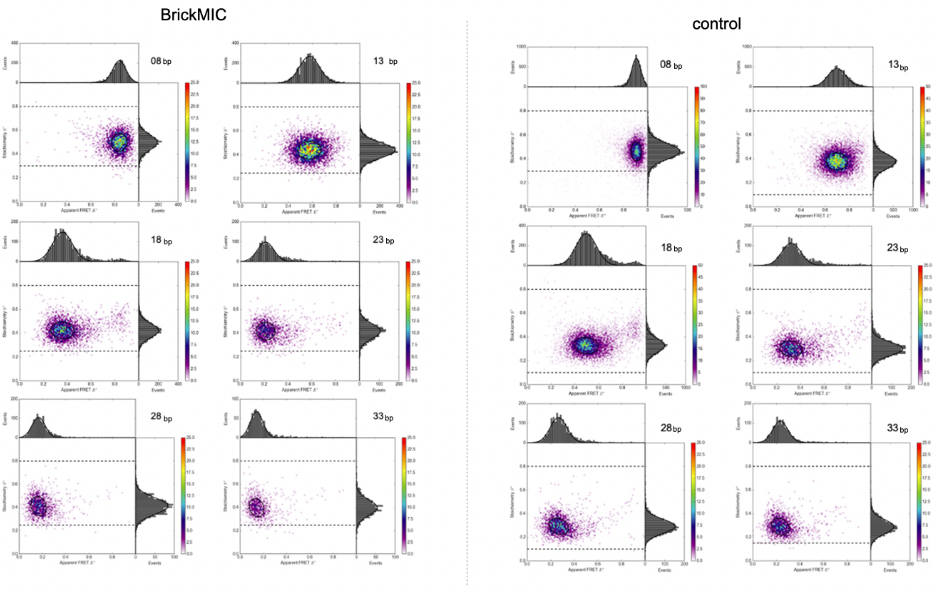

Figure 3.26: Raw smFRET data (apparent ES histograms) from the Cy3-Atto647N DNA ladder set, measured with Brick-MIC (left side) and the lab's ALEX microscope (right side). All measurements were carried out using 532 nm wavelength at 60 μW laser power for donor excitation and a 640 nm wavelength at 25 μW laser power for acceptor excitation. The corresponding interdye distances for Brick-MIC and the lab's ALEX microscope are 8 bp (top-left), 13 bp (top-right), 18 bp (middle-left), 23 bp (middle-right), 28 bp (lower-left), and 33 bp (lower-right), respectively.

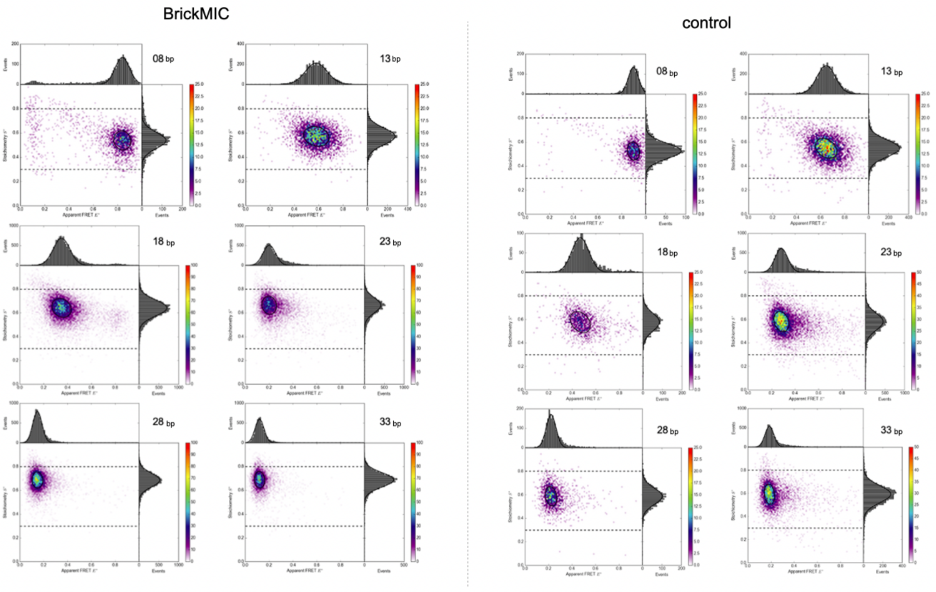

Figure 3.27: Raw smFRET data (apparent ES histograms) from the Cy3b-Atto647N DNA ladder set, measured with Brick-MIC (left side) and the lab's ALEX microscope (right side). All measurements were carried out using a 532 nm wavelength at 60 μW laser power for donor excitation and a 640 nm wavelength at 25 μW laser power for acceptor excitation. The corresponding interdye distances for Brick-MIC and the lab's ALEX microscope are 8 bp (top-left), 13 bp (top-right), 18 bp (middle-left), 23 bp (middle-right), 28 bp (lower-left), and 33 bp (lower-right), respectively.

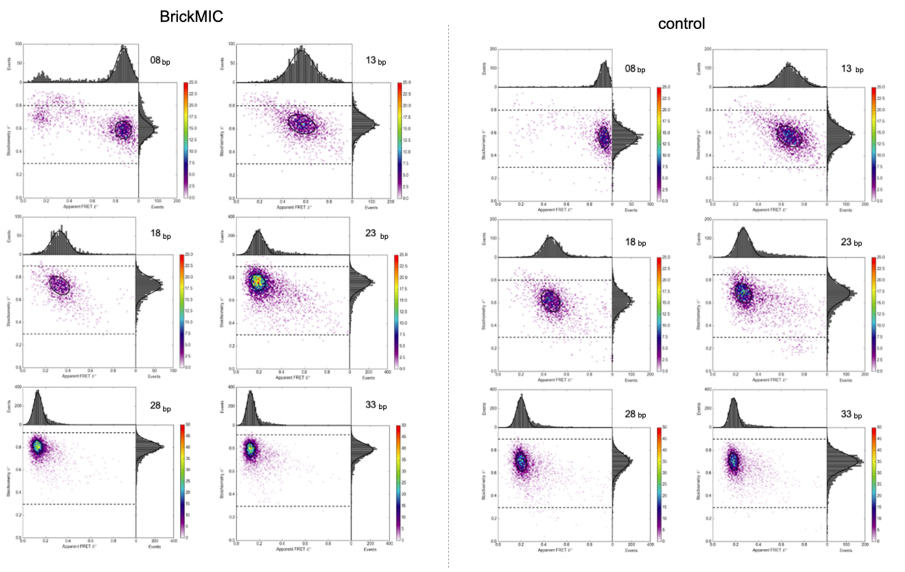

Figure 3.28: Raw smFRET data (apparent ES histograms) from the Cy3b-Cy5 DNA ladder set, measured with Brick-MIC (left side) and the lab's ALEX microscope (right side). All measurements were carried out using 532 nm wavelength at 60 μW laser power for donor excitation and a 640 nm wavelength at 25 μW laser power for acceptor excitation. The corresponding interdye distances for Brick-MIC and the lab's ALEX microscope are 8 bp (top-left), 13 bp (top-right), 18 bp (middle-left), 23 bp (middle-right), 28 bp (lower-left), and 33 bp (lower-right), respectively.

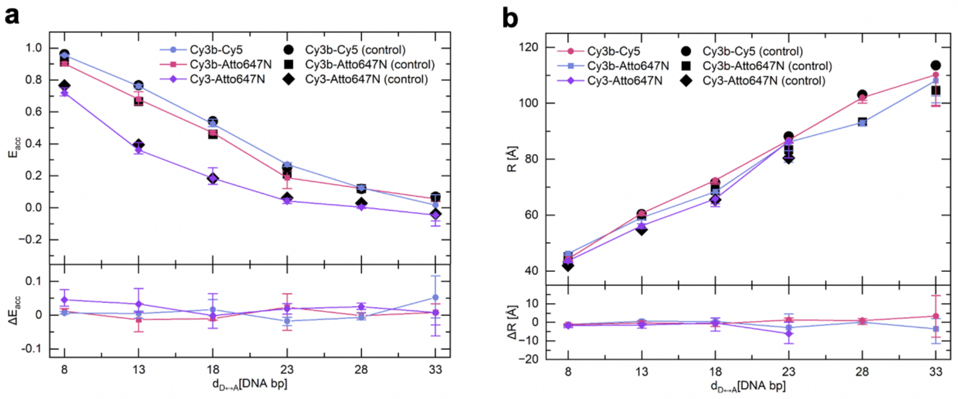

Figure 3.29: Accurate FRET values and inferred distances comparison between Brick-MIC and the lab's ALEX microscope. smFRET measurements were performed on 40mer double-stranded DNA samples with a set of donor and acceptor fluorophore pairs Cy3b-Cy5, Cy3b-Atto647N, and Cy3-Atto647N, and with different interdye distances in terms of DNA base pairs (8, 13, 18, 23, 28, and 33). All measurements were carried out using 532 nm wavelength at 60 μW laser power for donor excitation and 640 nm wavelength at 25 μW laser power for acceptor excitation. Panel **a** (upper panel) shows setup-independent accurate FRET values (E_{acc}) acquired from Brick-MIC (colored symbols) and the laboratory's ALEX microscope (black filled symbols). Error bars represent standard deviations from $n > 3$ repeats. The lower panel shows the difference between accurate FRET values (ΔE_{acc}) between Brick-MIC and the laboratory's ALEX microscope in a given donor-acceptor fluorophore set. Panel **b** shows the calculated interdye distances ($R[\AA]$) from FRET values in **a**. The respective Förster radii used for the conversion were 51$\AA$ for Cy3-Atto647N, 67$\AA$ for Cy3b-Atto647N, and 74$\AA$ for Cy3b-Cy5. The lower panel shows the difference between determined interdye distances ($\Delta R[\AA]$) between Brick-MIC and the laboratory's ALEX microscope in a given donor-acceptor fluorophore set.

Camera-based light microscopy, single-molecule fluorescence detection and super-resolution imaging modality

In a final step, the potential of Brick-MIC for camera-based imaging was explored. Figure 3.30 A, B illustrates the developed wide-field epi-fluorescence modality. In this configuration, the excitation layer is connected to the light source via an optical fiber, similar to the previously described µsALEX modality.

The microscope was then tested for localization-based super-resolution imaging using STORM[28,97] and DNA-PAINT[29,30]. For this purpose, DNA-origami nano-rulers from GATTAquant with a single 95 nm distance (STORM) and two 80 nm distances (DNA-PAINT) between dye attachment positions on the respective origami structure were obtained.

These fluorescent structures were sparsely immobilized on BSA/BSA-biotin coated surfaces and provided images as shown in the left panels of Figure 3.30 C and Figure 3.31. Applying thiol-containing photoswitching buffer[28,97] or DNA-imager strands to the solution[29] enabled the use of the blinking emission of individual labels to construct super-resolved images with the ImageJ plugin Thunderstorm[96]. We found that beads were helpful but not strictly necessary as fiducial markers to compensate for lateral drift, since lateral drift was ¡250 nm over time spans of 30 min (Figure 3.32. Both structures were resolvable, and a localization precision of approximately 30 nm FWHM for STORM and 65 nm FWHM for PAINT was obtained from isolated dyes or binding sites (Figure 3.30 D). Importantly, this localization precision was achieved from analyzing 2500 consecutive frames. While the device was specifically tailored for fluorescence imaging, its versatility was demonstrated through its use in standard transmission light microscopy or contrast-enhancing techniques such as dark-field and oblique illumination. This was exemplified by images of Radiolarians recorded with the setup (Figure 3.30 E). To obtain these images, minimal modifications of the optical components were required (Figure 3.33). A LED desktop lamp was used as transmission light, positioned right on top of the sample holder. Additionally, the objective was interchanged for a 20x air objective with a low numerical aperture (NA=0.4, 1-U2B225, Olympus). Darkfield imaging, as well as oblique illumination, was achieved by covering the sample holder with aluminum foil and punching small holes in it with different patterns. For darkfield, a round pattern approximately 5 cm in diameter was used. For oblique illumination, a crescent moon shape was punctured in the foil approximately 3 cm away from the objective's axis.

As shown, Brick-MIC is a high-performance and cost-effective multi-functional microscopy platform that facilitates various state-of-the-art microscopy applications including single-molecule detection and super-resolution microscopy. The modular philosophy of the platform allows for development of additional new modalities not shown here, e.g., TIRF[81], FLIM[198] or light-sheet[80] microscopy. This versatility might make it a valuable technology platform not only for imaging, but also for a wide range of other scientific directions, e.g., flow cytometry or spectroscopy. Notably, the compact size of the platform offers advantages beyond the confines of the laboratory and that of previous works in terms of performance and portability. The portability and small footprint of Brick-MIC make it ideal for conducting research in challenging conditions or real-world scenarios, opening new possibilities for scientific exploration.

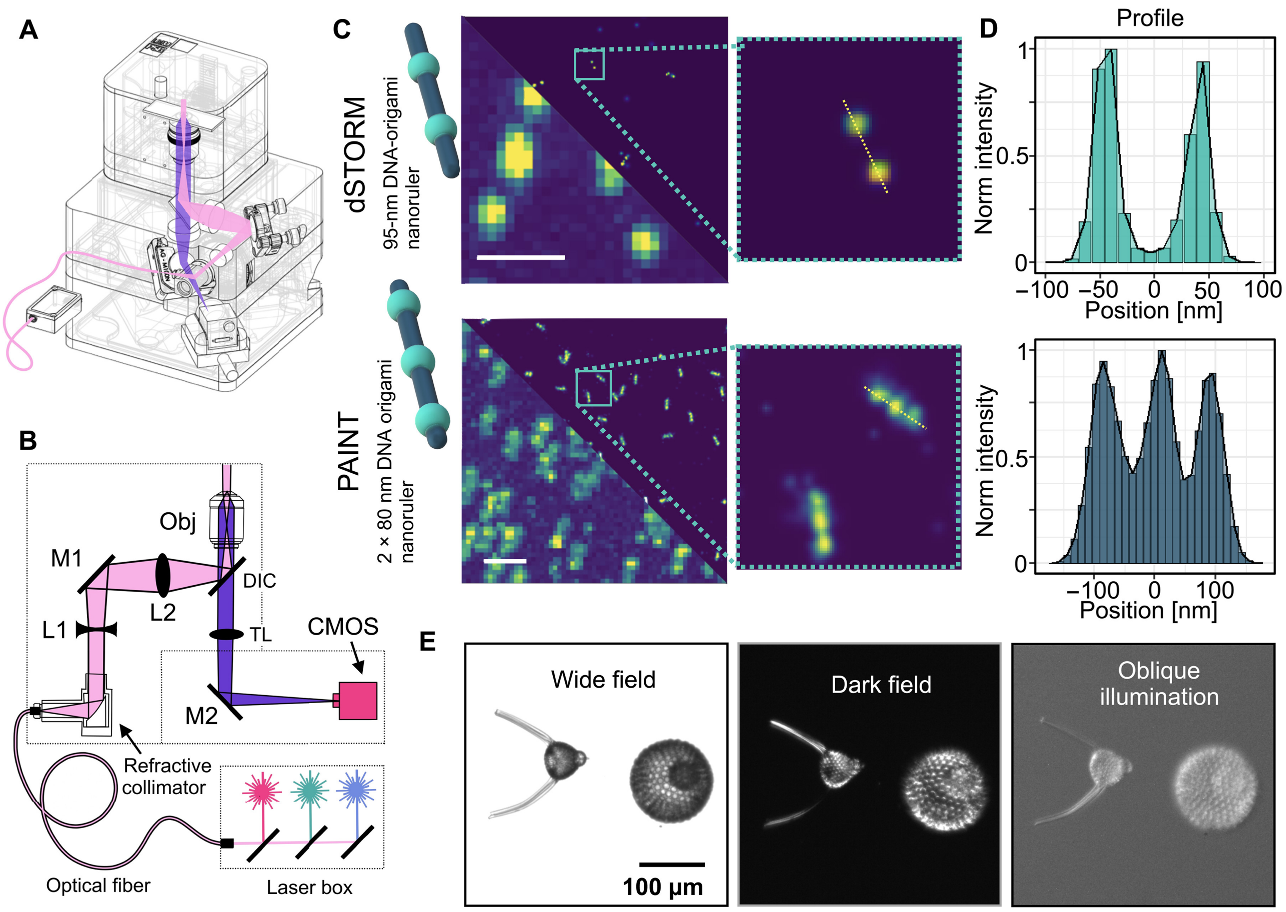

Figure 3.30: Camera-based light microscopy, single-molecule fluorescence detection and single molecule localization microscopy superresolution imaging. **A** CAD model showing all optical components, as well as the light path (pink: excitation; purple: emission). **B** Overview of the optical layout: The modality uses an external laser box coupled to the microscope through an OF. In this arrangement, the excitation beam is collimated with a reflective collimator, which is expanded using a plano-concave lens (L1) and focused with a plano-convex lens (L2) into the back focal plane of the objective lens, resulting in an even illumination of the sample. The emission is collected by the same objective lens and focused via an achromatic tube lens (TL) onto a CMOS camera creating a real image of the sample. **C** dSTORM and DNA-PAINT imaging (up and down, respectively) using 2 x 95 nm and 3 x 80 nm DNA-origami nano-ruler structures, respectively. Representative epi-fluorescence image and reconstructed super-resolution single-molecule localization image (left, white line represents 1 µm), with a zoom in (right). **D** Representative cross-section profile of a single DNA-origami showing the zoom (yellow dotted line). **E** Imaging of Radiolarians using classical contrast methods: transmission light microscopy (left), darkfield illumination (middle), and oblique illumination (right).

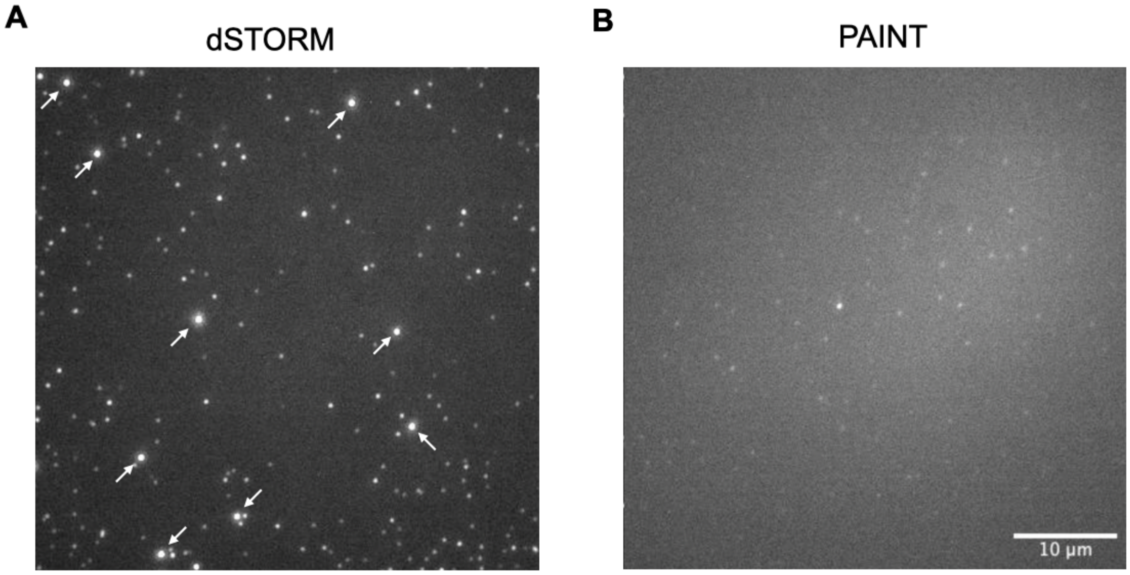

Figure 3.31: Raw epi-fluorescent dSTORM and DNA-PAINT images using Brick-MIC. All images were acquired using a 100 ms exposure time and exciting the sample with a 640 nm wavelength laser at 30 mW laser power, measured after the objective. The white ruler represents a distance of 10 μm for both images. Panel **A** shows surface-immobilized DNA origami nano rulers interspaced at 95 nm with Alexa647 fluorophores for dSTORM imaging. The arrows point at 100 nm diameter surface-immobilized tetra speck beads used as fiducial markers for drift correction. Panel **B** shows surface-immobilized DNA origami nano rulers. Target sequences for PAINT measurements are interspaced two times at 80 nm. Corresponding freely diffusing DNA-probes are labeled with ATTO 655 at a concentration of approximately 100 pM resulting in high background for epi illumination. In contrast to dSTORM measurements, PAINT measurements did not use fiducial markers for drift correction.

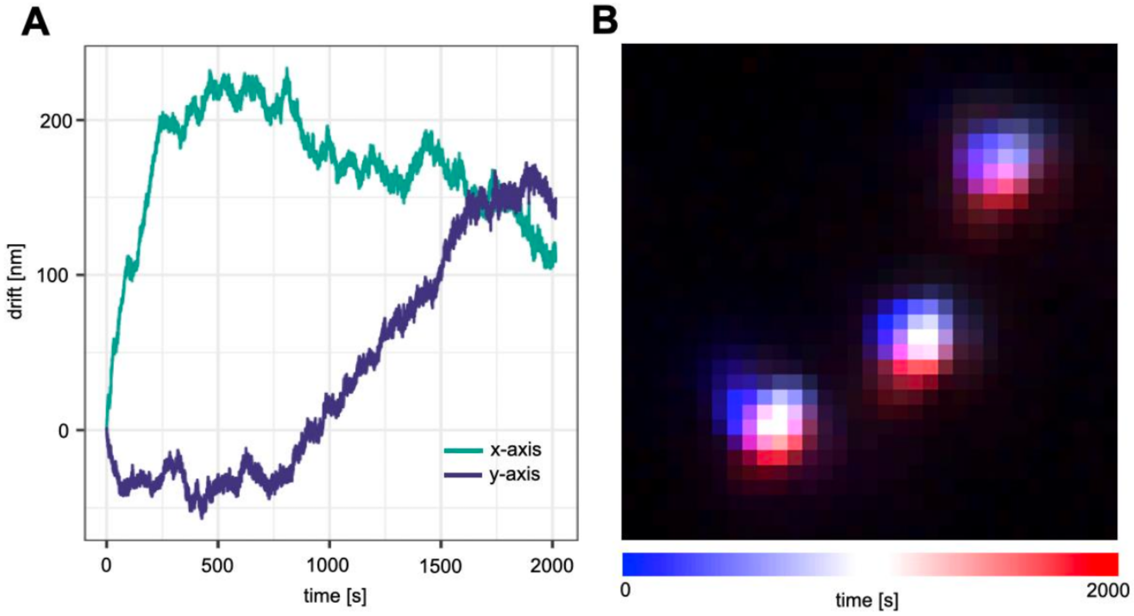

Figure 3.32: Quantifying long-term lateral drift. Panel A depicts the x-y drift of 100-nm- sized Tetraspeck beads (image shown in panel B) over a time interval of 2000 s, where the initial location is shown in blue and later locations in red.

Figure 3.33: Transmission light microscopy using Brick-MIC. The left panel shows the Brick-MIC video modality with an LED desktop lamp used as light source, which was positioned right on top of the sample holder. The sample holder is covered with aluminum foil with a punctured circular pattern for darkfield imaging (middle right panel). The upper right panel shows an uncovered sample holder used for bright field imaging. The lower right panel shows the aluminum covering used for oblique illumination, where the foil has a punctured crescent moon shape.

3.4 Expanding Brick-MIC for rapid and specific detection of single nanoparticles and viruses[§]

The sensitive and rapid detection of bio-nanoparticles (bio-NPs), including viruses, liposomes, extracellular vesicles, or specific biomolecules, is key in life science research and its subsequent transition into application-oriented diagnostics and treatment. Nonetheless, conventional methods and equipment utilized in diagnostic facilities continue to depend on labor-intensive lab procedures, sample purification, and signal amplification of the targeted analyte. This is evident in techniques such as polymerase chain reaction (PCR)[208,209,210], DNA sequencing[211,212], serological tests[213,214], and ELISA assays[215].

The COVID-19 pandemic in 2020 presented significant challenges to current diagnostic methodologies, highlighting weaknesses in existing approaches, especially in a pandemic scenario[216]. These shortcomings included the low accuracy and high false-negative rates of rapid antigen-based test kits[217], the time-consuming nature of PCR assays, limitations in the availability of diagnostic labs, and shortages of highly qualified personnel to conduct experiments[208].

Hence, the concept of directly detecting virus particles using confocal fluorescence microscopy became appealing, as it addressed many of the limitations described previously[218].

Importantly, the addition of the Brick-MIC microscopy platform addressed in the first place the accessibility of confocal setups, through its 3D-printing nature, and additionally facilitated operation with a low training barrier.

The concept of directly detecting virus particles using confocal fluorescence microscopy was explored in a study conducted in collaboration between the Lerner lab, the Cordes lab (which designed and conceived the study), and the Zahavy lab (which prepared and provided viral samples).

My contribution to the study involved customizing the confocal PMT Brick-MIC variant to suit the requirements of the assay. I conducted initial tests and characterized the setup using fluorescent nanobeads in flow through microfluidics. Additionally, I provided training for the use of Brick-MIC at the Lerner lab.

The presented assay detects single nanoparticles (NPs) in microfluidic laminar flow by correlating fluorescent signals associated with the virus volume and specific antibody labels on its capsid. Inspired by inverse fluorescence cross-correlation spectroscopy (iFCCS)[219,220], which utilizes high dye concentrations to count cross-correlated events of signals from single NPs, this assay relies on changes

---

[§] The study titled ”Rapid and specific detection of nanoparticles and viruses one at a time using microfluidic laminar flow and confocal fluorescence microscopy” was published in iScience in 2024[102]. My contributions to this work involved the customization of the confocal PMT Brick-MIC variant to meet the specific requirements of the assay. I also performed initial characterization of the setup by conducting tests with fluorescent nanobeads in flow-through microfluidic systems. Additionally, I provided training on the use of the Brick-MIC platform at the Lerner Lab. This research was conducted in close collaboration with the Lerner Lab.

in nonspecific and specific fluorescence signals to indicate the presence of NPs in the sample. As an NP moves through the confocal volume, the nonspecific signal decreases creating a dip, due to the exclusion of free dye molecules by the particle volume, accompanied by a specific burst signal from the specific antibody labels on its capsid (Figure 3.34).

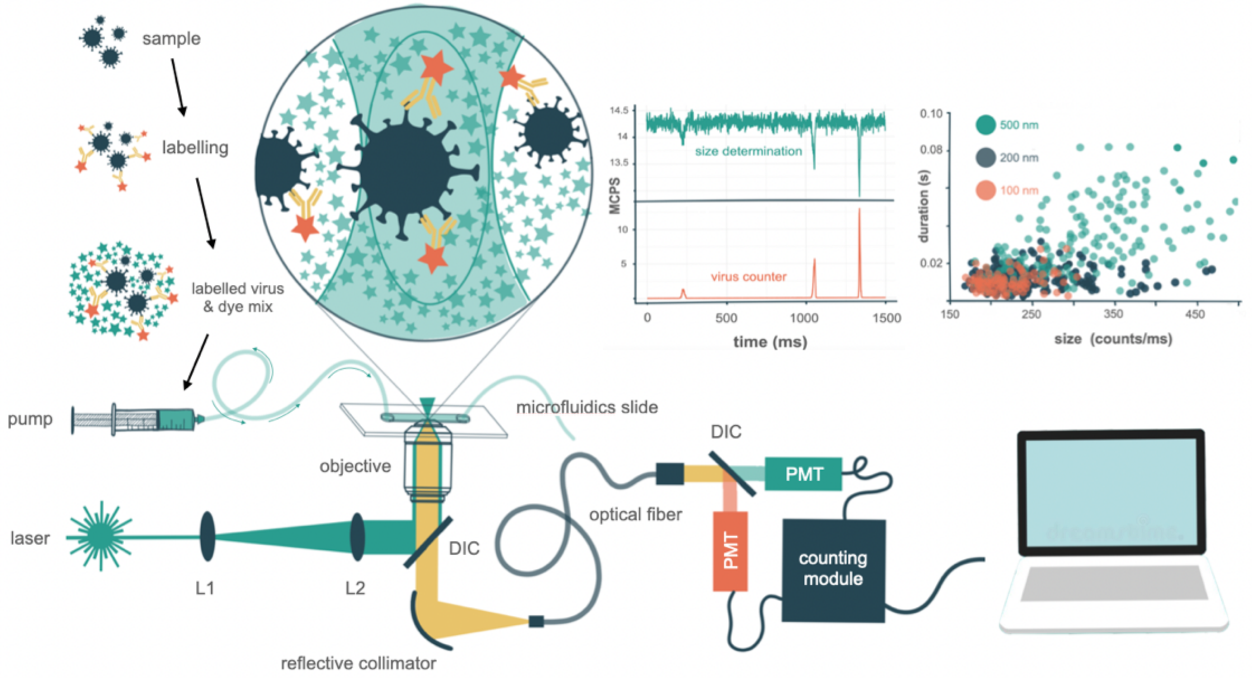

Figure 3.34: Overview of the confocal-based viral detection workflow: Viral samples undergo specific labeling with fluorescent antibodies and are then mixed with a solution containing a high concentration of a different fluorophore. The analyte, comprising the labeled viruses and the fluorophore solution, is pushed through a microfluidics slide in laminar flow. It is then measured using a confocal setup, which splits the collected fluorescence signal into specific (fluorescent antibody) and unspecific (fluorophore milieu) acquisition channels. The highly concentrated fluorophore milieu generates a constant unspecific signal, which is disrupted when a particle traverses the confocal volume, displacing the fluorophores. The resulting signal dip is directly proportional to the volume of the transversing particle, represented through the loss signal magnitude and its duration time. If the particle is additionally labeled with a fluorescent antibody, such as a virus particle, the unspecific signal dip will coincide with the fluorescent burst detected in the specific acquisition channel.

To mitigate the heterogeneity of the sizes and durations of changes in the signal, experiments were conducted under laminar flow conditions within a commercially-available microfluidic channel (Figure 3.35). Laminar flow conditions minimize variations in both the durations and sizes of changes in the signal, thus refining the direct relation between signal changes and NP volumes. Additionally, laminar flow conditions contribute to higher particle count rates (Figure 3.35).

The principle of detecting a dip or burst in the specific or nonspecific channel is based on identifying local extrema of the signal and defining the initial and final time points of the event. The data is initially divided into 1,000 ms time frames. For each time frame, the mean and standard deviation of the signal are calculated, and a threshold line is defined based on 3-5 standard deviations above or below the mean. Local extreme points are then identified between the data and threshold lines.

The initial and final time points of the dip or burst are determined by finding intersection time points between the data and a line equal to the mean before and after the local extreme point. The size of the signal is calculated by subtracting the mean value from the value of the extreme point, while the duration is calculated by subtracting the value of the final time point from the value of the initial time point. For coincident detection events, the initial and final time points of the event in the nonspecific signal are compared with those of the burst in the specific signal to determine if there is a time overlap between the two.

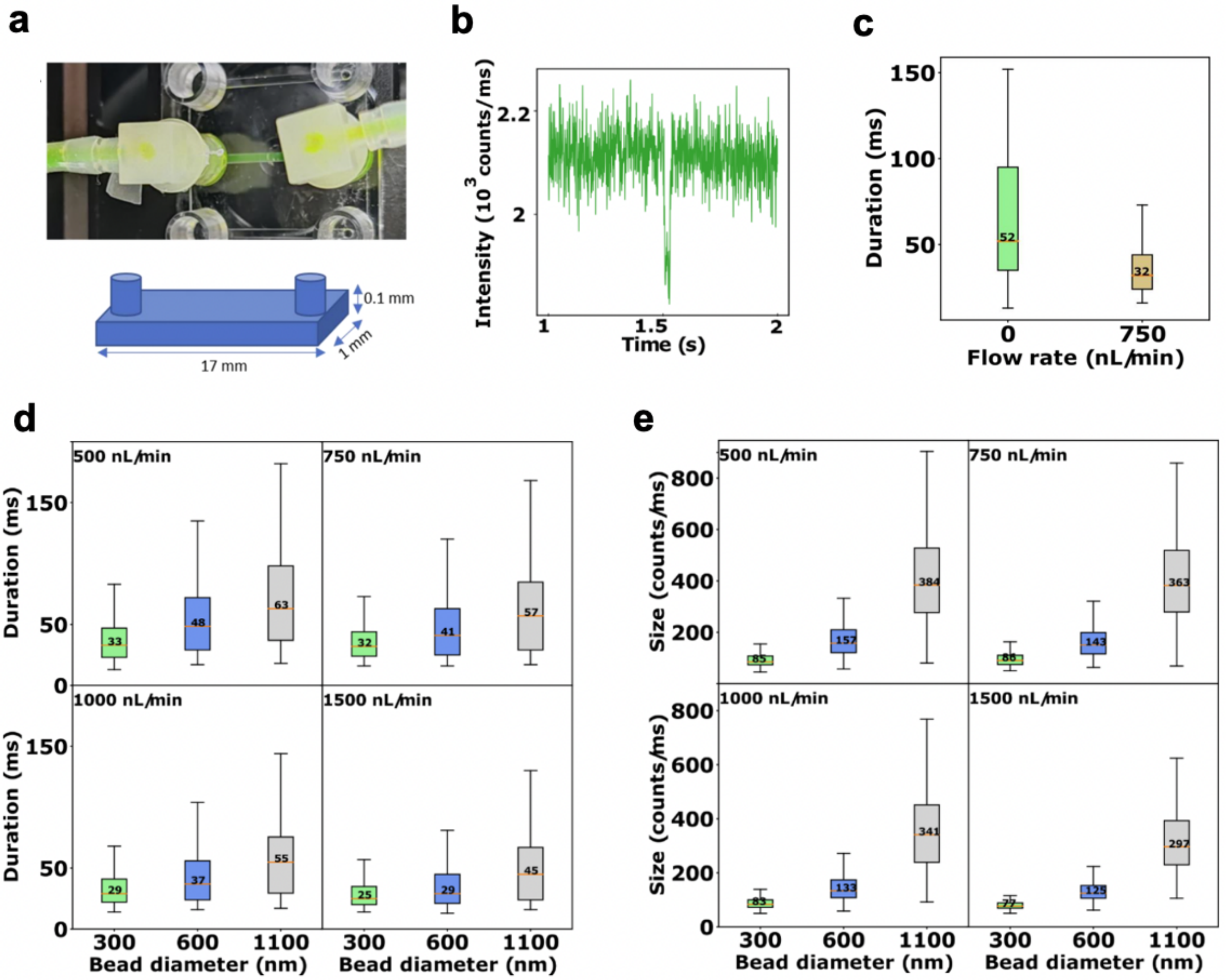

Figure 3.35: Characterization of unspecific signal properties using different bead sizes and flow rates, adapted from Drori et al.: **a** . Ibidi µ-slide VI 0.1, with sample flow through, mounted on top of microscope stage. **b** depicts a representative dip in the nonspecific signal caused by the flow of beads with diameters of 600 nm through the confocal volume in a 1-second time window. **c** Distributions of signal duration of 7-minute measurements of 300 nm beads in the presence of 500 µM fluorescein with either without flow (green, accumulation of 65 detection events from 3 repetitions) or flow rate of 750 nL/min (brown, accumulation of 314 detection events from 4 repetitions). The orange horizontal line represents the median value. The durations (**d**) and sizes (**e**) of the dips in the nonspecific signal from measurements of beads with diameters 300, 600, and 1,100 nm, traversing the confocal volume at flow rates 500, 750, 1000, and 1500 nL/min.

Initially, the concept of detecting fluorescence reduction in the nonspecific signal was tested using unlabeled polystyrene beads with various diameters in the presence of 500 µM fluorescein at different flow rates (Figure 3.35 d,e) within a microfluidic channel featuring a 100x1,000 μm^2 cross-section area, utilizing a costume build confocal microscope (Figure 3.35 a). As polystyrene beads traversed the confocal volume, a temporal reduction in the constant nonspecific signal occurred, resulting in a signal dip (Figure 3.35 b). The sizes and durations of the signal dips per bead diameter were recorded, and their distributions were calculated (Figure 3.35 d,e). Discrepancies between the histograms of sizes and durations of the observed dips confirmed the assay's capability to differentiate between nanoparticles (NPs) of various diameters. At fast flow rates, the variance of dip sizes and durations decreased; however, the distinguishability between the different diameter NPs also diminished. Consequently, a flow rate of 750 nL/min was selected for further experiments, offering optimal discrimination between NPs of different diameters. The lower limit for employing this approach was the detection of particles with a diameter of 300 nm.

As the next step, the assay described above was implemented using the Brick-MIC platform[101] (Figure 3.36). For the assay requirements, the single laser diode with PMT detection variant was utilized. Here, the single laser diode (532 nm wavelength) was used to excite both, the unspecific and specific signals at the same time (see below). Importantly, using photomultiplier tubes (PMTs) instead of the more sensitive hybrid PMTs (as in the setup in Figure 3.35) allows for recording larger signals due to higher detection saturation levels, without the risk of damaging the point detectors. This, in turn, enables the reduction of signal variances for larger signals, thereby enhancing the signal-to-background ratio in the signal change detection procedure. Since a detection scheme based solely on one nonspecific signal does not reveal the identity of a particle, but only its volume, the information from the nonspecific signal was combined with a specific signal from spectrally distinct fluorophores that uniquely tag the NP surface. This produces a specific fluorescence burst as a temporal change in the specific signal (Figure 3.36 c-e). Both the changes in the nonspecific and specific signals are detected simultaneously using two spectrally-separated PMTs (Figure 3.34 and Figure 3.36 b-e). Based on this layout, the detection of coincident pairs of nonspecific and specific signal changes, i.e., a coincident pair of dip and burst, allows the unequivocal identification of a specific NP.

To evaluate this approach, labeled polystyrene beads were initially used, where the red dyes on the beads mimic specific binders, such as antibodies (Figure 3.34 and Figure 3.36 c-e). Using this approach, it was possible to detect coincident bursts and dips (Figure 3.36 e) arising from beads with diameters ≥ 100 nm. There is a well-established direct relationship between the duration of a signal burst and the diameter of a spherical NP[221] (Figure 3.36 c). The burst durations in the specific signal and the dip durations in the nonspecific signal are correlated. Therefore, one can use the duration of either the dip in the nonspecific signal or the burst in the specific signal to assess the NP diameters. Note that only coincident dip-burst detection events are considered as specific NP events.

Importantly, the size of a burst in the specific signal is affected by the concentration of fluorescein interacting with the NP. In contrast, the duration of a burst remains unaffected by the number of interacting dyes. Therefore, to ensure an unbiased assessment of NP diameters, the focus is on analyzing burst durations of coincident signal events in both detection channels. In laminar flow, it is expected that spherical NPs will experience increasing drag as their diameters increase. This, in turn, results in velocity reduction as their size increases, thereby extending burst durations.

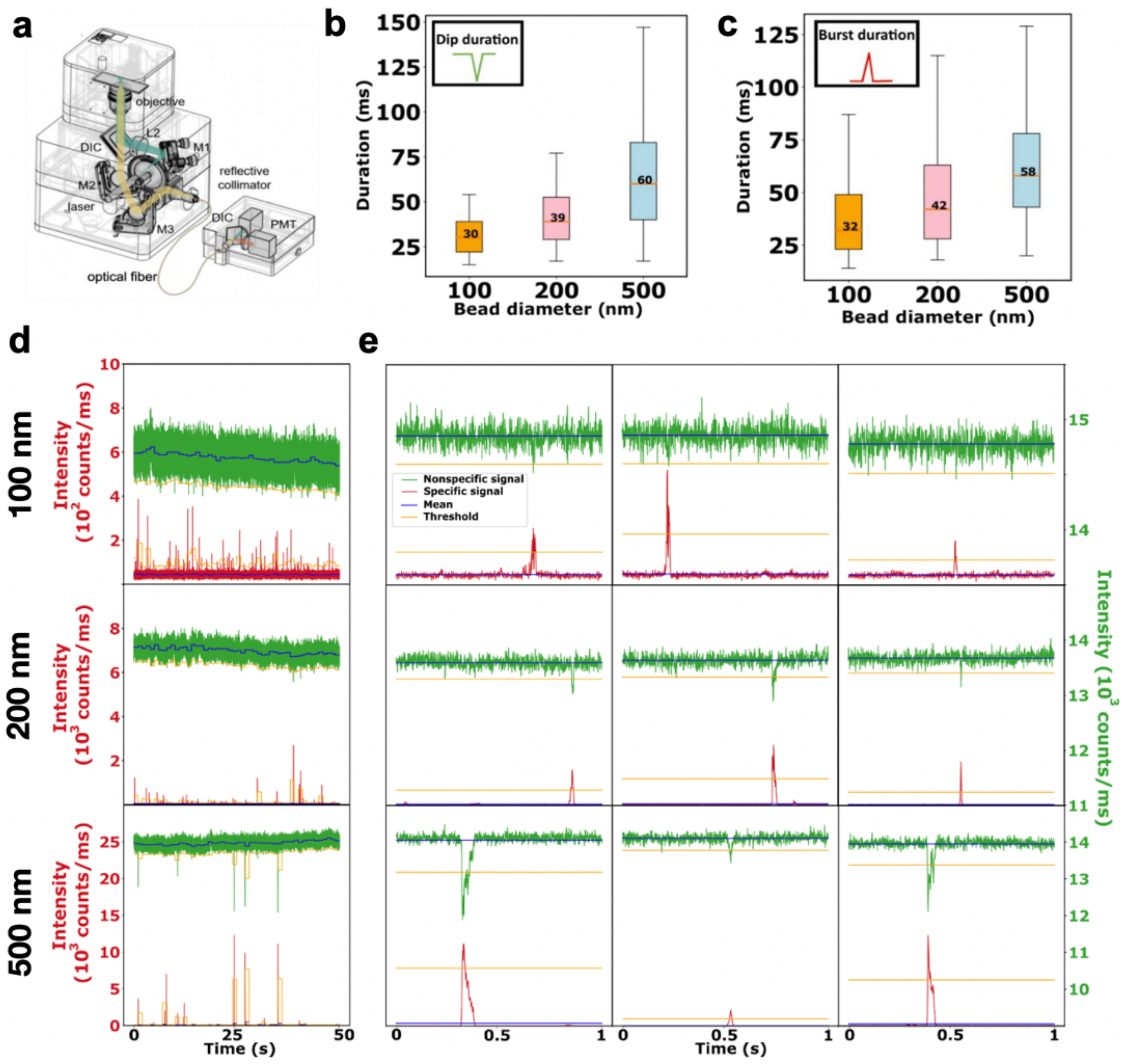

Figure 3.36: Detection of fluorescent beads using the Brick-MIC confocal PMT modality, adapted from Drori et. al.: **a** CAD render of the Brick-MIC confocal PMT modality. The durations of signal dips (**b**) and bursts (**c**) from coincident dip-burst detection events of fluorescent polystyrene beads with diameters of 100, 200, and 500 nm. (accumulation of 37, 114 and 169 detection events from 4, 5 and 5 repetitions of 5 min. acquisitions, respectively). Measurements in **b** and **c** were conducted in the presence of 500 µM fluorescein at a constant flow rate of 750 nL/min. **d** Depicts 50-second time traces from measurements of beads with diameters of 100 nm (upper panel), 200 nm (middle panel), and 500 nm (lower panel). **e** Close-up of measurements in **d** depicting 1-second time trace windows. Blue line indicates the mean of 1-second measurement time, orange line represents the threshold of 3 standard deviations below the mean of 1-second measurement time for dips, and the threshold of 5 standard deviations above the mean of 1-second measurement time for bursts.

The assay was further tested for the detection of bio-nanoparticles samples, starting with paraformaldehyde (PFA)-fixed and neutralized rVSV-ΔG-spike virus particles (Figure 3.37 a and b left panels). The rVSV-ΔG-spike virus is a vesicular stomatitis virus (VSV), genetically-modified to express the SARS-CoV-2 Spike protein, replacing its native G-protein[222]. In contrast to the observed dips in the nonspecific signal for polystyrene beads (Figure 3.36 d and e), virus solutions exhibited bursts in the nonspecific signal, likely due to the integration of free dyes onto the virus (Figure 3.37 a). All measurements using the Brick-MIC platform with virus particles were conducted with 5-minute acquisition times, and the detection event rate was calculated for each measurement.

For the specific detection of rVSV-ΔG-spike, Alexa594-labeled antibodies targeting the SARS-CoV-2 spike protein were employed as the source of bursts in the specific signal, with BSA-fluorescein serving as the source of changes in the nonspecific signal[223]. This approach facilitated the identification of antibody-labeled virus particles via coincident bursts in both the nonspecific and specific signals (Figure 3.37 a). The rVSV-ΔG-spike virus, with a bullet-shaped morphology and dimensions of approximately 70 nm in diameter and 180 nm in height[224], showed burst durations corresponding to spherical nanoparticles with diameters of around 100 nm, indicating a similarity with experimental results. In contrast, the burst durations of PFA-fixed rVSV-ΔG-spike viruses, which tend to cluster, corresponded to spherical nanoparticles with diameters exceeding 500 nm, indicating a deviation from the detection of non-clustered single particles (Figure 3.37 a and b, left and center panels).

The virus detection assay was further tested with PFA-fixed and neutralized SARS-CoV-2 viruses. These viruses, known to be spherical with diameters in the 60-140 nm range[225], exhibited burst parameters similar to beads with 100 nm diameters (Figure 3.37 a and b, right panels).

The virus detection assay successfully detected viral particles and reasonably associated burst signals (specific and nonspecific signals) with corresponding beads sizes. However, the average recorded rate of events was relatively low (8.72 ± 4.32 per 5 minutes), considering the initial particle load of the sample ranging from 10^7 to 10^8 particles per mL (Figure 3.38 a). To adapt the assay for the detection of viruses in patient samples, particularly from bodily fluids like saliva where typical SARS-CoV-2 loads range from 10^3 to 10^7 particles per mL[226], modifications are necessary.

Intertignly, doubling the flow rate to 1500 nL per minute enhances the detection rate by 3 fold (23.6 ± 6.6 per 5 minutes), albeit compromising the signal with shorter burst durations, thereby reducing the detectability of signal changes (Figure 3.38 a, b).

The low detection rate is likely attributable to the large cross-section of the microfluidic channel (100x1,000 m^2), resulting in many particles not traversing through the femtoliter confocal volume. To address this limitation, hydrodynamic focusing was explored within the assay using a commercially available 3-to-1 microfluidic chip. This focusing mechanism involves increasing the sheath flow rate relative to a constant analyte flow rate, resulting in a reduction in the cross-sectional area of the analyte stream[227].

However, it's important to highlight that hydrodynamic focusing requires precise x-y control over the sample holder to accurately position the squeezed analyte stream within the confocal volume.

Unfortunately, this capability was not available with the Brick-MIC sample holder at the time of the study. As a result, the hydrodynamic focusing experiments had to be reverted back to the custom-built laboratory's confocal microscope setup. In this setup, 1000 nm fluorescent nano beads were utilized as the analyte for further experimentation (Figure 3.38).

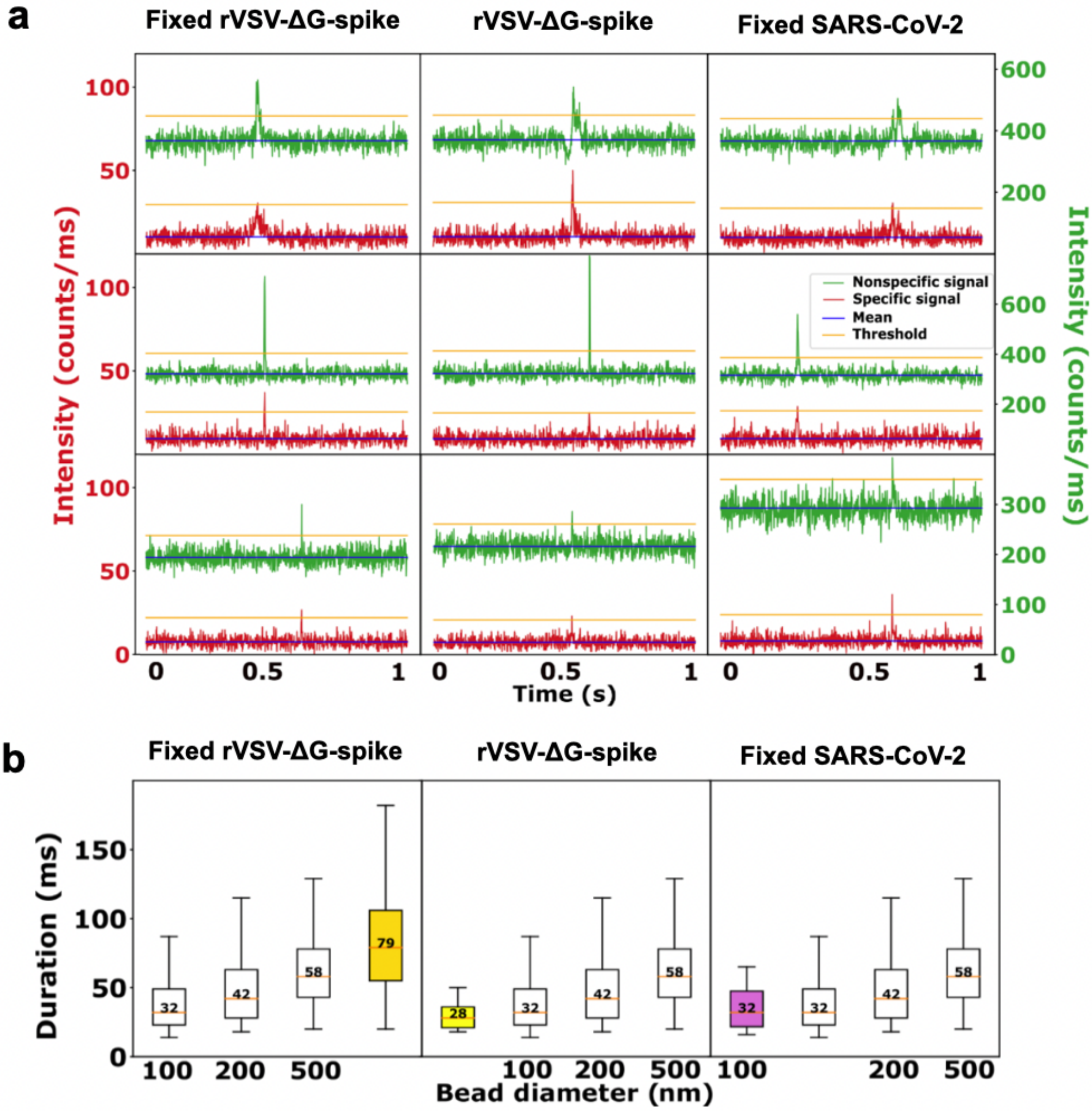

Figure 3.37: Counting single virus detection events, adapted from Drori et al.: **a** 1 s time trace windows of fixed rVSV-ΔG-spike (left panel), live rVSV-ΔG-spike (middle panel), and fixed SARS-CoV-2 (right panel) viral particles. Time traces show coincident bursts, where the green bursts arise from the high-density accumulation of fluorescein on top of the particles detected in the nonspecific signal, and the red bursts arise from fluorescence of the bound antibodies observed in the specific signal. **b** The duration of bursts in the specific signal of coincident burst events of detected viruses from **a** shown together with the burst durations of beads with different diameters. All virus samples were measured in the presence of 10 µM BSA-fluorescein at a constant flow rate of 750 nL/min.

Once the probe volume is successfully focused within the hydrodynamically-focused analyte stream, single detection events with fluorescent beads were counted. This approach significantly enhanced the count rate of detection events, exemplified by an increase from approximately 5 to about 150 detections per 5 minutes acquisition time with an increase in sheath flow rate from 2 to 30 L/min while maintaining a constant analyte flow rate of 1 L/min.

The maximal focusing of the analyte stream, resulting in a reduction from a width of 1,000 m to 30 m, is achieved at a sheath flow rate of 700 L/min.

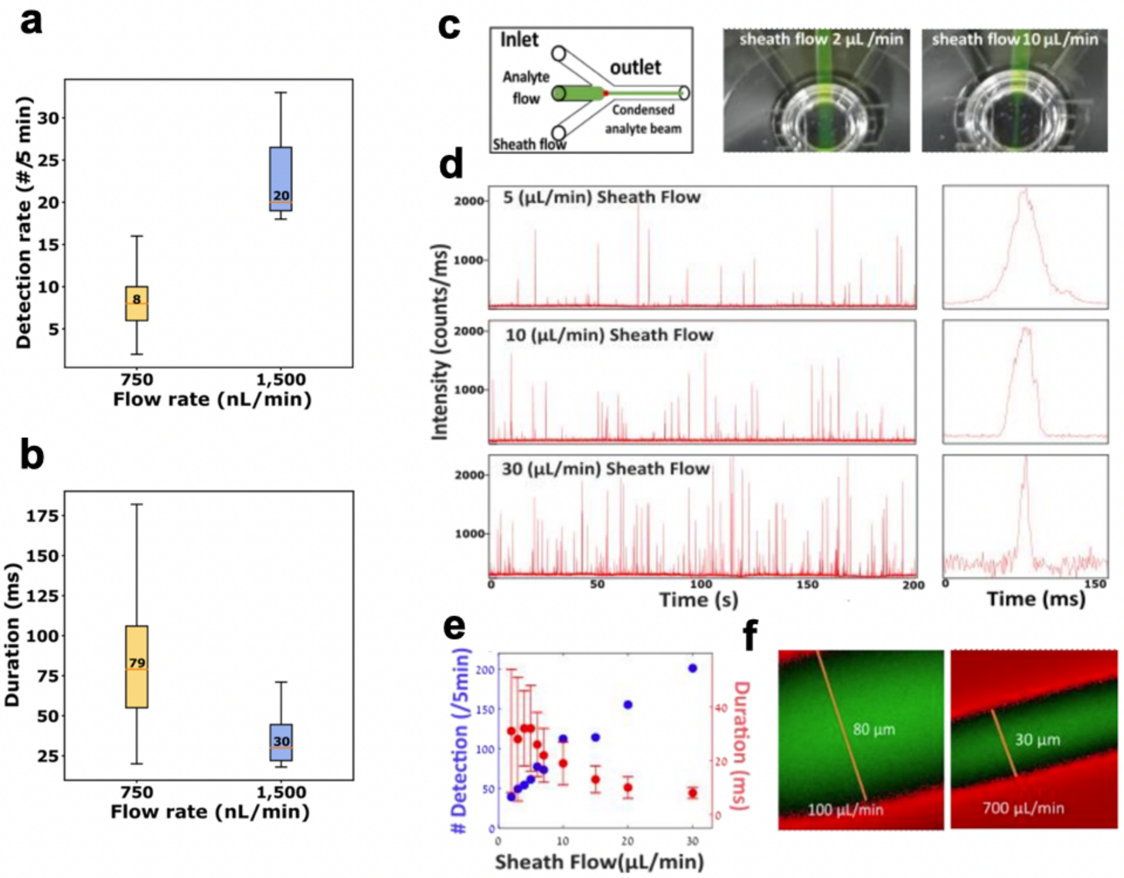

Figure 3.38: Increasing NP detection rate with microfluidic hydrodynamic focusing, adapted from Drori et al.: **a,b** Measurement of fixed and neutralized rVSV-ΔG-spike at different flow rates. **a** Burst durations from a 5 min. acquisition at different flow rates, 750 and 1500 nL/min. **b** Number of events detected from **a**. **c** Illustration of a 3-to-1 microfluidic chip (left panel). The analyte stream (green) is focused at the junction between the analyte flow channel (central channel) and two peripheral sheath flow channels (lower and upper channels) at higher flow rates relative to the analyte flow rate. The probe volume (red dot) is placed at the center of the hydrodynamically-focused analyte. The middle and right panels show pictures of the 3-to-1 microfluidic chip with the analyte flow rate at 1 L/min while being focused by the sheath flow at 2 L/min (middle panel) and 10 L/min (right panel). **d** Time traces of fluorescent 1,000 nm latex beads flowing at a rate of 1 μL/min measured with sheath flow rates of 5 μL/min (upper panel), 10 μL/min (middle panel), and 30 μL/min (lower panel). The right panel shows a close-up of the time traces demonstrating a representative burst duration shortening as the sheath to analyte flow rate ratio increases. **e** The average number of detected single particle bursts (blue) and their durations (red) as a function of the sheath to analyte flow rate ratio. **f** The higher the sheath to analyte flow rate ratio, the more focused the analyte stream becomes. Sheath flow rates 100 (left) and 700 (right) μL/min.

3.5 Blue-Green smFRET: A Cost-Effective and Minimalist Instrumentation Approach[§]

The design of smFRET instrumentation has increasingly centered on a framework that reflects the state-of-the-art in the field, with Alternating Laser Excitation (ALEX) systems as a key feature[93,94,98,114,228]. ALEX requires two lasers, which are modulated by fast triggering electronics to alternate the excitation sources. Additionally, high numerical aperture objectives, expensive single-photon avalanche diodes (SPADs), and fast counting electronics—used for counting the photons detected by the SPADs—are the components of choice for enhancing detection efficiency and temporal resolution[98,190]. However, these features significantly contribute to the high cost associated with state-of-the-art smFRET setups[188,190,191,196,189]. More importantly, they may not be critical for many smFRET applications, particularly for users focused on application-driven studies. In such cases, FRET is often employed not as an absolute ruler but as a tool to monitor relative biomolecular movements and interactions[127,39,229,230,231,232,233,115,234]. For instance, in drug screening assays, the primary questions typically focus on the behavior of the target: Is there binding? How strong is the interaction? Does the target adopt an open, closed, or intermediate conformational state? These requirements highlight the need for accessible and application-specific instrumentation. For these reasons, it may be helpful to take a step back and pursue good science with less complexity and cost.

There remains significant potential for instrumental trade-offs that could align more closely with the needs of application-oriented users. One such trade-off could be the elimination of the ALEX system, which, while enabling the sorting of different labeled sample species and providing the ability to correct raw data for accurate FRET efficiency values[93,94], may not be necessary for many users, given that the extra information provided by state-of-the-art instrumentation may not significantly contribute to the questions being asked. It is also common for smFRET data to be presented uncorrected in papers until absolute distance values are required. In fact, the majority of smFRET use cases, particularly in routine applications, do not involve data correction for precise FRET efficiency values[127,39,229,230,231,232,233,115,234]. Instead, instruments are commonly used for biomolecular characterization under various conditions, as previously mentioned, where the calculation of absolute distances is relevant only once the system is well understood or when real distances are required. In these cases, the presence of an ALEX system does not provide substantial additional information unless data processing is involved[161,235]. The sorting of different labeled species could be achieved using alternative methods, such as the double-channel burst search (DCBS) algorithm[92], which processes the photon streams digitally and through software, rather than using ALEX, which filters the photon streams directly in an analog manner.

[§] This section presents preliminary data (unpublished) from the master's thesis of Jorge R. Luna Piedra, titled "1D smFRET Through the Usage of the Brick-MIC Microscopy Platform", submitted in November 2024. The work is being continued and prepared for publication under the tentative title "A Minimalistic Single-Molecule FRET Setup: Can it Get Even Cheaper?" with a preliminary author list including Gabriel G. Moya Muñoz, Jorge R. Luna Piedra, Pazit Con, Siyu Lu, and Thorben Cordes. My contributions included conceiving and designing the microscope layout, planning the experimental design, and evaluating the data. The data and figures presented were adapted or replotted from Jorge R. Luna Piedra's master's thesis.

Building on the Brick-Mic FCS modality, which already incorporated essential elements for advancing this new project, previous studies demonstrated the system's capability for single-molecule detection using a single CW laser and two photomultiplier tube detectors (PMTs) (figure 3.18)[101]. This setup enabled the detection of freely diffusing FRET-DNA samples (Cy3B-ATTO647N) in both donor and acceptor channels with a 532 nm CW laser excitation. While FRET events were recorded, the acceptor channel's poor detection efficiency in the red spectrum (figure 3.39) resulted in low apparent FRET efficiencies (E = 0.12), even for samples with short interdye distances. Consequently, the system lacked a sufficient FRET efficiency dynamic range, making it challenging to distinguish between samples with even large interdye distances (e.g., 8 and 23 base pairs).

However, by shifting the acquisition wavelength windows to regions with higher sensitivity for the PMTs in use (between 500–600 nm), fine-tuning experimental conditions, and selecting appropriate dye pair combinations, there is significant potential to improve the detected photon budget[236]. This approach could enable the measurement of FRET efficiencies with an unprecedentedly low entry cost in terms of instrumentation. While the quality of the data may be compromised compared to state-of-the-art systems, this trade-off offers a cost-effective solution for many application-driven studies, where precision may be less critical.

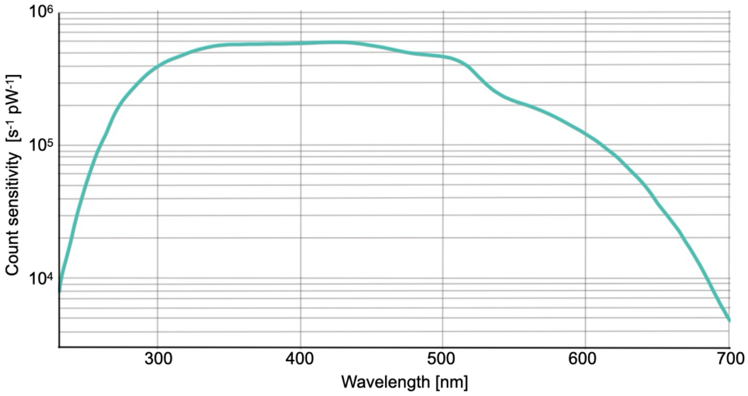

Figure 3.39: Detection efficiency of the Hamamatsu PMT counting head model H10682-210.

The modifications made to the system included, first and foremost, the use of an affordable, generic USB-powered 488 nm CW laser pointer (488-30-1235-BL, Q-LINE). Due to its undesirable laser profile, the laser was coupled into an optical fiber using the excitation layer of the ALEX modality (figure 3.24), as opposed to being used directly, as in the case of the FCS excitation layer modality (figure 3.18). Additionally, the DIC mirrors and emission filters were switched out accordingly to match the new excitation and emission wavelengths (DIC_{ex}: ZT491rdc, Chroma; DIC_{em}: ZT543rdc, Chroma; Donor channel: FF03-525/50, Semrock). To maximize photon collection in the acceptor photon-stream, a notch filter (NF488-15, Thorlabs) was employed solely to block reflected or scattered light from the excitation laser, enabling the collection of photons across the full emission spectrum of the acceptor, unlike a band-pass filter that restricts detection to a narrower wavelength range (figure 1.10). While this approach enhances the overall photon collection, it also introduces the potential drawback of increased cross-talk by capturing photons from the donor. Nevertheless, the primary objective was to maximize the photon budget in the acceptor channel, addressing the poor dynamic range observed in previous setups. Data were collected using an affordable USB counter module, previously used with the FCS modality, along with the same Python-based acquisition software. This software features the ability to save recorded data per photon-stream in binned format (1 ms bins) in a CSV file. Apparent FRET efficiencies were calculated bin-by-bin using a DCBS-like algorithm[92], which filtered FRET events from donor-only bursts when a burst had signal in both photon-streams, and applied a minimum photon threshold for each channel independently.

Initial tests were performed using DNA-FRET-based samples with an 8 bp interdye separation, testing two dye combinations: Alexa488-Alexa594 and Alexa488-ATTO542, both with similar Förster radii ($R_0 \approx 6, \text{nm}$). Photon streams from both samples were analyzed using a DCBS-like sorting algorithm with thresholds set to 10 and 25 *counts*/ms in the donor and acceptor channels, respectively. Single FRET populations were obtained, yielding mid-to-high FRET efficiencies of 57% for Alexa488-Alexa594 and 66% for Alexa488-ATTO542 (Figure 3.40).

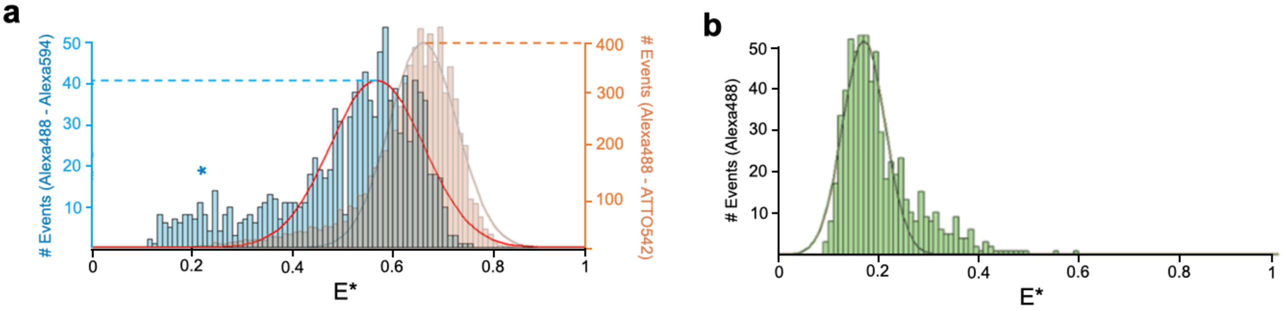

Figure 3.40: Apparent FRET efficiency histograms measured under 488 nm excitation at 100 μW laser power. (a) FRET efficiency histograms comparing DNA labeled Alexa488–Alexa594 (blue) and Alexa488–ATTO542 (orange) dye pairs with an 8 bp interdye separation distance, analyzed using a DCBS-like algorithm where the thresholds where set to 10 and 25 *counts/ms* in the donor and acceptor channels, respectively. The blue star indicates donor photobleaching events observed in the Alexa488–Alexa594 sample. (b) Leakage contribution of an Alexa488-only sample under 488 nm excitation at 100 μW laser power, analyzed using an APBS-like algorithm, where the threshold in the acceptor photon-stream was lowered to 10 *counts/ms* .

The DCBS sorting algorithm successfully captured FRET species while effectively filtering out donor-only populations. Additionally, the leakage (Lk) contribution, measured with a donor-only DNA sample and using an All-Photon-Bust-Search-like algorithm (APBS)[89,91], was considerably high at around 16% (Figure 3.40 b). This was not unexpected, given the use of the notch filter in the acceptor channel, compared to the typical 6% leakage observed in state-of-the-art smFRET setups that use band-pass filters[98]. The two dye combinations showed significant differences in performance, with Alexa488-ATTO542 demonstrating clear superiority over Alexa488-Alexa594. Alexa488-ATTO542 recorded 10-fold more events (400 compared to 40) and exhibited fewer donor photophysical effects, presumably donor bleaching events, as indicated by the non-Gaussian shape and long tail in the FRET histogram distributions toward low FRET efficiency values. For this reason, Alexa488-ATTO542 was selected as the primary dye combination for the setup characterization.

The optimal laser power was estimated based on the power dependence of the dye combinations, aiming for peak performance in terms of the highest photon collection, which is reflected in the higher number of FRET events recorded while avoiding photophysical effects that often widen and distort the FRET distribution, as mentioned above. The laser powers tested were 100, 200, and 500 µW, respectively (Figure 3.41). The lowest laser power used showed a Gaussian-shaped FRET histogram with the narrowest distribution ($\sigma E \approx 0.06$). Similarly, using 200 µW excitation resulted in a Gaussian-shaped FRET histogram with minor photophysical effects, causing a slight increase in distribution width ($\sigma E \approx 0.068$), but more importantly, it recorded 2-fold more FRET events (18.6k events compared to 6.5k events) in comparison when excited with 100 µW laser power. The highest laser power resulted in a widened, non-symmetrical distribution ($\sigma E \approx 0.087$), presumably due to donor photobleaching, which also explains the lower number of FRET events recorded (12.4k events). Therefore, 200 µW was determined to be the optimal laser power for balancing photon collection and minimizing unwanted photophysical effects.

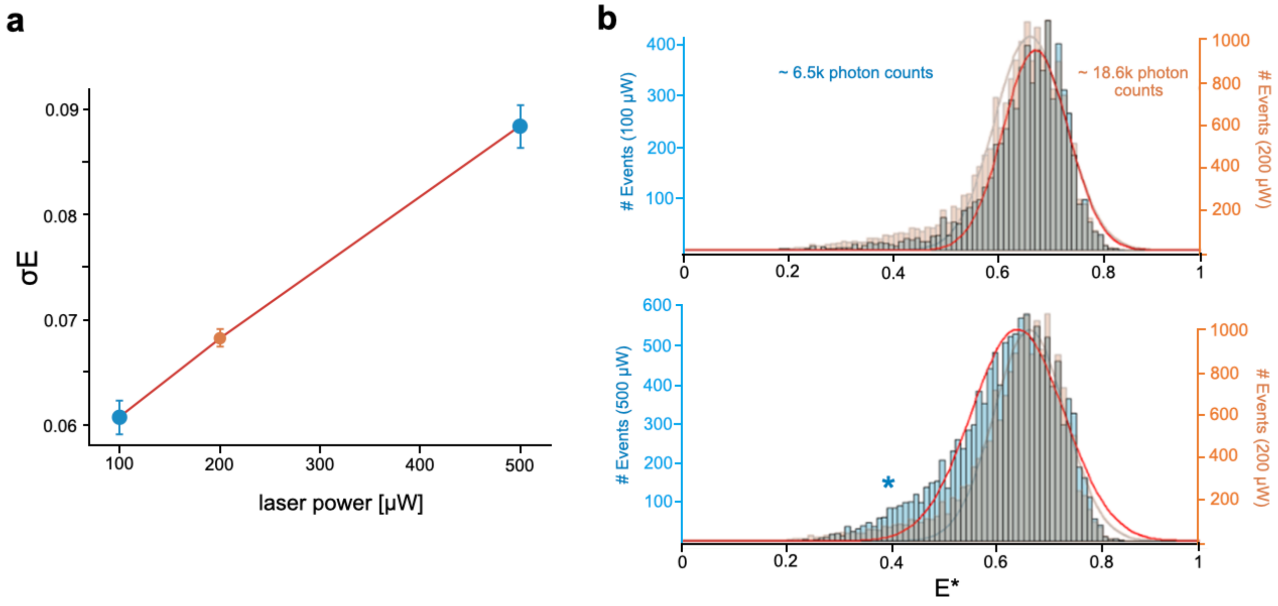

Figure 3.41: Laser power dependency of Alexa488–ATTO542 dye pairs: (a) shows the relationship between FRET efficiency standard deviation (σE) and the laser power used. Error bars represent technical triplicate measurements. (b) Apparent FRET efficiency histograms comparing excitation at 100 μW (blue) and 200 μW laser power (orange) in the upper panel, and 200 μW (orange) and 500 μW laser power (blue) in the lower panel. The blue star indicates donor photobleaching events observed at 500 μW excitation.

The remaining photophysical effects observed when using 200 µW laser excitation were examined using FCS (Figure 3.42 a). The autocorrelation FCS curve revealed a significant triple-state fraction of approximately 33%, indicating a corresponding loss in energy transfer rate. To prevent this, seven photostabilizers were tested with varying outcomes. Trolox, for example, worsened the effect by increasing the triple-state fraction to 40%, while other candidates, such as (Dimethylaminomethyl)ferrocene (DAMF) and (+)-Sodium L-ascorbate (ascorbic acid), reduced the triple-state fraction to 15% and 19%, respectively (figure 3.42 b, c and e). The reduction in the triple-state fraction was also reflected in the molecular brightness of the donor, which increased from $17k\ \frac{counts}{s \cdot mol}$ with no photostabilizer used to $37k\ \frac{counts}{s \cdot mol}$. DAMF was chosen as the photostabilizer due to its slightly better performance compared to ascorbic acid. It reduced the triplet-state fraction by 25% compared to ascorbic acid and improved molecular brightness by 5%.

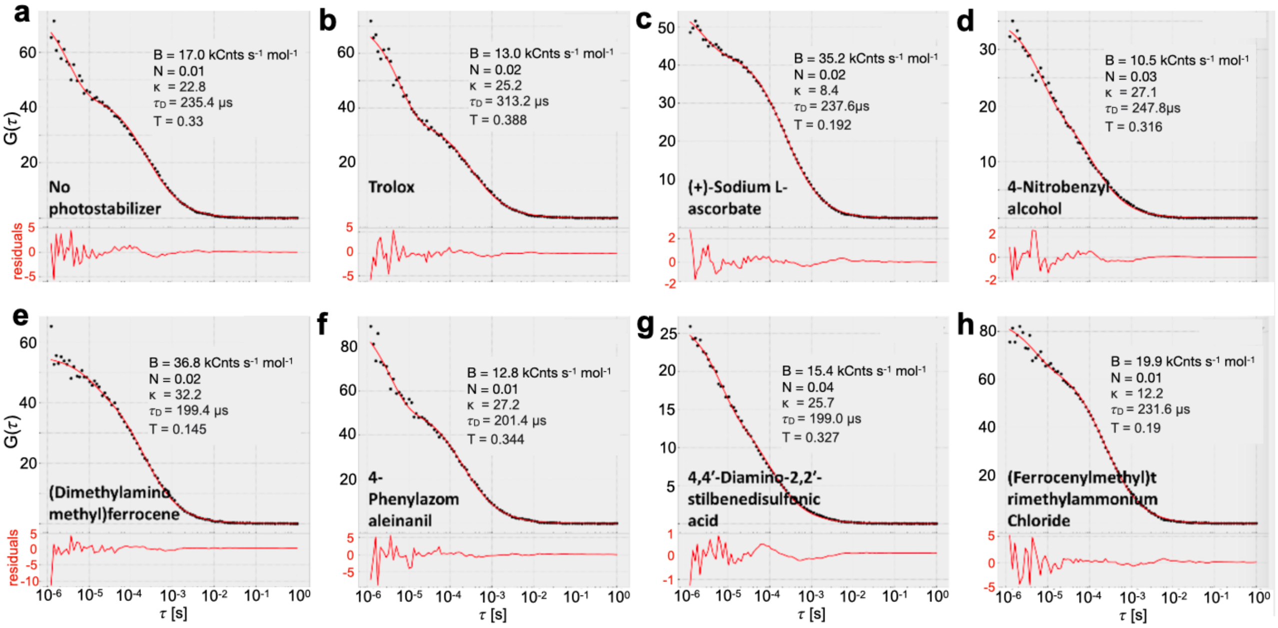

Figure 3.42: Photostabilizer screening of Alexa488 using FCS under 488 nm excitation at 200 μW laser power. Fit parameters include molecular brightness (B), number of molecules (N), geometry parameter (κ), diffusion time (τ_D), and triplet fraction (T). Photostabilizer concentrations used when measured where 1 mM, for e) (DAMF) and h) (FTAC) the final concentrations where set to 100 µM

By depopulating the triplet state of Alexa488 more efficiently with the use of DAMF, the energy transfer pathway was favored, as reflected by the 2-fold increase in FRET events recorded compared to when no photostabilizer was used under 200 µW laser power excitation[49] (Figure 3.43). Additionally, this reduction in the triplet state fraction minimized photobleaching events, which occur when prolonged triplet state transitions facilitate reactions with molecular oxygen, causing irreversible chemical damage to the fluorophore. This effect is reflected as a non-Gaussian distribution stretched toward lower FRET efficiencies, resulting from donor bleaching occurring mid-acquisition.

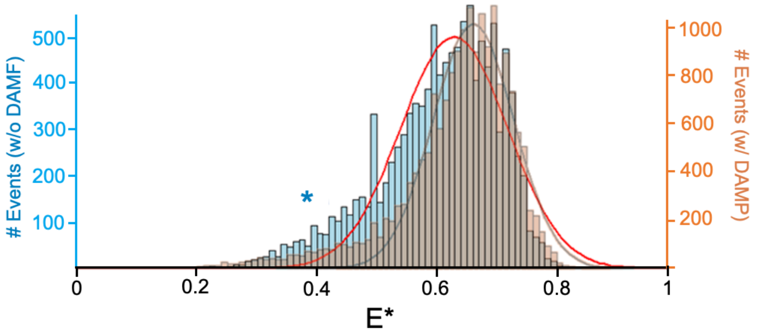

Figure 3.43: FRET efficiency histograms comparing the effects of (Dimethylaminomethyl)ferrocene (DAMF) as a photostabilizer: Apparent FRET efficiency histograms comparing the effects of DAMF (orange) as a photostabilizer and no photostabilizer (blue) for a DNA-Alexa488–ATTO542 sample. The samples were measured under 488 nm excitation at $200\,\mu W$ laser power. The blue star indicates donor photobleaching events observed under conditions without a photostabilizer.

These optimized conditions were further tested by measuring a series of FRET-DNA samples with varying inter-dye distances, including 8, 18, and 23 bp (Figure 3.44). Measurements of individually prepared homogeneous samples yielded clear, Gaussian-shaped distributions with distinct apparent FRET efficiencies as expected: 66% for the 8 bp sample, 42% for the 18 bp sample, and 35% for the 23 bp sample. Importatly, these FRET efficiencies where clearly distinguishable when measuring a heterogeneous mix of two samples combined between the 8bp and 18bp sample (figure 3.44 a, lower panel). This was also the case when mixing all three samples thogherte, the 8 and 18 bp samples where clearly distinguishable, however this was not the case for the 18 and 23 bp sample. Here the 23 bp sample population merged with the 18 bp resulting in a wider FRET population (figure 3.44 b, lower panel). The underlying reason for this may be attributed to the limited detection efficiency of the acceptor photon-stream and the DCBS-like algorithm. In this algorithm, a FRET event is only considered when a burst contains signals in both photon-streams and surpasses the minimal photon thresholds imposed (10 $counts/ms$ in the donor channel and 25 $counts/ms$ in the acceptor channel). Samples with higher interspaced dye separations reduce the emission rate of the acceptor, emitting fewer photons, which results in lower FRET efficiency. However, this reduction in emitted photons, combined with the poor detection efficiency of the acceptor channel, may have prevented the detection of more FRET events, as the photons did not surpass the threshold imposed by the algorithm, resulting in fewer events being recorded. Consistent with this, the systematic reduction in the number of recorded FRET events from high- to low-FRET samples, despite using the same sample concentrations for all measurements (Figure 3.44b), supports this explanation. The 8 bp sample yielded 1000 events, the 18 bp sample yielded 500 events, and the 23 bp sample yielded only 130 events.

Despite challenges in detection sensitivity, the shift from green-red to blue-green FRET with a single CW laser enabled us to achieve detectable FRET events at a fraction of the cost. While state-of-the-art smFRET setups require expensive modulable lasers (≈€4,000 each), APDs (≈€8,000 each), and specialized electronics (≈€2,000), our Blue-Green FRET system, using a €35 laser pointer, two PMTs

(€1,000 each), and a USB counter module (€400), totals just €2,435. This cost-effective approach demonstrates that reliable FRET data can be obtained without high-end components, making it accessible for labs with limited resources.

While less sensitive than traditional setups, the Blue-Green method still provides reliable measurements, offering a promising, budget-friendly alternative for FRET research. These results represent the first steps toward more accessible FRET experiments, with further improvements and advancements to come.

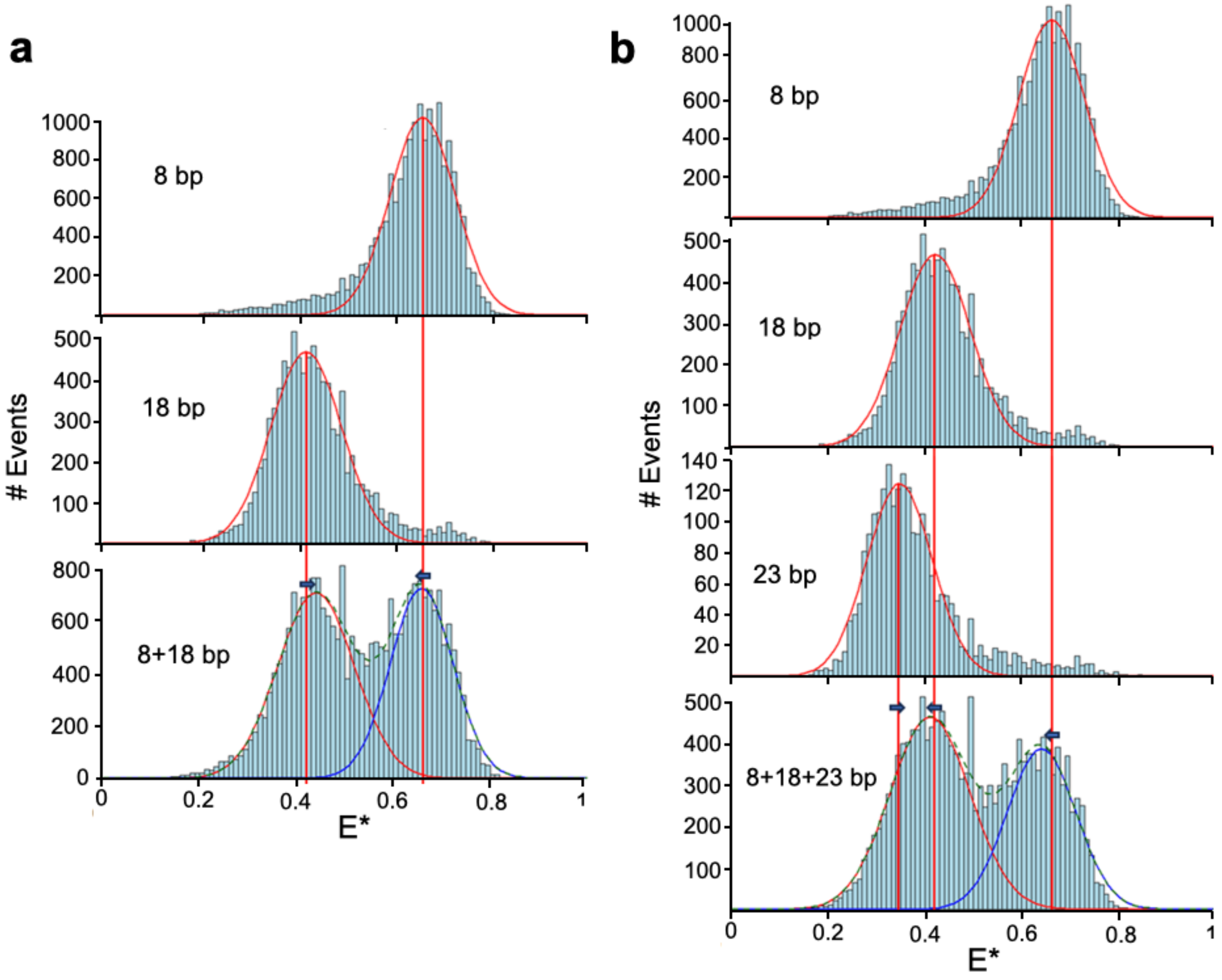

Figure 3.44: FRET efficiencies of Alexa488–ATTO542 dye pairs at different interspacer distances, shown separately for each sample and combined in a single experiment. All samples were measured under 488 nm excitation at 200, μW laser power with the addition of 1 mM (Dimethylaminomethyl)ferrocene (DAMF). (a) shows measurements of individual interspacer samples: 8 bp (upper panel) and 18 bp (middle panel), as well as the combined measurements of both sample recorded simultaneously (lower panel). (b) presents measurements for the same interspacer samples as in (a), along with an additional 23 bp sample. The lower panel depicts the combined measurement of all three samples.

4

Discussion & outlook

Progress in optical instrumentation has enabled the detection and study of individual molecules and of a macromolecule, providing a valuable tools to comprehend life at the fundamental building block. This achievement originates not only from enhancements in the spatial and temporal resolution of optical systems but more importantly from a profound comprehension of fluorophores and fluorescence. The comprehensive studies of proteins with smFRET in this thesis not only confirmed prior understanding of the technique, but also uncovered unexpected fluorescence anomalies, likely stemming from interactions between proteins and dyes, while shedding light on critical and intricate steps of data analysis. Furthermore, discrepancies in smFRET assays were found to be primarily setup-independent. To allow a broader use of the techniques for researches with a non-physics background, we intruduced a user-friendly and 3D-printed microscopy platform called, Brick-MIC. The versatile modular design of Brick-MIC enabled the execution of smFRET experiments, fluorescence correlation spectroscopy (FCS) assays, and single molecule localization microscopy with data quality comparable to the state-of-the-art. Its 3D-printed nature facilitated rapid prototyping tailored for specialized applications, as envisioned for an experimental and rapid virus detection assay. Importantly, Brick-MIC democratizes access to state-of-the-art single-molecule spectroscopy and super-resolution microscopy for non-specialized users, while also serving as an experimental platform for the advancement of fluorescence-based methods, oriented towards upcoming applications.

4.1 Accuracy and reproducibility of protein-based single-molecule FRET experiments

The multilaboratory study, involving 19 participants, yielded significant insights into the precision and accuracy determination of distances in proteins. Despite the inherent challenges associated with studying proteins, the study achieved a precision in FRET efficiencies comparable to that reported for double-stranded DNA samples. The study showcased the capacity of smFRET to accurately determine distances between different conformational states of proteins. Notably, all experiments were conducted using well-established techniques and analyzed independently with freely available software, achieving overall good agreement between the different outcomes but importantly highlighting crucial and potential pitfalls in data analysis and interpretation. The study reduced variables linked to the sample and the dyes of choice, leaving only a direct comparison of the different confocal setups and the chosen laser powers for each group. The established data analysis procedures were then tested individually to correct for all the remaining setup-dependent variables. Of the 19 laboratories taking part in the study, three labs were not able to create the necessary data quality mainly because of setup-specific properties and measurement procedures. The problems reported were minor: for one lab, a nonfunctional red laser impeded the stoichiometric filtration of the different sample populations, leading to the missing of the vital ES-histograms used for determining the needed correction factor. The second lab used an inappropriate acceptor filter, resulting in poor detection efficiency in its photon-streams and thus reporting a γ-factor of 0.09, which consequently affected the determination of accurate FRET values. In the case of the third lab, the individual populations could not be clearly separated in the data due to photoblinking and/or photobleaching that may be potentially caused by the high laser powers used. The reported problems were overall minor and easy to fix from the setup perspective. However, from the procedure side, it shed some light on inadequacies with the chosen laser power. Nonetheless, this issue is easily fixed, as photophysical effects are readily detectable in ES-histograms, displaying characteristic tails from FRET populations, thereby making the separation of individual FRET populations challenging. Choosing adequate laser powers would address the issue. However, since the lab was not able to identify photophysical effects in their procedure, smFRET assays might potentially necessitate a consensus on optimal laser power settings and photophysical effects identification.

The remaining 16 laboratories reported accurate FRET efficiencies, notably with a high level of consensus despite the diversity of setups. The mean standard deviation of ± 0.06 was largely influenced by systematic errors in the data analysis procedures, as evidenced by the comparison of the FRET efficiency changes ($\langle E_{holo} \rangle - \langle E_{apo} \rangle$), which reduced the spread by roughly twofold. Despite the strong agreement among the results from different laboratories, this observation indicates potential areas for improvement in the data analysis procedures. It might be necessary to implement control tests for each step in the analysis procedure to ensure that the correction factor is functioning as intended. For example, in the case of leakage (lk) and direct excitation (dir), a sanity check would involve testing whether the mean of the donor-only and acceptor-only populations equals zero in E and S, respectively, after their application. For β testing whether the mean of the FRET-populations equal 0.5 would provide further validation of the correction factor's effectiveness in accurately representing the FRET efficiency. Although the suggested sanity checks may improve marginally the reliability and systematic errors of the analysis procedure, the correction factor γ was found to be the most crucial and sensible of all, describing the majority of the total FRET efficiency uncertainty reported among the participating laboratories. The determination of γ requires at least two or a ladder of multiple static FRET populations on an ES-histogram to be accurately established and hence its correct determination depends by a large margin on the sample itself. The observed experimental uncertainty ΔE was well described by a relative uncertainty of $\frac{\Delta\gamma}{\gamma} = 23\%$ corresponding to a γ uncertainty of

0.07. Importantly, it was observed in error propagation simulations that the relative uncertainty $\frac{\Delta\gamma}{\gamma}$ was mostly independent in a big range of different absolute γ and β values, starting to be affected by extreme values (< 0.1 and > 3) and that the relative uncertainty $\frac{\Delta\gamma}{\gamma}$ was mostly dependent on the dynamic range of the sample and thus on separation of their FRET populations.

By refining analysis methodologies and emphasizing key parameters such as γ, the accuracy of FRET measurements could be enhanced, thereby achieving higher reproducibility with improved precision and accuracy. As a rule of thumb, higher FRET uncertainty can be expected if the determined γ and β values are extreme. Screening for alternative fluorophore pairs could help improve such values. From the sample perspective, if the dynamic range of the sample is limited and the difference between the FRET populations ($E_2 - E_1$) is less than 10%, the use of a calibration ladder, for example, DNA labeled with different interspaced fluorophore pairs, would be a recommended practice for determining the γ-factor.

Further, reproducible interdye distances with a precision of 3Å and an accuracy of 5Å against structural models of MalE were obtained from accurate FRET efficiencies. This result was in high agreement with findings observed in dsDNA samples[120]. This positive result was notable, especially considering that dsDNA provides a consistent, homogeneous chemical environment for each labeling position, unlike the variable dye environment encountered in proteins[237,238,239,240].

However, this achievement was made possible by identifying key interactions between fluorophores and specific protein-variant surfaces through fluorescence anisotropy assays, thus incorporating these interactions into the in-silico calculations (ACV). Despite the improved precision and accuracy against structural models of MalE, the result exposed potential pitfalls in interpretation, protein design, and dye selection: without fluorescence anisotropy assays that evolved to produce additional single cysteine variants, fluorophore-protein interactions wouldn't be identified, potentially leading to misinterpretation of the results. Although the improved ACV calculations found better agreements with FRET-inferred distance determinations, they do not address the presence of fluorophore-protein interactions in the experimental approach initially. Therefore, as in the case of the γ-factor determination, it would be advisable to additionally conduct smFRET assays using a different pair of fluorophores with different molecular properties, such as hydrophobicity or chemical structure, to gain a deeper understanding and mitigate potential effects of fluorophore-protein interactions on the experimental results.

4.2 Evaluating smFRET against comparative distance measurement methods

Biophysical methods are essential in life sciences, but they are vulnerable to unforeseen artifacts, complicating data interpretation. Comparing various tools with similar outputs can refine the understanding of a biosystem's ground truth. Here, smFRET-derived protein distance measurements were compared and cross-validated with Pulsed Electron-Electron Double Resonance Spectroscopy

(PELDOR/DEER) and Anomalous X-ray Scattering Interferometry (AXSI), alternative biophysical methods that also rely on the use of site-specific-labels to determine distances inter alia. Overall, the results of the comparative study were consistent across each method, indicating good agreement. However, also weaknesses and challenges associated with each method were identified, offering comprehensive insights into potential pitfalls for each technique.

Overview of analytical challenges in bulk vs. single-molecule data acquisition procedures.

The low sensitivity in both Pulsed Electron-Electron Double Resonance Spectroscopy (PELDOR/DEER) and Anomalous X-ray Scattering Interferometry (AXSI) results in the need for high concentrations of the sample (approximately 20 μM and approximately 200 nM, respectively) and long measurement times, which can extend up to several hours. In contrast, the single-molecule sensitivity and high temporal resolution of smFRET enable the observation of dynamic biomolecular processes in real time. The nature of imaging each molecule one by one additionally makes the acquired data easier to handle by already sorting each species and conformational state out on an ES-histogram, thus providing a real-time preview of the acquired data without needing to process it. Exactly this aspect was the major challenge in AXSI measurements. The poor labeling efficiency of the gold nanoparticle labels and the bulk measuring nature of the method made it difficult to differentiate scattering signals from double, single, and non-labeled species. Although the resulting distance distribution after data analysis showed predominantly the expected inter-dye distances, it was accompanied by additional peaks in the distance distribution, making its interpretation challenging. These additional peaks were corrected by first measuring the scattering contributions of single and non-labeled proteins and, secondly, subtracting these scattering contributions from the raw sample based on their respective population percentages. In the case of PELDOR/DEER, although it's also a bulk method, it exclusively detects interactions between probe or pulse labels, which, given its dipole-dipole nature, must be in close proximity, and thus, present within the same biomolecule. However, as in the case AXSI, PELDOR/DEER necessitates complex data processing to obtain distance distributions.

Temporal resolution.

The high sensitivity of single-photon detectors used for smFRET instruments leads to an enhanced temporal resolution, requiring less acquisition time to achieve a satisfactory signal-to-noise ratio. The time resolution of smFRET by now reaches microseconds to nanoseconds, which represents fast biomolecular dynamics[241,242,243,244]. While PELDOR/DEER experiments are almost always conducted on bulk frozen samples, limiting the ability to study real-time molecular motions directly, dynamic processes can be inferred indirectly by interpreting the width of distance distributions or by employing freeze-quench experiments. In contrast, anomalous X-ray scattering interferometry holds promise for its high spatial resolution; it's an emerging method used primarily for absolute intramolecular distance determination in biomolecules and not for real-time observation of dynamic processes.

Potential for sample distortion and/or deterioration.

Every method can cause artifacts e.g., by sample damage or influences. SmFRET, as well as AXSI assays, have the advantage of operating within a wide temperature window, e.g. at room temperature or cell culture conditions. On the other hand, PELDOR/DEER experiments are conducted with frozen sample solutions, inevitably influencing the kinetics, binding affinities, and dynamics of the sample. Furthermore, cryoprotectant additives are commonly employed to prevent crystal formations. Yet, as evidenced by experiments of certain MalE variants, these additives can impact the sample, potentially yielding misleading results.

Further, AXSI assays come with the drawback of potential radiation damage to the sample. The intense X-ray radiation employed in anomalous X-ray scattering experiments can induce structural alterations or degradation in the sample. In line with this, smFRET assays entail continuous exposure to the excitation laser, which can lead to blinking or even photobleaching of fluorophores. As observed in the multilaboratory study, this can result in wider FRET populations, making the distinction between multiple FRET populations challenging. More importantly, such photophysical effects are difficult to differentiate from fast biomolecule dynamics.

Another aspect to consider when choosing smFRET is its low sample concentration, which in some cases can be incompatible with protein complexes which might dissociate. Holoenzymes tend to have lower binding affinities between each protein subunit and thus tend to be unstable at picomolar concentrations.

Labels

Fluorescent dyes, heavy atoms, and paramagnetic spin labels serve as distance indicators from which spatial relationships and interactions within biomolecules are derived. Due to the diverse physical phenomena in which they operate, these labels vary considerably in their shape, size, and composition. These differences ultimately impact the determined outcome of their distance distribution.

Paramagnetic spin labels and gold nanoparticles, utilized in PELDOR/DEER and AXSI respectively, are generally smaller and possess shorter linkers in comparison to fluorescent dyes. In smFRET, the orientation and rotational freedom of fluorescent labels attached to biomolecules are crucial as they influence the efficiency of energy transfer between them[245,246,247,61]. Similarly, in PELDOR/DEER experiments, the spin labels attached to biomolecules must have some rotational freedom for accurate distance measurements. Constraints on label rotation can impact the orientation-dependent dipolar interactions between spin labels, thereby affecting the precision of distance measurements[248]. However, the differences in size and linker length play a significant role in their distance determination. Distances measured with PELDOR/DEER were on average about 5 Å shorter than those measured with smFRET, as the labels do not protrude as far from the globular surface of proteins. Additionally, the broader occupancy radii of the fluorophore accessible volumes results in a wider distance distribution of $\pm 5\mathring{A}$ compared to $\pm 3.5\mathring{A}$ in PELDOR/DEER (Figure 3.8). Gold nanoparticles used in AXSI are highly resilient in their environment and are orientation-independent, theoretically not requiring a linker to the protein's surface. As a result, AXSI offers absolute distance measurements between the labels, rather than average distance distributions as seen in smFRET and PELDOR/DEER. However, the absence of a linker and the spherical geometry of the labels may have contributed to the low labeling efficiency with cysteines that have hindered solvent exposure. Additionally, due to the rigidity and lack of movement of the gold nanoparticles, it is plausible to assume hindered protein motion or even disruption in their secondary structures.

Moreover, a notable advantage of AXSI and PELDOR/DEER is their utilization of two identical label, which can be further employed to measure multiple distances within the same experiment or biomolecule without requiring modifications to the equipment or data analysis procedures[249]. In contrast, smFRET necessitates a minimum of two distinct fluorescent dyes, which may exhibit varying labeling efficiencies on the target. While smFRET can be expanded to include multimeric measurements with the inclusion of a third fluorophore, this approach is technically demanding[250]. Further, the wide range of various fluorophores and their different properties, such as hydrophobicity and charge, along with their large accessible volumes, make them prone to interact with local chemical surface environments of proteins. Local pH changes, electrostatic interactions, and hydrogen bonding can affect fluorophores, altering their quantum yield, rotational freedom, or even inducing spectral shifts[61]. This, combined with stoichiometric labeling, may lead to the existence of different Förster radii within the same sample using the same fluorophore pair. To detect such artifacts from the acquired data is difficult, if not impossible, without a comparative control. For instance, in the case of the MalE variant K29C-S352C, discrepancies were observed from the expected distances computed with the theoretical crystal structure model using AV (Figure 3.11), or HiSiaP variants 175/228 and 112/175, which were not in agreement with results obtained with PELDOR/DEER (Figure 3.8). In both cases, it was demonstrated through time-resolved fluorescence anisotropy the inherent mobility of specific fluorophores at specific labeling residues and even at different conformational states of the protein. In the case of the HiSiaP variant 175/228, agreement between PELDOR/DEER and smFRET was achieved by changing the dye pair to others with different chemical properties (Figure 3.9).

Equipment

Anomalous X-ray Scattering Interferometry (AXSI) is indeed one of the most complex and expensive methods in biophysical research, both in terms of instrumentation and accessibility. Unlike many other techniques, AXSI relies on synchrotrons, specialized facilities housing cyclic particle accelerators. These synchrotrons generate X-ray beams by accelerating electrons along a closed-loop path, producing high-energy photons suitable for scattering experiments.

Synchrotrons are massive facilities that require substantial infrastructure and maintenance. They typically consist of large experimental halls housing beamlines, which are pathways for the X-ray beams to reach the experimental stations. The equipment within these experimental stations includes X-ray sources, detectors, and sample handling systems, all of which are complex and expensive to operate.

Access to synchrotron facilities is limited and highly competitive, further contributing to the complexity and expense of AXSI experiments. Researchers must submit proposals and undergo a peer-review process to gain access to beamline time, often requiring collaborations with experts in the field and extensive planning.

PELDOR/DEER experiments typically require specialized Electron Paramagnetic Resonance (EPR) spectrometers with pulsed capabilities, which are commercially available. The EPR spectrometer serves as the core instrument for PELDOR/DEER experiments. It generates and detects microwave pulses used to manipulate and probe the electron spin states of paramagnetic centers in the sample. Microwave sources provide the microwave pulses necessary for manipulating the electron spin states during PELDOR/DEER experiments. These sources are typically high-frequency generators capable of producing precise and adjustable microwave pulses.

Operating these instruments remains challenging, requiring familiarity with EPR spectroscopy techniques, instrument setup, parameter adjustment, and data analysis.

As for the cost, commercial EPR spectrometers with pulsed capabilities are commonly priced in the range of hundreds of thousands of euros. Constructing an EPR spectrometer from scratch, particularly one with pulsed capabilities for PELDOR/DEER experiments, is a highly complex and challenging work that demands expertise in multiple disciplines, including physics, engineering, electronics, and spectroscopy. While theoretically possible, most laboratories and institutions opt to purchase commercial instruments due to the complexity and cost-effectiveness of building custom systems.

Single-Molecule Förster Resonance Energy Transfer (smFRET) offers a more accessible approach to studying biomolecular interactions. SmFRET setups are generally more compact compared to the two other techniques. Confocal fluorescence microscopes used in intensity-based smFRET experiments involve the addition of two alternating modulated lasers with different wavelengths for donor and acceptor excitation, as well as the addition of two single-photon counter detectors for donor-acceptor emission recording. SmFRET setups have recently become commercially available, typically priced in the hundreds of thousands of euros. However, it's common for specialized optical labs to choose to construct their own setups, taking advantage of the reduced number of parts required to adapt microscopy bodies, which significantly reduces costs to even below one hundred thousand euros. This relieves to some extent the availability of smFRET microscopes; however, their home-built nature, combined with the high precision in light paths required in confocal microscopes, requires periodic and extensive tedious adjustments and alignment procedures that necessitate expertise and training. Additionally, the customization process involved in constructing smFRET setups can lead to variability in performance and stability, potentially requiring ongoing maintenance and troubleshooting. Despite these challenges, the flexibility and cost-effectiveness of home-built smFRET systems make them a valuable option for research labs.

4.3 Democratization of single-molecule detection setups

The multi-laboratory smFRET study demonstrated strong agreement with independently accurate FRET determinations across various home-built confocal setups. Importantly, the study revealed that challenges associated with smFRET procedures primarily originated from systematic errors in the established data analysis procedure rather than being dependent on the setup or the user during data acquisition. This crucial recognition served as a pivotal starting point for identifying the factors influencing accessibility for non-smFRET specialists:

Clearly, reaching a more rigid consensus on the established data analysis procedure is crucial to reduce user-dependent errors. By doing so and incorporating additional checkpoints in the data processing, automating the entire procedure becomes feasible. This could lead to the generation of accurate FRET values in real-time, thereby further reducing the entry barrier for non-smFRET specialists.

Despite the consistent outcomes observed across various confocal setups following data analysis, their maintenance requires expert knowledge and are to less accessible to non-optics specialists[188,195]. Further, even specialist labs can suffer from accessibility to the equipment since it is often a bottleneck in terms of availability and the high demand from multiple users. This issue can be attributed to how currently home-built confocal setups are constructed, which are often designed for various applications rather than being dedicated to a single purpose. Consequently, the setups incorporate numerous components tailored for specific applications, thereby increasing their complexity and size, often requiring a separate specialized room for operation.

The introduction of the Brick-MIC platform represents a significant step forward in terms of setup accessibility and was designed with a focus on addressing the majority of the points listed above:

In the past decade, advancements in 3D printing technology, marked by increased precision, affordability, and user-friendliness, have transformed it into a hobby for enthusiasts without expertise, and a common additional service offered in copy shops. Consequently, the 3D printed nature of Brick-MIC, aligns with the widespread accessibility and familiarity of 3D printing technology, expanding its reach to such setups worldwide.

The core concept behind Brick-MIC was to prioritize a single application and modality while allowing flexibility to switch between different microscopy modalities through its interchangeable modules, with a strong emphasis on addressing one application at a time. This guiding principle resulted in a reduction in required parts, simplifying complexity and leading to a significant decrease in size and costs. Particularly for the confocal modalities, the design eliminated or replaced additional components, diverging considerably from the orthodox layout of conventional confocal setups. Specifically, regarding the workings of the pinhole, which in a conventional setup involves at least three parts: a tube lens to focus the emission beam through a pinhole, followed by a second lens to focus the filtered light beam onto the point detectors. This assembly is the most critical part in terms of alignment precision, requiring precise focusing of the light path to hit a 50 μm target twice consecutively, making it challenging to align and a weak point in terms of stability. In the Brick-MIC PMT detection variant, the entire pinhole assembly was streamlined into a single continuous unit. This unit comprises two collimators interconnected by an optic fiber, eliminating the need for alignment procedures between the three components. For the APD detection variant, the entire assembly was simplified to a single lens. This lens focuses the emission beam directly into the detectors, utilizing the small aperture of the detectors as the pinhole. Consequently, the alignment procedure was simplified to a single variable, focusing solely on hitting the first element of the pinhole assembly. This simplification made the alignment procedure suitable for automation, facilitated by a mirror mounted onto a motorized x-y piezo mount.

Furthermore, the reduction in size significantly shortens the light path from several meters in traditional setups to approximately 30 cm, thereby enhancing the strength and stability of the Brick-MIC platform. Despite the lower material stiffness of PLA (with a modulus of elasticity of 3.5 GPa\cite{atakok2022tensile}) compared to steel (200 GPa\cite{spittel20094}), it proves suitable for the task. Recent advancements in 3D printing filaments now offer more robust alternatives, such as carbon-fiber-reinforced PLA, carbon-fiber-reinforced nylon, and polycarbonate composites, which significantly enhance mechanical strength and thermal stability, making them ideal candidates for higher-performance applications.

In general, all tested Brick-MIC modalities demonstrated remarkable and comparable data quality, yielding results similar to those obtained with the lab's microscope assemblies, and providing a higher level of user-friendliness. However, while the platform has taken a step forward in usability, it still presents obstacles for non-optic specialists. These challenges stem from incomplete automatic alignment procedures and the unconventional design and assembly of the platform, highlighting the need for further revision:

As mentioned, only the emission layer of all modalities possesses auto-alignment capabilities, leaving the excitation layer to be aligned manually. On one hand, the ALEX modality is more forgiving regarding minor misalignment in the excitation layer because the method relies solely on capturing photons from the diffusing sample rather than on the shape of the confocal volume. The emission layer compensates for any misalignment in the excitation layer and aligns to the mispositioned excitation focus. However, for FCS experiments, precise alignment of the excitation path is crucial, as the method relies on several assumptions regarding the shape of the confocal volume, which can otherwise lead to inaccurate results. Although misalignment can be detected through fit parameters (κ factor, which describes the ellipticity of the confocal volume), fine-tuning of the excitation layer is still necessary. In the case of the epi-fluorescent modality, misalignment in the excitation layer can pose challenges, particularly in experiments requiring precise and uniform field-of-view illumination, such as photophysics studies.

The modular design of the platform facilitated rapid interchangeability between modalities and easy access to replaceable components such as filters. However, in practice, this concept introduced some stability issues. The interlocking mechanism between the modules relies on friction and pressure, similar to the mechanism used in Lego building blocks. Consequently, the modules are subjected to constant mechanical stress, leading to an initial rapid loss of stability and misalignment when the setup is freshly assembled. However, over time (approximately 30 minutes), the assembly reaches an equilibrium in terms of inter- and intra-module stress forces, allowing for long-term measurements. Therefore, while the intended rapid interchangeability between modalities theoretically takes only minutes, in reality, it takes longer until measurements become feasible, which requires high mechanical stability. One potential solution could be to utilize the platform's auto-alignment feature, incorporating periodic automated fine-tuning and alignment checks during measurements. Moreover, the epi-fluorescent modality, which relies on bolts rather than friction for assembly, exhibited significantly enhanced stability compared to other configurations. Therefore, implementing this approach would be beneficial. However, concerning practicality, the interchangeable modality feature of Brick-MIC does not offer significant advantages for users, as real-world scenarios rarely require this capability. Particularly for non-optic specialists, the motivation to interchange parts may be low due to concerns about incorrect handling, damage, and data reproducibility. Therefore, for certain applications, it would be beneficial for end-users to have multiple Brick-MICs, each tailored for a specific application, rather than needing to switch between modalities. The modularity feature of Brick-MIC adds value in terms of flexibility and rapid prototyping when the platform is used for method development, allowing for the rapid testing of new configurations, parts, or ideas by creating new modules within the platform without designing a completely new setup, it also enriches the Brick-MIC toolbox by potentially incorporating new modalities.

Of all the modules, the sample holder presents the most significant challenges in terms of usability and stability. The sample holder operates using a manually operated commercially available translational stage in combination with a fully 3D printed pinion and rack system, restricting its movement to only a z-axis displacement. This setup functions sufficiently for diffusion-based assays, where no x-y translation of the sample is necessary, and variations in z-dependent signals are compensated for using a water immersion objective. However, imaging surface-immobilized samples revealed significant limitations of the system: The micrometer head of the translational stage has poor resolution, as a complete rotation of the head displaces the stage by 500 microns. Consequently, users are left with only about 2 degrees to precisely position the sample in the focal plane of the objective, demanding fine motor skills from the user. Furthermore, it was noted that the sample holder drifted over time toward the objective, necessitating continuous refocusing. However, the z-drift also exhibited time dependency, becoming less prominent over time. Once equilibrium was reached, it became feasible to image for up to 10 minutes without requiring refocusing. It is evident that the current state of the sample holder does not meet the criteria of immobilized molecules or appliocations such as FLIM imaging. Implementing at least an auto-alignment system, similar to those found in common TIRF microscope assemblies, is a minimum requirement to elevate this modality to a user-friendly category. In line with this, automated x-y translation is also desirable, not only for navigating through the sample but also for extending scanning capabilities for the confocal modalities.

The unconventional design of the platform brought both benefits and challenges to the individual modalities, which impacted their usability and performance in various ways:

Confocal modality with PMT based detection

The pinhole design, comprising two collimators interconnected by an optical fiber, in combination with the large apertures of the PMTs (8 mm in diameter), made this assembly by far the most robust in terms of stability. Additionally, the capability to adjust the size of the confocal volume by simply interchanging the optical fiber for different core sizes is a major advantage compared to conventional confocal microscopes, where exchanging the pinhole would require extensive and tedious realignment of the assembly. However, while the modality demonstrated single-molecule detection capabilities, the poor detection efficiency of the red photon-stream made it impractical for reliably measuring FRET efficiencies (50-fold less efficient compared to the green channel).

Modifications to adapt the modality to operate with wavelengths more suitable for the PMTs' detection efficiency range have already been implemented and are detailed in Section 3.5 (blue-green smFRET). This shift towards blue-green detection now enables more reliable FRET efficiency measurements and significantly lowers operational costs, given that PMTs are typically 4 to 8 times cheaper than APDs. Furthermore, coupling the complete emission into an optical fiber extends the modality's adaptability, facilitating integration with other devices that accept optical fiber input. This includes its expansion into a fluorimeter by replacing the detection box containing the PMTs with an optical fiber-coupled spectrometer. This configuration has been preliminarily tested and shown to work (see Outlook section).

Confocal modality with APD-based detection

The data quality of the ALEX modality was comparable to that of the laboratory-built ALEX microscope, with practically indistinguishable differences between the two when computing accurate FRET values. However, this outcome was expected, as both pieces of equipment share the same components for the most part, with the exception of a different tube lens, APD manufacturer, and red filter. However, its design, where the pinhole is directly replaced by the aperture of the APDs, introduced an additional alignment challenge not found in conventional confocal layouts. This issue arises from having two different point detectors, resulting in two independent pinholes for donor and acceptor emissions, respectively. As a consequence, both confocal volumes can vary in shape and positioning, leading to mismatches in the overlap between donor and acceptor detection volumes. While both detectors shared the same tube lens, aperture size, and x-y autoalignment capabilities, the only independent variable requiring manual calibration is the z-positioning of both detectors. Initial measurements demonstrated this issue as wider FRET populations compared to the laboratory's confocal setup when measuring the same sample. This issue could have been addressed through an extensive iterative fine-tuning of the z-positioning of both detectors through measurements until the width of the FRET populations became comparable to that of the reference measurements. This issue could potentially be addressed by fixing the APDs in their z-positioning directly from the CAD design. However, the high tolerances required raise questions about the 3D printer's resolution and accuracy for the task. Consequently, the current design opted to place the detectors on translational stages rather than fixing them. However, given the challenges associated with the current design, it is worth experimenting with fixed detectors instead of relying solely on speculation regarding the capabilities of the 3D printer.

Epi-fluorescence wide-field modality

The Epi fluorescent modality, the most recent addition to the Brick-MIC platform, addressed construction issues observed in previous modalities, thereby enhancing stability through minor changes such as fixing modules with screws, using reinforced PLA filament with carbon fiber, and positioning the tube lens directly under the dichroic mirror in the excitation layer rather than in an intermediate layer as in the Confocal ALEX modality, consequently reducing complexity and shortening the light path. However, as previously mentioned, the sample holder, whose design remained unchanged from the first modalities, proved to be the weak point in terms of stability. The tendency of the sample holder to drift towards the objective until reaching equilibrium meant that refocusing using the translational stage of the sample holder was not feasible, as it would require reaching equilibrium again. This issue was addressed with a non-optimal approach involving the adjustment of the z-positioning of the CMOS camera, which is mounted on a translational stage, akin to the mounting of the APDs in the ALEX modality. This approach enabled imaging of immobilized samples for extended periods but at the expense of compromising the proper operating distance of the objective. As a result, this leads to a reduction in its numerical aperture, loss in z-dependent signal due to the nature of oil immersion, resulting in reduced resolution, and may also be accompanied by other aberrations. Furthermore, the CMOS camera suffered from overheating, commonly resulting in higher noise levels and promoting the appearance of hot pixels. Nevertheless, although these issues are addressable for future builds, it was possible to resolve nanostructures using PAINT or dSTORM approaches with a reasonable localization precision of approximately 30 nm FWHM for dSTORM and 65 nm FWHM for PAINT.

Insights from Brick-MIC: Overview and Learnings
The Brick-MIC microscopy platform has proven to be a valuable and promising upcoming option by enhancing the accessibility of state-of-the-art microscopy techniques, primarily through its focus on cost-effectiveness and usability. More importantly, the broader lessons of the Brick-MIC project lie in identifying key factors contributing to the growing gap between non-optic specialists and state-of-the-art technology. This disparity may stem in part from current microscopy know-how conventions and mindsets, which opens a discussion on rethinking how microscopy can be done and reconsidering other alternative approaches. The Brick-MIC project demonstrated that alternative manufacturing techniques, different optical layouts, and a focused approach on individual applications can significantly reduce the entry barrier for non-microscopy specialists. The experimental nature of this approach has revealed various unique challenges associated with each modality. However, the knowledge gained has provided valuable insights, which have engineering solutions that will be addressed in future iterations and advancements of the platform.

Additionally, focusing on equipping application-oriented users with state-of-the-art microscopy techniques has the potential to uncover new opportunities for implementing the technology in other fields, identifying new solutions, problems, and additional needs of the setups. This, in turn, will directly drive advancements in microscopy across different fields.

4.4 Exploring new scientific fields

Direct virus detection

The 2019-2022 SARS-CoV-2 pandemic presented unprecedented challenges to global health and prevention systems[216]. In my view, these systems were unprepared, revealing a lack of flexibility in scientific methods, facilities, and qualified personnel. The pandemic particularly highlighted the limited capabilities of developing countries and the selfishness of developed nations, which raced to purchase equipment and supplies for themselves. This approach is unsustainable, especially during a pandemic.

During the SARS-CoV-2 pandemic, the Brick-MIC demonstrated its strengths in flexibility and rapid assay prototyping. In a real-case scenario, a specific virus detection test was conceived from scratch, tested, and able to detect the pathogen in less than two years. This achievement was significant, but the key value revealed by the Brick-MIC project in emergency scenarios was its low cost, easy access, portability, and ease of use in terms of instrumentation and assay workflow procedures. It was designed so that every country could implement it, regardless of its economic situation, infrastructure, and availability of qualified personnel.

Starting with the instrumentation itself, where the assays were initially tested in a full-scale custom-made confocal microscope. Besides the high costs involved and the expertise required to operate such a device, the sheer size and scarcity of similar setups worldwide would not meet the requirements needed in an emergency situation.

Additionally, conducting validation tests with actual SARS-CoV-2 viral particles would be impractical, as it necessitates high biohazard safety laboratories. Integrating a full-scale custom-made confocal microscope into such a facility is challenging due to limited lab space and the extensive training required for personnel. This is particularly problematic considering the experimental phase of the assay and the competing priorities of these facilities, especially during a pandemic scenario.

Furthermore, working in high biohazard safety laboratories poses another challenge: any item brought into the facility must be rigorously decontaminated or destroyed, typically through incineration, to prevent any potential pathogen from exiting the facility. This adds another layer of impracticality, especially in terms of the potential loss of expensive equipment for a single experiment, or the feasibility of disposing of large instrumentation such as microscope bodies and optical tables.

The Brick-MIC platform addresses the issues listed above, starting with its accessibility in terms of its 3D printable design, straightforward assembly, and ease of use. This implies that anyone worldwide could set up the device, provided they have access to a 3D printer and the necessary optical parts. Even in cases where these requirements are unavailable, its tiny footprint makes it portable and ready to use in any situation of need.

Although this was not detailed in the results, this feature of Brick-MIC was successfully tested in a collaborative study with the Lerner Lab. In this study, two identical setups (one without optical elements) were transported to Israel in common luggage on an economy flight. The team at Lerner Lab successfully assembled and learned how to operate Brick-MIC independently with the provided instructions and minimal supervision. This positive outcome suggests that Brick-MIC could be effectively used in high biohazard safety laboratories, where specialized personnel can be trained outside the biohazard zone and conduct experiments independently without the support of an optics specialist.

Additionally, the Brick-MIC variant built for this application-oriented study was specifically designed to be cost-effective (less than €10,000), which would not be a significant financial sacrifice if the device were to be incinerated or otherwise disposed of after use in a high biohazard environment. This affordability, combined with its portability and ease of use, makes Brick-MIC a promising tool for widespread, rapid deployment in emergency situations.

Further, the sample preparation and assay workflow were meticulously designed to ensure that individuals with no lab experience could handle the samples using a straightforward two-step process. The original idea was to have a test tube containing Alexa594-labeled antibodies targeting the SARS-CoV-2 spike protein, mixed with a highly concentrated Fluorescein-BSA solution (approximately 100 µM in 50 µL volume).

The first step involves adding approximately 500 µL of saliva (or a similar fluid) to the test tube and mixing it. After a specified incubation time, the analyte must be transferred into a syringe and placed in a perfusion pump. This design ensures that the assay can be performed with minimal technical expertise.

Although the results were encouraging, having detected SARS-CoV-2 virus particles directly, the data revealed numerous issues and significant room for improvement for it to become a viable tool and compete with existing virus detection methods. The most predominant issues were the low counting rate of viral particles and the wide size distribution inferred from the duration of bursts and dips caused by particles traversing the detection volume. Both issues relate to the large cross-sectional area of the microfluidic channel (100x1,000 m^2) compared to the detection volume, which is approximately 1 fL. This discrepancy means that the vast majority of viral particles will miss the confocal volume, reducing the count rate, and particles that partially pass through the confocal volume will generate varying burst/dip durations. Consequently, measuring times have to be extended considerably to gather enough data to make a statistically meaningful conclusion, which could take up to hours. This makes the assay non-competitive in terms of time efficiency compared to other methods, such as PCR.

The solution to this was implementing hydrodynamic focusing, which employs a commercially available 3-to-1 microfluidic chip. This focusing mechanism involves increasing the sheath flow rate relative to a constant analyte flow rate, resulting in a reduction in the cross-sectional area of the analyte stream. This approach elevated the count rate by 30-fold and consequently reduced acquisition time. However, the addition of hydrodynamic focusing added considerable complexity in terms of usability. Hydrodynamic focusing requires fine-tuning of both the sheath flow and the analyte flow, as well as precise positioning of the microfluidic chip relative to the confocal volume, which, in my opinion, is a step back from the user-friendly workflow of the assay.

It is worth mentioning that the measures taken were implemented to fine-tune the original principle of the assay, which involved identifying a virus particle by a specific signal from the labeled virus and correlating this signal with the size of the viral particle. This was originally intended to be inferred from the size and duration of the signal dip in the nonspecific channel caused by the dispersion of highly concentrated fluorescein molecules when the virus particle traversed the confocal volume. Accordingly, the analyte flow rate was fine-tuned to maximize the size and duration of the dips without losing inferred particle size determination due to excessively high flow rates. However, experiments showed that viral capsids incorporated fluorescein molecules, which produced a burst rather than a dip in the nonspecific channel. This unforeseen interaction could not be prevented even by using BSA-labeled fluorescein instead of freely diffusing fluorescein. Additionally, the data showed that the burst durations in the specific and nonspecific channels were not distinguishable from each other, and therefore, either burst duration was used to infer the viral particle size.

In my opinion, by omitting the original inferred viral particle size determination, the assay remains robust enough to detect specific virus particles without any changes, although it may potentially increase the false positive detection rate: The Alexa594-labeled antibodies targeting the SARS-CoV-2 spike protein do not produce any signal change in terms of dips or bursts in the nonspecific channel. If the signal of the labeled antibodies correlates with any signal change in the nonspecific channel, it is a good indication of a potential positive hit.

Therefore, significantly increasing the analyte flow rate would elevate the viral count rate at the expense of not being able to determine its size from signal durations. The new limitation is to address how specific the binding of the antibody is toward its target, which would require extensive control experiments with real analyte compositions, such as patient saliva. Another idea would be to establish a two-step screening assay, where an initial quick screen is performed under a high analyte flow rate to explore if signals appear cross-correlated in both channels. Having acquired enough evidence of possible infection, the flow rate can then be reduced to the point where viral sizes can be inferred from signal duration.

Despite the unforeseen results of the assay, the most significant takeaway from this study was the rapid development and deployment of the Brick-MIC platform for an application-oriented assay. Notably, the device was independently assembled and operated by another team, who successfully utilized the acquired data. This experience highlights the platform's adaptability and user-friendly design, promoting its potential application in diverse fields of science.

This success encourages further exploration in various areas of science and the exploration of potential solutions through the implementation of single-molecule spectroscopy assays. Such initiatives could enable application-oriented researchers with no background in optics to effectively use advanced microscopy techniques. This approach not only widens the accessibility of sophisticated microscopy tools but also encourages innovation and collaboration across disciplines.

4.4.1 CW Blue-Green smFRET: Challenges, Insights, and Future Directions

The Blue-Green Brick-MIC approach demonstrates a cost-effective alternative for single-molecule FRET (smFRET) studies, transitioning from traditional green-red systems to a simplified setup that is approximately 10 times less expensive.

This optimized system successfully measured DNA-FRET samples with inter-dye distances of 8, 18, and 23 bp, yielding FRET efficiencies of 66%, 42%, and 35%, respectively. Challenges such as reduced detection efficiency for low-FRET samples and photon thresholds were mitigated with the use of

(Dimethylaminomethyl)ferrocene (DAMF), which minimized photobleaching and doubled the number of recorded FRET events.

Recently, more biologically relevant samples were measured using this system, revealing the open and closed conformational states of the substrate-binding protein MalE upon the binding of maltose (data not shown). These findings highlight the potential of the system for studying dynamic processes in biomolecules.

The primary goal moving forward is to further enhance the signal from the acceptor, a current bottleneck in the system, which limits the detection of low-FRET samples. To achieve this, future work will involve testing additional dye combinations better suited for blue-green excitation, as well as systematically optimizing the concentration of photostabilizers. A particular focus will be placed on identifying photostabilizers specifically tailored for the acceptor dye to increase its brightness and stability.

A promising acceptor candidate is Cy3B, due to its high molecular brightness, especially when combined with the photostabilizer Trolox[66]. However, as previously shown, Trolox negatively impacts the donor dye (Alexa488) used in the current setup (Figure 3.42b). Recent tests using the Alexa488-Cy3B dye pair combination with both DAMF and Trolox (data not shown) showed reduced performance compared to conditions without Trolox. Balancing the concentrations of these two photostabilizers could improve performance, particularly by reducing Trolox concentrations. To date, only the combination of 100 μM DAMF and 1 mM Trolox has been tested, and if no improvement is observed, exploring alternative donor dyes will be necessary.

Another approach to improve the data from the setup would be to experiment with increasing the confocal volume. Currently, the system is operating with a diffraction-limited spot, achieved by expanding the excitation laser beam to fill the back aperture of the objective. By reducing the laser profile, a larger detection volume can be produced. The idea is that increasing the detection volume will allow molecules to remain in focus for a longer period, providing more time to collect photons[98]. However, this will require testing with different laser powers, as a larger volume will reduce light density.

Additionally, the possibility of obtaining accurate FRET measurements without the need for an ALEX system is being revisited. This concept was previously explored in my master's thesis in 2019, titled "Development of Accurate Ensemble FRET and Comparison to Single Molecule FRET," where the aim was to generate accurate FRET efficiency values in bulk using a series of different measurements. However, in that work, the presence of donor-only populations consistently introduced artifacts, leading to lower-than-expected FRET efficiencies due to the limitations of the bulk approach. With the current ability to identify single molecules and filter out donor-only species, this approach is now being reexamined to assess its potential for obtaining accurate FRET efficiency values without the reliance on an ALEX system.

In this procedure, the correction factors—such as background, crosstalk (including leakage and direct excitation), and the γ factor—are calculated by measuring a series of species involving FRET-labeled samples, donor-only samples (for Lk correction), acceptor-only samples (for Dir correction), and just the buffer (for background correction) independently. The γ factor, which is one of the more complex values to obtain, is determined by comparing the difference in photons collected from the two FRET populations with different FRET efficiencies in both the donor and acceptor photon.-streams and dividing them, as shown below.

From Equation 1.31, the γ factor is derived as follows:

$$\begin{aligned}\Delta f_{Dex}^{Dem} &= I_{Dex} \cdot \sigma_{Dex}^{D} \cdot \phi_D \cdot \eta_{Dem}^{D} \; [(1-E_2) \cdot P_D^A + P_D^D] \\ &- \; I_{Dex} \cdot \sigma_{Dex}^{D} \cdot \phi_D \cdot \eta_{Dem}^{D} \; [(1-E_1) \cdot P_D^A + P_D^D] \\ \Rightarrow \Delta f_{Dex}^{Dem} &= I_{Dex} \cdot \sigma_{Dex}^{D} \cdot \phi_D \cdot \eta_{Dem}^{D} \; (-E_2 - E_1) \cdot P_D^A\end{aligned} \tag{4.1}$$

$$\begin{aligned}\Delta f_{Dex}^{Aem} &= I_{Dex} \cdot \sigma_{Dex}^{D} \cdot \phi_A \cdot \eta_{Aem}^{A} \; \cdot E_2 \cdot P_D^A \\ &- \; I_{Dex} \cdot \sigma_{Dex}^{D} \cdot \phi_A \cdot \eta_{Aem}^{A} \; \cdot E_1 \cdot P_D^A \\ \Rightarrow \Delta f_{Dex}^{Aem} &= I_{Dex} \cdot \sigma_{Dex}^{D} \cdot \phi_A \cdot \eta_{Aem}^{A} \; (E_2 + E_1) \cdot P_D^A\end{aligned} \tag{4.2}$$

$$\Rightarrow \quad \gamma \;=\; -\,\frac{\Delta f_{Dex}^{Aem}}{\Delta f_{Dex}^{Dem}} \;=\; \frac{\phi_A \;\cdot\; \eta_{Aem}^{A}}{\phi_D \;\cdot\; \eta_{Dem}^{D}} \tag{4.3}$$

Where E_1 and E_2 represent the different FRET efficiencies recorded from varying interspaced dye separations.

The ALEX-free Blue-Green Brick-MIC approach revisits an older but valuable concept, demonstrating that while ALEX is a powerful tool, it may not always be necessary for FRET measurements, making it worthwhile to explore simpler alternatives. While the primary goal is not necessarily achieving data of the same high quality as state-of-the-art setups, this approach is still a significant advancement, offering measurements at a fraction of the cost—roughly ten times cheaper. With room for fine-tuning and optimization, there is potential to further increase the signal and enhance the performance of the system. Additionally, revisiting accurate FRET measurements to explore the limits of this approach is valuable. Ongoing efforts will continue to focus on optimizing the acceptor signal and refining the method, with the potential for future advancements that could lead to more precise, accessible, and cost-effective FRET experiments.

4.5 Outlook

Single-molecule detection has revolutionized the ability to directly analyze rapidly changing, metastable, and temporally heterogeneous biomolecular states—processes often obscured and averaged out in traditional bulk measurements. As this technology becomes increasingly accessible, it holds the potential to make conventional bulk methods and common laboratory practices, such as purifying and amplifying biochemical signals, obsolete or far less relevant. This advancement unlocks new possibilities for the development of more sensitive and versatile tools with transformative implications for diagnostics, drug screenings, environmental monitoring, and even high-security barcoding.

The Brick-MIC platform represents a significant advancement in enabling the transition to single-molecule-based assays across various scientific fields. Currently, the platform is being expanded in collaboration with the Stibor lab at LMU, as well as the Lerner lab and the Keren lab at the Hebrew University of Jerusalem, to monitor and distinguish individual phytoplankton species based on the unique fluorescence spectra and fluorescence lifetime fingerprints of their multiple light-harvesting pigments.

This collaboration builds on previous work by the Lerner lab, which found that phytoplankton species employ different strategies to acclimate to light intensity changes. Cyanobacteria transition to a long fluorescence lifetime state, while dinoflagellates reduce their fluorescence lifetime through non-photochemical quenching (NPQ) mechanisms. These distinct fluorescence signatures can be used to differentiate phytoplankton species and monitor their respective metabolism in various environmental conditions.

Building on these findings, the Brick-MIC platform has already been customized for fluorescence lifetime measurements and as a fluorimeter, creating an on-site, field-ready, highly sensitive water quality and environmental monitoring system. This system could help detect early algal blooms, preventing ecological disruptions and public health risks.

Initial tests using the upgrades successfully recorded individual phytoplankton cells, capturing fluorescence lifetimes across two spectral windows and their spectra (Figure 4.1). Ongoing work involves validating the system, with future plans for deployment in floating stations across various aquatic environments, including the Red Sea, the Sea of Galilee, and five lakes in Bavaria, Germany. These efforts aim to demonstrate the system's potential for in situ environmental monitoring and single-cell fluorescence analysis.

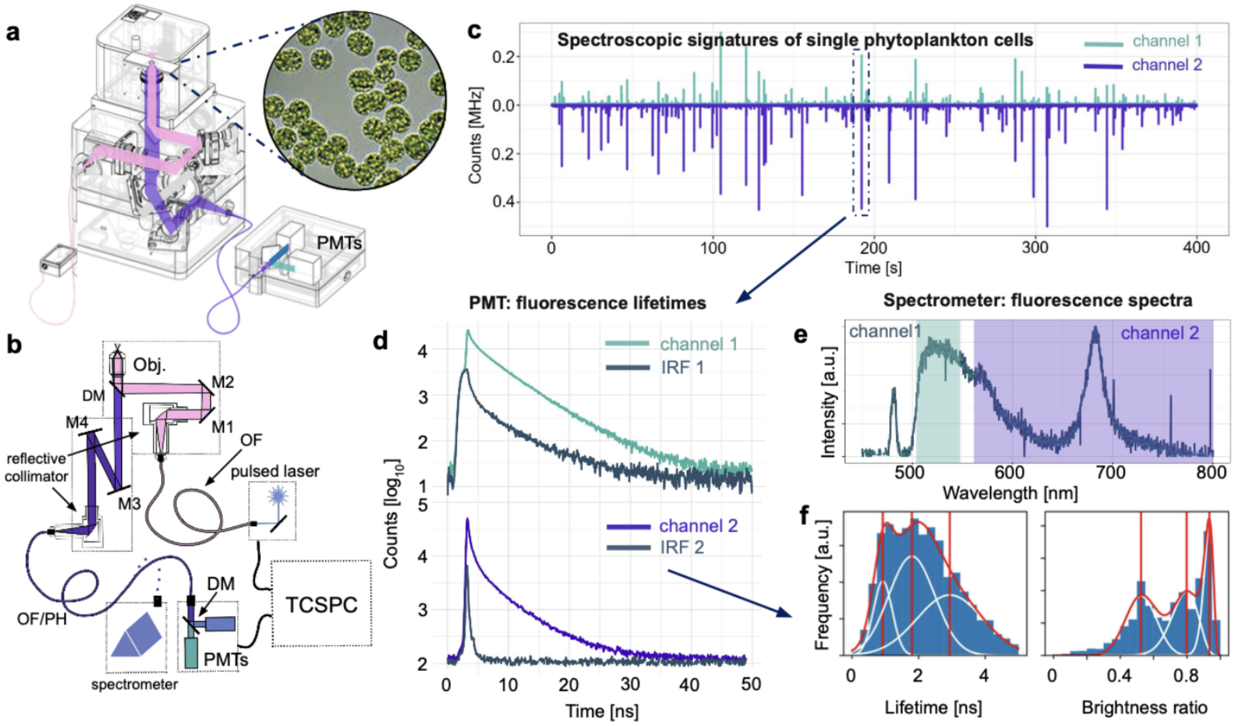

Figure 4.1: Overview and workflow of the field-deployable micro-spectroscopy setup for single phytoplankton cells, based on Brick-MIC. (a-b) Schematic drawing of a new Brick-MIC variant for single phytoplankton cell analysis with one-color pulsed excitation and two-color PMT detection and spectrometer. (c-f) Preliminary data of fluorescence intensity traces of single Chlamydomonas cells (c) in laminar flow and fluorescence lifetime decays (d) with spectra (e) and analysis of multiple single phytoplankton cell detection events as viewed through two parameters (f): fluorescence lifetime in one detection channel and the brightness ratio of two detection channels.

While the fluorimeter modality was developed for phytoplankton fluorescence spectra analysis, it also has broader applications. It provides a valuable tool for routine fluorescence spectra recordings of small sample volumes and low concentrations, where conventional cuvette-based setups face limitations. By utilizing a high numerical aperture (NA) objective, this modality can acquire spectra from as little as 10 microliters of sample and fluorescence concentrations as low as 1 nM (Figure 4.2). For example, protein labeling and purification procedures often result in low concentrations and volumes, making the fluorimeter particularly useful for protein labeling analysis, where standard fluorimeters may struggle to measure accurate fluorescent spectra.

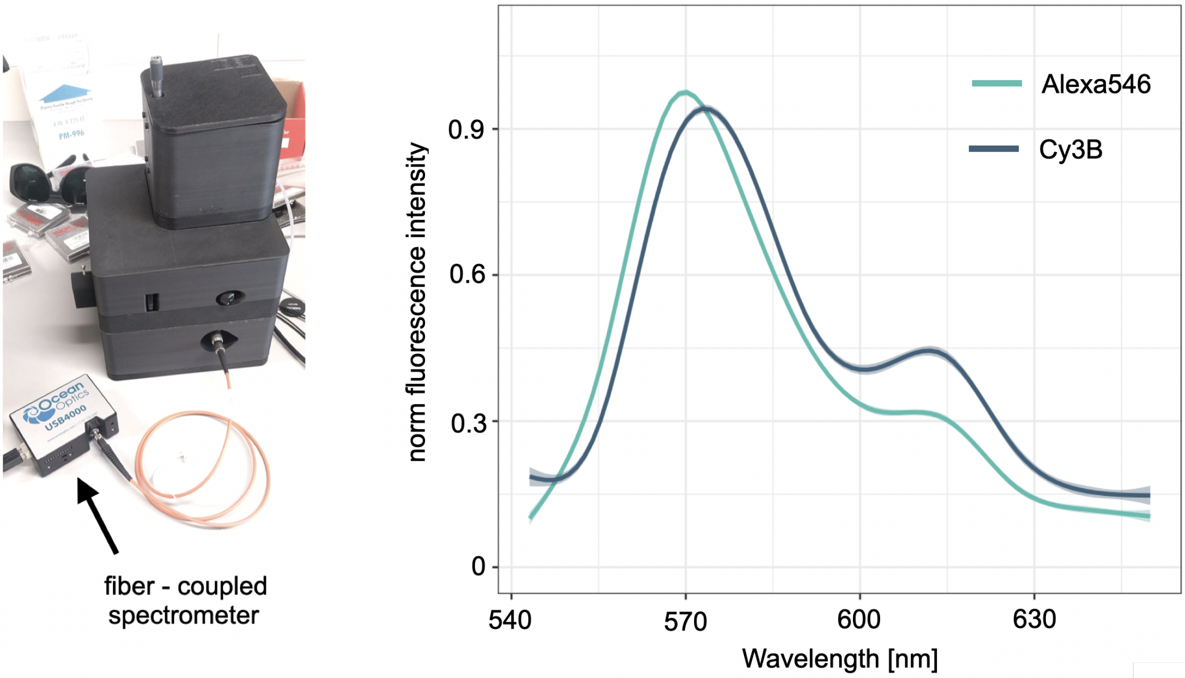

Figure 4.2: µ-fluorimeter. The left image shows the detection box of Brick-MIC replaced by a commercially available fiber-coupled spectrometer (USB4000, Ocean Optics). The right panel displays normalized fluorescence spectra of 40-mer dsDNA labeled with Alexa546 or Cy3B, acquired from a 10 µL sample volume at a 1 nM concentration, respectively. Excitation was performed at a 532 nm wavelength with 1 mW laser power.

In line with the growing potential of the Brick-MIC platform, it is being explored for its application in the diagnostics sector through a collaboration with the startup AIcendence, founded by Johannes Strodel and Moritz Koch. Their goal is to automate white blood cell diagnostics, a process that is currently done manually with microscopy. The current manual method involves identifying and counting cell types by eye, such as monocytes, eosinophils, basophils, and neutrophils. However, Strodel and Koch identified several challenges with the existing workflow: it is time-consuming, requires specialized training, and is prone to human error.

Initial tests with the existing Brick-MIC system were successful, capturing images of single cells that were identified by the AI algorithm (Figure 4.3 a). However, scanning capabilities are necessary to capture a larger number of cells and ensure the required statistics for reliable diagnostics. To meet these requirements, the Brick-MIC platform is being further developed with upgrades, including the integration of a motorized x-y sample scanner, a new LED array for transmitted light, and an RGB camera (Figure 4.3 b, c). These enhancements will enable a fully autonomous, cost-effective cell-counting system, improving the efficiency of white blood cell diagnostics and making it more accessible and reliable than traditional methods.

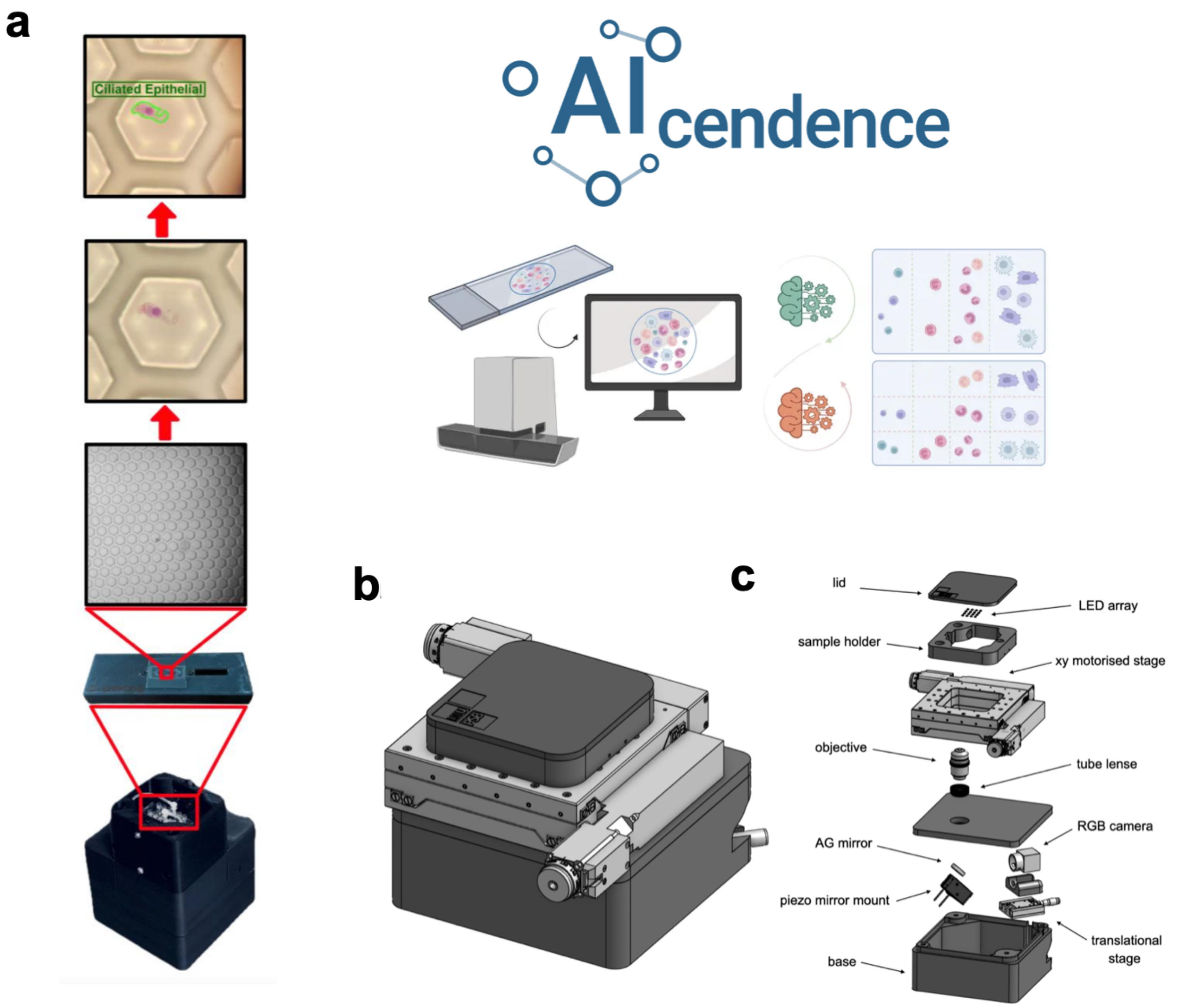

Figure 4.3: Aicendence preliminary test and future plans: (a) Single cells acquired with the Brick-MIC system using a microcavity chip for single-cell sorting. The imaged cell was identified by the AI workflow as a ciliated epithelial cell. (b-c) CAD renderings of Brick-MIC's next modality, which incorporates a motorized x-y stage to enable automated scanning of the entire sample.

The Brick-MIC project represents a significant advancement in making single-molecule spectroscopy and super-resolution imaging more accessible, especially for non-optical specialists. Its modular design, inspired by a "LEGO-like" philosophy, allows for easy expansion and customization for specific applications. This modularity, combined with the flexibility of 3D printing, encourages experimentation and the development of application-specific solutions. Each new module can be integrated with existing components to create customized setups.

Much like how Muybridge's motion photography laid the groundwork for the video camera, making high-speed motion capture available to all, the Brick-MIC platform is opening the door for single-molecule techniques to become a routine tool in scientific research.

Looking forward, as more researchers contribute to this open-source project, the potential for further improvements grows. We may see the development of additional modules that push the limits of what's possible with microscopy, making advanced imaging techniques more accessible and adaptable. This collaborative, iterative process holds the potential to make high-end microscopy tools more widely available, facilitating breakthroughs across various scientific disciplines by making powerful tools available to a broader community.

Bibliography

[1] PAUL BONAVENTURA. The horse: 30,000 years of the horse in art by tamsin pickeral. *The Art Book*, 14(4):47–48, 2007.

[2] J. Baskett. *The Horse in Art*. Yale University Press, 2006.

[3] Walter Benjamin. A short history of photography. *Screen*, 13(1):5–26, 1972.

[4] John Ott. Iron horses: Leland stanford, eadweard muybridge, and the industrialised eye. *Oxford Art Journal*, 28(3):407–428, 2005.

[5] Eadweard Muybridge. *Animal locomotion*, volume 534. Da Capo Press Oxford, 1887.

[6] Rita Grandori. Protein structure and dynamics in the era of integrative structural biology. *Frontiers in Biophysics*, 1:1219843, 2023.

[7] Martin Beck, Roberto Covino, Inga Hänelt, and Michaela Müller-McNicoll. Understanding the cell: Future views of structural biology. *Cell*, 187(3):545–562, 2024.

[8] Alev Baysoy, Zhiliang Bai, Rahul Satija, and Rong Fan. The technological landscape and applications of single-cell multi-omics. *Nature Reviews Molecular Cell Biology*, 24(10):695–713, 2023.

[9] Yigong Shi. A glimpse of structural biology through x-ray crystallography. *Cell*, 159(5):995–1014, 2014.

[10] AJ Miles, Robert W Janes, and Bonnie A Wallace. Tools and methods for circular dichroism spectroscopy of proteins: a tutorial review. *Chemical Society Reviews*, 50(15):8400–8413, 2021.

[11] Maliheh Sadat Atri, Ali Akbar Saboury, and Faizan Ahmad. Biological applications of isothermal titration calorimetry. *Physical Chemistry Research*, 3(4):319–330, 2015.

[12] Blanca López-Méndez, Bruno Baron, Chad A Brautigam, Thomas A Jowitt, Stefan H Knauer, Stephan Uebel, Mark A Williams, Arthur Sedivy, Olga Abian, Celeste Abreu, et al. Reproducibility and accuracy of microscale thermophoresis in the nanotemper monolith: a multi laboratory benchmark study. *European biophysics journal*, 50:411–427, 2021.

[13] Julie L Brunelle and Rachel Green. One-dimensional sds-polyacrylamide gel electrophoresis (1d sds-page). In *Methods in enzymology*, volume 541, pages 151–159. Elsevier, 2014.

[14] Sadao Mori and Howard G Barth. *Size exclusion chromatography*. Springer Science & Business Media, 1999.

[15] David Alsteens. Grand challenges in biophysics. *Frontiers in Biophysics*, 1:1215594, 2023.

[16] Harold P Erickson. Size and shape of protein molecules at the nanometer level determined by sedimentation, gel filtration, and electron microscopy. *Biological procedures online*, 11:32–51, 2009.

[17] Helen R Saibil. Cryo-em in molecular and cellular biology. *Molecular Cell*, 82(2):274–284, 2022.

[18] L Missiaen, F Wuytack, Y Kanmura, H Van Belle, J Wynants, J Minten, and R Casteels. Measurement of microsomal atpase activities: a comparison between the inorganic phosphate-release assay and the nadh-coupled enzyme assay. *Biochimica et Biophysica Acta (BBA)-General Subjects*, 990(1):40–44, 1989.

[19] Jianshu Cao. Event-averaged measurements of single-molecule kinetics. *Chemical Physics Letters*, 327(1-2):38–44, 2000.

[20] WE Moerner. A dozen years of single-molecule spectroscopy in physics, chemistry, and biophysics, 2002.

[21] WE Moerner, Yoav Shechtman, and Quan Wang. Single-molecule spectroscopy and imaging over the decades. *Faraday discussions*, 184:9–36, 2015.

[22] Helen Miller, Zhaokun Zhou, Jack Shepherd, Adam JM Wollman, and Mark C Leake. Single-molecule techniques in biophysics: a review of the progress in methods and applications. *Reports on Progress in Physics*, 81(2):024601, 2017.

[23] Ashok A Deniz, Samrat Mukhopadhyay, and Edward A Lemke. Single-molecule biophysics: at the interface of biology, physics and chemistry. *Journal of the Royal Society Interface*, 5(18):15–45, 2008.

[24] Felix Ritort. Single molecule research: When biology meets physics. 2016.

[25] Megan A Steves, Changdong He, and Ke Xu. Single-molecule spectroscopy and super-resolution mapping of physicochemical parameters in living cells. *Annual Review of Physical Chemistry*, 75, 2024.

[26] Birka Hein, Katrin I Willig, and Stefan W Hell. Stimulated emission depletion (sted) nanoscopy of a fluorescent protein-labeled organelle inside a living cell. *Proceedings of the National Academy of Sciences*, 105(38):14271–14276, 2008.

[27] Eric Betzig, George H Patterson, Rachid Sougrat, O Wolf Lindwasser, Scott Olenych, Juan S Bonifacino, Michael W Davidson, Jennifer Lippincott-Schwartz, and Harald F Hess. Imaging intracellular fluorescent proteins at nanometer resolution. *science*, 313(5793):1642–1645, 2006.

[28] Michael J Rust, Mark Bates, and Xiaowei Zhuang. Stochastic optical reconstruction microscopy (storm) provides sub-diffraction-limit image resolution. *Nature methods*, 3(10):793, 2006.

[29] Ralf Jungmann, Christian Steinhauer, Max Scheible, Anton Kuzyk, Philip Tinnefeld, and Friedrich C Simmel. Single-molecule kinetics and super-resolution microscopy by fluorescence imaging of transient binding on dna origami. *Nano letters*, 10(11):4756–4761, 2010.

[30] Ralf Jungmann, Maier S Avendaño, Johannes B Woehrstein, Mingjie Dai, William M Shih, and Peng Yin. Multiplexed 3d cellular super-resolution imaging with dna-paint and exchange-paint. *Nature methods*, 11(3):313–318, 2014.

[31] Lan Yu, Yunze Lei, Ying Ma, Min Liu, Juanjuan Zheng, Dan Dan, and Peng Gao. A comprehensive review of fluorescence correlation spectroscopy. *Frontiers in physics*, 9:644450, 2021.

[32] JR Lakowicz. Principles of fluorescence spectroscopy. *University of Maryland School of Medicine Baltimore*, 132, 2006.

[33] MA Osborne, S Balasubramanian, WS Furey, and D Klenerman. Optically biased diffusion of single molecules studied by confocal fluorescence microscopy. *The Journal of Physical Chemistry B*, 102(17):3160–3167, 1998.

[34] Th Förster. Intermolecular energy migration and ffuorescence. *Ann. Physik*, 2:55–75, 1948.

[35] Nam Ki Lee, Achillefs N Kapanidis, You Wang, Xavier Michalet, Jayanta Mukhopadhyay, Richard H Ebright, and Shimon Weiss. Accurate fret measurements within single diffusing biomolecules using alternating-laser excitation. *Biophysical journal*, 88(4):2939–2953, 2005.

[36] Taekjip Ha, Thilo Enderle, DF Ogletree, Daniel S Chemla, Paul R Selvin, and Shimon Weiss. Probing the interaction between two single molecules: fluorescence resonance energy transfer between a single donor and a single acceptor. *Proceedings of the National Academy of Sciences*, 93(13):6264–6268, 1996.

[37] Achillefs N Kapanidis, Nam Ki Lee, Ted A Laurence, Sören Doose, Emmanuel Margeat, and Shimon Weiss. Fluorescence-aided molecule sorting: analysis of structure and interactions by alternating-laser excitation of single molecules. *Proceedings of the National Academy of Sciences*, 101(24):8936–8941, 2004.

[38] Devdoot S Majumdar, Irina Smirnova, Vladimir Kasho, Eyal Nir, Xiangxu Kong, Shimon Weiss, and H Ronald Kaback. Single-molecule fret reveals sugar-induced conformational dynamics in lacy. *Proceedings of the National Academy of Sciences*, 104(31):12640–12645, 2007.

[39] Giorgos Gouridis, Gea K Schuurman-Wolters, Evelyn Ploetz, Florence Husada, Ruslan Vietrov, Marijn De Boer, Thorben Cordes, and Bert Poolman. Conformational dynamics in substrate-binding domains influences transport in the abc importer glnpq. *Nature structural & molecular biology*, 22(1):57, 2015.

[40] Nicole C Robb, Thorben Cordes, Ling Chin Hwang, Kristofer Gryte, Diego Duchi, Timothy D Craggs, Yusdi Santoso, Shimon Weiss, Richard H Ebright, and Achillefs N Kapanidis. The transcription bubble of the rna polymerase–promoter open complex exhibits conformational heterogeneity and millisecond-scale dynamics: implications for transcription start-site selection. *Journal of molecular biology*, 425(5):875–885, 2013.

[41] Yusdi Santoso, Catherine M Joyce, Olga Potapova, Ludovic Le Reste, Johannes Hohlbein, Joseph P Torella, Nigel DF Grindley, and Achillefs N Kapanidis. Conformational transitions in dna polymerase i revealed by single-molecule fret. *Proceedings of the National Academy of Sciences*, 107(2):715–720, 2010.

[42] S Markus, H Johan, and E Jörg. Handbook of fluorescence spectroscopy and imaging: From single molecules to ensembles, 2011.

[43] Terri C Lovell, Bruce P Branchaud, and Ramesh Jasti. An organic chemist's guide to fluorophores–understanding common and newer non-planar fluorescent molecules for biological applications. *European Journal of Organic Chemistry*, 27(9):e202301196, 2024.

[44] Jochem H Smit, Jasper HM van der Velde, Jingyi Huang, Vanessa Trauschke, Sarah S Henrikus, Si Chen, Nikolaos Eleftheriadis, Eliza M Warszawik, Andreas Herrmann, and Thorben Cordes. On the impact of competing intra-and intermolecular triplet-state quenching on photobleaching and photoswitching kinetics of organic fluorophores. *Physical Chemistry Chemical Physics*, 21(7):3721–3733, 2019.

[45] Peter Jomo Walla. *Modern biophysical chemistry: detection and analysis of biomolecules*. John Wiley & Sons, 2014.

[46] Ute Resch-Genger, Markus Grabolle, Sara Cavaliere-Jaricot, Roland Nitschke, and Thomas Nann. Quantum dots versus organic dyes as fluorescent labels. *Nature methods*, 5(9):763–775, 2008.

[47] Roger Y Tsien. The green fluorescent protein. *Annual review of biochemistry*, 67(1):509–544, 1998.

[48] Alexander L Efros and Louis E Brus. Nanocrystal quantum dots: from discovery to modern development. *ACS nano*, 15(4):6192–6210, 2021.

[49] Taekjip Ha and Philip Tinnefeld. Photophysics of fluorescent probes for single-molecule biophysics and super-resolution imaging. *Annual review of physical chemistry*, 63(1):595–617, 2012.

[50] Kai Kikuchi, Liam D Adair, Jiarun Lin, Elizabeth J New, and Amandeep Kaur. Photochemical mechanisms of fluorophores employed in single-molecule localization microscopy. *Angewandte Chemie*, 135(1):e202204745, 2023.

[51] Lei Zhang, Michael Isselstein, Jens Köhler, Nikolaos Eleftheriadis, Nadia M Huisjes, Miguel Guirao-Ortiz, Alessandra Narducci, Jochem H Smit, Janko Stoffels, Hartmann Harz, et al. Linker

molecules convert commercial fluorophores into tailored functional probes during biolabelling. *Angewandte Chemie*, 134(19):e202112959, 2022.

[52] Bernard Juskowiak. Nucleic acid-based fluorescent probes and their analytical potential. *Analytical and bioanalytical chemistry*, 399:3157–3176, 2011.

[53] Lin Tian, S Andrew Hires, and Loren L Looger. Imaging neuronal activity with genetically encoded calcium indicators. *Cold Spring Harbor Protocols*, 2012(6):pdb–top069609, 2012.

[54] George Gabriel Stokes. Xxx. on the change of refrangibility of light. *Philosophical transactions of the Royal Society of London*, (142):463–562, 1852.

[55] James Clerk Maxwell. Viii. a dynamical theory of the electromagnetic field. *Philosophical transactions of the Royal Society of London*, (155):459–512, 1865.

[56] Jun John Sakurai and Jim Napolitano. *Modern quantum mechanics*. Cambridge University Press, 2020.

[57] Hans H Jaffé and Albert L Miller. The fates of electronic excitation energy. *Journal of chemical education*, 43(9):469, 1966.

[58] EB Priestley and A Haug. Phosphorescence spectrum of pure crystalline naphthalene. *The Journal of Chemical Physics*, 49(2):622–629, 1968.

[59] Pei-Hua Chung, Carolyn Tregidgo, and Klaus Suhling. Determining a fluorophore's transition dipole moment from fluorescence lifetime measurements in solvents of varying refractive index. *Methods and applications in fluorescence*, 4(4):045001, 2016.

[60] Petro Khoroshyy, Hector Martinez-Seara, Jitka Myšková, and Josef Lazar. Dynamics of transition dipole moment orientation in representative fluorescent proteins. *Physical Chemistry Chemical Physics*, 25(33):22117–22123, 2023.

[61] Christian Gebhardt, Martin Lehmann, Maria M Reif, Martin Zacharias, Gerd Gemmecker, and Thorben Cordes. Molecular and spectroscopic characterization of green and red cyanine fluorophores from the alexa fluor and af series. *ChemPhysChem*, 22(15):1566–1583, 2021.

[62] Mikhail Y Berezin and Samuel Achilefu. Fluorescence lifetime measurements and biological imaging. *Chemical reviews*, 110(5):2641–2684, 2010.

[63] Kathryn P Wall, Rebecca Dillon, and Michelle K Knowles. Fluorescence quantum yield measurements of fluorescent proteins: a laboratory experiment for a biochemistry or molecular biophysics laboratory course. *Biochemistry and Molecular Biology Education*, 43(1):52–59, 2015.

[64] Lee K Fraiji, David M Hayes, and TC Werner. Static and dynamic fluorescence quenching experiments for the physical chemistry laboratory. *Journal of chemical education*, 69(5):424, 1992.

[65] Marcelo H Gehlen. The centenary of the stern-volmer equation of fluorescence quenching: From the single line plot to the sv quenching map. *Journal of Photochemistry and Photobiology C: Photochemistry Reviews*, 42:100338, 2020.

[66] Thorben Cordes, Jan Vogelsang, and Philip Tinnefeld. On the mechanism of trolox as antiblinking and antibleaching reagent. *Journal of the American Chemical Society*, 131(14):5018–5019, 2009.

[67] Jan Vogelsang, Robert Kasper, Christian Steinhauer, Britta Person, Mike Heilemann, Markus Sauer, and Philip Tinnefeld. A reducing and oxidizing system minimizes photobleaching and blinking of fluorescent dyes. *Angewandte Chemie-International Edition*, 47(29), 2008.

[68] Sören Doose, Hannes Neuweiler, and Markus Sauer. Fluorescence quenching by photoinduced electron transfer: a reporter for conformational dynamics of macromolecules. *ChemPhysChem*, 10(9-10):1389–1398, 2009.

[69] Lubert Stryer and Richard P Haugland. Energy transfer: a spectroscopic ruler. *Proceedings of the National Academy of Sciences*, 58(2):719–726, 1967.

[70] Robert M Clegg. [18] fluorescence resonance energy transfer and nucleic acids. In *Methods in enzymology*, volume 211, pages 353–388. Elsevier, 1992.

[71] Ben Corry, Dylan Jayatilaka, Boris Martinac, and Paul Rigby. Determination of the orientational distribution and orientation factor for transfer between membrane-bound fluorophores using a confocal microscope. *Biophysical journal*, 91(3):1032–1045, 2006.

[72] Frits Zernike. Phase contrast, a new method for the microscopic observation of transparent objects. *Physica*, 9(7):686–698, 1942.

[73] Peng Fei Gao, Gang Lei, and Cheng Zhi Huang. Dark-field microscopy: recent advances in accurate analysis and emerging applications. *Analytical Chemistry*, 93(11):4707–4726, 2021.

[74] Maksymilian Pluta. Nomarski's dic microscopy: a review. In *Phase contrast and differential interference contrast imaging techniques and applications*, volume 1846, pages 10–25. SPIE, 1994.

[75] Jeff W Lichtman and José-Angel Conchello. Fluorescence microscopy. *Nature methods*, 2(12):910–919, 2005.

[76] Konan Peck, Lubert Stryer, Alexander N Glazer, and Richard A Mathies. Single-molecule fluorescence detection: autocorrelation criterion and experimental realization with phycoerythrin. *Proceedings of the National Academy of Sciences*, 86(11):4087–4091, 1989.

[77] E Brooks Shera, Newton K Seitzinger, Lloyd M Davis, Richard A Keller, and Steven A Soper. Detection of single fluorescent molecules. *Chemical Physics Letters*, 174(6):553–557, 1990.

[78] Shuming Nie, Daniel T Chiu, and Richard N Zare. Probing individual molecules with confocal fluorescence microscopy. *Science*, 266(5187):1018–1021, 1994.

[79] Philippe IH Bastiaens and Anthony Squire. Fluorescence lifetime imaging microscopy: spatial resolution of biochemical processes in the cell. *Trends in cell biology*, 9(2):48–52, 1999.

[80] Ernst HK Stelzer, Frederic Strobl, Bo-Jui Chang, Friedrich Preusser, Stephan Preibisch, Katie McDole, and Reto Fiolka. Light sheet fluorescence microscopy. *Nature Reviews Methods Primers*, 1(1):73, 2021.

[81] Kenneth N Fish. Total internal reflection fluorescence (tirf) microscopy. *Current protocols in cytometry*, 50(1):12–18, 2009.

[82] Stephen W Paddock, TJ Fellers, and MW Davidson. *Confocal microscopy*. Springer, 2014.

[83] Amicia D Elliott. Confocal microscopy: principles and modern practices. *Current protocols in cytometry*, 92(1):e68, 2020.

[84] Colin JR Sheppard, Min Gu, and Maitreyee Roy. Signal-to-noise ratio in confocal microscope systems. *Journal of Microscopy*, 168(3):209–218, 1992.

[85] Minsky Marvin. Microscopy apparatus, December 19 1961. US Patent 3,013,467.

[86] Lukas Novotny and Bert Hecht. *Principles of nano-optics*. Cambridge university press, 2012.

[87] S Rüttinger, V Buschmann, B Krämer, R Erdmann, R Macdonald, and F Koberling. Determination of the confocal volume for quantitative fluorescence correlation spectroscopy. In *European Conference on Biomedical Optics*, page 6630_12. Optica Publishing Group, 2007.

[88] Robert H Webb. [1] theoretical basis of confocal microscopy. In *Methods in enzymology*, volume 307, pages 3–20. Elsevier, 1999.

[89] C Eggeling, S Berger, L Brand, JR Fries, J Schaffer, A Volkmer, and CAM Seidel. Data registration and selective single-molecule analysis using multi-parameter fluorescence detection. *Journal of biotechnology*, 86(3):163–180, 2001.

[90] C Eggeling, JR Fries, L Brand, R Günther, and CAM Seidel. Monitoring conformational dynamics of a single molecule by selective fluorescence spectroscopy. *Proceedings of the National Academy of Sciences*, 95(4):1556–1561, 1998.

[91] Joachim R Fries, Leif Brand, Christian Eggeling, Malte Köllner, and Claus AM Seidel. Quantitative identification of different single molecules by selective time-resolved confocal fluorescence spectroscopy. *The Journal of Physical Chemistry A*, 102(33):6601–6613, 1998.

[92] Eyal Nir, Xavier Michalet, Kambiz M Hamadani, Ted A Laurence, Daniel Neuhauser, Yevgeniy Kovchegov, and Shimon Weiss. Shot-noise limited single-molecule fret histograms: comparison between theory and experiments. *The Journal of Physical Chemistry B*, 110(44):22103–22124, 2006.

[93] Achillefs N Kapanidis, Ted A Laurence, Nam Ki Lee, Emmanuel Margeat, Xiangxu Kong, and Shimon Weiss. Alternating-laser excitation of single molecules. *Accounts of chemical research*, 38(7):523–533, 2005.

[94] Johannes Hohlbein, Timothy D Craggs, and Thorben Cordes. Alternating-laser excitation: single-molecule fret and beyond. *Chemical Society Reviews*, 43(4):1156–1171, 2014.

[95] Mickaël Lelek, Melina T Gyparaki, Gerti Beliu, Florian Schueder, Juliette Griffié, Suliana Manley, Ralf Jungmann, Markus Sauer, Melike Lakadamyali, and Christophe Zimmer. Single-molecule localization microscopy. *Nature reviews methods primers*, 1(1):39, 2021.

[96] Martin Ovesnỳ, Pavel Křížek, Josef Borkovec, Zdeněk Švindrych, and Guy M Hagen. Thunderstorm: a comprehensive imagej plug-in for palm and storm data analysis and super-resolution imaging. *Bioinformatics*, 30(16):2389–2390, 2014.

[97] Mike Heilemann, Sebastian Van De Linde, Mark Schüttpelz, Robert Kasper, Britta Seefeldt, Anindita Mukherjee, Philip Tinnefeld, and Markus Sauer. Subdiffraction-resolution fluorescence imaging with conventional fluorescent probes. *Angewandte Chemie-International Edition*, 47(33), 2008.

[98] Ganesh Agam, Christian Gebhardt, Milana Popara, Rebecca Mächtel, Julian Folz, Benjamin Ambrose, Neharika Chamachi, Sang Yoon Chung, Timothy D Craggs, Marijn de Boer, et al. Reliability and accuracy of single-molecule fret studies for characterization of structural dynamics and distances in proteins. *Nature methods*, 20(4):523–535, 2023.

[99] Martin F Peter, Christian Gebhardt, Rebecca Mächtel, Gabriel G Moya Muñoz, Janin Glaenzer, Alessandra Narducci, Gavin H Thomas, Thorben Cordes, and Gregor Hagelueken. Cross-validation of distance measurements in proteins by peldor/deer and single-molecule fret. *Nature Communications*, 13(1):4396, 2022.

[100] Samuel Stubhan, Anna V Baptist, Caroline Körösy, Alessandra Narducci, Gustavo Gabriel Moya Muñoz, Nicolas Wendler, Aidin Lak, Michael Sztucki, Thorben Cordes, and Jan Lipfert. Determination of absolute intramolecular distances in proteins by anomalous x-ray scattering interferometry. *Nanoscale*, 2025.

[101] Gabriel G Moya Muñoz, Oliver Brix, Philipp Klocke, Paul D Harris, Jorge R Luna Piedra, Nicolas D Wendler, Eitan Lerner, Niels Zijlstra, and Thorben Cordes. Single-molecule detection and super-resolution imaging with a portable and adaptable 3d-printed microscopy platform (brick-mic). *Science Advances*, 10(39):eado3427, 2024.

[102] Paz Drori, Odelia Mouhadeb, Gabriel G Moya Muñoz, Yair Razvag, Ron Alcalay, Philipp Klocke, Thorben Cordes, Eran Zahavy, and Eitan Lerner. Rapid and specific detection of nanoparticles and viruses one at a time using microfluidic laminar flow and confocal fluorescence microscopy. *Iscience*, 27(10), 2024.

[103] Evelyn Ploetz, Eitan Lerner, Florence Husada, Martin Roelfs, SangYoon Chung, Johannes Hohlbein, Shimon Weiss, and Thorben Cordes. Förster resonance energy transfer and protein-induced fluorescence enhancement as synergetic multi-scale molecular rulers. *Scientific reports*, 6(1):33257, 2016.

[104] Kevin L Holmes and Larry M Lantz. Protein labeling with fluorescent probes. *Methods in cell biology*, 63:185–204, 2001.

[105] Christian Gebhardt, Pascal Bawidamann, Konstantin Schütze, Gabriel G Moya Muñoz, Anna-Katharina Spring, Douglas A Griffith, Jan Lipfert, and Thorben Cordes. Labelizer: systematic selection of protein residues for covalent fluorophore labeling. *bioRxiv*, pages 2023–06, 2023.

[106] Yau-Tsz Lai, Yuen-Yan Chang, Ligang Hu, Ya Yang, Ailun Chao, Zhi-Yan Du, Julian A Tanner, Mee-Len Chye, Chengmin Qian, Kwan-Ming Ng, et al. Rapid labeling of intracellular his-tagged proteins in living cells. *Proceedings of the National Academy of Sciences*, 112(10):2948–2953, 2015.

[107] Tanja Bartoschik, Stefanie Galinec, Christian Kleusch, Katarzyna Walkiewicz, Dennis Breitsprecher, Sebastian Weigert, Yves A Muller, Changjiang You, Jacob Piehler, Thomas Vercruysse, et al. Near-native, site-specific and purification-free protein labeling for quantitative protein interaction analysis by microscale thermophoresis. *Scientific reports*, 8(1):4977, 2018.

[108] Kyung Jin Lee, Deokhee Kang, and Hee-Sung Park. Site-specific labeling of proteins using unnatural amino acids. *Molecules and cells*, 42(5):386–396, 2019.

[109] Antonino Ingargiola, Eitan Lerner, SangYoon Chung, Francesco Panzeri, Angelo Gulinatti, Ivan Rech, Massimo Ghioni, Shimon Weiss, and Xavier Michalet. Multispot single-molecule fret: High-throughput analysis of freely diffusing molecules. *PLoS One*, 12(4):e0175766, 2017.

[110] Th Förster. Zwischenmolekulare energiewanderung und fluoreszenz. *Annalen der physik*, 437(1-2):55–75, 1948.

[111] Robin Diekmann, Katharina Till, Marcel Müller, Matthias Simonis, Mark Schüttpelz, and Thomas Huser. Characterization of an industry-grade cmos camera well suited for single molecule localization microscopy–high performance super-resolution at low cost. *Scientific reports*, 7(1):14425, 2017.

[112] Moran Jerabek-Willemsen, Timon André, Randy Wanner, Heide Marie Roth, Stefan Duhr, Philipp Baaske, and Dennis Breitsprecher. Microscale thermophoresis: Interaction analysis and beyond. *Journal of Molecular Structure*, 1077:101–113, 2014.

[113] Ute Resch-Genger. *Standardization and quality assurance in fluorescence measurements II: Bioanalytical and biomedical applications*, volume 6. Springer Science & Business Media, 2008.

[114] Eitan Lerner, Anders Barth, Jelle Hendrix, Benjamin Ambrose, Victoria Birkedal, Scott C Blanchard, Richard Börner, Hoi Sung Chung, Thorben Cordes, Timothy D Craggs, et al. Fret-based

dynamic structural biology: Challenges, perspectives and an appeal for open-science practices. *Elife*, 10:e60416, 2021.

[115] Eitan Lerner, Thorben Cordes, Antonino Ingargiola, Yazan Alhadid, SangYoon Chung, Xavier Michalet, and Shimon Weiss. Toward dynamic structural biology: Two decades of single-molecule förster resonance energy transfer. *Science*, 359(6373):eaan1133, 2018.

[116] Adam Muschielok, Joanna Andrecka, Anass Jawhari, Florian Brückner, Patrick Cramer, and Jens Michaelis. A nano-positioning system for macromolecular structural analysis. *Nature methods*, 5(11):965–971, 2008.

[117] Stanislav Kalinin, Thomas Peulen, Simon Sindbert, Paul J Rothwell, Sylvia Berger, Tobias Restle, Roger S Goody, Holger Gohlke, and Claus AM Seidel. A toolkit and benchmark study for fret-restrained high-precision structural modeling. *Nature methods*, 9(12):1218–1225, 2012.

[118] Timothy D Craggs and Achillefs N Kapanidis. Six steps closer to fret-driven structural biology. *nature methods*, 9(12):1157–1158, 2012.

[119] Lena Voith von Voithenberg and Don C Lamb. Single pair förster resonance energy transfer: a versatile tool to investigate protein conformational dynamics. *BioEssays*, 40(3):1700078, 2018.

[120] Björn Hellenkamp, Sonja Schmid, Olga Doroshenko, Oleg Opanasyuk, Ralf Kühnemuth, Soheila Rezaei Adariani, Benjamin Ambrose, Mikayel Aznauryan, Anders Barth, Victoria Birkedal, et al. Precision and accuracy of single-molecule fret measurements—a multi-laboratory benchmark study. *Nature methods*, 15(9):669–676, 2018.

[121] Amy L Davidson, Elie Dassa, Cedric Orelle, and Jue Chen. Structure, function, and evolution of bacterial atp-binding cassette systems. *Microbiol. Mol. Biol. Rev.*, 72(2):317–364, 2008.

[122] Rebecca Mächtel, Alessandra Narducci, Douglas A Griffith, Thorben Cordes, and Cédric Orelle. An integrated transport mechanism of the maltose abc importer. *Research in microbiology*, 170(8):321–337, 2019.

[123] Ajamaluddin Malik. Protein fusion tags for efficient expression and purification of recombinant proteins in the periplasmic space of e. coli. *3 Biotech*, 6(1):44, 2016.

[124] Hiren Banerjee, Andrew Rahn, William Davis, and Ravinder Singh. Sex lethal and u2 small nuclear ribonucleoprotein auxiliary factor (u2af65) recognize polypyrimidine tracts using multiple modes of binding. *Rna*, 9(1):88–99, 2003.

[125] E Allen Sickmier, Katherine E Frato, Haihong Shen, Shanthi R Paranawithana, Michael R Green, and Clara L Kielkopf. Structural basis for polypyrimidine tract recognition by the essential pre-mrna splicing factor u2af65. *Molecular cell*, 23(1):49–59, 2006.

[126] Jie-rong Huang, Lisa R Warner, Carolina Sanchez, Frank Gabel, Tobias Madl, Cameron D Mackereth, Michael Sattler, and Martin Blackledge. Transient electrostatic interactions dominate the

conformational equilibrium sampled by multidomain splicing factor u2af65: a combined nmr and saxs study. *Journal of the American Chemical Society*, 136(19):7068–7076, 2014.

[127] Marijn de Boer, Giorgos Gouridis, Ruslan Vietrov, Stephanie L Begg, Gea K Schuurman-Wolters, Florence Husada, Nikolaos Eleftheriadis, Bert Poolman, Christopher A McDevitt, and Thorben Cordes. Conformational and dynamic plasticity in substrate-binding proteins underlies selective transport in abc importers. *Elife*, 8:e44652, 2019.

[128] Simon Sindbert, Stanislav Kalinin, Hien Nguyen, Andrea Kienzler, Lilia Clima, Willi Bannwarth, Bettina Appel, Sabine Muller, and Claus AM Seidel. Accurate distance determination of nucleic acids via forster resonance energy transfer: implications of dye linker length and rigidity. *Journal of the American Chemical Society*, 133(8):2463–2480, 2011.

[129] Fabio D Steffen, Roland KO Sigel, and Richard Börner. An atomistic view on carbocyanine photophysics in the realm of rna. *Physical Chemistry Chemical Physics*, 18(42):29045–29055, 2016.

[130] Ines Reinartz, Claude Sinner, Daniel Nettels, Brigitte Stucki-Buchli, Florian Stockmar, Pawel T Panek, Christoph R Jacob, Gerd Ulrich Nienhaus, Benjamin Schuler, and Alexander Schug. Simulation of fret dyes allows quantitative comparison against experimental data. *The Journal of chemical physics*, 148(12), 2018.

[131] Martin Hoefling, Nicola Lima, Dominik Haenni, Claus AM Seidel, Benjamin Schuler, and Helmut Grubmüller. Structural heterogeneity and quantitative fret efficiency distributions of polyprolines through a hybrid atomistic simulation and monte carlo approach. *PLoS One*, 6(5):e19791, 2011.

[132] Mykola Dimura, Thomas O Peulen, Christian A Hanke, Aiswaria Prakash, Holger Gohlke, and Claus AM Seidel. Quantitative fret studies and integrative modeling unravel the structure and dynamics of biomolecular systems. *Current opinion in structural biology*, 40:163–185, 2016.

[133] Markus Burger, Stephan Rein, Stefan Weber, Peter Gräber, and Sylwia Kacprzak. Distance measurements in the f0f1-atp synthase from e. coli using smfret and peldor spectroscopy. *European Biophysics Journal*, 49(1):1–10, 2020.

[134] Daniel Klose, Johann P Klare, Dina Grohmann, Christopher WM Kay, Finn Werner, and Heinz-Jürgen Steinhoff. Simulation vs. reality: a comparison of in silico distance predictions with deer and fret measurements. *PLoS one*, 7(6):e39492, 2012.

[135] Dina Grohmann, Daniel Klose, Johann P Klare, Christopher WM Kay, Heinz-Jurgen Steinhoff, and Finn Werner. Rna-binding to archaeal rna polymerase subunits f/e: a deer and fret study. *Journal of the American Chemical Society*, 132(17):5954–5955, 2010.

[136] Evzen Boura, Bartosz Różycki, Dawn Z Herrick, Hoi Sung Chung, Jaroslav Vecer, William A Eaton, David S Cafiso, Gerhard Hummer, and James H Hurley. Solution structure of the escrt-i

complex by small-angle x-ray scattering, epr, and fret spectroscopy. *Proceedings of the National Academy of Sciences*, 108(23):9437–9442, 2011.

[137] Hugo Sanabria, Dmitro Rodnin, Katherina Hemmen, Thomas-Otavio Peulen, Suren Felekyan, Mark R Fleissner, Mykola Dimura, Felix Koberling, Ralf Kühnemuth, Wayne Hubbell, et al. Resolving dynamics and function of transient states in single enzyme molecules. *Nature communications*, 11(1):1231, 2020.

[138] Beth M Stadtmueller, Michael D Bridges, Kim-Marie Dam, Michael T Lerch, Kathryn E Huey-Tubman, Wayne L Hubbell, and Pamela J Bjorkman. Deer spectroscopy measurements reveal multiple conformations of hiv-1 sosip envelopes that show similarities with envelopes on native virions. *Immunity*, 49(2):235–246, 2018.

[139] Daniel Klose, Andrea Holla, Christoph Gmeiner, Daniel Nettels, Irina Ritsch, Nadja Bross, Maxim Yulikov, Frédéric H-T Allain, Benjamin Schuler, and Gunnar Jeschke. Resolving distance variations by single-molecule fret and epr spectroscopy using rotamer libraries. *Biophysical Journal*, 120(21):4842–4858, 2021.

[140] Tatyana I Smirnova, Maxim A Voinov, and Alex I Smirnov. Spin probes and spin labels. *Encyclopedia of Analytical Chemistry: Applications, Theory and Instrumentation*, 2006.

[141] AD Milov, AG Maryasov, and Yu D Tsvetkov. Pulsed electron double resonance (peldor) and its applications in free-radicals research. *Applied Magnetic Resonance*, 15:107–143, 1998.

[142] Gunnar Jeschke. The contribution of modern epr to structural biology. *Emerging Topics in Life Sciences*, 2(1):9–18, 2018.

[143] Gunnar Jeschke. Deer distance measurements on proteins. *Annual review of physical chemistry*, 63(1):419–446, 2012.

[144] Olav Schiemann and Thomas F Prisner. Long-range distance determinations in biomacromolecules by epr spectroscopy. *Quarterly reviews of biophysics*, 40(1):1–53, 2007.

[145] Johann P Klare and Heinz-Jürgen Steinhoff. Spin labeling epr. *Photosynthesis research*, 102:377–390, 2009.

[146] Peter P Borbat, Jack H Freed, D Goldfarb, and S Stoll. Dipolar spectroscopy—single-resonance methods. *EPR Spectroscopy: Fundamentals and Methods*, page 425, 2018.

[147] Gunnar Jeschke. Dipolar spectroscopy—double-resonance methods. *EPR Spectroscopy: Fundamentals and methods*, pages 401–423, 2016.

[148] Axel Muller, Emmanuele Severi, Christopher Mulligan, Andrew G Watts, David J Kelly, Keith S Wilson, Anthony J Wilkinson, and Gavin H Thomas. Conservation of structure and mechanism in primary and secondary transporters exemplified by siap, a sialic acid binding virulence factor from haemophilus influenzae. *Journal of Biological Chemistry*, 281(31):22212–22222, 2006.

[149] Christopher Mulligan, Marcus Fischer, and Gavin H Thomas. Tripartite atp-independent periplasmic (trap) transporters in bacteria and archaea. *FEMS microbiology reviews*, 35(1):68–86, 2011.

[150] Stephen J Juris, Amy E Rudolph, Don Huddler, Kim Orth, and Jack E Dixon. A distinctive role for the yersinia protein kinase: actin binding, kinase activation, and cytoskeleton disruption. *Proceedings of the National Academy of Sciences*, 97(17):9431–9436, 2000.

[151] Claudia Trasak, Gerhardt Zenner, Annette Vogel, Gulnihal Yuksekdag, René Rost, Ilka Haase, Markus Fischer, Lars Israel, Axel Imhof, Stefan Linder, et al. Yersinia protein kinase yopo is activated by a novel g-actin binding process. *Journal of Biological Chemistry*, 282(4):2268–2277, 2007.

[152] Jason A Hall, Thorgeir E Thorgeirsson, Jun Liu, Yeon-Kyun Shin, and Hiroshi Nikaido. Two modes of ligand binding in maltose-binding protein ofescherichia coli: Electron paramagnetic resonance study of ligand-induced global conformational changes by site-directed spin labeling. *Journal of Biological Chemistry*, 272(28):17610–17614, 1997.

[153] Chun Tang, Charles D Schwieters, and G Marius Clore. Open-to-closed transition in apo maltose-binding protein observed by paramagnetic nmr. *Nature*, 449(7165):1078–1082, 2007.

[154] Faizah Fulyani, Gea K Schuurman-Wolters, Andreja Vujičić Žagar, Albert Guskov, Dirk-Jan Slotboom, and Bert Poolman. Functional diversity of tandem substrate-binding domains in abc transporters from pathogenic bacteria. *Structure*, 21(10):1879–1888, 2013.

[155] Gea K Schuurman-Wolters and Bert Poolman. Substrate specificity and ionic regulation of glnpq from lactococcus lactis: an atp-binding cassette transporter with four extracytoplasmic substrate-binding domains. *Journal of Biological Chemistry*, 280(25):23785–23790, 2005.

[156] Jasper HM Van Der Velde, Jens Oelerich, Jingyi Huang, Jochem H Smit, Atieh Aminian Jazi, Silvia Galiani, Kirill Kolmakov, Giorgos Gouridis, Christian Eggeling, Andreas Herrmann, et al. A simple and versatile design concept for fluorophore derivatives with intramolecular photostabilization. *Nature communications*, 7(1):10144, 2016.

[157] Yun-Wei Chiang, Peter P Borbat, and Jack H Freed. The determination of pair distance distributions by pulsed esr using tikhonov regularization. *Journal of Magnetic Resonance*, 172(2):279–295, 2005.

[158] Gunnar Jeschke, Victor Chechik, Petre Ionita, Adelheid Godt, Herbert Zimmermann, J Banham, Christiane R Timmel, D Hilger, and H Jung. Deeranalysis2006—a comprehensive software package for analyzing pulsed eldor data. *Applied magnetic resonance*, 30:473–498, 2006.

[159] Steven G Worswick, James A Spencer, Gunnar Jeschke, and Ilya Kuprov. Deep neural network processing of deer data. *Science advances*, 4(8):eaat5218, 2018.

[160] Gregor Hagelueken, Richard Ward, James H Naismith, and Olav Schiemann. Mtsslwizard: in silico spin-labeling and generation of distance distributions in pymol. *Applied magnetic resonance*, 42:377–391, 2012.

[161] Marijn de Boer, Giorgos Gouridis, Yusran Abdillah Muthahari, and Thorben Cordes. Single-molecule observation of ligand binding and conformational changes in feua. *Biophysical journal*, 117(9):1642–1654, 2019.

[162] Fahad Rashid, Vlad-Stefan Raducanu, Manal S Zaher, Muhammad Tehseen, Satoshi Habuchi, and Samir M Hamdan. Initial state of dna-dye complex sets the stage for protein induced fluorescence modulation. *Nature communications*, 10(1):2104, 2019.

[163] Helen Hwang, Hajin Kim, and Sua Myong. Protein induced fluorescence enhancement as a single molecule assay with short distance sensitivity. *Proceedings of the National Academy of Sciences*, 108(18):7414–7418, 2011.

[164] Eitan Lerner, Evelyn Ploetz, Johannes Hohlbein, Thorben Cordes, and Shimon Weiss. A quantitative theoretical framework for protein-induced fluorescence enhancement–forster-type resonance energy transfer (pife-fret). *The Journal of Physical Chemistry B*, 120(26):6401–6410, 2016.

[165] OTTO Glatter. A new method for the evaluation of small-angle scattering data. *Journal of applied crystallography*, 10(5):415–421, 1977.

[166] Michel HJ Koch, Patrice Vachette, and Dmitri I Svergun. Small-angle scattering: a view on the properties, structures and structural changes of biological macromolecules in solution. *Quarterly reviews of biophysics*, 36(2):147–227, 2003.

[167] Jan Lipfert and Sebastian Doniach. Small-angle x-ray scattering from rna, proteins, and protein complexes. *Annu. Rev. Biophys. Biomol. Struct.*, 36(1):307–327, 2007.

[168] HB Stuhrmann. Resonance scattering in macromolecular structure research. In *Characterization of Polymers in the Solid State II: Synchrotron Radiation, X-ray Scattering and Electron Microscopy*, pages 123–163. Springer, 2005.

[169] HB t Stuhrmann, H Notbohm, et al. The configuration of the four iron atoms in dissolved human hemoglobin as studied by anomalous dispersion. *Acta Crystallographica Section A: Foundations of Crystallography*, 37:C308–C308, 1981.

[170] RC Miake-Lye, S Doniach, and KO Hodgson. Anomalous x-ray scattering from terbium-labeled parvalbumin in solution. *Biophysical Journal*, 41(3):287–292, 1983.

[171] HB Stuhrmann. Anomalous small angle scattering. *Quarterly reviews of biophysics*, 14(3):433–462, 1981.

[172] Valerie J Pinfield and David J Scott. Anomalous small angle x-ray scattering simulations: Proof of concept for distance measurements for nanoparticle-labelled biomacromolecules in solution. *PLoS One*, 9(4):e95664, 2014.

[173] Thomas Zettl, Rebecca S Mathew, Sonke Seifert, Sebastian Doniach, Pehr AB Harbury, and Jan Lipfert. Absolute intramolecular distance measurements with angstrom-resolution using anomalous small-angle x-ray scattering. *Nano Letters*, 16(9):5353–5357, 2016.

[174] Gunnar Jeschke. Distance measurements in the nanometer range by pulse epr. *ChemPhysChem*, 3(11):927–932, 2002.

[175] Richard Ward, Andrew Bowman, Erman Sozudogru, Hassane El-Mkami, Tom Owen-Hughes, and David G Norman. Epr distance measurements in deuterated proteins. *Journal of Magnetic Resonance*, 207(1):164–167, 2010.

[176] Zhongyu Yang, Gonzalo Jimenez-Oses, Carlos J Lopez, Michael D Bridges, KN Houk, and Wayne L Hubbell. Long-range distance measurements in proteins at physiological temperatures using saturation recovery epr spectroscopy. *Journal of the American Chemical Society*, 136(43):15356–15365, 2014.

[177] Georg Krainer, Andreas Hartmann, and Michael Schlierf. farfret: extending the range in single-molecule fret experiments beyond 10 nm. *Nano letters*, 15(9):5826–5829, 2015.

[178] Florante A Quiocho, John C Spurlino, and Lynn E Rodseth. Extensive features of tight oligosaccharide binding revealed in high-resolution structures of the maltodextrin transport/chemosensory receptor. *Structure*, 5(8):997–1015, 1997.

[179] Patrick G Telmer and Brian H Shilton. Insights into the conformational equilibria of maltose-binding protein by analysis of high affinity mutants. *Journal of Biological Chemistry*, 278(36):34555–34567, 2003.

[180] Mathias Brust, Merryl Walker, Donald Bethell, David J Schiffrin, and Robin Whyman. Synthesis of thiol-derivatised gold nanoparticles in a two-phase liquid–liquid system. *Journal of the Chemical Society, Chemical Communications*, (7):801–802, 1994.

[181] Fabio D Steffen, Roland KO Sigel, and Richard Börner. Fretraj: integrating single-molecule spectroscopy with molecular dynamics. *Bioinformatics*, 37(21):3953–3955, 2021.

[182] Xiaoni Fang, Yongzan Zheng, Yaokai Duan, Yang Liu, and Wenwan Zhong. Recent advances in design of fluorescence-based assays for high-throughput screening. *Analytical chemistry*, 91(1):482–504, 2018.

[183] J Lizbeth Reyes Zamora and Hector C Aguilar. Flow virometry as a tool to study viruses. *Methods*, 134:87–97, 2018.

[184] George C Brittain IV, Yong Q Chen, Edgar Martinez, Vera A Tang, Tyler M Renner, Marc-André Langlois, and Sergei Gulnik. A novel semiconductor-based flow cytometer with enhanced

light-scatter sensitivity for the analysis of biological nanoparticles. *Scientific reports*, 9(1):16039, 2019.

[185] Azam Bagheri Pebdeni, Amirreza Roshani, Ensiyeh Mirsadoughi, Shakila Behzadifar, and Morteza Hosseini. Recent advances in optical biosensors for specific detection of e. coli bacteria in food and water. *Food Control*, 135:108822, 2022.

[186] Shaik Ahmadsaidulu, Oindrila Banik, Prasoon Kumar, Santosh Kumar, and Earu Banoth. Microfluidic point-of-care diagnostics for multi-disease detection using optical techniques: a review. *IEEE Transactions on NanoBioscience*, 2023.

[187] Guillermo Marqués, Thomas Pengo, and Mark A Sanders. Imaging methods are vastly underreported in biomedical research. *Elife*, 9:e55133, 2020.

[188] Rory M Power and Jan Huisken. Putting advanced microscopy in the hands of biologists. *Nature Methods*, 16(11):1069–1073, 2019.

[189] Johannes Hohlbein, Benedict Diederich, Barbora Marsikova, Emmanuel G Reynaud, Séamus Holden, Wiebke Jahr, Robert Haase, and Kirti Prakash. Open microscopy in the life sciences: quo vadis? *Nature methods*, 19(9):1020–1025, 2022.

[190] Benjamin Ambrose, James M Baxter, John Cully, Matthew Willmott, Elliot M Steele, Benji C Bateman, Marisa L Martin-Fernandez, Ashley Cadby, Jonathan Shewring, Marleen Aaldering, et al. The smfbox is an open-source platform for single-molecule fret. *Nature communications*, 11(1):5641, 2020.

[191] Rita Strack. The micube open microscope. *Nature Methods*, 16(10):958–958, 2019.

[192] Ryan P McNamara, Yijun Zhou, Anthony B Eason, Justin T Landis, Meredith G Chambers, Smaranda Willcox, Tiffany A Peterson, Blake Schouest, Nicholas J Maness, Andrew G MacLean, et al. Imaging of surface microdomains on individual extracellular vesicles in 3-d. *Journal of Extracellular Vesicles*, 11(3):e12191, 2022.

[193] Andrew McMahon, Rebecca Andrews, Danielle Groves, Sohail V Ghani, Thorben Cordes, Achillefs N Kapanidis, and Nicole C Robb. High-throughput super-resolution analysis of influenza virus pleomorphism reveals insights into viral spatial organization. *PLoS Pathogens*, 19(6):e1011484, 2023.

[194] Mark F Santos, Germana Rappa, Jana Karbanová, Patrizia Diana, Girolamo Cirrincione, Daniela Carbone, David Manna, Feryal Aalam, David Wang, Cheryl Vanier, et al. Hiv-1-induced nuclear invaginations mediated by vap-a, orp3, and rab7 complex explain infection of activated t cells. *Nature Communications*, 14(1):4588, 2023.

[195] James WP Brown, Arnaud Bauer, Mark E Polinkovsky, Akshay Bhumkar, Dominic JB Hunter, Katharina Gaus, Emma Sierecki, and Yann Gambin. Single-molecule detection on a portable 3d-printed microscope. *Nature communications*, 10(1):5662, 2019.

[196] Benedict Diederich, René Lachmann, Swen Carlstedt, Barbora Marsikova, Haoran Wang, Xavier Uwurukundo, Alexander S Mosig, and Rainer Heintzmann. A versatile and customizable low-cost 3d-printed open standard for microscopic imaging. *Nature communications*, 11(1):5979, 2020.

[197] Ando Christian Zehrer, Ana Martin-Villalba, Benedict Diederich, and Helge Ewers. An open-source, high-resolution, automated fluorescence microscope. *Elife*, 12:RP89826, 2024.

[198] RR Duncan, A Bergmann, MA Cousin, David K Apps, and Michael J Shipston. Multi-dimensional time-correlated single photon counting (tcspc) fluorescence lifetime imaging microscopy (flim) to detect fret in cells. *Journal of microscopy*, 215(1):1–12, 2004.

[199] Ashok A Deniz, Maxime Dahan, Jocelyn R Grunwell, Taekjip Ha, Ann E Faulhaber, Daniel S Chemla, Shimon Weiss, and Peter G Schultz. Single-pair fluorescence resonance energy transfer on freely diffusing molecules: observation of förster distance dependence and subpopulations. *Proceedings of the National Academy of Sciences*, 96(7):3670–3675, 1999.

[200] Rahul Roy, Sungchul Hohng, and Taekjip Ha. A practical guide to single-molecule fret. *Nature methods*, 5(6):507–516, 2008.

[201] Evangelos Sisamakis, Alessandro Valeri, Stanislav Kalinin, Paul J Rothwell, and Claus AM Seidel. Accurate single-molecule fret studies using multiparameter fluorescence detection. In *Methods in enzymology*, volume 475, pages 455–514. Elsevier, 2010.

[202] Björn Hellenkamp, Philipp Wortmann, Florian Kandzia, Martin Zacharias, and Thorsten Hugel. Multidomain structure and correlated dynamics determined by self-consistent fret networks. *Nature methods*, 14(2):174–180, 2017.

[203] Benjamin Schuler, Everett A Lipman, and William A Eaton. Probing the free-energy surface for protein folding with single-molecule fluorescence spectroscopy. *Nature*, 419(6908):743–747, 2002.

[204] Jürgen J Schmied, Mario Raab, Carsten Forthmann, Enrico Pibiri, Bettina Wünsch, Thorben Dammeyer, and Philip Tinnefeld. Dna origami–based standards for quantitative fluorescence microscopy. *Nature protocols*, 9(6):1367–1391, 2014.

[205] Kira Bartnik, Anders Barth, Mauricio Pilo-Pais, Alvaro H Crevenna, Tim Liedl, and Don C Lamb. A dna origami platform for single-pair forster resonance energy transfer investigation of dna–dna interactions and ligation. *Journal of the American Chemical Society*, 142(2):815–825, 2019.

[206] Seamus J Holden, Stephan Uphoff, Johannes Hohlbein, David Yadin, Ludovic Le Reste, Oliver J Britton, and Achillefs N Kapanidis. Defining the limits of single-molecule fret resolution in tirf microscopy. *Biophysical journal*, 99(9):3102–3111, 2010.

[207] Ludovic Le Reste, Johannes Hohlbein, Kristofer Gryte, and Achillefs N Kapanidis. Characterization of dark quencher chromophores as nonfluorescent acceptors for single-molecule fret. *Biophysical journal*, 102(11):2658–2668, 2012.

[208] Dieter Klein. Quantification using real-time pcr technology: applications and limitations. *Trends in molecular medicine*, 8(6):257–260, 2002.

[209] Franz Watzinger, K Ebner, and T Lion. Detection and monitoring of virus infections by real-time pcr. *Molecular aspects of medicine*, 27(2-3):254–298, 2006.

[210] Ian M Mackay, Katherine E Arden, and Andreas Nitsche. Real-time pcr in virology. *Nucleic acids research*, 30(6):1292–1305, 2002.

[211] Kishore R Kumar, Mark J Cowley, and Ryan L Davis. Next-generation sequencing and emerging technologies. In *Seminars in thrombosis and hemostasis*. Thieme Medical Publishers, 2024.

[212] Jay Shendure and Hanlee Ji. Next-generation dna sequencing. *Nature biotechnology*, 26(10):1135–1145, 2008.

[213] Anna Andrew, Tholasi Nadhan Navien, Tzi Shien Yeoh, Marimuthu Citartan, Ernest Mangantig, Magdline SH Sum, Ewe Seng Ch'ng, and Thean-Hock Tang. Diagnostic accuracy of serological tests for the diagnosis of chikungunya virus infection: A systematic review and meta-analysis. *PLoS Neglected Tropical Diseases*, 16(2):e0010152, 2022.

[214] Marcarious M Tantuoyir and Nima Rezaei. Serological tests for covid-19: Potential opportunities. *Cell Biology International*, 45(4):740–748, 2021.

[215] Seiichi Sakamoto, Waraporn Putalun, Sornkanok Vimolmangkang, Waranyoo Phoolcharoen, Yukihiro Shoyama, Hiroyuki Tanaka, and Satoshi Morimoto. Enzyme-linked immunosorbent assay for the quantitative/qualitative analysis of plant secondary metabolites. *Journal of natural medicines*, 72:32–42, 2018.

[216] Marco Ciotti, Massimo Ciccozzi, Alessandro Terrinoni, Wen-Can Jiang, Cheng-Bin Wang, and Sergio Bernardini. The covid-19 pandemic. *Critical reviews in clinical laboratory sciences*, 57(6):365–388, 2020.

[217] Nahal Eshghifar, Ali Busheri, Rojeet Shrestha, and Safedin Beqaj. Evaluation of analytical performance of seven rapid antigen detection kits for detection of sars-cov-2 virus. *International journal of general medicine*, pages 435–440, 2021.

[218] Qian Niu, Ling Ma, Shaobin Zhu, Lan Li, Qisheng Zheng, Jibo Hou, Hong Lian, Lina Wu, and Xiaomei Yan. Quantitative assessment of the physical virus titer and purity by ultrasensitive flow virometry. *Angewandte Chemie*, 133(17):9437–9442, 2021.

[219] Stefan Wennmalm and Jerker Widengren. Inverse-fluorescence cross-correlation spectroscopy. *Analytical chemistry*, 82(13):5646–5651, 2010.

[220] Stefan Wennmalm and Jerker Widengren. Inverse-fluorescence correlation spectroscopy: more information and less labeling. *Frontiers in Bioscience*, 3:385–392, 2011.

[221] Joshua B Edel and Andrew J de MELLO. Single particle confocal fluorescence spectroscopy in microchannels: Dependence of burst width and burst area distributions on particle size and flow rate. *Analytical sciences*, 19(7):1065–1069, 2003.

[222] Yfat Yahalom-Ronen, Hadas Tamir, Sharon Melamed, Boaz Politi, Ohad Shifman, Hagit Achdout, Einat B Vitner, Ofir Israeli, Elad Milrot, Dana Stein, et al. A single dose of recombinant vsv- g-spike vaccine provides protection against sars-cov-2 challenge. *Nature communications*, 11(1):6402, 2020.

[223] Beata Sweryda-Krawiec, Halagowder Devaraj, George Jacob, and James J Hickman. A new interpretation of serum albumin surface passivation. *Langmuir*, 20(6):2054–2056, 2004.

[224] Paula Rozo-Lopez, Barbara S Drolet, and Berlin Londoño-Renteria. Vesicular stomatitis virus transmission: A comparison of incriminated vectors. *Insects*, 9(4):190, 2018.

[225] Na Zhu, Dingyu Zhang, Wenling Wang, Xingwang Li, Bo Yang, Jingdong Song, Xiang Zhao, Baoying Huang, Weifeng Shi, Roujian Lu, et al. A novel coronavirus from patients with pneumonia in china, 2019. *New England journal of medicine*, 382(8):727–733, 2020.

[226] Kelvin Kai-Wang To, Owen Tak-Yin Tsang, Wai-Shing Leung, Anthony Raymond Tam, Tak-Chiu Wu, David Christopher Lung, Cyril Chik-Yan Yip, Jian-Piao Cai, Jacky Man-Chun Chan, Thomas Shiu-Hong Chik, et al. Temporal profiles of viral load in posterior oropharyngeal saliva samples and serum antibody responses during infection by sars-cov-2: an observational cohort study. *The Lancet infectious diseases*, 20(5):565–574, 2020.

[227] Sungmin Hong, Pei-Hsiang Tsou, Chao-Kai Chou, Hirohito Yamaguchi, Chin B Su, Mien-Chie Hung, and Jun Kameoka. Microfluidic three-dimensional hydrodynamic flow focusing for the rapid protein concentration analysis. *Biomicrofluidics*, 6(2), 2012.

[228] Daniel Nettels, Nicola Galvanetto, Miloš T Ivanović, Mark Nüesch, Tianjin Yang, and Benjamin Schuler. Single-molecule fret for probing nanoscale biomolecular dynamics. *Nature Reviews Physics*, 6(10):587–605, 2024.

[229] Joana Fort, Adrià Nicolàs-Aragó, Luca Maggi, Maria Martinez-Molledo, Despoina Kapiki, Paula González-Novoa, Patricia Gómez-Gejo, Niels Zijlstra, Susanna Bodoy, Els Pardon, et al. The conserved lysine residue in transmembrane helix 5 is pivotal for the cytoplasmic gating of the l-amino acid transporters. *PNAS nexus*, 4(1):pgae584, 2025.

[230] Kilian Roßmann, Kerem C Akkaya, Pascal Poc, Corentin Charbonnier, Jenny Eichhorst, Hannes Gonschior, Abha Valavalkar, Nicolas Wendler, Thorben Cordes, Benjamin Dietzek-Ivanšić, et al. N-methyl deuterated rhodamines for protein labelling in sensitive fluorescence microscopy. *Chemical Science*, 13(29):8605–8617, 2022.

[231] Benjamin Schuler. Single-molecule fret of protein structure and dynamics-a primer. *Journal of nanobiotechnology*, 11(Suppl 1):S2, 2013.

[232] Kim Bartels, Tanya Lasitza-Male, Hagen Hofmann, and Christian Löw. Single-molecule fret of membrane transport proteins. *ChemBioChem*, 22(17):2657–2671, 2021.

[233] Marko Sustarsic and Achillefs N Kapanidis. Taking the ruler to the jungle: single-molecule fret for understanding biomolecular structure and dynamics in live cells. *Current opinion in structural biology*, 34:52–59, 2015.

[234] Zhongying Han, Sabrina Panhans, Sophie Brameyer, Ecenaz Bilgen, Marija Ram, Anna Herr, Alessandra Narducci, Michael Isselstein, Paul D Harris, Oliver Brix, et al. Dissecting mechanisms of ligand binding and conformational changes in the glutamine-binding protein. *bioRxiv*, 2023-08.

[235] Lauren Ann Metskas and Elizabeth Rhoades. Single-molecule fret of intrinsically disordered proteins. *Annual Review of Physical Chemistry*, 71(1):391–414, 2020.

[236] Niels Vandenberk, Anders Barth, Doortje Borrenberghs, Johan Hofkens, and Jelle Hendrix. Evaluation of blue and far-red dye pairs in single-molecule forster resonance energy transfer experiments. *The Journal of Physical Chemistry B*, 122(15):4249–4266, 2018.

[237] Fabio CL Almeida, Karoline Sanches, Ramon Pinheiro-Aguiar, Vitor S Almeida, and Icaro P Caruso. Protein surface interactions—theoretical and experimental studies. *Frontiers in Molecular Biosciences*, 8:706002, 2021.

[238] Dominique Hagemans, Ianthe AEM Van Belzen, Tania Morán Luengo, and Stefan GD Rüdiger. A script to highlight hydrophobicity and charge on protein surfaces. *Frontiers in molecular biosciences*, 2:56, 2015.

[239] Marco Scarsi, Nicolas Majeux, and Amedeo Caflisch. Hydrophobicity at the surface of proteins. *Proteins: Structure, Function, and Bioinformatics*, 37(4):565–575, 1999.

[240] Yan Yuan Tseng and Wen-Hsiung Li. Classification of protein functional surfaces using structural characteristics. *Proceedings of the National Academy of Sciences*, 109(4):1170–1175, 2012.

[241] Paul David Harris, Alessandra Narducci, Christian Gebhardt, Thorben Cordes, Shimon Weiss, and Eitan Lerner. Multi-parameter photon-by-photon hidden markov modeling. *Nature communications*, 13(1):1000, 2022.

[242] Neil T Hunt. Biomolecular infrared spectroscopy: making time for dynamics. *Chemical Science*, 15(2):414–430, 2024.

[243] Tamar Schlick, Eric Barth, and Margaret Mandziuk. Biomolecular dynamics at long timesteps: Bridging the timescale gap between simulation and experimentation. *Annual review of biophysics and biomolecular structure*, 26(1):181–222, 1997.

[244] Steffen Wolf, Benjamin Lickert, Simon Bray, and Gerhard Stock. Multisecond ligand dissociation dynamics from atomistic simulations. *Nature communications*, 11(1):2918, 2020.

[245] BW Van der Meer. Kappa-squared: from nuisance to new sense. *Reviews in Molecular Biotechnology*, 82(3):181–196, 2002.

[246] Dilip Shrestha, Attila Jenei, Péter Nagy, György Vereb, and János Szöllősi. Understanding fret as a research tool for cellular studies. *International journal of molecular sciences*, 16(4):6718–6756, 2015.

[247] Silvia E Braslavsky, Eduard Fron, Hernán B Rodríguez, Enrique San Román, Gregory D Scholes, Gerd Schweitzer, Bernard Valeur, and Jakob Wirz. Pitfalls and limitations in the practical use of förster's theory of resonance energy transfer. *Photochemical & Photobiological Sciences*, 7:1444–1448, 2008.

[248] N Erlenbach, B Endeward, P Schöps, DB Gophane, S Th Sigurdsson, and TF Prisner. Flexibilities of isoindoline-derived spin labels for nucleic acids by orientation selective peldor. *Physical Chemistry Chemical Physics*, 18(24):16196–16201, 2016.

[249] Silvia Valera, Katrin Ackermann, Christos Pliotas, Hexian Huang, James H Naismith, and Bela E Bode. Accurate extraction of nanometer distances in multimers by pulse epr. *Chemistry–A European Journal*, 22(14):4700–4703, 2016.

[250] Anders Barth, Lena Voith von Voithenberg, and Don C Lamb. Quantitative single-molecule three-color forster resonance energy transfer by photon distribution analysis. *The Journal of Physical Chemistry B*, 123(32):6901–6916, 2019.